

UNIVERSIDADE DE LISBOA
INSTITUTO SUPERIOR TÉCNICO
AALTO UNIVERSITY
UNDER ERASMUS MUNDUS PROGRAM

**Application of biodegradable substrates and inkjet
printing in dye-sensitized solar cells**

Merve Özkan

Supervisors: Doctor Jouni Paltakari
Doctor Carlos Augusto Santos Silva

Thesis approved in public session to obtain the PhD
degree in Sustainable Energy Systems

2017

UNIVERSIDADE DE LISBOA
INSTITUTO SUPERIOR TÉCNICO
AALTO UNIVERSITY

UNDER ERASMUS MUNDUS PROGRAM

**Application of biodegradable substrates and inkjet
printing in dye-sensitized solar cells**

Merve Özkan

Supervisors: Doctor Jouni Paltakari
Doctor Carlos Augusto Santos Silva

JURY

Doctor Neil Robertson, School of Chemistry, University of
Edinburgh, UK

Doctor Antti Karttunen, School of Chemical Engineering, Aalto
University, Finland

Doctor Killian Lobato, Faculdade de Ciências, Universidade de
Lisboa

Doctor Carlos Augusto Santos Silva, Instituto Superior Técnico,
Universidade de Lisboa

Doctor João Manuel Gregório Mascarenhas, Laboratório Nacional de
Energia e Geologia

Funding Institution

Education, Audio-visual, and Culture Executive Agency (EACEA)
(Nr 2012-0034) of the European Commission.

2017

Resumo

As células solares sensibilizadas por corantes (DSSCs) são dispositivos eletroquímicos, que convertem a energia dos fótons em energia elétrica. Estas células são candidatos promissores a unidades alternativas de energia para equipamentos eletrônicos de pequena escala. Apesar dos enormes esforços dedicados à pesquisa do DSSC, a integração de dispositivos de alta eficiência nos substratos à base de celulose não foi ainda alcançada, devido aos desafios impostos pelo eletrólito líquido do dispositivo. Para além disso, o desperdício de precursores, ao mesmo tempo que produzem camadas processáveis em solução desses dispositivos, a quantidade de deposição descontrolada e a posição das camadas, bem como a dependência dos substratos de vidro pré-perfurados, não são práticas para muitas das aplicações.

Os objetivos deste trabalho foram explicar as consequências da substituição do contra-eletrodo convencional (CE), geralmente produzido no substrato de vidro, com uma alternativa baseada em celulose e a introdução do método de impressão a jato de tinta na sequência de fabricação do dispositivo.

Inicialmente, os CEs alternativos foram produzidos numa folha de celulose laminada, cobrindo-a com uma tinta de nanotubo de carbono de parede simples (SWCNT) e, posteriormente, tinta de poli (3,4-etilenodioxitiofeno) (PEDOT-TsO) dopada com toluenosulfonato. Os novos CE apresentaram flexibilidade e baixa resistência à transferência de carga. Além disso, as células produzidas com estas CE revelaram apenas cerca de 20% menos eficiência de conversão de energia em comparação com as células de referência contendo óxido de estanho / FTC / platina com gás fluorado.

EM seguida, o trabalho focou-se na impressão a jato de tinta das camadas de corante e platina, bem como do eletrólito de DSSCs. Inicialmente, os três eletrólitos mais populares de acordo com a pesquisa DSSC foram caracterizados em termos das propriedades físico-químicas. Então, o eletrólito menos dilatante com a maior tensão superficial e ponto de ebulição foi impresso a jacto de tinta na superfície de óxido mesoporoso sensibilizado para produzir DSSCs.

Graças a este método, a sequência de fabricação do dispositivo ficou obviamente mais fácil e o dispositivo contendo eletrólito impresso a jato de tinta apresentou menos perdas resistivas e boa estabilidade.

A maneira convencional de sensibilizar a superfície do óxido mesoporoso é expondo-a a uma solução diluída de corante por longas horas. Além da carga ambiental de desperdiçar corantes à base de Ru, a precisão na posição e na quantidade da camada de corante não pode ser controlada. Para superar todos esses desafios acima mencionados, a impressão a jato de tinta foi proposta como um novo método para a etapa de sensibilização. Não apresentando desvantagem nem no desempenho fotovoltaico nem na estabilidade do desempenho, as células feitas de elétrodos fotográficos com corantes impressos a jato de tinta abrem a porta para dispositivos solares feitos sob medida com intensidade sintonizada de várias cores. A platina, um material escasso e caro, é o catalisador tradicional para os DSSCs. É depositado lançando uma gota nos substratos de vidro revestidos com FTO para a produção em escala de laboratório de DSSCs. Para minimizar o desperdício de platina e criar camadas de catalisador com precisão, com transparência feita sob medida, o precursor de platina foi impresso a jato de tinta. Posteriormente, as camadas impressas foram caracterizadas em termos de morfologia, transmitância e eletroquímica. O catalisador impresso a jato de tinta com a mesma quantidade de carregamento de platina que as células de referência, exibiu uma eficiência de conversão de potência similar de cerca de 7% às células de referência. Além disso, as células com platina impressa a jato de tinta foram capazes de manter as suas eficiências após um teste de envelhecimento acelerado.

Palavras-Chave: células solares sensibilizadas por corantes, impressão por jacto de tinta, substratos biodegradáveis, eficiência, estabilidade

Abstract

Dye-sensitized solar cells (DSSCs) are electrochemical devices, which convert the photon energy to electrical energy. They are promising alternative power unit candidates for small-scale electronics. Despite of enormous efforts devoted to the DSSCs research, the integration of high efficiency devices onto the cellulose based substrates have not been achieved due to the challenging liquid electrolyte in the device. Additionally, the precursor wastage while producing solution processable layers of these devices, uncontrolled deposition amount and position of the layers as well as the dependence on the pre-drilled glass substrates are not practical for many applications.

The aims of this work were to explain the consequences of replacing the conventional counter electrode (CE) generally produced on the glass substrate with a cellulose based alternative and introducing the inkjet printing method into the device fabrication sequence.

In this thesis, initially, the alternative CEs were produced on a laminated cellulose sheet by coating it with a single walled carbon nanotube (SWCNT) ink and subsequently p-toluenesulfonate doped poly (3,4-ethylenedioxythiophene) (PEDOT-TsO) ink. The new CEs exhibited flexibility and low charge transfer resistance. Additionally, the cells produced with these CEs revealed only around 20% less power conversion efficiency compared to the reference cells containing glass/ fluorine-doped tin oxide (FTO)/platinum.

The rest of the thesis was devoted to the inkjet printing of the dye and platinum layers as well as the electrolyte of DSSCs. Initially, the popular three electrolytes in DSSC research were characterized in terms of their physiochemical properties. Then, the least dilatant electrolyte with the highest surface tension and boiling point was inkjet-printed on the sensitized mesoporous oxide surface to produce DSSCs. Thanks to this method, the device fabrication sequence remarkably got easier and the device containing inkjet-printed electrolyte exhibited less resistive losses and good stability.

The conventional way of sensitizing the mesoporous oxide surface is exposing it to a dilute solution of dye for long hours. In addition to the environmental burden of wasting Ru based dyes, the precision in the position and amount of the dye layer cannot be controlled. In order to overcome all these aforementioned challenges, the inkjet printing was proposed as a new method for sensitization step. Exhibiting no disadvantage neither in the photovoltaic performance nor in the performance stability, the cells made of photo electrodes with inkjet printed dyes open the door for tailor-made solar devices with tuned intensity of various colors.

Platinum, a scarce and expensive material, is the traditional catalyst for the DSSCs and it is deposited by casting a drop on the FTO coated glass substrates for the lab-scale production of DSSCs. To minimize the platinum wastage and create precisely patterned catalyst layers with custom-made transparency, the platinum precursor was inkjet printed. Afterwards, the printed layers were characterized in terms of morphology, transmittance and electrochemistry. The inkjet printed catalyst with the same amount of platinum loading as the reference cells, exhibited a similar power conversion efficiency of around 7% to the reference cells. Moreover, the cells with inkjet Printed platinum were able to maintain their efficiencies after an accelerated aging test. Key-words: inkjet printing, dye-sensitized solar cells, biodegradable substrates, efficiency, stability

Acknowledgments

The work presented in this thesis was carried out in the research group of Paper Converting and Packaging, in the Department of Bioproducts and Biosystems (previously Department of Forest Products Technology), at the School of Chemical Engineering of Aalto University, between 2013 and 2017. Erasmus Mundus Joint Doctorate program, Environomical Pathways for Sustainable Energy Services (SELECT+) and Stora Enso are acknowledged for funding of the research work. Under SELECT+ program frame, my host university was Instituto Superior Técnico. School of Chemical Engineering of Aalto University supported the final writing work of the thesis.

First of all, I am grateful to Prof. Jouni Paltakari for the opportunity to join his research group and his constant support. I also thank my instructor Dr. Ghufan Hashmi for his guidance and help. I also owe thanks to my coauthors, Dr. Janne Halme, Dr. Alp Karakoc and Dr. Katarina Dimic-Misic as well as my co-supervisor Prof. Carlos Silva and co-instructor Prof. Killian Lobato. I am also thankful to Prof. Peter Lund for our collaboration.

I am grateful to SELECT+ team for creating this career opportunity. The coordination team worked so hard for us. Sirje Liukko, Chamindie Senaratne, Anja Hänninen and Leena Hauhio, thank you so much for everything! Anja, I still remember the moment you welcomed me to Finland in Vantaa airport. During my doctoral research, Saija Helasuo and Ulla Ahlgren made the travelling so easy for me.

This work would not have been accomplished in the absence of the Stora Enso support and I appreciate their interest in my research. Thank you Simo Siitonen and Duncan Mayes.

I wish to thank preliminary examiners Prof. Ronald Österbacka and Associate Prof. Jonas Örtengren for their constructive feedback, which helped me in finalizing this thesis.

Department of Bioproducts and Biosystems has a great team of the laboratory personnel and this team made everything easier for me. I would also like to thank to the contributors of the scientific symposiums held in coffee room and corridors of Department of Bioproducts and Biosystems. I especially enjoyed the time spent in my office thanks to my roommate, Lourdes Rodríguez. I also wish to thank my friends. This work was completed thanks to their support.

Finally, my deepest appreciation goes to my parents and my brother for their love and support.

A handwritten signature in black ink, appearing to read 'Merve Özkan', written in a cursive style.

Merve Özkan
Espoo, August 2017

Contents

Abstract (Portuguese).....	ii
Abstract (English)	iv
Acknowledgments.....	vi
List of Figures	4
List Of Tables.....	6
Nomenclature	8
Personal references.....	10
Chapter 1: Introduction	14
1.1 Research motivation	14
1.2 Thesis scope and outline.....	15
Chapter 2: Background.....	20
2.1. Inkjet printing technology	20
2.1.1. Introduction.....	20
2.1.2. Piezoelectric DOD inkjet printing	21
2.1.3. Inkjet printing inks	23
2.1.4. Droplet formation and jet trajectory.....	26
2.2. Substrate-ink interaction.....	27
2.3. Dye-sensitized solar cells (DSSCs)	28
2.3.1. Device performance characteristics	29
Chapter 3: Materials and Methods	36
3.1. Inkjet printing	36
3.1.1. Ink characterization.....	36
3.1.2. Printing process.....	37
3.1.3. Printed layers	40
3.2. DSSC	40
3.2.1. Substrate evaluation	40
3.2.2. Device fabrication	43
3.2.3. Electrochemical cell parameters	44

3.3. Other characterization methods	44
3.3.1. Transmittance	44
3.3.2. Microscopy	46
Chapter 4: Solar cells on natural fiber based substrates (Publication I).....	50
Chapter 5: Characterization of liquid electrolytes (Publication 2).....	56
Chapter 6: Inkjet-printed electrolyte in DSSCs (Publication 3).....	64
Chapter 7: Inkjet-printed dyes in DSSCs (Publication 4)	70
Chapter 8: Inkjet-printed platinum in DSSCs(Publication 5)	76
Chapter 9: Conclusions	84
9.1 Significance of this work	86
9.2. Future research recommendations	86
Chapter 10: References	90
APPENDIX 1	105
APPENDIX 2.....	117
APPENDIX 3.....	129
APPENDIX 4	149
APPENDIX 5.....	179
APPENDIX 6.....	205

List of Figures

Figure 1: Schematic of DOD printers with different deformation of the ink channel: **a)** squeeze, **b)** bend, **c)** push and **d)** shear mode [23]

Figure 2: Waveform consisting of typical four segments [28] [29]

Figure 3: Schematic of DSSC consisting of glass (grey), TCO (green), platinum (Pt) catalyst (dark grey), electrolyte (yellow), dye (red) and TiO₂ (turquoise) [58]

Figure 4: An example *J-V* curve of DSSCs

Figure 5: Impedance circuit model for DSSC [58]

Figure 6: An example of EIS: **a)** Nyquist plot and **b)** *Z''* plot with alternating frequency (solid lines = fitted data and points = measured data) [58]

Figure 7: Inkjet printing system used through the doctoral research: **a)** Fujifilm's Dimatix Materials Printer DMP-2831 (print carriage was marked with a red circle) and **b)** Printer cartridge including a 10 pL print head and ink storage module

Figure 8: The drop ejected from the nozzle orifice and in flight between the orifice and the substrate: **a)** raw image and **b)** binary image in white colored foreground pixels

Figure 9: **a)** EPTR, **b)** Components of the substrate and **c)** Optical microscope image of the substrate after staining with N,N,N',N'-Tetramethylacridine-3,6-diamine (Acridine orange)

Figure 10: Cobb test setup and procedure steps: **a)** 7 × 7 cm² FBS and Mini Cobb with its water container ring filled with DI, **b)** FBS is fastened between the security plate and water container and **c)** FBS is exposed to water for 24 h in Mini Cobb setup in the inverted position

Figure 11: **a)** Picture of DSSC integrated on SWCNT and PEDOT coated FBS and **b)** *J-V* curves of the best cells (FBS/DSSC and Glass/DSSC were represented as blue circles and red squares, respectively).

Figure 12: EIS measurements of the best cells (reference and FBS based cell) **a)** Nyquist plot and **b)** imaginary impedance by frequency (solid lines = fitted data and points = measured data)

Figure 13: Surface tension of the inks between 23 °C and 60 °C

Figure 14: Viscosity change of the inks during the 3ITT tests with low-high-low shear exposure: **a)** one step increase of shear from 0.1 s⁻¹ to 500 s⁻¹ and **b)** linearly increasing shear from 0.1 s⁻¹ to 500 s⁻¹ in second interval

Figure 15: Inkjet print-outs at room temperature: a) unprinted paper as a reference, b), c) and d) AFM height images of the inkjet-printed surfaces with ACN, MPN and SFN, respectively, e), f) and g) 4 x 3 cm size print-outs prepared with ACN, MPN and SFN, respectively. The scale bar presented in g) is also valid for e) and f). The inset in e) is a fiducial camera image taken from the area which is marked with a red square.

Figure 16: *J-V* curves of the best fresh and aged cells

Figure 17. EIS measurements of the best cells (reference and hole-free cell): **a)** Nyquist plot and **b)** imaginary impedance by frequency (solid lines = fitted data and points = measured data)

Figure 18: Washed and non-washed samples for small DSSCs (8 x 5 mm active area) with gradient and two color samples for big DSSCs (88 x 5 mm active area)

Figure 19: Absorbance spectra of the 4 ml dye desorption solutions with C101 dye measured through the cuvette having 1 cm optical path.

Figure 20: Short circuit photocurrent density values of the gradient and two-color DSSCs

Figure 21: SEM images of Pt on FTO-glass surface thermal treatment: a) drop-cast and b) inkjet-printed samples

Figure 22: Height and phase (insets) AFM images of: a) uncoated FTO-glass, b) drop-cast Pt and c) inkjet-printed Pt samples

Figure 23: Transmittance values of bare FTO-glass as well as drop-cast and inkjet-printed Pt layers on FTO-glass samples at 450, 550 and 650 nm wavelength as a function of Pt loading

Figure 24: EIS measurements of the best symmetrical CE-CE cells (reference and inkjet-printed cell): **a)** Nyquist plot and **b)** imaginary impedance by frequency (solid lines = fitted data and points = measured data)

Figure 25: Stability of the inkjet-printed and drop-cast Pt CEs: **a)** power conversion efficiency and **b)** charge transfer resistance of the CE

List Of Tables

Table 1: Inkjet printing inks tested on different substrates in the published articles

Table 2: Optimal physicochemical properties of the inks for DMP-2831 [28].

Table 3: Average photovoltaic parameters of cells

Table 4: Average electrochemical impedance spectroscopy (EIS) parameters

Table 5: List of electrolytes with their components and their molar ratios

Table 6: Photovoltaic characteristics of initial and aged cells

Table 7: Photovoltaic characteristics of initial and aged cells

Table 8: Calculated Z , R_e and W_e values and velocity of platinum precursor

Table 9: Average R_s , R_D , R_{CT} and R'_{CT} values of CE-CE cells obtained from EIS measurements

Nomenclature

AFM	Atomic force microscopy
CA	Contact angle
CE	Counter electrodes
DMF	Dimethylformamide
DMII	1,3-dimethylimidazolium iodide
DMP	Dimatix materials printer
DSSC	Dye-sensitized solar cell
EIS	Electrochemical impedance spectroscopy
EMII	1-ethyl-3-methylimidazolium iodide
EMITCB	1-ethyl-3-methylimidazolium tetracyanoborate
FBS	Fiber based substrate
<i>FF</i>	Fill factor
FTO	Fluorine doped tin oxide
GuSCN	Guanidine thiocyanate
H ₂ PtCl ₄ .6H ₂ O	Chloroplatinic acid hydrate
I ₂	Iodine
<i>J</i> _{sc}	Short circuit current density
<i>J-V</i>	Current density-voltage
LiI	Lithium iodide
NBB	N-butylbenzoimidazole
PE	Photo electrode
PEDOT:TsO	p-toluenesulfonate doped poly(3,4-ethylenedioxythiophene)
PMII	1-methyl-3-propylimidazolium iodide
Pt	Platinum

PV	Photovoltaics
R_{CT}	Charge transfer resistance
R_D	Diffusion resistance
Re	Reynolds number
R_{REC}	Recombination resistance
R_S	Series resistance
R_{SH}	Sheet resistance
RT	Room temperature
SEM	Scanning electron microscope
<i>t</i> BP	4-tert-butylpyridine
TCO	Transparent conducting oxide
TiO ₂	Titanium dioxide
TMAOH	Tetramethylammonium hydroxide
UV	Ultraviolet
V_{oc}	Open circuit voltage
We	Weber number
Z	Inverse Ohnesorge number
γ	Surface tension or strain
η	Viscosity or power conversion efficiency of DSSC
ρ	Density

Personal references

This thesis consists of an overview of the following five publications, which from here on are referred to as Roman numerals in the text:

- I. Hashmi, S. G., Özkan, M., Halme, J., Paltakari, J., Lund, P. D. (2014) Highly conductive, non-permeable, fiber based substrate for counter electrode application in dye-sensitized solar cells. *Nano Energy*, 9, 212-220. DOI: 10.1016/j.nanoen.2014.07.013.
- II. Özkan, M., Dimic-Misic, K., Karakoc, A., Hashmi, S. G., Lund, P. D., Maloney, T., Paltakari, J. (2016) Rheological characterization of liquid electrolytes for drop-on-demand inkjet printing. *Organic Electronics*, 38, 307-315. DOI: 10.1016/j.orgel.2016.09.001.
- III. Hashmi, S. G., Özkan, M., Halme, J., Dimic-Misic, K., Zakeeruddin, S. M., Paltakari, J., Lund, P. D. (2015) High performance dye-sensitized solar cells with inkjet-printed ionic liquid electrolyte. *Nano Energy*, 17, 206-215. DOI: 10.1016/j.nanoen.2015.08.019.
- IV. Hashmi, S. G., Özkan, M., Halme, J., Zakeeruddin, S. M., Paltakari, J., Grätzel, M. and Lund, P. D. (2016) Dye-sensitized solar cells with inkjet-printed dyes. *Energy and Environmental Science*, 9, 2453-2462. DOI: 10.1039/C6EE00826G.
- V. Özkan, M., Hashmi, S. G., Halme, J., Karakoc, A., Sarikka, T., Paltakari, J., Lund, P. D. (2017) Inkjet-printed platinum counter electrodes for dye-sensitized solar cells. *Organic Electronics*, 44, 159-167 DOI: 10.1016/j.orgel.2017.02.015.

INTRODUCTION

1.1 Research motivation

With the increase of awareness in many societies and stricter “green” regulations, various innovative alternative energy technologies have been proposed instead of their conventional counterparts either to replace the traditional ways with more efficient processes or to provide new functionalities [1] [2]. Developed after crystalline silicon based solar cells, one successful invention in the renewable energy sector is the thin film solar cell, which is also known as the “second generation solar cell” [3]. The key factors in the success of these products is both the successful achievement of efficient mass production and flexibility of use that allows their integration into various applications or platforms, in contrast to silicon based photovoltaics [4].

One promising technology in the third generation solar cell category is the dye-sensitized solar cell (DSSC), although they are currently restricted by considerably shorter lifespans and lower energy conversion performance (latest record efficiency is 13% [5]) compared to conventional solar converters (for instance, current record efficiency of crystalline based silicon cells is $25.6 \pm 0.5\%$ [6] [7]). Nevertheless, DSSC technology offers the possibility for flexibility, light weight, adaptable design, ease of production and good low-light performance. Furthermore, DSSC can also provide power for applications, which are not possible with conventional solar cells. In this regard, many research activities have been undertaken to boost performance, reduce production cost, enhance device life-time and design new versatile production methods. In particular, the solution-processable compounds that form the layer-by-layer architecture in these devices allows the application of various printing techniques (such as inkjet printing) by means of functionalized nanoparticle based inks [8] [9].

To date, two of the crucial targets for the printed electronics, best precision results and accurate controllability over the deposition layer, have been attained by inkjet printing method [10] [11] [12] [13]. As a result, inkjet printing was investigated as a new production scheme for DSSC technology throughout this thesis. In order to ensure reliable printing, the characteristics of the inks need to be intensively studied alongside the ink-substrate-ambient interactions prior to the printing process. Even

layers and efficiently infiltrated interfaces have been frequently reported to increase the performance of the printed electronics, which is directly related to the quality of the printing process.

Last but not least, the exploration of new ways to integrate these converters onto different substrates is of critical importance for the design of alternative power supplies for different cordless applications (for instance small electronics and intelligent packaging products [14] [15] [16]) and enhance their adoption into everyday life by consumers. Additionally, by choosing bio based substrates, the recyclability of these devices will be increased and in this regard, utilization of cellulosic substrates can open up many opportunities as a platform for solar converters.

1.2 Thesis scope and outline

This thesis work is component part of the Positive Energy Building (PEB). PEB is an advanced version of a Zero Energy Building (ZEB), which is intended to generate an amount of energy from the renewables equal to the energy it consumes [17]. The PEB concept additionally includes a surplus energy on the production side and both types of design have been stipulated by the Energy Efficiency Directive from European Union (EU) [18]. One of the stipulations is that all the new buildings in Europe must be nearly zero-energy buildings (NZEB) by 31 December 2020 (public buildings by 31 December 2018). The NZEB implementation concepts have been defined differently by EU countries, however, all the definitions have the common intention of integrating renewable energy sources (RES) into the buildings and using them as primary resources to balance the imported/exported energy within the structure. In order to achieve this mandatory target - which not only includes newly constructed buildings but also refurbishment scenarios in many cases - the use of innovative technologies has been identified as “vital” especially those that can harvest the abundant solar energy like photovoltaics [19].

During the implementation of such a concept, it is inevitable that not only numerous new products will be launched in the market but also the novel approaches will create further scientific challenges. This dissertation aims to elucidate the technical aspects of a modern digital deposition technique, inkjet printing, as a manufacturing method for third generation solar cells, which are new power unit candidates for

cordless applications thus both reducing the dependency on plugs and the energy consumed from the central generation units. Additionally, this work investigates the potential of cellulosic substrates as an alternative platform to integrate these devices.

Associated with the objectives listed above, this dissertation is focused on the following research questions:

Research question 1: Is it possible to produce DSSCs on biobased substrates that consist of cellulosic materials without any compromise in the device efficiency? (Publication I)

Research question 2: Is inkjet printing method applicable in the production of solar cells including the liquid electrolyte without any compromise in the power conversion efficiency and device stability? (Publication II, Publication III, Publication IV, Publication V)

First of all, the influence of replacing the conventional counter electrode (platinum) and substrate (glass) with more abundant alternatives on cell parameters was investigated. Keeping in mind the limitations coming from the absorbing nature of cellulose, a single walled carbon nanotube layer was initially coated on a laminated cellulosic sheet. To reach the required catalytic performance for DSSCs, this layer was then decorated with a p-toluenesulfonate doped poly(3,4-ethylenedioxythiophene) (PEDOT:TsO) layer, and was used to assemble DSSCs (Publication I).

The next step had the aim of integrating the inkjet printing method in DSSC fabrication in order to avoid the hole-drilling (holes on the glass substrate) step and injection of the electrolyte through these pre-drilled holes. Therefore, initially the physicochemical properties of three popular electrolytes were investigated and the effect of different operation temperatures during the printing process were assessed (Publication II). Subsequently, the electrolyte with the least dilatant nature was integrated in DSSCs by means of inkjet printing and the device characteristics of the DSSCs were studied (Publication III).

Encouraged by the previous results, the inkjet printing technique was also introduced for the sensitization step for DSSCs. Subsequently, the controlled amount of the dye was investigated through the optical measurements. Additionally,

the influence of the new sensitization method on the device parameters was evaluated by assembling DSSCs and performing stability tests (Publication IV).

The problems associated with the alternative counter electrodes are their cost and incompatible catalytic/optical properties when compared to the conventional drop-cast platinum layers. As an alternative deposition method, the inkjet printing was successfully demonstrated for catalytic platinum layer deposition in DSSCs. This work also included meticulous optical, morphological, and electrocatalytical analyses of the precisely patterned counter electrodes as well as their integration in DSSCs and related aging studies (Publication V).

Background

2.1. Inkjet printing technology

2.1.1. Introduction

Inkjet printing is a direct writing technique through which the ink of desired materials can be transferred onto a substrate in order to create patterns with micro-scale precision. There are two main modes of inkjet printing: continuous inkjet (CIJ) and drop-on-demand (DOD) inkjet depending on the drop ejection nature. In CIJ printing systems, the ink is expelled continuously from the printing nozzles even if the drop is not needed and unnecessary droplets are collected by means of a gutter [20]. CIJ printers are commonly used in conventional labeling, coding and marking applications where a fast process is a priority [21] [22]. In contrast, DOD printers only release drops whenever they are required. As a result, DOD printing reduces the possibility for contamination as it does not entail the collection and reuse of the ink.

Currently, the most common DOD printing technologies rely on thermal- and piezoelectric-based methods [23]. Thermal DOD printers (or bubble-jet), as the name suggests, produce drops via a heating step that provides the required pressure by a bubble coming from the vapor of the printing ink [24]. In the thermal-driven printing systems, the composition of the ink is a limiting factor on the variety of the application possibilities due to the required high temperature procedure. On the other hand, in the piezoelectric printers, the drops are ejected upon the deformation of the printing chamber wall by a voltage driven lead zirconate titanate (PZT) piezoelectric ceramic (piezoceramic) element.

Depending on how the deformation of the ink channel is realized, there are four key groups in piezoelectric printers: squeeze, bend, push and shear modes (Figure 1) [23]. In the squeeze mode configuration, the printing chamber is squeezed and a droplet is produced when a user defined voltage is applied to the piezoelectric element that consists of a radially polarized hollow tube (Figure 1a). In the bend mode, the pressure inside the channel is provided through the bending of a diaphragm attached to a piezo element which is also driven by an electrical signal (Figure 1b). In the push mode actuation (also called bump mode), the drops are expelled after a piezoelectric ceramic rod pushes against a diaphragm (Figure 1c).

In the bend and push modes, the polarization of the piezo element - thus its deformation - and electric field generated are in parallel. In the shear mode, the structural deformation is provided by a perpendicular electric field, which provides the shearing of the ink by the piezoelectric elements (Figure 1d) [25] [26].

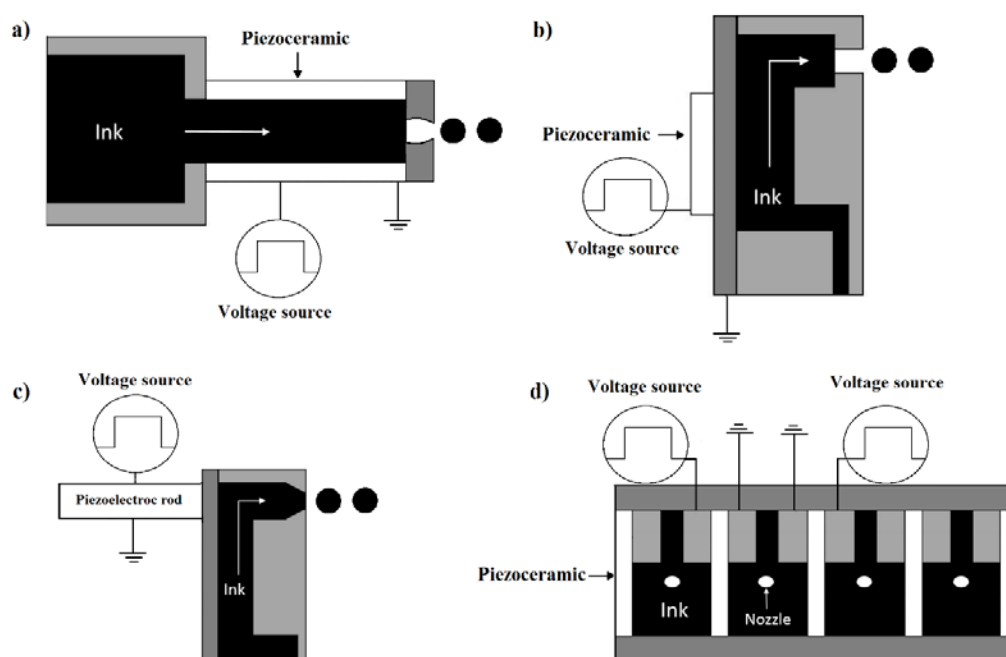


Figure 1: Schematic of DOD printers with different deformation of the ink channel: **a)** squeeze, **b)** bend, **c)** push and **d)** shear mode [23]

2.1.2. Piezoelectric DOD inkjet printing

In printed electronics, the tunability of the drop properties (size, shape, flying trajectory and velocity) is of critical significance and by changing the user defined nozzle driving signal “*waveform*”, it is possible to modify the aforementioned characteristics. A typical waveform usually contains four segments as depicted in Figure 2 and the user can change the duration, amplitude and slew rate of each segment [27]. Upon the relaxation of the piezoelectric element by the amplitude decline in segment one, the ink flows from the storage module to the printing channel, which expands. Thereafter, the steady amplitude in this segment provides the settling time of the ink inside the channel. Segment two provides the compression which delivers the pressure in the chamber needed to form a drop. The two subsequent stepwise segments bring the piezoelectric element back to the original starting shape. The amount of bending within the ink chamber is associated with the amplitude of the voltage, whilst the speed of the bending is dependent on the slew rate. In particular, the steepness of the slope in the second segment delivers

the energy required for the initial ejection, whereas the overall duration of the waveform is defined by ink viscosity *i.e.* more viscous inks require longer pulses.

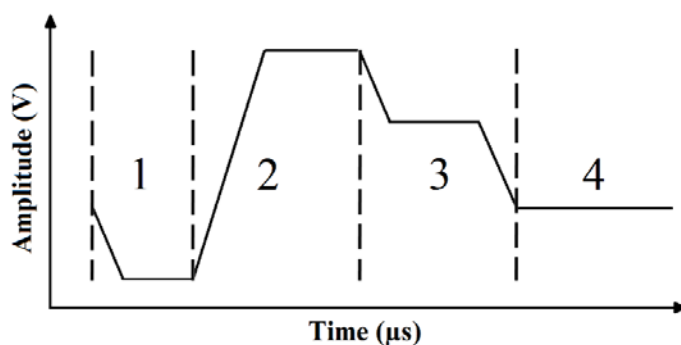


Figure 2: Waveform consisting of typical four segments [28] [29]

Other influential printing parameters can be listed as: jetting frequency, cartridge temperature, printing distance, platen temperature and drop spacing. The jetting frequency (drop production rate) is related to the ink conditions, which in turn affect the printing quality and the speed of deposition [23]. Inks with low viscosities require lower energies for droplet ejection, however, asymmetric tail formation is a possible issue [30]. In general, too high frequencies result in a low resolution of the patterns, while too low frequencies result in increased deposition time [31].

Cartridge temperature (also termed as “printing temperature”) can greatly affect the movement of the ink through the printing channel and the jetting of the droplets due to the temperature dependence of the ink viscosity. For instance, an ink with a high viscosity at room temperature (RT) can have its viscosity reduced by heating thus facilitating drop ejection and printing. On the other hand, this can also result in evaporation related clogging that may reduce the jetting quality in case of a low boiling point solvent. In order to overcome this problem humectants or less volatile solvents can be used.

Printing distance between the substrate and the nozzle is mostly set to the minimum in order to reduce the inaccuracy of droplet placement on the substrate that stems from ambient-droplet interaction during the travel between the nozzle and the substrate [23]. On the other hand, there must be sufficient distance between the nozzles and the substrate so as to let satellite drops (secondary unwanted drops jetted along with the main drop [32]) merge with the main drop (“stand-off distance”) [21] [33].

Platen temperature (together with the nature of the ink, substrate and their interaction) plays an important role on the drop impact and ultimate pattern creation on the substrate. For instance, conducting the inkjet printing experiments on the heated substrates may reduce the well-known “coffee-stain” effect [34] - the uneven pattern formation on the substrate due to the high evaporation rate towards the edge of the droplet - by decreasing the solute transfer to the contact line where three phases co-exist [35].

The resolution of the print is related to the number of drops on a specific area and this is adjusted by the drop spacing (DS) parameter, which is determined by the distance between the centers of two neighboring drops (Equation 1) [28]:

$$\text{Drop Spacing } [\mu\text{m}] = 25400/\text{Resolution } [\text{dpi}] \quad (1)$$

Practically, the correct distance between the neighboring drops in X and Y directions are provided by the x-axis encoder (adjusted by the equipment according to the given DS value through the operation software) and the cartridge angle (manually adjusted on the equipment), respectively. A too high DS value leads to isolated drops on the substrate, which is detrimental for electronics applications where conductivity is necessary. Moreover, a too low DS amount should also be avoided in order to prevent extremely overlapped droplets. Typically a fiducial camera is used for the evaluation of the practical accuracy of the droplet positioning and DS on the substrate, in addition to the droplet spread, in order to attain the desired final pattern on the substrate.

A crucial point related to inkjet printing operation is the clogging of the nozzles that can rapidly deteriorate the printing quality. In addition to the proper ink selection, the application of a cleaning cycle sequence is an important maintenance step that helps nozzles to function properly during the whole printing process. Usually a cleaning cycle is completed with three main actions which are: spitting (firing the nozzles at the cleaning station of the printer without a substrate), purging (applying pressure to the ink to get rid of the trapped air) and blotting (automatically cleaning the nozzles with a special pad).

2.1.3. Inkjet printing inks

The physicochemical characteristics of the inks used in an inkjet deposition process are of immense importance for desired droplet formation, proper movement of the

droplets (or jets) between the print head orifice and substrate and finally for high quality outputs on the substrate. These characteristics can be listed as viscosity, surface tension, density, particle size and boiling point.

The movement of printing ink in the nozzle channel depends on its viscosity when the firing voltage is applied to the piezoelectric ceramic [36]. In addition, whether the ink droplet leaves or remains in the orifice also depends on the surface tension of the ink [37]. Therefore, it is essential to extensively study two major features, viscosity and surface tension of the ink, prior to the design of any inkjet printing experiment.

The flow parameters and print-out quality can be correlated by profiling the viscosity of the ink over a wide shear rate window that is related to drop formation, straight travelling path of the flying drops and pattern formation on the substrate. Inks which are not optimal for the window of operation tend to suffer from satellite formation and also have limited high frequency performance if the viscosity is too low [38]. Nevertheless, use of highly viscous inks is also restricted by the pressure pulse capabilities of the inkjet printer [39]. Additionally, dilatant inks (inks with increasing viscosity in high shear rates compared to the low shearing conditions) create a resistance against the droplet formation by preventing or making it difficult to break away from the ink. Another disadvantage associated with dilatant inks is the restricted movement of the ink along the micro nozzle, whilst Newtonian inks (inks that maintain a constant viscosity over the whole shear window of interest) are commonly preferred for inkjet printing applications [38] [40].

The printing inks have both Newtonian and non-Newtonian behavior, depending on the rheological window of their application. After strain is applied, ink first exhibits an induced elasticity and rheological parameters are within the domain of viscoelastic measurements that are expressed with complex viscosity, whilst when shear rate increases the rheological parameters are within the domain of dynamic viscosity measurements. Both complex viscosity response from low to high frequencies and dynamic viscosity response over a broad shear rate ranges, are necessary to simulate the factors that affect droplet formation, ink recovery rate and trajectory formation that affect droplet setting. Therefore, this thesis correlates the complex flow parameters of both Newtonian and Non-

Newtonian behavior of inks with their printout performance, without going into details of theoretical background of complex and dynamic viscosity [41].

The surface tension of the ink, which is measured by the curvature of the surface of the pending drop, plays a significant role during the drop formation and the pattern creation on the substrate. Laplace equation relates the surface tension at the interface of a pendant drop (γ) to the pressure difference at the interface ($\Delta p = p_{\text{inner phase}} - p_{\text{outer phase}}$) and the radii of vertical and horizontal circles of drop curvature (principal radii of curvature: R_1 and R_2) as:

$$\Delta p = \gamma \left(\frac{1}{R_1} + \frac{1}{R_2} \right) \quad (2)$$

Inks that possess low surface tension values may uncontrollably drip from the printing nozzle under low pressure values, whilst the internal forces of the nozzle should not constantly exceed the surface tension forces of the inks, as this hinders drop formation [42]. In order to avoid these cases, the intermolecular forces of the ink can be reformulated through the use of appropriate surface tension modifiers, such as, co-solvents or surfactants.

Depending on the nozzle geometry, the particle size of an ink should be selected such that it is small enough to prevent the clogging of the nozzles [38] and in general, the maximum size of the particles in the printing ink should be around 1% of the nozzle orifice [43]. Suspensions, which have too high densities and a tendency to agglomerate should be avoided or modified by means of additives to ensure a longer lifetime for the printing heads. Additionally, the agglomerates are generally eliminated from the ink by filtering it prior to the printing process. Another important factor related to nozzle blocking and ink stability is the choice of the ink carrier, which may consist of either a single solvent or multicomponent solvent system [44]. High boiling point ink solvents usually results in less clogging induced by the evaporation, whereas the deposition of the ink on the substrate requires the volatility of the ink to some extent. In order to balance these competing demands and minimize the possibility that the ink dries before it reaches the substrate, humectants can be included in the ink [45].

The benchmarking of Newtonian printing inks is mostly performed by use of a non-dimensional parameter set, i.e. inverse Ohnesorge number ($Z = Oh^{-1}$), Reynolds

number (Re) and Weber number (We) calculated by Equations 3, 4, 5 and 6 [46] [47].

$$Z = \sqrt{(d\rho\gamma)}/\eta \quad (3)$$

$$\text{Re} = \rho vd/\eta \quad (4)$$

$$\text{We} = \rho dv^2/\gamma \quad (5)$$

$$Z = \text{Oh}^{-1} = \text{Re}/\sqrt{\text{We}} \quad (6)$$

where, d , ρ , γ , η and v are the orifice size, ink density, ink surface tension, ink viscosity and drop velocity, respectively.

Various optimal ranges for these parameters have been reported in the literature as a product of being mostly experimental. For instance, in [48], the optimal range of Z is defined as 4-14, whereas in [49] and [50], this range was suggested as 2-40 and 0.67- 50. Higher Z values compared to the optimal range (determined by previous experimental studies) lead to the prediction that the main drops may travel to the substrate in the company of satellite droplets [51] [48]. In contrast, lower Z values may hinder the drop formation due to the high viscosity. Additionally, it profiles the spreading dynamics of the droplet on the substrate. For example, resistance against spreading stems from the ink viscosity at low Z values while inertial forces work against the spreading in the opposite case [23]. We and Re , represent the ratio of inertial forces to surface tension and viscous forces, respectively and they characteristically fall into 1 and 100 range for inkjet printers [52]. The higher limits of both parameters designate the splashing of the drop on the substrate, while the low values of We and Re restrict the system as there is insufficient energy for drop formation [21].

2.1.4. Droplet formation and jet trajectory

After the printing channel is filled, the drops are expelled from the orifice thanks to the channel movements. Since the surface tension is the main factor in keeping the ink in the nozzle, the drop formation only occurs if the kinetic energy (the main component of the drop velocity) can prevail over the surface tension of the ink promoting the breakup of the ink. A possible issue related to the drop ejection is “puddling”, which is the unwanted flow of the liquid and its coverage on the orifice. At this point, the addition of the blotting step in the cleaning cycles can be beneficial

in certain systems for the successful printing process. Alternatively, utilization of custom-made waveforms can remove the need for a separate blotting step as they provide the correct energy required for the drop to leave the orifice [53].

One important reason for the low quality of the printing results is improper tail formation. For example, a long tail may possibly break into satellite drops which create unwanted patterns on the substrate surface in the case when they do not merge with the main drop [45] [54]. Another key issue related to tail formation is the practical measurement of the drop volume in the presence of long tails. Keeping in mind all the challenges associated with the tail formation, use of tail-free droplets is recommended [55].

The flight of the drop between the nozzle and the substrate is typically evaluated by the flight path and the drop velocity. Ideally, the flight path must be straight and the jetting angle (the angle between the nozzle and the flight trajectory) must remain the same throughout the whole printing process. The velocity of the drops must be optimized due to the fact that slow droplets interact with the ambient more than the fast ones, whereas too fast droplets splash on the substrate and decrease the print quality.

Prior to the actual printing process, the formation of the drops and the movement of the drops are typically evaluated by means of the embedded stroboscopic drop watcher camera as explained further in “Materials and Methods” section.

2.2. Substrate-ink interaction

The aim of inkjet printing is to precisely deposit the ink onto the substrate in a consistent manner. This target can only be achieved by the combination of a reliable and sustainable drop ejection method with proper ink impact on the substrate and consequent pattern formation.

The impact and spreading of drops are characterized by means of the contact angle (CA) measurements from the side-view images of the sessile drop on the substrate. Once the substrate and the drop come in contact, the liquid alters its shape to diminish its energy and during this process, the CA is measured between the substrate and tangent of the drop outline at the ink-solid-air intersection. This

energy balancing system determining the wetting of the substrate is described by Equation 7 (Young's equation):

$$\gamma_{\text{substrate-vapor}} = \gamma_{\text{substrate-ink}} + \gamma_{\text{ink-vapor}} \cos \theta \quad (7)$$

where, $\gamma_{\text{substrate-vapor}}$, $\gamma_{\text{substrate-ink}}$, $\gamma_{\text{ink-vapor}}$ and θ represent the solid-vapor, solid-liquid, and liquid-vapor interfacial surface tension values, and contact angle, respectively.

The surface tension and viscosity control the spreading and drying behavior of the drops, which affects the characteristics of the printed layers. For instance, viscous inks result in thicker layers and a weaker coffee-stain effect, whereas inks with lower surface tension spread more than high surface tension inks [56].

2.3. Dye-sensitized solar cells (DSSCs)

Dye sensitized solar cells (DSSCs) are one of the most popular devices in printed electronics research due to their multi-layered device architecture and the solution processability of the associated layers. Typically, these devices consist of photo electrode (PE), counter electrode (CE), electrolyte and dye (Figure 3) [57]. The PE consists of a monolayer of dye on a semiconducting oxide (mostly titanium dioxide, TiO_2) and the counter electrode, CE, is a thin layer of catalyst. The most commonly used sensitizer is an organic dye, di-tetrabutylammonium cis-bis (isothiocyanato) bis (2,2-bipyridyl-4,4-dicarboxylate) ruthenium(II), N719.

In the standard device fabrication, the two electrodes are part of a thermoplastic sandwich that keeps them separated from each other and the space between these electrodes is filled by a liquid electrolyte containing an iodide/tri-iodide (I^-/I_3^-) redox couple. In the case of a traditional DSSC, both of the electrodes are fabricated on a transparent conducting oxide (TCO) layer coated glass.

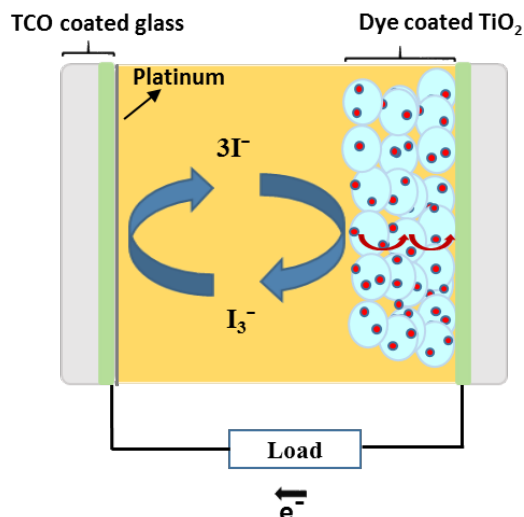


Figure 3: Schematic of DSSC consisting of glass (grey), TCO (green), platinum (Pt) catalyst (dark grey), electrolyte (yellow), dye (red) and TiO₂ (turquoise) [58]

The basic operation principle of DSSCs resembles that of plant photosynthesis with the difference that sunlight is used to create an electrical output. The cell becomes functional when a dye molecule is struck by a photon from the incident light. The electron of the excited dye molecule then travels from the mesoporous oxide surface (red arrows in Figure 3) to the TCO (Fluorine doped tin oxide, FTO, is commonly used) on the PE side through a diffusion process and passes through the external circuit to reach the CE. The catalyst coating on the CE side (typically, platinum) facilitates the reduction of tri-iodide ion to iodide ion ($I_3^- + 2e^- \rightarrow 3I^-$), which is followed by electron transport to the oxidized dye through the diffusion of iodide/iodine ions in the electrolyte. The regeneration of the dyes occurs after its reduction by the electrons carried from the catalyst surface and as a result I_3^- is produced. The total resistance of the cell and thus the energy losses/power conversion efficiency of the device depends on all these interfaces.

2.3.1. Device performance characteristics

Photocurrent-voltage measurements

The current-voltage (I - V) characteristics of the DSSCs are typically recorded by applying a potential between the electrodes while the cell is under standard illumination (light intensity of 1000 W/m² equivalent of 1 Sun). A J - V (current density-voltage) curve (Figure 4) gives the short circuit current density (J_{SC}), open circuit voltage (V_{OC}) and fill factor (FF) as well as the maximum power point (MPP). The power conversion efficiency of DSSC (η) is determined from Equation 8:

$$\eta = \frac{J_{SC} \times V_{OC} \times FF}{P_{in}} \quad (8)$$

J_{SC} is determined by the generated electrons and electron-hole recombination. It is the density of the current while the cell is short circuited and calculated from the short circuit current ($I_{SC} = \text{mA}$) and the active device area (A in cm^2), which is usually defined by mask aperture (Equation 9):

$$J_{SC} = \frac{I_{SC}}{A} \quad (9)$$

V_{OC} is determined from the difference between the redox potential of the electrolyte and the Fermi level of semiconducting oxide. It is measured in volts whilst the electrodes of the device are not connected. FF , a dimensionless parameter, expresses the deviation of the J - V curve from the black dashed rectangle illustrated in Figure 4. A J - V curve close to the rectangle shape would suggest a low amount of resistive losses.

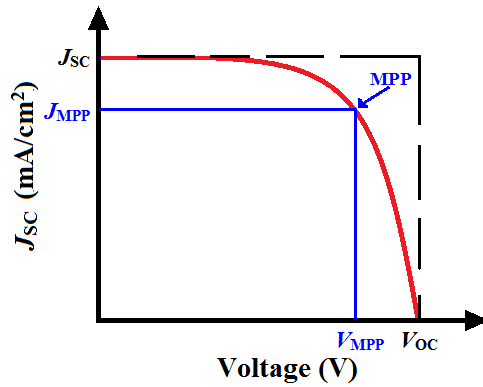


Figure 4: An example J - V curve of DSSCs

Electrochemical impedance spectra

In order to analyze the resistances and capacitances of each component of the DSSC, electrochemical impedance spectroscopy (EIS) is generally conducted. The response of the cell is recorded under open circuit conditions while a sinusoidal voltage at different frequencies (100 mHz to 100 kHz is the most common range) is applied to the cell. The equivalent circuit model of DSSCs is commonly used to interpret the recorded response (Figure 5).

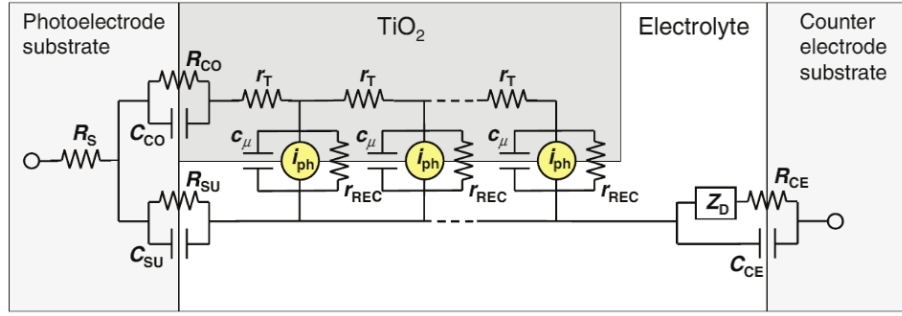


Figure 5: Impedance circuit model for DSSC [58]

The main circuit constituents of the equivalent circuit are listed as [58]:

R_s : Ohmic series resistance of the cell. The total R_s is the sum of contributions from the sheet resistance of the substrates, resistivity of the electrolyte and electrical contacts and wiring of the cell.

R_{CO} and C_{CO} : Contact resistance and capacitance at the interface between the conducting substrate and the TiO_2 photo electrode film.

R_{SU} and C_{SU} : Charge transfer resistance and double layer capacitance at the substrate/electrolyte interface.

r_T : Resistivity of electron transport in the photo electrode film (typically interconnected TiO_2 nanoparticles). The total transport resistance of the film is $R_T = r_T d$ where d is the film thickness.

r_{REC} : Charge transfer (recombination) resistance at the TiO_2 /dye/electrolyte interface per unit volume of the electrode. The total recombination resistance of the film is $R_{REC} = r_{REC} d$.

Z_D : Mass transport impedance at the counter electrode.

R_{CE} and C_{CE} : Charge transfer resistance and double layer capacitance at the counter electrode electrolyte interface.

The electrochemical impedance response of the cell can be analyzed from the Nyquist plot, where the real impedance Z' and the imaginary impedance Z'' are represented in the x-axis and in the y-axis, respectively (Figure 6 a). Additionally, the peak positions of the impedance arcs can be found via imaginary impedance ($-Z''$) and frequency plot (Figure 6 b).

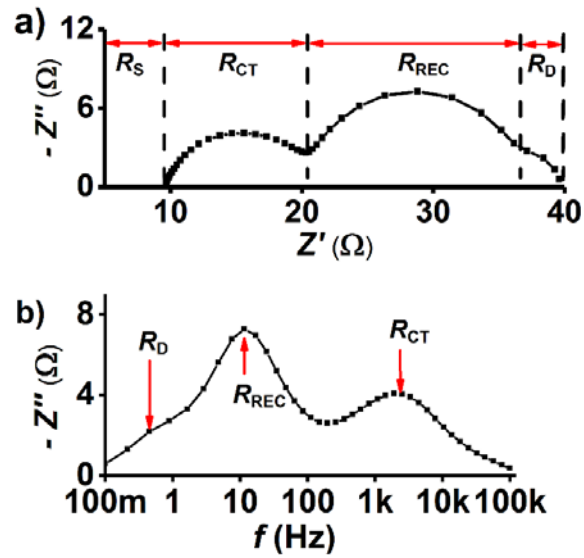


Figure 6: An example of EIS: **a)** Nyquist plot and **b)** Z'' plot with alternating frequency (solid lines = fitted data and points = measured data) [58]

In Figure 6 a, series resistance (R_S) is calculated from the distance between the origin and the starting point of the first semicircle at the left-most side of the Nyquist plot. This high frequency semicircle represents the charge transfer resistance (R_{CT}) at the counter electrode/electrolyte interface. The diameter of the second arc in the Nyquist plot determines R_{REC} (also denoted as R_{PE}) which is related to the recombination of electrons which have diffused into the mesoporous TiO_2 with I_3^- at the $\text{TiO}_2/\text{electrolyte}$ interface. The right most arc, which appears in the low frequency range, represents the electrolyte diffusion resistance (R_D).

Materials and Methods

Chloroplatinic acid hydrate ($\text{H}_2\text{PtCl}_4 \cdot 6\text{H}_2\text{O}$), guanidine thiocyanate (GuSCN, purity > 99%), N-methylbenzimidazole (NMBI, purity 99%), 4-tert-butylpyridine (TBP, purity 96%), iodine (I_2), N-butylbenzimidazole (NBB) and all solvents were purchased from Sigma Aldrich. 3-methoxypropionitrile based high stability electrolyte (EL-HSE), TiO_2 nanocrystalline (18-NRT) and scattering (WER2-0) pastes were obtained from Dyesol. Dye N719 was acquired from Solaronix. 1, 3-dimethylimidazolium iodide (DMII), 1-methyl-3 propylimidazolium iodide (PMII, >98% purity), 1-ethyl-3-methylimidazolium iodide (EMII, >98% purity) were purchased from Io-Li-Tec whereas 1-ethyl-3-methylimidazolium tetracyanoborate (EMITCB) and anhydrous lithium iodide (LiI) was obtained from Merck. All chemicals were used without further purification. The fiber based substrates were supplied by Stora Enso Oy and used without any surface pretreatment.

3.1. Inkjet printing

3.1.1. Ink characterization

The surface tension of the pendant drop in air and the CA of sessile drops on different substrates were investigated with a CAM 200 optical tensiometer (KSV instruments) using side-view imaging. The recorded images from both experiments were analyzed in accordance with Young and Laplace equations by using a built-in image analysis software. Table 1 summarizes the substrates and inks used in this dissertation.

Table 1: Inkjet printing inks tested on different substrates in the published articles

Publication	Ink	Substrate
II	Electrolytes	printing paper [59]
III	Electrolytes	dye coated TiO_2
IV	Dyes	TiO_2
V	Pt nanoparticle based precursor	FTO

The inks were studied in terms of their viscoelastic rheological behavior by using a rotational rheometer (Physica MCR 301, Anton Paar, Graz, Austria). The measurements were carried out under altered shear conditions for all inks. Additionally, in Publication II, the temperature related viscosity was profiled for a more in-depth characterization of the non-Newtonian behavior.

In order to rule out heterogeneities, each ink was first exposed to a mild pre-treatment by inserting it between two parallel plates (top: serrated and bottom: smooth configuration to avoid wall-slip formation) at 23 °C and the distance between two plates was adjusted to 0.5 mm. Subsequently, the ink was pre-sheared with an oscillation set up of up $\omega = 1$ (rad) s⁻¹ and strain deformation $\gamma = 0.01\%$ for 10 minutes followed by a two minutes rest period to equilibrate before conducting the measurements. A silicone oil was also used to encapsulate the ink in order to eliminate any evaporation related viscosity shifts.

The complex viscosity (η^*) dependence of the inks on the angular frequency (ω) in range 0.1 - 100 (rad)s⁻¹ and dynamic viscosity (η) dependence on three decades of shear rates (0.01 and 1000 s⁻¹), provide information about the samples when the structure is intact (within the linear viscoelastic region, LVE) and broken with shearing, η and η^* , respectively. Prior to the frequency sweep test, amplitude sweep oscillatory tests were run with strain $\gamma = 0.01 - 100\%$ and $\omega = 1$ (rad) s⁻¹.

The viscosity response of inks after high shear application was also investigated by two different variations of the Three Interval Thixotropic Test (3ITT) with low shear during the initial and third interval and high shear in the second interval. Commonly, during the first and third intervals, the ink was sheared at low shear rate (0.1 s⁻¹), and in contrast, the second interval was executed with both constant intermediate shear rate of 500 s⁻¹ or step-wise escalation of shear rate (0.1- 500 s⁻¹).

3.1.2. Printing process

During this research, a Fujifilm Dimatix Materials Printer, DMP-2831, equipped with shear mode DOD print heads was used. DMP-2831 is a benchtop inkjet printing system (Figure 7 a) with a micro-electro-mechanical system (MEMs) based disposable cartridge module consisting of 10 pL (nominal drop volume) print head and ink storage unit (Figure 7 b) [28]. The print head consisted of 16 nozzles with 21.5 μm orifice and the nozzles were placed on a single row at 254 μm spacing.

The substrate was placed on a platen equipped with an additional vacuum system that successfully immobilizes thin substrates and can be heated during the printing process. The printer was also equipped with two important camera systems which were intensively used during this research. The first system, called the “Fiducial Camera”, was embedded to the print carriage (circled in red in Figure 7 a) and was used to measure the drop spread and accuracy on the substrates. The second system, “Drop Watcher”, recorded images with stroboscopic illumination in order to define the paths of the drops starting from the nozzle orifice. Therefore, this system allows the identification of the vital jetting characteristics such as drop trajectory, drop velocity and jetting angle prior to the drop impact on the substrate.

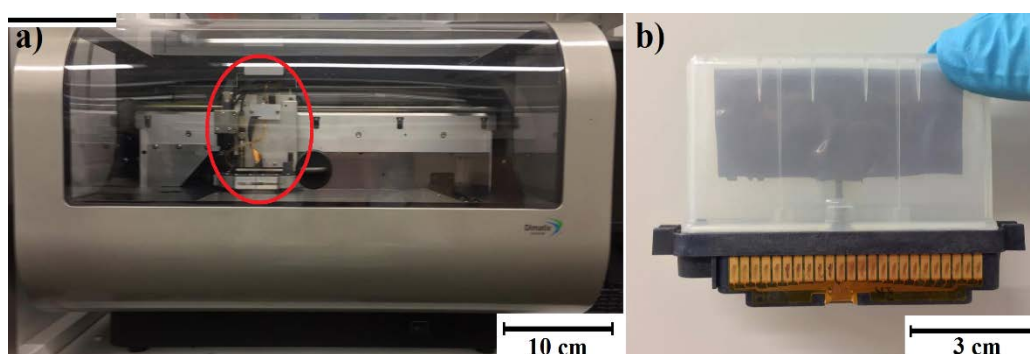


Figure 7: Inkjet printing system used through the doctoral research: **a)** Fujifilm's Dimatix Materials Printer DMP-2831 (print carriage was marked with a red circle) and **b)** Printer cartridge including a 10 pL print head and ink storage module

The features of the optimal ink published by the equipment manufacturer are tabulated in Table 2 [28]. In addition to these physicochemical properties of the inks, an ideal drop velocity range is defined as being between 7-9 m/sec.

Table 2: Optimal physicochemical properties of the inks for DMP-2831 [28].

Characteristics	Optimal Values for DMP-2831
Viscosity (mPa·s)	10-12
Surface tension (mN/m)	28-42
Particle size (nm)	< 200
Density (kg/m ³)	> 1000
Boiling point (°C)	> 100

Initially, the inks were filtered by a hydrophilic syringe filter with 0.2 μm pores (polytetrafluoroethylene filter, PTFE) and loaded into the reservoir of the DMC-

11610 (10 pL nominal drop volume) cartridge of the DMP-2831. The filled fluid module was attached to the jetting module, which included the nozzles and their electrical connector. In order to remove any trapped air bubbles within the ink kept in fluid bag, extra air was injected between the fluid bag and fluid case through the pressure port until drops were expelled from the nozzles. As the last step, the nozzle plate was wiped with a lint free tissue.

After the cartridge was prepared, the operational software of the device, Dimatix Drop Manager (DDM), was initiated and the cartridge was mounted onto the printer carriage. The cartridge settings including the waveform, which controls the action of the piezo element, were experimentally optimized. The drop formation, jetting trajectories and velocity of the ejected drops were investigated by the embedded stroboscopic drop watcher camera. The tail structure, satellite formation, flight path as well as the velocity of the travelling drops were fine-tuned by adjustment of the cartridge settings and printing temperature.

During the monitoring phase, initially the videos of the drop paths were recorded with the built-in camera of the printer and related frames were extracted. Afterwards, extracted frames were binarized and droplet region was represented using white color to refer to the foreground pixels as shown in Figure 8. After the binarization, morphological analysis was completed on the foreground pixels to outline droplet centroid coordinates for the i^{th} frame by Equation 10:

$$(X_i, Y_i) = \left(\frac{\sum_{j=1}^n x_j}{n}, \frac{\sum_{j=1}^n y_j}{n} \right) \quad (10)$$

in which (x_j, y_j) are the coordinates of j^{th} foreground pixel and n is the total number of foreground pixels inside the examined drop. Subsequently, the droplet trajectory was determined by the centroid data for each consecutive frame acquired from Equation 9 and the data was fitted to a first order polynomial to examine the drop trajectory. Here, Y coordinate data was simply taken to be dependent on the X coordinate data.

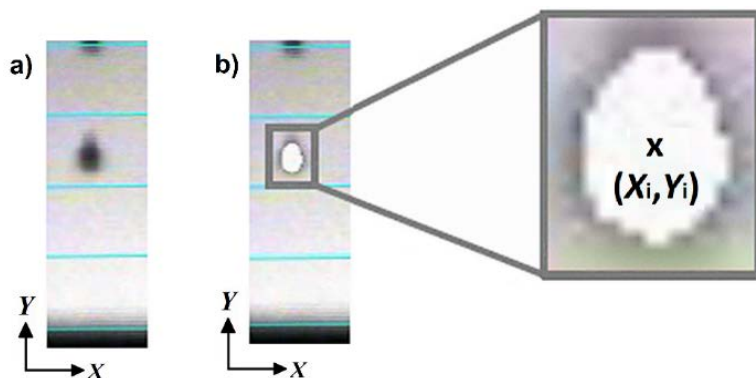


Figure 8: The drop ejected from the nozzle orifice and in flight between the orifice and the substrate: **a)** raw image and **b)** binary image in white colored foreground pixels

3.1.3. Printed layers

The inspection of the drop spread and drop positioning accuracy as well as the repeatability of experiments were carried out by recorded grey-scale pictures in bright field lighting mode from the fiducial camera system mounted on the carriage.

The material loading of coated layers (per cm^2) was calculated from the printer geometry. Each drop from the nozzles has a nominal volume of 10 pL ($\pm 20\%$) and by multiplying the number of drops with one drop volume gives the total volume of the solution dispensed on the substrate from the printer. The loading was determined from the solute amount of the dispensed ink. After the inkjet printing process, UV-Vis spectroscopy was used to cross-check the solute amount either on the solid substrates or after dissolving the deposited solute in a proper solvent (dissolution solvent) as further explained below in the “*Transmittance*” section (3.3.1) within “Other characterization methods”.

3.2. DSSC

3.2.1. Substrate evaluation

In Publication I, a commercial fiber based substrate (FBS) was initially coated with a low temperature single walled carbon nanotube (SWCNT) ink and subsequently with a commercial PEDOT based ink to replace the glass substrate and conventional catalyst, Pt. The SWCNT ink consists of 1 g of surfactant sodium dodecyl benzene sulfonic acid sodium salt (SDBS, Fluka Chemika), 0.05 g of SWCNT (Carbon solutions) and 10 ml of deionized water.

The FBS, Ensocard Pharma TR (EPTR), shown in Figure 9 a, was selected from a wide range of FBS through different tests (further explained below). The structure of FBS as well as its optical micrograph are shown in Figure 9 b and Figure 9 c, respectively.

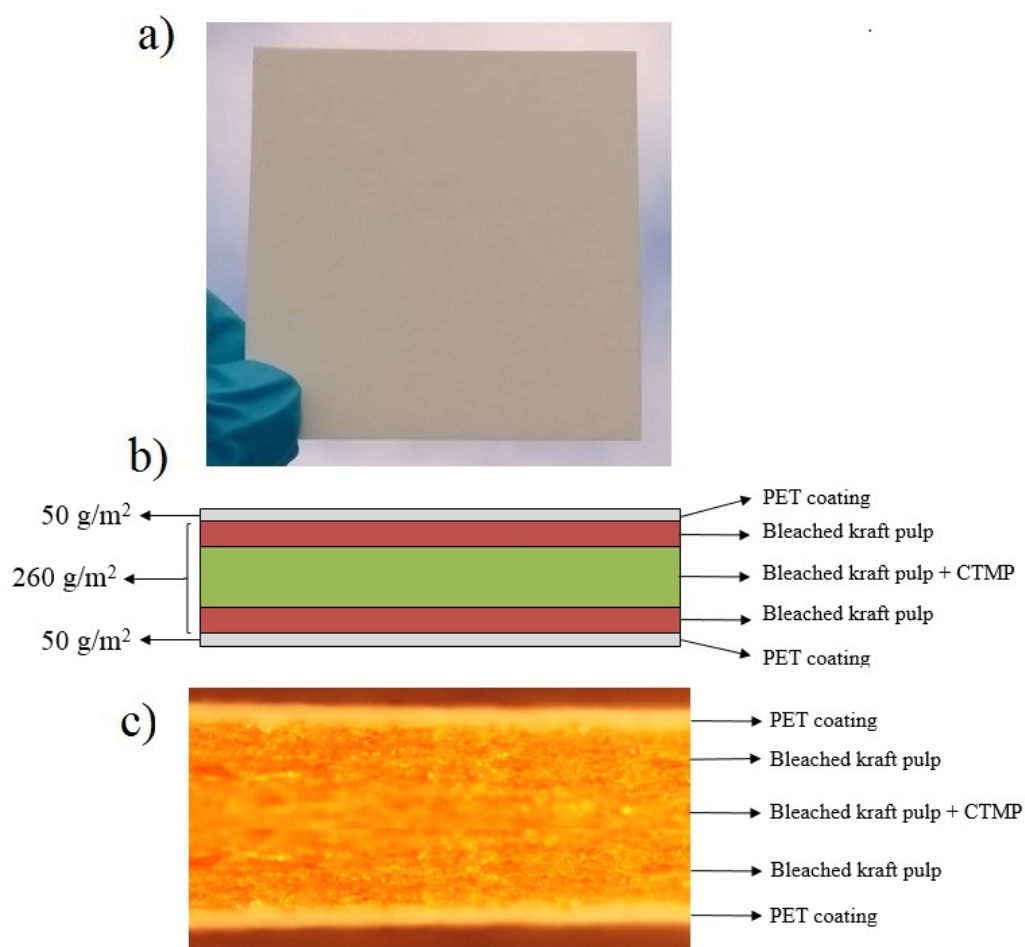


Figure 9: a) EPTR, b) Components of the substrate and c) Optical microscope image of the substrate after staining with N,N,N',N'-Tetramethylacridine-3,6-diamine (Acridine orange)

The well-known Cobb water absorption test [60], which was adapted with an in-house Mini Cobb test setup (Figure 10 a), was conducted to determine the water absorption amount of the substrate ($7 \times 7 \text{ cm}^2$) by exposure to water for 24 h. Initially, the substrate of a known weight was placed on the container ring filled with water and it was immobilized with the security plate. Thereafter, the setup was left upside down to provide continuous water exposure over the 24 h period. The weight of the FBS was re-measured after removal of the free water on the surface by wiping with lint free tissue. Next, the measured weight values before and after

the test were compared. This test was repeated 25 times and the measurement sensitivity was determined to be 0.42 g/m^2 .



Figure 10: Cobb test setup and procedure steps: **a)** $7 \times 7 \text{ cm}^2$ FBS and Mini Cobb with its water container ring filled with DI, **b)** FBS is fastened between the security plate and water container and **c)** FBS is exposed to water for 24 h in Mini Cobb setup in the inverted position

The electrolyte permeation was initially evaluated by casting a few drops of the electrolyte on a number of substrates and leaving the samples overnight. After the electrolyte exposure, the substrates were subjected to both a physical inspection as well as optical microscope micrograph analysis. Additionally, goniometric analysis of the contact angle of the electrolyte drop was used to determine the non-absorbing nature of the substrate. The electrolyte leakage was further investigated by assembly of “dummy cells”, which were prepared by sealing the SWCNT coated FBS and FTO coated glass with Bynel frame foil and injecting the electrolyte through the pre-drilled holes on the FTO glass substrate. The cells were examined after exposing them to the artificial light with 1000 W/m^2 intensity equivalent to 1 Sun illumination for 3 days.

In order to explore the mechanical properties of the alternative CE, the sheet resistance (R_{SH}) of SWCNT coated FBS substrate was calculated before and after the “bending” and “adhesion” tests using $R_{SH} = (R \cdot W)/L$ formula, in which R , W and L are the ohmic resistance, width and length of the coated area, respectively.

In the bending test, the FBS based CE was consecutively bent over various radii (1.5-2.5 cm) and relaxed (10 test cycles). In the adhesion test, two types of tapes (3M Removable and 3M Magic) were separately applied by attaching them to the coated surfaces with a round metallic disk (2 kg) and pulling the tapes off from the coating surface at 90° , respectively (5 test cycles).

3.2.2. Device fabrication

Photo electrode (PE): Clean and UV treated FTO-coated glass substrates were treated with a 40 mM aqueous TiCl_4 solution and dried with compressed air after rinsing with water and ethanol. The nanocrystalline and scattering TiO_2 layers were sequentially screen printed (active area = $0.8 \text{ mm} \times 0.5 \text{ mm}$) on TiCl_4 treated FTO-glass substrates. The substrates were then sintered at $450 \text{ }^\circ\text{C}$ for 30 min and cooled down to room temperature. After that, the second TiCl_4 treatment step was performed for 30 min and the substrates were once again subjected to sintering at $450 \text{ }^\circ\text{C}$ and then cooled down to room temperature. The TiCl_4 treatment was used to reduce the recombination rate at the TiO_2 and electrolyte while the scattering layer was used to trap the light into the device enhancing the absorption of the light. The mesoporous layer with a big surface area is the only layer which has the adsorbed dye molecules [57].

The photo electrodes with TiO_2 layers ($12 \text{ }\mu\text{m}$ nanocrystalline and $4 \text{ }\mu\text{m}$ scattering) were then sensitized at room temperature with either a 0.33 mM concentrated solution of dye (N-719) in ethanol for 16 h before the final cell assembly by dip coating (Publication I and Publication IV) or with 10-16 mM concentrated solution of dye (C101) by drop casting (Publication III and Publication IV). As an exception, the dye was also inkjet-printed from concentrated C101 dye solutions (10-16 mM in DMF or DMSO) in Publication IV.

Counter electrodes (CE): Clean FTO glass substrates were platinized by casting a $4 \text{ }\mu\text{L}$ drop from 5 mM $\text{H}_2\text{PtCl}_4 \cdot 6\text{H}_2\text{O}$ solution (in 2-propanol) for the conventional CE fabrication. The inkjet-printed samples were, in contrast, prepared by heating the substrate during the printing process ($50 \text{ }^\circ\text{C}$) (Publication V). After the deposition of the Pt precursor with different methods (inkjet printing or drop casting) the layers were sintered at $385 \text{ }^\circ\text{C}$ for 15 min. The alternative CE in Publication 1 was prepared by initially coating SWCNT on FBS by spreading it with a disposable pipette and drying it on a hotplate at $120 \text{ }^\circ\text{C}$ for 5 min followed by two step spin coating (firstly at 500 rpm for 30 sec, followed by 1000 rpm for 30s) of p-toluenesulfonate doped poly(3,4-ethylenedioxythiophene) (PEDOT-TsO).

DSSC assembly: The electrodes were separated by a Surlyn frame foil (inner dimensions: $15\text{mm} \times 8 \text{ mm}$) and were fused together on the hot plate at $155 \text{ }^\circ\text{C}$. The gap between the two electrodes was filled with electrolyte through the pre-drilled

holes on the CE side. Thereafter, the cell was sealed with a Surlyn cover foil and thin glass cover with a hot press. The cell contacts were fabricated by copper tape and quick drying silver paint on glass before being finally isolated with epoxy.

CE-CE symmetrical cells assembly: Identical elements and assembly technique were used to produce inkjet-printed (Publication V) and drop-cast Pt based CE-CE symmetrical cells. The electrodes of the same type, which were drop-cast or inkjet-printed, were sandwiched by a Surlyn frame foil spacer (25 μm) on a hot plate at 155 $^{\circ}\text{C}$ and the electrolyte was injected between the CEs through two holes. The sealing and the encapsulation steps were carried out as explained previously in the DSSC assembly procedure.

3.2.3. Electrochemical cell parameters

The J - V curves of the DSSCs were recorded in a xenon lamp solar simulator from Peccell Technologies-Japan (Model PEC-L01) under standard illumination (light intensity = 1000 W/m^2 equivalent of 1 Sun). A silicon reference solar cell (PV Measurements Inc.) was used in the calibration of the simulator.

EIS data was recorded at open circuit voltage conditions using a Zahner-Elektrik IM6 electrochemical workstation under the same illumination conditions described for the photovoltaic performance measurements. The measured data was fitted by Zview2 software (Scribner Associates Inc.). All data fitting was executed in accordance with the equivalent circuit model outlined in [58].

3.3. Other characterization methods

3.3.1. Transmittance

Throughout this research, a Perkin Elmer lambda 950 UV-Vis spectrophotometer was used either in the solid or liquid state mode depending on the experiment, as detailed below.

Solid state measurements

In Publication V, the transmittance spectra of differently Pt coated (inkjet-printed and drop-cast) FTO based glass substrates as well as uncoated FTO based glass were captured with air as the background. The transmittance of the counter electrode (T_{CE}) is approximated as the product of the transmittance of each

component of the electrode system, such as the FTO-glass substrate ($T_{\text{FTO-Glass}}$), and the Pt coating (T_{Pt}) as outlined by Equation 11.

$$T_{\text{CE}} = T_{\text{FTO-Glass}} T_{\text{Pt}} \quad (11)$$

The transmittance of the Pt layer is related to its thickness by:

$$T_{\text{Pt}} = (1 - R_{\text{Pt}}) e^{-\alpha d} \sim \frac{T_{\text{CE}}}{T_{\text{FTO-glass}}} \quad (12)$$

where R_{Pt} is the reflectance of the Pt layer, α is the absorption coefficient and d is the film thickness. The semilogarithmic relation between the transmittance of the Pt layers at 550 nm wavelength and the Pt loading amount is:

$$\log_{10}(T_{\text{Pt}}) = \log_{10}(1 - R_{\text{Pt}}) - \log_{10}(e) \alpha L / \rho \quad (13)$$

which was obtained from Equation 12, by connecting the film thickness d to the Pt loading L by the density of bulk Pt metal, ρ , (21.45 g/cm³) as $d=L/\rho$.

A linear fit of Equation 13 to the transmittance vs. loading data allowed an estimation of the (Napierian) Pt film absorption coefficient (α) from the slope ($\log_{10}(e)\alpha/L$) and the reflectance of the Pt layer from the y-intercept ($\log_{10}(1 - R_{\text{Pt}})$).

Liquid state measurements

In Publication III, a 10 mM C101 dye solution (prepared in DMF) was inkjet-printed on a TiO₂ electrode (thickness = 7 μm and area = 0.4 cm²) by dispensing 1.1 μL/cm² per layer. By taking into account the nominal drop volume 10 ± 2 pL and 30 μm drop spacing parameter, each printed layer consisted of 11.3 nmol/cm² of dye and the experiments were conducted by printing 1 to 5 layer(s). Thereafter, the sensitized TiO₂ electrodes were rinsed with DMF (defined as “washed”) or were processed further without the washing step (“non-washed”) either to assemble DSSCs or to run dye desorption tests.

In dye desorption tests, the sensitized electrodes were left in a solution that consisted of tetramethylammonium hydroxide (TMAOH) and dimethylformamide (DMF) (50/50 by volume) until the dye detached from the TiO₂. The transmittance spectra of the dye in the desorption solution, were captured using a cuvette filled

with the dissolution solvent as the background in order to calculate the dye loading ($\text{mol}\cdot\text{cm}^{-2}$) from Equation 14.

$$n_{dye} = \frac{Abs_{sol}}{\epsilon_{dye} \times L} \times \frac{V_{sol}}{A_f} \quad (14)$$

where Abs_{sol} , ϵ_{dye} , L , V_{sol} , A_f are the absorbance value of the desorption solution at around 535 nm, molar attenuation coefficient of the dye ($\epsilon_{dye} = 1.75 \times 10^3 \text{ m}^2 \text{ mol}^{-1} \equiv 17.5 \times 10^3 \text{ M}^{-1} \text{ cm}^{-1}$), optical path length of the cuvette ($L = 1 \text{ cm}$), volume of the desorption solution and area of the PE (0.4 cm^2), respectively.

3.3.2. Microscopy

A MultiMode 8 atomic force microscope (AFM) equipped with a NanoScope V controller (Bruker Corporation, Billerica, MA) and a scanning electron microscope (SEM) (Zeiss Ultra 55 FEG-SEM) were utilized to examine the surfaces at the micro and nanoscale. The images from AFM were processed by NanoScope 8.15 software (Bruker) without any image correction (except flattening). The information about the uniformity of different layers as well as cross-sectional view of the paper based substrates were recorded with a Leica DM750 optical microscope.

Solar cells on natural fiber based substrates (Publication I)

Chapter 4: Solar cells on natural fiber based substrates

(Publication I)

FTO coated glass and a thin layer of Pt coating are the conventional substrate and CE catalyst for DSSCs, respectively. Despite of their high transparency and high chemical performance, their excessive costs have given rise to many studies with the aim of find high-performance and stable alternatives. In Publication I, a PEDOT and SWCNT coated FBS was designed and integrated into DSSCs as an alternative CE and a substrate.

After successfully passing the electrolyte penetration and Cobb water absorption tests, EPTR was coated with SWCNT. Initially, the variation of the contact angle and the volume of the sessile electrolyte drop were determined with a goniometer on the coated substrate. The contact angle of the drop remained stable (27°) throughout 120 sec and only around 0.02% decrease was observed in the volume of the sessile drop after 120 sec. The electrolyte leakage from the sealant edges, permeation through the substrate and evaporation due to the weak attachment of the sealant to the SWCNT layer were further studied by use of the dummy cell assembly. As a result, no signs of electrolyte leakage, evaporation or penetration were observed.

The mechanical tests i.e. bending and adhesion tests were also conducted after coating the substrate with carbon based ink. The SWCNT film exhibited minimal variations (1.4% rise) in the R_{SH} (initial value = $6.2 \Omega/Sq$) after being subjected to bending with a 2.5 cm and 2 cm radii for 10 times, whereas a 2.3% increase was observed after the substrate was bent with a 1.5 cm radius 10 times. In both cases, the tests were completed without any noticeable crack formation on the coating surface. Moreover, the overall net change in R_{SH} following the 10 consecutive tape adhesion test cycle was calculated to be around 5% and the deposited layer lost only a very few particles attached to the sticky side of the tape after the test was completed. These initial results demonstrated the potential of FBS as a flexible substrate for electronics applications.

After the catalytic performance of SWCNT coated FBS was enhanced by spin coating of a PEDOT:TsO layer, the potential of the new CE was tested in DSSCs - named as FBS/DSSC (Figure 11 a) – and were compared to the reference type of

cells, that comprised of drop-cast and thermally post-treated Pt on glass substrate (Glass/DSSC). The average photovoltaic parameter set is tabulated in Table 3 and the J - V curves of the best cells from each batch are presented in Figure 11 b).

Table 3: Average photovoltaic parameters of cells

Cell type	J_{sc} (mA/cm ²)	V_{oc} (mV)	FF (%)	η (%)	R_{CELL} (Ω)
FBS/DSSC	14 ± 1	718 ± 12	61 ± 3	6.0 ± 0.3	29 ± 4
Glass/DSSC	15 ± 1	788 ± 15	66 ± 3	7.7 ± 0.3	27 ± 5

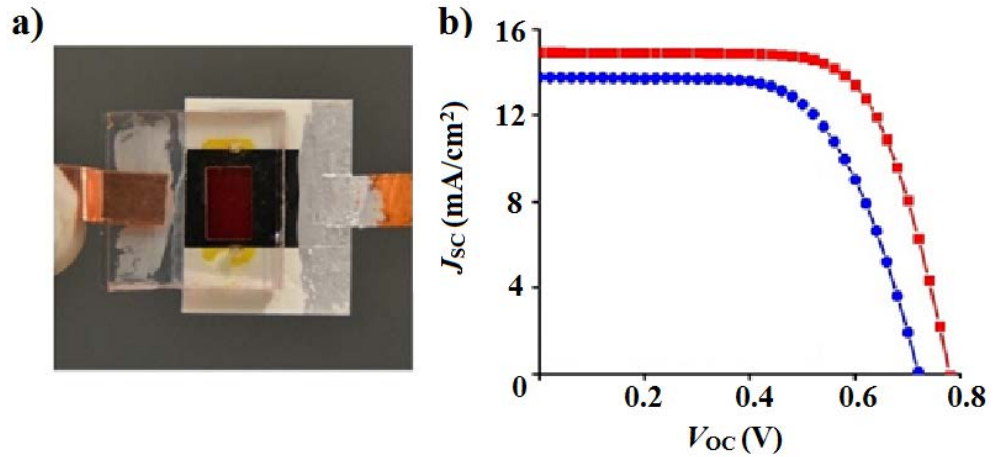


Figure 11: a) Picture of DSSC integrated on SWCNT and PEDOT coated FBS and b) J - V curves of the best cells (FBS/DSSC and Glass/DSSC were represented as blue circles and red squares, respectively).

From the results it can be determined that due to the slightly lower open circuit voltage, short circuit current density and higher cell resistance (affecting FF) when compared to the reference cell (with glass substrate), the FBS based cell exhibited around 20% less power conversion efficiency. In order to understand the mechanism behind this efficiency loss, which is related to the resistances of different layers, electrochemical impedance spectroscopy (EIS) measurements were performed over the 100 mHz to 100 kHz frequency range. The J - V curves of the best cells from each batch are presented in Figure 12, whereas the average EIS parameters are shown in Table 4.

The spectra of Glass/DSSC includes two low frequency peaks and one high frequency peak (Figure 12 b), as expected. The peak at 10-100 Hz corresponds to the recombination resistance at the TiO₂/dye/electrolyte interface ($R_{REC} = 2.7 \Omega\text{cm}^2$) and the other low frequency peak (1-10 Hz) represents the electrolyte diffusion

resistance ($R_D = 0.3 \Omega\text{cm}^2$). The peak in the high frequency region (1-10 kHz) reveals the charge transfer resistance at the catalyst/electrolyte interface ($R_{CT} = 1.4 \Omega\text{cm}^2$).

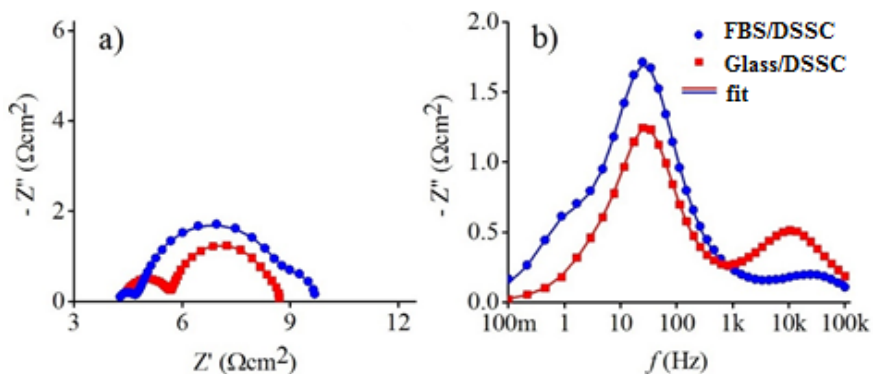


Figure 12: EIS measurements of the best cells (reference and FBS based cell) **a)** Nyquist plot and **b)** imaginary impedance by frequency (solid lines = fitted data and points = measured data)

Table 4: Average electrochemical impedance spectroscopy (EIS) parameters

EIS parameter (Ωcm^2)	FBS/DSSC	Glass/DSSC
R_S	5.5 ± 1.2	5.6 ± 1.3
$R_{REC+R_{CT}}$	5.0 ± 1.4	-
R_{REC}	-	2.7 ± 0.1
R_D	2.4 ± 0.4	1 ± 0.2
R_{PORE}	1.0 ± 0.3	-
R_{CT}	2.3 ± 1.3	2.7 ± 1.3
$R_{CT-TOTAL}$	3.3 ± 1.6	-

On the other hand, the PE and CE responses of FBS based DSSCs are overlapped in the low frequency range (10-100 Hz), therefore, the R_{CT} was estimated by subtracting the R_{REC} from the combined resistance response ($R_{CT} + R_{REC}$) as the same materials and process technique were employed to produce the PEs for each type of DSSC. At 10 kHz-100 kHz range (very high frequency), an extra peak appears and transforms to a very small semicircle in the Nyquist plot. This peak may be explained by the in-pore diffusion resistance ($R_{PORE} = 1.0 \pm 0.3 \Omega\text{cm}^2$) or contact (interfacial) resistance as outlined in the literature [61] [62].

Determined from the first semicircle, the series resistances of the cells were found to be comparable to each other (5.5 ± 1.2 and $5.6 \pm 1.3 \Omega\text{cm}^2$ for FBS and glass based cells, respectively). On the other hand, the R_{SH} of the FBS/DSSC ($5-10 \Omega/\text{Sq}$)

was found to be lower than the R_{SH} of the reference cell (15 Ω/Sq). Additionally, the catalytic activity of the new CE was found to be sufficient to facilitate the ion exchange at the CE/electrolyte interface.

In summary, a conductive, non-permeable and durable alternative CE was fabricated by coating a FBS with SWCNT and PEDOT in Publication I. It exhibited reasonable charge transfer resistance and efficiency as well as superior sheet resistance compared to the reference cell. This work demonstrated the feasibility of the paper based CEs, which are more flexible and economically-friendly when compared to the conventional CEs integrated on a glass substrate.

Characterization of liquid electrolytes (Publication 2)

Chapter 5: Characterization of liquid electrolytes (Publication 2)

In DSSCs, a redox couple (triiodide/iodide) based electrolyte provides the charge exchange between the CE and sensitizer. The most common lab-scale application method for the electrolyte is the injection of liquid through the pre-drilled holes on the glass substrates. Although many solid alternatives have been proposed, the best performing cells still contain a liquid electrolyte. One of the main reasons behind this search for alternatives is the impracticalities of the laboratory scale application of the liquid electrolytes into a DSSC. For instance, the pre-drilling of the glass substrate poses challenges due to the fragile nature of the glass and the injection of the electrolyte is mostly achieved with special injectors equipped with vacuum apparatus. Additionally, the pre-drilled holes on the substrate are required to be sealed after the injection of the liquid electrolyte to prevent electrolyte evaporation. Furthermore, the spatial variations in the characteristics of the cells that result from this methodology also leads to a reduction in the cell efficiency.

Due to the challenges associated with the electrolyte, inkjet printing was applied as an alternative method for the electrolyte deposition in DSSCs. Even though this method can overcome all the aforementioned difficulties and comes with many more advantages, the printing inks are required to be intensively examined prior to the inkjet printing process. With this motivation, in Publication II, three popular DSSC electrolytes (the components of which are outlined in Table 5) were characterized prior to the application of this method in the device fabrication sequence in Publication III. SFN, MPN and ACN electrolyte inks were prepared by dissolving the solutes in sulfolane, 3-methoxypropionitrile and acetonitrile ink based systems.

Table 5: List of electrolytes with their components and their molar ratios

Electrolyte	Components	Molar Ratio
SFN	DMII:EMII:EMITCB:I ₂ :NBB:GuSCN	12:12:16:1.67:3.33:0.67
MPN	I ₂ :GuSCN:NMBI:PMII	0.06:0.1:0.5:0.5
ACN	DMII:I ₂ :LiI:TBP:GuSCN	1:0.03:0.05:0.5:0.1

The low boiling point of the solvent can pose a problem with clogging, especially at higher nozzle temperatures, due to the evaporation of the ink. The solvents of the inks studied in this study i.e. sulfolane, 3-methoxypropionitrile and acetonitrile have the boiling points of 285 °C, 164 °C and 82 °C, respectively. As a result of its low with boiling point, ACN electrolyte was expected to have limited high temperature performance. On the other hand, normally some volatility of the solvent is necessary to dry the ink on the substrate. Nonetheless, since the electrolyte is encapsulated within DSSCs in liquid form and ideally kept in this phase throughout the device lifetime, there is no restriction on the upper limit of the boiling point.

Next, the goniometric measurements were conducted special printing paper [59]. Initially, the contact angle of sessile drops were measured over time and it was found that the SFN electrolyte maintained its contact angle for a prolonged time period and spread less when compared to other two electrolytes. This is especially important during the lab-scale cell assembly as after the electrolyte is inkjet-printed on the active area of the cell, the electrolyte pattern should not spread towards the inactive area of the cell whilst the sealant is aligned and heat applied to fuse the electrodes together.

As a second goniometric analysis step, the surface tension of pendant drops were examined over a temperature range between 23 °C and 60 °C (Figure 13). ACN demonstrated the lowest RT surface tension (24.5 ± 0.6) and a major alteration in the surface tension under different temperature conditions (around 30% decrease at 60 °C compared to RT condition). In contrast, the highest and most temperature stable surface tension was observed with SFN ink (42.7 ± 0.09 mN/m) with only a minor change measured throughout the applied temperature window. The MPN ink, which had an initial surface tension of 33.9 ± 0.14 mN/m, displayed a similar reduction in surface tension profile as that of ACN reaching almost 20% less at 60 °C compared to its initial surface tension. As a result, the surface tension analysis shows that MPN and SFN inks stay within the optimal limits of the surface tension defined by the manufacturer at all examined temperature points.

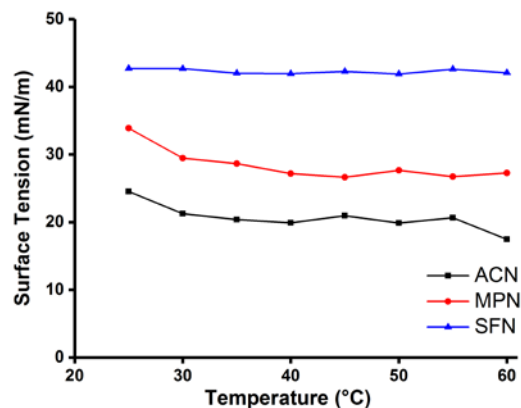


Figure 13: Surface tension of the inks between 23 °C and 60 °C

As a result of the measured lower evaporation rates at RT compared to the cases with higher temperature, the viscoelastic behaviors of the electrolyte inks were initially investigated at room temperature (RT = 23 °C) to allow the profiling of their dynamic viscosity (η) through strain (γ). It was found that all the inks had a shear thinning tendency in low to medium angular frequencies (over a small range) whereas a shear thickening behavior was observed through the rest of the strain window (200-1000s⁻¹). In particular, sulfolane based ink had the most uniform rheological behavior amongst all inks, while the MPN was found to be less dilatant compared to ACN. Additionally, the effect of the elevated process temperatures (40 °C and 60 °C) on the dynamic viscosity (η) of these electrolyte inks were tested through different strain (γ) amounts. Consequently, the dilatant nature of the inks almost vanished for all three inks at both 40 °C and 60 °C and their viscosity remained almost constant between 100-1000 s⁻¹ strain deformation rates making them Newtonian-like.

The recovery features of the inks were studied by 3ITT tests at room temperature in two different ways (Figure 14a and Figure 14b). As the common steps, a low shear rate of 0.1 s⁻¹ was applied during the first and third time intervals to the inks whereas the viscosity in the second interval were measured by imposing 500 s⁻¹ either stepwise (Figure 14a) or in a linearly increasing manner starting from 0.1 s⁻¹ (Figure 14b). In both cases, the viscosity of the inks exhibited a decrease in the high shear condition and the viscosity increased upon the reduction in the shear rate. Such a behavior is typical for the inks with dilatant nature [63]. Additionally, the stability during the ink recovery of SFN was found to be more prominent after subjecting the inks to a low-high-low shear intervals regime during 3ITT tests indicating that SFN ink would be the least affected by printing speed.

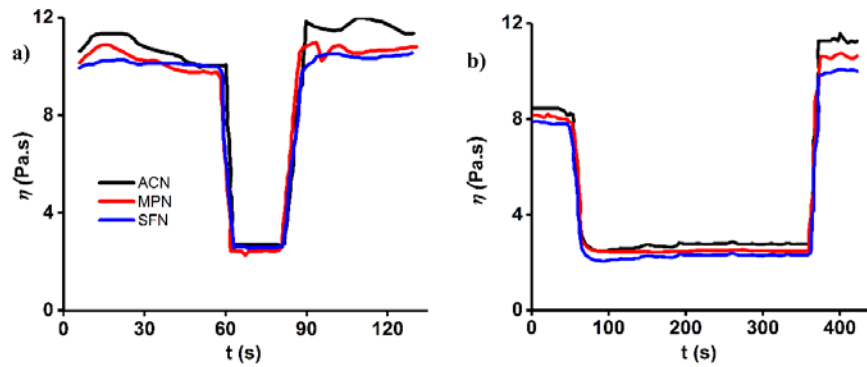


Figure 14: Viscosity change of the inks during the 3ITT tests with low-high-low shear exposure: **a)** one step increase of shear from 0.1 s^{-1} to 500 s^{-1} and **b)** linearly increasing shear from 0.1 s^{-1} to 500 s^{-1} in second interval

Next, the jet behavior of the inks was determined by applying different temperatures to the inks during the printing process. Only at $60 \text{ }^{\circ}\text{C}$, the drop formation from the ACN electrolyte failed due to the extreme evaporation at the nozzle orifice and the rest of the jetting trials were successful. Under RT conditions, the velocities of the electrolyte jets were measured as 3.5, 4 and 5 m/s for ACN, MPN and SFN inks, respectively. As expected, the drops travel faster in case of the elevated temperatures, i.e. 5, 6, 7 m/s at $40 \text{ }^{\circ}\text{C}$ and 0, 7, 9 at $60 \text{ }^{\circ}\text{C}$ m/s for ACN, MPN and SFN inks, respectively.

The print-outs of these inks were investigated by AFM micrographs (Figure 15 b-d) by comparing them to the bare substrate (Figure 15 a). The height images revealed that the highest uniformity was obtained by SFN ink and the surface decorated with ACN ink had the greatest height differences. Additionally, the pictures of the $4 \times 3 \text{ cm}$ size print-outs prepared at room temperature are presented in Figure 15 e-g. The pattern created with SFN ink had almost no failed jets whereas ACN ink resulted in many failed jets. In contrast, the MPN ink was slightly different as even though very few failed jets were observed on the pattern, the accuracy of the pattern precision was observed to be somewhat lower than the SFN ink. This is possibly due to 20% slower droplet speed of MPN ink when travelling between the nozzle and the substrate.

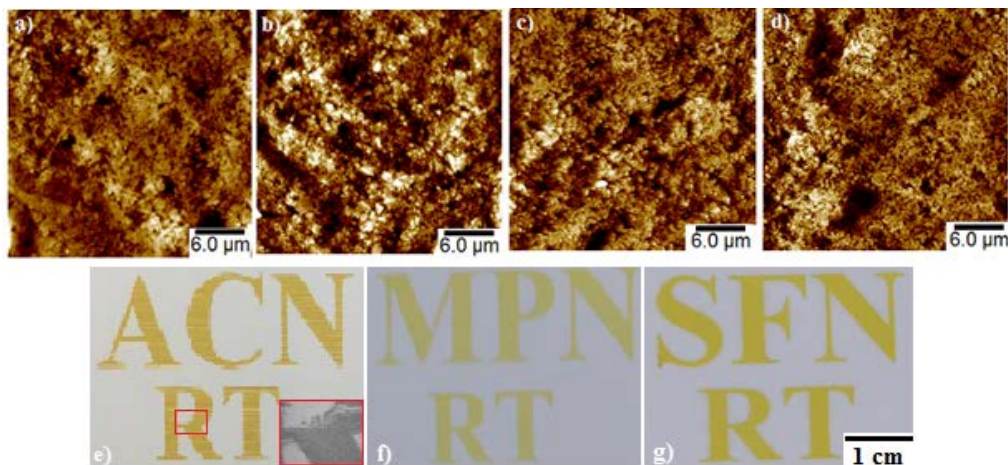


Figure 15: Inkjet print-outs at room temperature: a) unprinted paper as a reference, b), c) and d) AFM height images of the inkjet-printed surfaces with ACN, MPN and SFN, respectively, e), f) and g) 4 x 3 cm size print-outs prepared with ACN, MPN and SFN, respectively. The scale bar presented in g) is also valid for e) and f). The inset in e) is a fiducial camera image taken from the area which is marked with a red square.

The influence of the printing temperature on the printing quality was also investigated by examination of the isolated droplet patterns on the substrate as well as with 4 x 3 cm size print-outs. The failed jets for the ACN ink were almost eliminated at 40 °C, probably due to both the reduction in the time spent between the printing nozzle and the substrate as well as the less dilatant ink profile obtained. Similarly, the inaccuracy of the drops dispensed from MPN ink was decreased, whereas the quality of the print-outs from the SFN ink only exhibited minor changes.

As a result of these analyses, an inkjet printing process using the SFN ink was suggested to be the practical one due to its superior physicochemical performance and its operability at a wide range of temperature window compared to ACN and MPN inks. In particular, the RT condition might be more favorable compared to the elevated temperature due to the lower evaporation rate and minor changes in the quality of the output at different temperatures.

Inkjet-printed electrolyte in DSSCs (Publication 3)

Chapter 6: Inkjet-printed electrolyte in DSSCs (Publication 3)

In Publication III, inkjet printing method was utilized as an alternative method to fill the gap between CE and PE with electrolyte in a DSSC. The SFN based electrolyte was chosen to manufacture DSSCs with inkjet-printed electrolyte due to its superior printing quality as demonstrated in Publication II. The SFN electrolyte (termed as Z988-EL in the published article) was inkjet-printed over the dye (C101) sensitized mesoporous layer (TiO₂). After the printing process, Surlyn foil was positioned as a spacer for the electrolyte around the printed area and the two electrodes were fused together at 130-135 °C on a hot plate. The twin advantages of printing the electrolyte was the elimination of the pre-drilled holes on the glass and control of the amount of electrolyte. On the other hand, the reference cells were assembled with pre-drilled glass substrates, as previously explained in the “Device fabrication” section above.

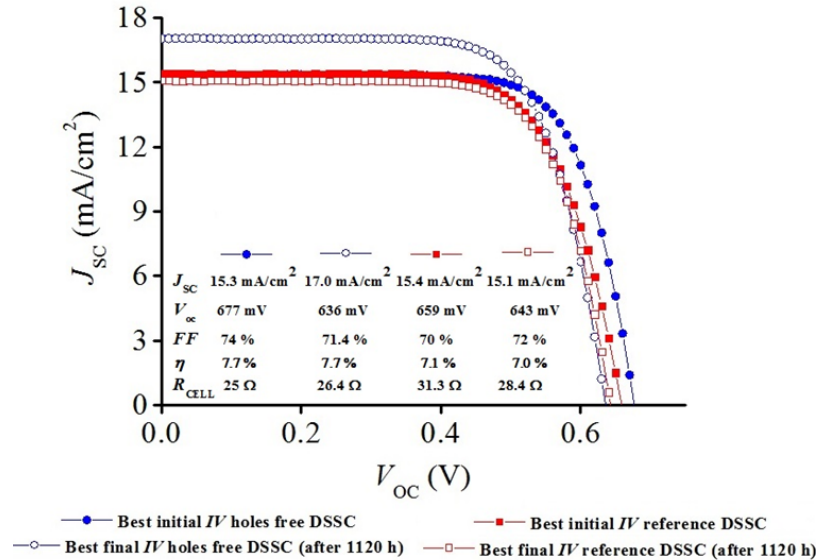
Initially the goniometric sessile drop studies were conducted on the CE side of the device which consists of a Pt coated FTO-glass. However, unsatisfactory goniometric results were obtained due to the uneven drop spread, possibly as a result of the uneven distribution of the coating. In contrast, the electrolyte drop on the PE side spread evenly on each side and created perfectly round drop patterns after remaining at around a 10 ° contact angle on the three phase intersection point. At this point, the surface tension is highly important not only for the jetting procedure and pattern creation on the substrate but also for the prevention of electrolyte spread towards the sealant.

After the cells were produced, the photovoltaic parameters of the DSSCs were recorded and the cells were subjected to a stability test, which consisted of light exposure (1 Sun) of open circuited cells at 35 °C for 1120 hours. Thereafter, the cells were measured under the same conditions as the initial measurements were performed. The average photovoltaic parameters are presented in Table 6 and the *J-V* curves of the best devices are shown in Figure 16. All the cells were measured with 0.17 cm² mask.

Table 6: Photovoltaic characteristics of initial and aged cells

	J_{SC} (mA/cm ²)	V_{OC} (mV)	FF (%)	η (%)	R_{cell} (Ω)
Initial					
Printed	14.9 ± 0.5	675 ± 3	73.7 ± 0.4	7.39 ± 0.26	27 ± 1
Ref.	14.9 ± 0.5	667 ± 11	70.3 ± 0.7	6.98 ± 0.15	32 ± 1
Aged					
Printed	17.1 ± 0.3	624 ± 9	69.9 ± 1.7	7.47 ± 0.21	29 ± 2
Ref.	14.7 ± 0.3	649 ± 9	72.3 ± 0.6	6.91 ± 0.08	30 ± 2

Due to the lower cell resistance and high FF , the hole-free inkjet-printed DSSCs resulted in a higher power conversion efficiency ($7.39 \pm 0.26\%$) when compared to the conventional cells ($6.98 \pm 0.15\%$) in the initial measurements. Additionally, the stability tests proved the durability of the inkjet-printed devices, which had a final efficiency of $7.47 \pm 0.21\%$. Interestingly, the FF and V_{OC} of the printed cells reduced whilst the J_{SC} increased had the effect of keeping the overall efficiency of the cells almost constant.

**Figure 16:** J - V curves of the best fresh and aged cells

The resistances of each component were analyzed by EIS and the EIS spectra of the best cells from both categories are presented in Figure 17. Logically, the reference cell in this work exhibited a similar response as the previous reference DSSCs. On the other hand, a small high frequency peak (10 kHz-100 kHz) was observed in the spectra of DSSCs with inkjet-printed electrolyte corresponding to a lower R_{CT} value ($1.0 \pm 0.1 \Omega$) compared to the R_{CT} of reference cell ($3.58 \pm 0.37 \Omega$). Additionally,

diffusion resistance of the new types of cell ($R_D = 4.8 \pm 0.1 \Omega$) was remarkably lower than the reference cells ($6.8 \pm 0.6 \Omega$).

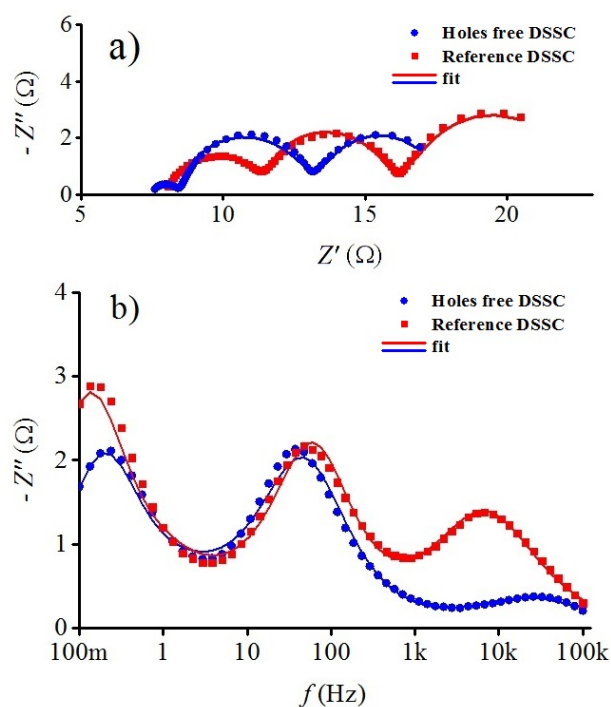


Figure 17. EIS measurements of the best cells (reference and hole-free cell): **a)** Nyquist plot and **b)** imaginary impedance by frequency (solid lines = fitted data and points = measured data)

In summary, Publication III was the first step to integrate inkjet printing deposition technique in the device fabrication sequence of DSSCs. As a result of the omission of the substrate pre-drilling and sealing process during encapsulation after the electrodes are fused, the cell preparation was much more straightforward when compared to the conventional device fabrication. Additionally, the resistive losses were decreased compared to the conventionally manufactured cells and the inkjet printing process had no discernable impact on the robustness of the cells.

Inkjet-printed dyes in DSSCs

(Publication 4)

Chapter 7: Inkjet-printed dyes in DSSCs (Publication 4)

In Publication IV, the dye sensitization process was attained through the inkjet printing of the dye solutions on the TiO₂ films. The accurate control of the dispensed dye allowed the coloration of the mesoporous PE to be tuned without any dye solution waste. Moreover, neither performance nor stability of the cells were compromised.

Initially, 1 to 5 layers of C101 dye solution (10 mM in DMF) was inkjet-printed on separate TiO₂ electrodes (7 μm thick). In this step, 1.1 μL/cm² solution was dispensed per dye layer on the electrodes with 0.4 cm² surface area. Thereafter, the sensitized TiO₂ electrodes were rinsed with DMF (“washed”) or were processed further without the washing step (named as “non-washed”) either to assemble the small DSSCs or to run the dye desorption tests. On the other hand, the reference cells were prepared by drop casting of the inkjet printing dye solution on the mesoporous oxide. Additionally, a “two color PE” was prepared by printing 10 mM Z749 in DMF solution along with the aforementioned C101 solution and the “gradient PE” was obtained by printing 1-5 layers close to each other on the same TiO₂ surface from the same C101 dye solution. All the fabricated samples are outlined in Figure 18.

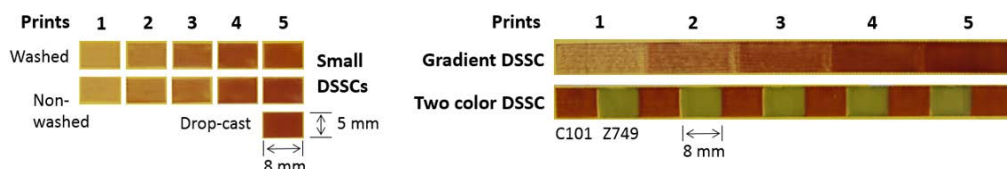


Figure 18: Washed and non-washed samples for small DSSCs (8 x 5 mm active area) with gradient and two color samples for big DSSCs (88 x 5 mm active area)

The absorbance spectra of the dye desorption solutions after the dye desorption tests (procedure and equations were presented in Chapter Three: Materials and Methods) shows a gradual increase with the printed layers (Figure 19). The precise dye loading through the inkjet printing process was proven by comparing the calculated and experimental results. According to the printer geometry, 11.3 nmol.cm⁻² was dispensed per print and the absorbance spectra of the dye desorption solutions of the non-washed samples revealed 12.5 nmol.cm⁻² per layer whereas a dye amount of 9.1 nmol.cm⁻² was observed for the washed samples.

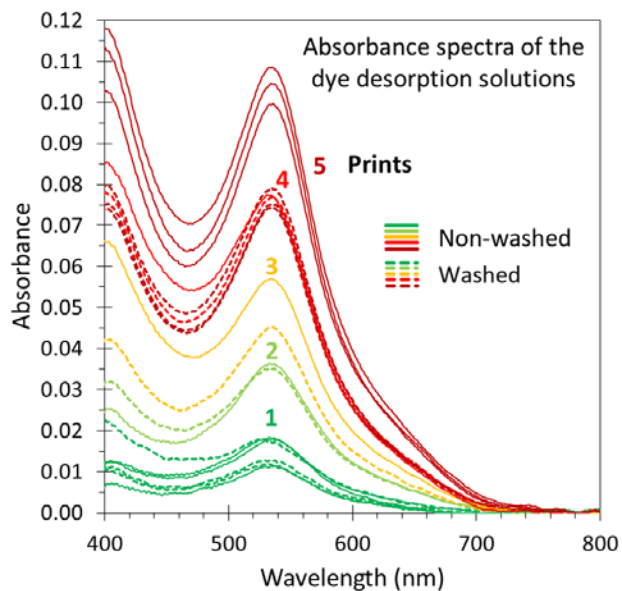


Figure 19: Absorbance spectra of the 4 ml dye desorption solutions with C101 dye measured through the cuvette having 1 cm optical path.

The effect of inkjet printing was further investigated by assembling large gradient and two-color DSSCs as well as small DSSCs. The systematic change in the dye loading in the small cells was also clearly noticed from the short circuit photocurrent density (J_{SC}) which gradually reached $\sim 10 \text{ mA/cm}^2$ with 5 layers of printing, whereas the drop-cast sample had $\sim 10\%$ more dye loading. On the other hand, the total resistance of the printed cells was reduced by adding more layers of dye due to the reduction in losses that stem from the recombination resistance at the PE side.

The J_{SC} change in the gradient cell with five segments followed the same trend as the small cells. It started from $\sim 1.5 \text{ mA/cm}^2$ short circuit photocurrent density with one layer of dye deposition and increased to around 8 mA/cm^2 with five layers of dye deposition (Figure 20). The two color cell that consisted of 11 segments also exhibited a J_{SC} that corresponded to the five layer printed cells in the gradient cell. Such a correlation in the results is an indication of the capability of inkjet printing to print precisely without any unwanted mixing of the deposition solution.

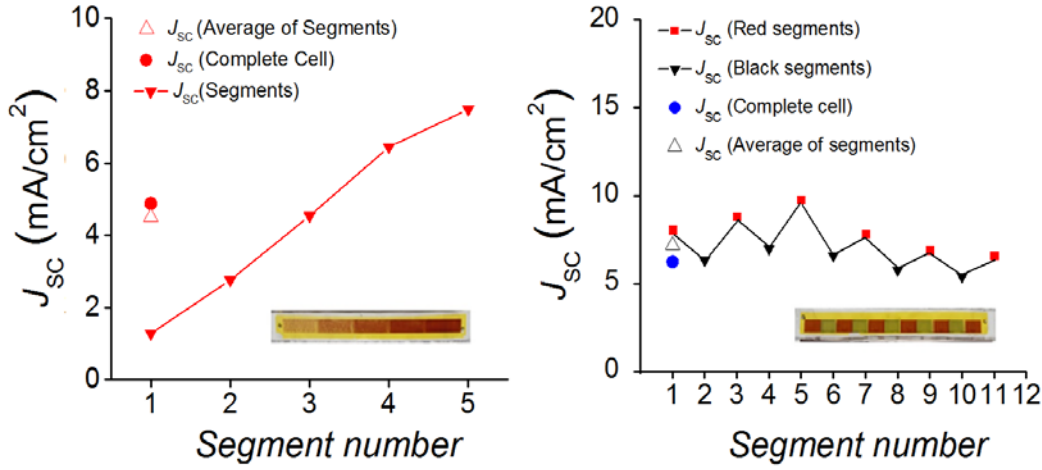


Figure 20: Short circuit photocurrent density values of the gradient and two-color DSSCs

Small DSSCs, including inkjet-printed dye over the PE of 12 μm thick mesoporous and 4-6 μm thick scattering TiO_2 , were produced to investigate the stability of the devices along with the reference cells (Table 7). Both type of cells exhibited almost the same device parameters except V_{OC} (5% higher average in reference cells). After the stability test of the cells was completed no significant signs of a decrease in the photovoltaic performance was measured.

Table 7: Photovoltaic characteristics of initial and aged cells

	J_{sc} (mA/cm ²)	V_{oc} (mV)	FF (%)	η (%)	R_{cell} (Ω)
Initial					
Printed	14.1 \pm 0.1	650 \pm 10	71.5 \pm 1.4	6.53 \pm 0.15	36 \pm 6
Ref.	13.8 \pm 0.3	660 \pm 8	71.2 \pm 1.6	6.47 \pm 0.13	38 \pm 6
Aged					
Printed	14.2 \pm 0.6	636 \pm 8	71.1 \pm 1.4	6.44 \pm 0.2	32 \pm 2
Ref.	13.1 \pm 0.8	672 \pm 16	72 \pm 0.7	6.34 \pm 0.28	35 \pm 3

To conclude, different dye solutions were inkjet-printed to produce PEs for DSSCs in Publication IV. Thanks to this method, the dye loading was controlled and the precise dye patterning of the TiO_2 layer was achieved. Additionally, the necessity of removing the excess dye after casting the dye solution was omitted and the dye was deposited only in the required amount, which reduces solution wastage. The cells prepared with inkjet-printed dye demonstrated no disadvantage in terms of the photovoltaics parameters when compared to the reference cells both in the initial

measurements but also in the measurements taken after the cells were subjected to ageing.

Inkjet-printed platinum in DSSCs(Publication 5)

Chapter 8: Inkjet-printed platinum in DSSCs(Publication 5)

The CE in a DSSC consists of Pt catalyst layer coated on FTO-glass substrate and the most popular lab scale production method is to cast a drop of 5-10 mM chloroplatinic acid hydrate ($\text{H}_2\text{PtCl}_4 \cdot 6\text{H}_2\text{O}$) solution (in 2-propanol) followed by the thermal decomposition at 385-410 °C. This method results in superior optical and electrochemical characteristics of the catalyst i.e. 90-96% light transmittance and 0.4-1.2 Ωcm^2 charge transfer resistance [64] [65] compared to other deposition techniques such as sputtering or electrodeposition [66] [67]. However, the uncontrollable patterns on the glass surface and the wastage of the Pt precursor still remain as the major drawbacks of this method.

In Publication V, Pt precursor of 5 mM $\text{H}_2\text{PtCl}_4 \cdot 6\text{H}_2\text{O}$ solution in 2-propanol was initially characterized for the inkjet printing process: viscosity of the ink was almost constant 1.2 mPa over the whole shear window investigated, surface tension was found to be 20.92 ± 0.4 mN/m and the solvent density and boiling point were 790 kg/m^3 and 82.6 °C, respectively. After characterization, the jetting properties of this ink was evaluated by calculating the jetting angle and flight trajectory. This was subsequently followed by printing parameter and substrate condition optimization, before the catalytic performance of the layers were studied by CE-CE cells and DSSCs.

The experiments were designed to control the Pt loading and thickness of the Pt layer on FTO-glass by changing the DS parameter in the printing process. 9.8, 8.1, 6.8, 5.8, 5, 4.4, 2.4, 0.6, 0.3 ($\pm 20\%$) $\mu\text{g}/\text{cm}^2$ Pt loading corresponding to 4.6 nm, 3.8 nm, 3.2 nm, 2.7 nm, 2.3 nm, 2 nm, 1.1 nm, 0.3 nm and 0.1 nm average Pt layer thicknesses were obtained with 10, 11, 12, 13, 14, 15, 20, 40 and 60 μm DS settings, respectively. The Pt loading was calculated by multiplying the number of drops with 10 pL ± 2 pL nominal drop volume and the layer thickness was calculated by dividing Pt loading to Pt density (21.45 g/cm^3). The Pt loading values of the reference cells prepared with 5 mM and 10 mM of 4 μL drops were around 2.5 $\mu\text{g}/\text{cm}^2$ and 5.1 $\mu\text{g}/\text{cm}^2$ corresponding to 1.2 nm and 2.4 nm average thicknesses, respectively.

The drop formation, jettability and impact were evaluated by the non-dimensional parameter set, i.e. Z, Re and We, which are presented in Table 8 along with the

velocity value of the drops. It can be determined from the high Z that the low viscosity of the ink may lead to satellites and the firing signal needs to be optimized accordingly. In addition, due to convenient Re and We numbers, no splashing on the substrate is foreseen and the system has enough energy to produce droplets.

Table 8: Calculated Z , Re and We values and velocity of platinum precursor

Parameter	Platinum precursor
Z	16
Re	75
We	23
v (m/sec)	5.3

The jetting performance of the Pt cursor was enhanced by fine-tuning the waveform signal with a 5 kHz jetting. The drop velocity and satellite formation as well as the trajectory were found to be dependent on the amplitude of this signal *i.e.* when the amplitude was increased, the drops moved faster such that satellite formation and deviation from the straight trajectory were observed at amplitudes > 21 V. At this amplitude, the velocity was found to be 5.3 m/sec and the trajectory fitted polynomial was $Y=76.03X - 1690.49$ with an angular difference of only 0.8° from Y -axis, an angular difference that remained the same throughout all experiments.

The Pt cursor exhibits complete wetting on the FTO surface. Thus, uncontrollable printing patterns are formed also due to the lack of absorption of the ink by the substrate. In order to minimize this effect, the temperature of the printing platform was adjusted to 50°C leading a uniformly Pt decorated FTO surface with approximately 10 nm clusters (Figure 21 and Figure 22). On the other hand, the Pt layer obtained by drop casting consisted of larger, unevenly distributed clusters.

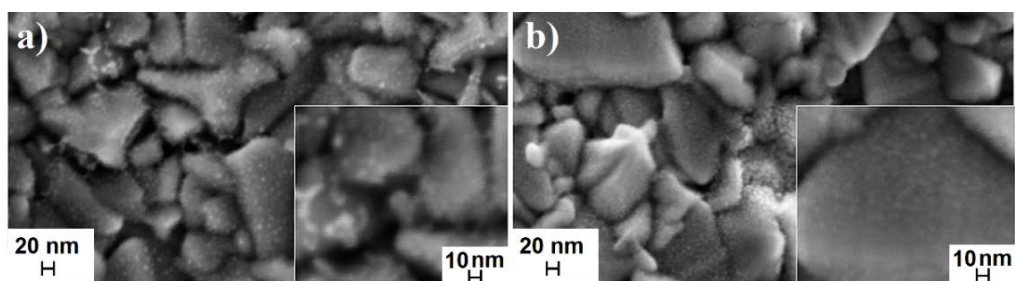


Figure 21: SEM images of Pt on FTO-glass surface thermal treatment: **a)** drop-cast and **b)** inkjet-printed samples

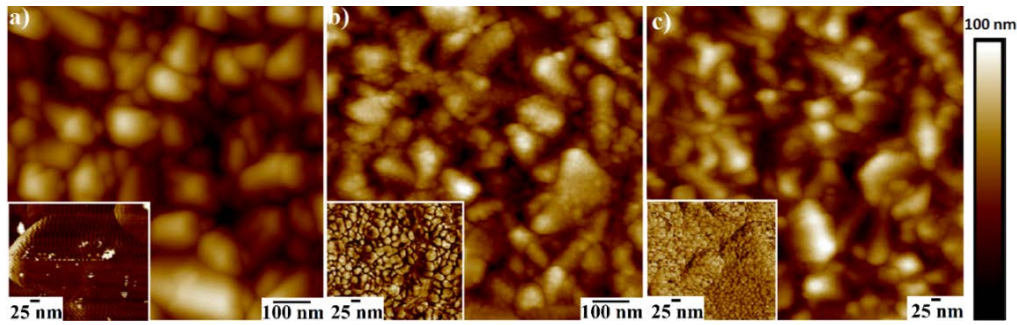


Figure 22: Height and phase (insets) AFM images of: **a)** uncoated FTO-glass, **b)** drop-cast Pt and **c)** inkjet-printed Pt samples

The transmittance of the platinized FTO-glasses and bare FTO-glass at 450 nm, 550 nm and 650 nm are shown in Figure 23 according to their corresponding platinum loading. Probably as a result of a more even morphology, the inkjet-printed Pt has a slightly higher transmittance than the drop-cast Pt for the same Pt loading. The transmittance of drop-cast samples prepared with 5 and 10 mM precursor have 93% and 91.2% at 550 nm respectively, whereas the transmittance of the printed Pt layers increases from 90.5% to 95.9% when DS is increased from 10 μm to 60 μm .

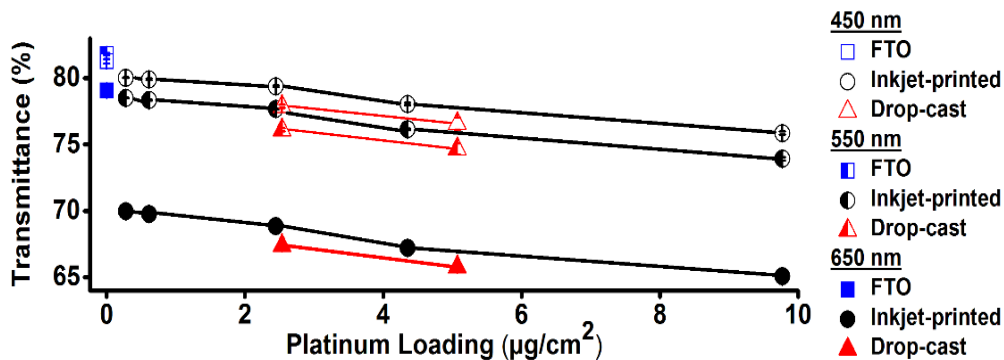


Figure 23: Transmittance values of bare FTO-glass as well as drop-cast and inkjet-printed Pt layers on FTO-glass samples at 450, 550 and 650 nm wavelength as a function of Pt loading

In addition, the reflectance of the Pt layers as well as (Napierian) absorption coefficient of the Pt film, α , were estimated by Equations 11-13. The inkjet-printed Pt layers resulted $\alpha \approx 0.00289 \text{ m}^{-1}$ and $R_{\text{Pt}} = 0.04\%$ whereas $\alpha \approx 0.00324 \text{ m}^{-1}$ and $R_{\text{Pt}} = 0.05\%$ were calculated for the drop-cast samples. These reflectance values are in accordance with the results of physical inspection, i.e. the coatings are not shiny.

In order to investigate the potential of the inkjet-printed Pt layers in DSSC, initially the CE-CE symmetrical cells were fabricated and then characterized by EIS measurements (100 mHz and 100 kHz frequency range). The Nyquist plot and

imaginary impedance of the CE-CE cells are presented in Figure 24. The average values of the series resistance (R_S), diffusion resistance (R_D), charge transfer resistance of two electrodes (R_{CT}) and normalized charge transfer resistance for one electrode calculated from 1.2 cm^2 sealant area (R'_{CT}) are shown in Table 9. Irrespective of the coating technique and the DS setting used for the inkjet printing process, all the cells exhibited standard EIS characteristics with two peaks. The controlled dispensing of Pt resulted in a gradual change in the EIS response with respect to the Pt loading in inkjet-printed cells.

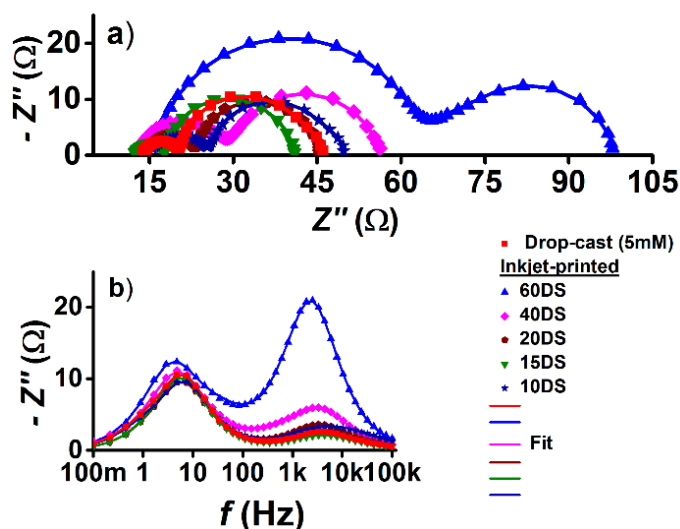


Figure 24: EIS measurements of the best symmetrical CE-CE cells (reference and inkjet-printed cell): **a)** Nyquist plot and **b)** imaginary impedance by frequency (solid lines = fitted data and points = measured data)

Table 9: Average R_S , R_D , R_{CT} and R'_{CT} values of CE-CE cells obtained from EIS measurements

	R_S (Ω)	R_D (Ω)	R_{CT} (Ω)	R'_{CT} (Ωcm^2)
10 DS	9.9 ± 0.6	0.6 ± 0.1	7.1 ± 0.2	4.2 ± 0.1
15 DS	10.4 ± 0.3	0.5 ± 0	11.8 ± 1.4	7.1 ± 0.8
20 DS	10.7 ± 0.1	0.6 ± 0	15.1 ± 0.6	9 ± 0.4
40 DS	12.7 ± 1.1	0.7 ± 0.1	44.9 ± 4	26.9 ± 2.4
60 DS	11.6 ± 0.9	-	71.7 ± 12.5	43 ± 7.5
Drop Cast	10.7 ± 0.3	0.5 ± 0.1	10.4 ± 3.7	6.2 ± 2.2

The controlled Pt loading on the FTO-coating resulted in a tuned R'_{CT} of the CE as presented in Table 9. Another important finding from the CE-CE study was that the

same amount of Pt loadings with different preparation methods, *i.e.* drop cast and inkjet-printed (20 DS) cells resulted no significant difference. On the other hand, 20 DS cells were prepared by using only 1 μL solution whereas the drop-cast sample consumed 4 μL .

As a consequence of the positive CE-CE cell results, DSSCs were prepared by using the same platinization methods and DS values for the inkjet printing. Interestingly, 10 DS and 15 DS cell as well as the reference cell exhibited similar catalytic performances (1.2, 1.0, 1.2 Ωcm^2 , respectively). Therefore, the stability of the devices was studied with platinized CEs with 11-15 μm DS settings by exposing them to 1000 h aging. The catalyst area in this case was calculated from the active area of the device (0.4 cm^2). Figure 25 shows the trends of the power conversion efficiency of the cells and the charge transfer resistance trends of the CEs prior to and after the 1000 h aging test. After the aging tests, it was found that both types of cell maintained their efficiencies and the charge transfer resistances of the cells reduced over the time period demonstrating the stability of the devices. Interestingly, the charge transfer resistance and the efficiencies of the inkjet-printed cells did not improve statistically with increased levels of Pt.

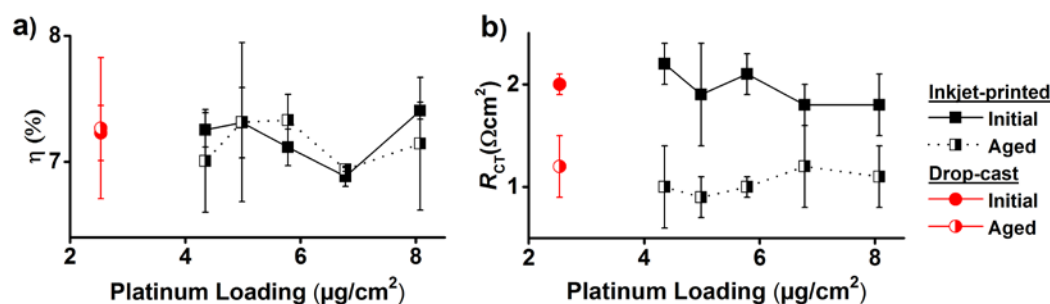


Figure 25: Stability of the inkjet-printed and drop-cast Pt CEs: **a)** power conversion efficiency and **b)** charge transfer resistance of the CE

In summary, in Publication V, a Pt precursor was inkjet-printed to produce CEs for DSSCs. In addition to remarkable savings of expensive Pt possible, the inkjet printing method potentially allows the properties of the Pt layer like transparency and charge transfer resistance to be tuned with respect to the Pt loading.

Conclusions

Thanks to the low cost and tailorable design possibilities, DSSC technology offers opportunities to create various versatile products for the printed electronics industry. Commonly, DSSCs have been produced by conventional methods, such as dip coating, drop casting or sputtering on glass substrates in the laboratory environment. On the other hand, utilization of diverse manufacturing methods as well as device integration on various substrates can provide alternative solutions for various application areas.

The conventional conductive substrate for the DSSCs is rigid and hard-to-process glass coated by an FTO layer. After addition of the catalyst (Pt) layer, the total cost of these components easily accounts for more than 50% of the total device cost. Motivated by also the flexibility and sustainability of the cellulosic substrates, a fiber based carton board was used as a platform to integrate the solar cells. By coating it with low temperature carbon and PEDOT based inks, an alternative CE and substrate combination was designed for DSSCs. Devices with this new design gave a comparable charge transfer resistance ($3.3 \pm 1.6 \Omega\text{cm}^2$), which is the main evaluation the criteria for the catalytic activity of CEs. This characteristic of the new design was only 20% more than the conventional alternative. Moreover, the cellulosic sheet coated with the carbon nanotube exhibited considerable flexibility with only a minor reduction observed in the conductivity during the adhesion and bending tests. As a result, it was possible to produce DSSCs on a bio-based cellulosic substrate with a promising power conversion efficiency ($6.0 \pm 0.3\%$), which was only 20% less than the conventional devices (Publication I).

The inkjet printing method, taking into consideration of its advantages like mask-free and no-material-waste precise patterning as well as enabling the control over the amount and the position of the latter, allows for new DSSC design opportunities. In order to benefit entirely from aforementioned advantages, the reliability of the printing process must be guaranteed starting from the movement of the ink inside the micro-channels of the printer until the drops reach to the substrate and the desired layer is deposited. In particular, the physicochemical characteristics of the printing inks are critical in this process and they are needed to be examined prior to the printing. In Publication II, the viscoelasticity of the three most popular electrolyte inks - a factor that impacts on print quality - was determined and an

alternative heating method was proposed to reduce this feature of the inks. The print-outs suggested that high temperature operation reduced the dilatancy of the inks and remarkably enhanced results were achieved for two of the inks investigated. As a result, the least dilatant ink was found to be optimal due to its physicochemical properties and superior performance at each temperature point (Publication II).

The effects of inkjet printing were explored to produce highly efficient dye-sensitized solar cells in comparison to conventional lab-scale production approaches (Publication III-V). The printing of the electrolyte layer instead of inserting it through the pre-drilled holes into the space between the electrodes removed the necessity of pre-drilling of the holes in the glass and sealing the holes without any compromise in the power conversion efficiency and the stability of the devices (Publication III).

The sensitization of the PE in a DSSC is normally achieved by either drop casting a concentrated solution of dye on the TiO₂ or keeping the TiO₂ coated glass substrate in a dilute solution of dye for extended time periods. The printing of the dye layer offers many advantages such as co-sensitization of the same electrode with more than one dye without disruption of the previously deposited dye. Furthermore, transparency and electrochemical functionality of the sensitized layer can also be tailored by knowing how much solution is dispensed and eliminating the regular washing step of the TiO₂ exposed to the dye. Results showed that these benefits can be obtained without any compromise in the power conversion efficiency (maximum 6.68%) and the stability of the devices (Publication IV).

Finally, inkjet platinization method was integrated into the device fabrication sequence of DSSCs instead of the standard platinization method used in lab-scale production (casting of a drop of dilute platinum solution on the conductive glass). A saving of more than 70 % of the expensive Pt was achieved in comparison to the drop-cast case. Moreover a similar charge transfer resistance of $9 \pm 0.4 \Omega\text{cm}^2$ was achieved in CE-CE cells *cf.* $6.2 \pm 2.2 \Omega\text{cm}^2$ for conventionally produced cells. Additionally, the cells with inkjet-printed CEs did not degrade over time (1000 hours aging) demonstrating the method's suitability for catalyst deposition (Publication V).

During the inkjet printing experiments, surface tension and viscosity were found to be important for the jetting process and pattern formation. For instance, the

platinum precursor, characteristically having a low viscosity, travels between the nozzle and the substrate longer time than the drop with an optimal velocity (around 50% more time spent). Additionally, its low surface tension resulted in extreme spreading lowering the quality of the print and heating of the substrate was proposed as a solution.

Overall, Publications III-V, show inkjet printing to be a very promising deposition technique for DSSC layers that offers similar levels of performance and stability.

9.1 Significance of this work

This dissertation presents the influence of inkjet printing technique used in the fabrication of DSSCs on the device parameters as well as on the characteristics of the deposited layer. In general, the solar conversion efficiencies of the devices with one inkjet-printed component was always comparable to the reference cells either in the initial evaluations or in the measurements taken after the stability tests. This proves the non-contaminating nature of the deposition process is suitable for the fabrication of such interesting electronic devices. In addition, the layers required no masking and the material wastage was minimized during the deposition, whilst the versatile production possibilities were increased (i.e. printing dyes in more than one color on the same surface or tuning the optical properties of the catalyst).

The electrochemical and mechanical results obtained during the integration of the cellulosic substrate coated with carbon and PEDOT based layers also evidently verified that this combination can be a viable alternative to the Pt and FTO coated glass components of a DSSC. Such a case would also provide the possibility for roll-to-roll production, which is currently impossible with conventional DSSCs.

9.2. Future research recommendations

Although there are still open questions about the consequences of integrating digital printing into the fabrication process of DSSCs, such as life-cycle assessment, the results in this study can be considered as the first step for such work in a broader context. Additionally, research aimed at determining the effects of inkjet printing of more than one layer, or even 100% inkjet-printed DSSCs, might be inspiring for many researchers. A possible drawback of the inkjet printing method is the cost of the equipment and the disposable cartridges. For instance, drop casting of platinum

or dye solution can be achieved by an inexpensive pipette with volume control whereas each ink must be stored in separate cartridges. Additionally, the reuse of relatively expensive cartridges brings up contamination as a possible issue, especially while jetting different type of inks.

In this study, the carbon based ink coated cellulose substrate was tested in a device and the initial device parameters were reported in Publication I. In order to be sure about the limits of the integration, the device can undergo the stability tests, which were applied in the Publications III, IV and V. Additionally, the absorbent nature of the substrate might bring certain drawbacks in extreme moist conditions from the open structure, which occurs on the edges of the substrate after cutting it prior to the coating step and using it in a device. An extra edge lamination might be proposed as a solution at this point.

The alternative substrate utilized in this work was an opaque cellulose based carton board with a thin layer of PET coating. First of all, recyclable, liquid-proof conductive coatings may be facilitated by the need for the sustainability of these types of devices. Furthermore, use of a substrate that consists of nano-sized cellulose fibers means that the light penetration into a device can be enhanced, paving the way for futuristic designs for solar converters based on bifacial and bio-based substrates. Another interesting study can aim the design of a fully flexible device from the alternative substrate utilized in this work. Such a target can be achieved by coupling the conductive carton board with a conductive plastic substrate

References

- [1] O. Ellabban, H. Abu-Rub, and F. Blaabjerg, “Renewable energy resources: Current status, future prospects and their enabling technology”, *Renew. Sustain. Energy Rev.*, vol. 39, pp. 748–764, 2014. DOI: 10.1016/j.rser.2014.07.113.
- [2] F. Boons, C. Montalvo, J. Quist, and M. Wagner, “Sustainable innovation, business models and economic performance: An overview”, *J. Clean. Prod.*, vol. 45, pp. 1–8, 2013. DOI: 10.1016/j.jclepro.2012.08.013.
- [3] K. L. Chopra, P. D. Paulson, and V. Dutta, “Thin-film solar cells: an overview”, *Prog. Photovoltaics Res. Appl.*, vol. 12, no. 23, pp. 69–92, 2004. DOI: 10.1002/pip.541.
- [4] Y. Hamakawa, “Thin-film solar cells: Next generation photovoltaics and its applications”, Springer Science & Business Media, Berlin, Germany, pp. 151-152, 2004. DOI: 10.1007/978-3-662-10549-8.
- [5] S. Mathew, A. Yella, P. Gao, R. Humphry-Baker, B. F. E. Curchod, N. Ashari-Astani, I. Tavernelli, U. Rothlisberger, M. K. Nazeeruddin, and M. Grätzel, “Dye-sensitized solar cells with 13% efficiency achieved through the molecular engineering of porphyrin sensitizers”, *Nat. Chem.*, vol. 6, no. 3, pp. 242–7, 2014. DOI:10.1038/nchem.1861.
- [6] M. A. Green, K. Emery, Y. Hishikawa, W. Warta, E. D. Dunlop, “Solar cell efficiency tables (version 49)”, *Prog. Photovolt. Res. Appl.* 25, pp. 3-13, 2017. DOI: 10.1002/pip.2788.
- [7] K. Masuko, M. Shigematsu, T. Hashiguchi, D. Fujishima, M. Kai, N. Yoshimura, T. Yamaguchi, Y. Ichihashi, T. Mishima, N. Matsubara, T. Yamanishi, T. Takahama, M. Taguchi, E. Maruyama, and S. Okamoto, “Achievement of More Than 25% Conversion Efficiency With Crystalline Silicon Heterojunction Solar Cell”, *IEEE J. Photovoltaics*, vol. 4, no. 6, pp. 1433–1435, 2014. DOI: 10.1109/JPHOTOV.2014.2352151.
- [8] Y. C. Wang, D. Y. Wang, Y. T. Jiang, H. A. Chen, C. C. Chen, K. C. Ho, H. L. Chou, and C. W. Chen, “FeS₂ nanocrystal ink as a catalytic electrode for dye-

- sensitized solar cells”, *Angewandte Chemie International Edition*, vol. 52, no. 26, pp. 6694–6698, 2013. DOI: 10.1002/anie.201300401.
- [9] B. E. Hardin, H. J. Snaith, and M. D. McGehee, “The renaissance of dye-sensitized solar cells”, *Nat. Photonics*, vol. 6, no. 3, pp. 162–169, 2012. DOI: 10.1038/nphoton.2012.22.
- [10] J. F. Dijkman, P. C. Duineveld, M. J. J. Hack, A. Pierik, J. Rensen, J.-E. Rubingh, I. Schram, and M. M. Vernhout, “Precision ink jet printing of polymer light emitting displays”, *J. Mater. Chem.*, vol. 17, no. 6, pp. 511–522, 2007. DOI: 10.1039/b609204g.
- [11] J. T. Delaney, P. J. Smith, and U. S. Schubert, “Inkjet printing of proteins”, *Soft Matter*, vol. 5, no. 24, p. 4866, 2009. DOI: 10.1039/b909878j.
- [12] H. Okimoto, T. Takenobu, K. Yanagi, Y. Miyata, H. Shimotani, H. Kataura, and Y. Iwasa, “Tunable carbon nanotube thin-film transistors produced exclusively via inkjet printing”, *Adv. Mater.*, vol. 22, no. 36, pp. 3981–3986, 2010. DOI: 10.1002/adma.201000889.
- [13] Z. P. Yin, Y. A. Huang, N. B. Bu, X. M. Wang, and Y. L. Xiong, “Inkjet printing for flexible electronics: Materials, processes and equipments”, *Chinese Sci. Bull.*, vol. 55, no. 30, pp. 3383–3407, 2010. DOI: 10.1007/s11434-010-3251-y.
- [14] K. Huff, "Active and intelligent packaging: innovations for the future", Department of Food Science & Technology. Virginia Polytechnic Institute and State University, Blacksburg, 1-13, 2008.
- [15] Solar Chargers for Photography, <https://www.voltaicsystems.com/solar-camera-charger>, accessed on 6/6/2017.
- [16] Portable Solar Power, <http://www.go-green-solar-energy.com/portable-solar-power.html>, accessed on 6/6/2017.
- [17] Nearly Zero Energy Buildings Definitions Across Europe, Factsheet, BPIE, http://www.bpie.eu/uploads/lib/document/attachment/128/BPIE_factsheet_nZEB_definitions_across_Europe.pdf, accessed on 6/6/2017.

- [18] Directive 2010/31/EU on the energy performance of buildings (recast) - 19 May 2010, <http://www.buildup.eu/en/practices/publications/directive-201031eu-energy-performance-buildings-recast-19-may-2010>, accessed on 6/6/2017.
- [19] D. K. Serghides, S. Dimitriou, M. C. Katafygiotou, and M. Michaelidou, “Energy efficient refurbishment towards nearly zero energy houses, for the mediterranean region”, *Energy Procedia*, vol. 83, pp. 533–543, 2015. DOI: 10.1016/j.egypro.2015.12.173.
- [20] S. D. Hoath, “Fundamentals of Inkjet Printing: The Science of Inkjet and Droplets”, John Wiley & Sons, Weinheim, Germany, pp. 1-2, 2016.
- [21] B. Derby, “Inkjet printing of functional and structural materials: Fluid property requirements, feature stability, and resolution”, *Annu. Rev. Mater. Res.*, vol. 40, no. 1, pp. 395–414, 2010. DOI: 10.1146/annurev-matsci-070909-104502.
- [22] J. Izdebska and S. Thomas, “Printing on Polymers: Fundamentals and Applications”, Elsevier, Waltham, p. 232, 2016.
- [23] G. Cummins and M. P. Y. Desmulliez, “Inkjet printing of conductive materials: a review”, *Circuit World*, vol. 38, no. 4, pp. 193–213, 2012. DOI: 10.1108/03056121211280413.
- [24] E. Özkol, J. Ebert, K. Uibel, A. M. Wätjen, and R. Telle, “Development of high solid content aqueous 3Y-TZP suspensions for direct inkjet printing using a thermal inkjet printer”, *Journal of the European Ceramic Society*, vol. 29, no. 3, pp. 403–409, 2009. DOI: 10.1016/j.jeurceramsoc.2008.06.020.
- [25] J. Brunahl, A. M. Grishin, S. I. Khartsev, and C. Osterberg, “Piezoelectric shear mode inkjet actuator”, *Sensors and Actuators A: Physical*, vol. 101, no. 3, pp. 371-382, 2002. DOI: 10.1016/S0924-4247(02)00212-1.
- [26] H. Le, “Progress and trends in ink-jet printing technology”, *Journal of Imaging Science and Technology*, vol. 42, no. 1, pp. 49-62(14), 1998.
- [27] Fujifilm Dimatix Materials Printer, Dimatix Ink Tutorial, <http://seen.spidergraphics.com/cnf5/doc/Ink%20formulation%20tutorial.pdf>, accessed on 6/6/2017.
- [28] Fujifilm, Dimatix Materials Printer DMP-2800 Series User Manual, (2008).

- [29] G. Cummins, R. Kay, J. Terry, M. P. Y. Desmulliez, and A. J. Walton, “Optimization and characterization of drop-on-demand inkjet printing process for platinum organometallic inks”, 2011, IEEE 13th Electron. Packag. Technol. Conf. EPTC 2011, pp. 256–261, 2011. DOI: 10.1109/EPTC.2011.6184427.
- [30] H. Wijshoff, “The dynamics of the piezo inkjet printhead operation”, *Phys. Rep.*, vol. 491, no. 4–5, pp. 77–177, 2010. DOI: 10.1016/j.physrep.2010.03.003.
- [31] A. Loi, “Inkjet printing: technique and applications for organic electronic devices”, Doctoral dissertation, Dipartimento di Ingegneria elettrica ed elettronica, Università degli Studi di Cagliari, 2013.
- [32] P. K. Notz, A. U. Chen, and O. A. Basaran, “Satellite drops: Unexpected dynamics and change of scaling during pinch-off” *Phys. Fluids*, vol. 13, no. 3, pp. 549–551, 2001. DOI: 10.1063/1.1343906.
- [33] S. D. Hoath, S. Jung, W. K. Hsiao, and I. M. Hutchings, “How PEDOT:PSS solutions produce satellite-free inkjets” *Org. Electron. Physics, Mater. Appl.*, vol. 13, no. 12, pp. 3259–3262, 2012. DOI: 10.1016/j.orgel.2012.10.004.
- [34] R. D. Deegan, O. Bakajin, and T. F. Dupont, “Capillary flow as the cause of ring stains from dried liquid drops” pp. 827–829, 1997. DOI: 10.1038/39827.
- [35] E. Tekin, P. J. Smith, and U. S. Schubert, “Inkjet printing as a deposition and patterning tool for polymers and inorganic particles” *Soft Matter*, vol. 4, no. 4, p. 703, 2008. DOI: 10.1039/b711984d.
- [36] H. Yoo and C. Kim, “Generation of inkjet droplet of non-Newtonian fluid” *Rheol. Acta*, vol. 52, no. 4, pp. 313–325, 2013. DOI: 10.1007/s00397-013-0688-4.
- [37] D. Cibis and K. Krüger, “System analysis of a DoD print head for direct writing of conductive circuits” *Int. J. Appl. Ceram. Technol.*, vol. 4, no. 5, pp. 428–435, 2007. DOI: 10.1111/j.1744-7402.2007.02160.x.
- [38] J. G. Korvink, P. J. Smith and D.-Y. Shin “Inkjet-based micromanufacturing” Wiley-VCH Verlag & Co, Weinheim, Germany, 2012, pp 3-5.
- [39] E. Tekin, P. J. Smith, S. Hoepfner, A. M. J. Van Den Berg, A. S. Susa, A. L. Rogach, J. Feldmann, and U. S. Schubert, “Inkjet printing of luminescent CdTe

- nanocrystal-polymer composites” *Adv. Funct. Mater.*, vol. 17, no. 1, pp. 23–28, 2007. DOI: 10.1002/adfm.200600587.
- [40] B. Derby and N. Reis, “Inkjet printing of highly loaded particulate suspensions” *MRS Bull.*, vol. 28, no. 11, pp. 815–818, 2003. DOI: 10.1557/mrs2003.230.
- [41] K. Dimic-Misic, *Micro and nanofibrillated cellulose (MNFC) as additive in complex suspensions: influence on rheology and dewatering*, doctoral dissertation, Aalto University, 2014.
- [42] H. Dong, W. W. Carr, and J. F. Morris, “An experimental study of drop-on-demand drop formation” *Phys. Fluids*, vol. 18, no. 7, 2006. DOI: 10.1063/1.2217929.
- [43] Fujifilm Dimatix Materials Printer. *Jettable Fluid Formulation Guidelines*, <https://www.fujifilmusa.com/shared/bin/Dimatix-Materials-Printer-Jettable-Fluid-Formulation-Guidelines.pdf>, accessed on 6/6/2017.
- [44] S. Magdassi, “The Chemistry of Inkjet Inks”, Section “Ceramic Inks” by S. Güttler and A. Gier, World Scientific Pub. , Singapore , 2009.
- [45] P. D. Angelo and R. R. Farnood, “Poly (3,4-ethylenedioxythiophene) :poly(styrene sulfonate) inkjet inks doped with carbon nanotubes and a polar solvent: the effect of formulation and adhesion on conductivity” *Journal of Adhesion Science and Technology*, vol. 24, no. 3, pp. 643–659, 2010. DOI: 10.1163/016942409X12561252292189.
- [46] J. E. Fromm, “Numerical calculation of the fluid dynamics of drop-on-demand jets”, *IBM Journal of Research and Development*, vol. 28, no. 3, pp. 322 – 333, 1984. DOI: 10.1147/rd.283.0322.
- [47] N. Reis and B. Derby, “Ink jet deposition of ceramic suspensions: modeling and experiments of droplet formation”, vol. 625, 2000. DOI: 10.1557/PROC-625-117.
- [48] D. Jang, D. Kim, J. Moon, D. Jang, D. Kim, and J. Moon, “Influence of fluid physical properties on ink-jet printability” *Langmuir*, vol. 25, no. 5, pp. 2629–2635, 2009. DOI: 10.1021/la900059m.

- [49] L.-Y. Wong, G.-H. Lim, T. Ye, F. B. S. Silva, J.-M. Zhuo, R.-Q. Png, S.-J. Chua, and P. K. H. Ho, "Jettable fluid space and jetting characteristics of a microprint head" *J. Fluid Mech.*, vol. 713, pp. 109–122, 2012. DOI: 10.1017/jfm.2012.440.
- [50] J. Y. Tai, H. Y. Gan, Y. N. Liang, B. K Lok, "Control of droplet formation in inkjet printing using Ohnesorge number category: Materials and processes", *Proceedings of the 10th Electronics Packaging Technology Conference (ECTC2008)*, Singapore, pp 761–766, 2008.
- [51] B. Derby, "Inkjet printing ceramics: From drops to solid," *J. Eur. Ceram. Soc.*, vol. 31, no. 14, pp. 2543–2550, 2011. DOI: 10.1016/j.jeurceramsoc.2011.01.016.
- [52] A. Kosmala, Q. Zhang, R. Wright, and P. Kirby, "Development of high concentrated aqueous silver nanofluid and inkjet printing on ceramic substrates," *Mater. Chem. Phys.*, vol. 132, no. 2–3, pp. 788–795, 2012. DOI: 10.1016/j.matchemphys.2011.12.013.
- [53] S. Lim, "Inkjet Printability of Electronic Materials Important to the Manufacture of Fully Printed OTFTs," 2012.
- [54] B. J. de Gans, P. C. Duineveld, and U. S. Schubert, "Inkjet printing of polymers: state of the art and future developments" *Adv. Mater.*, vol. 16, no. 3, pp. 203–213, 2004. DOI: 10.1002/adma.200300385.
- [55] J. G. Korvink, P. J. Smith and D.-Y. Shin "Inkjet-based micromanufacturing" *Wiley-VCH Verlag & Co, Weinheim, Germany*, 2012, pp 153-163.
- [56] A. Friederich, J. R. Binder, and W. Bauer, "Rheological control of the coffee stain effect for inkjet printing of ceramics," *J. Am. Ceram. Soc.*, vol. 96, no. 7, pp. 2093–2099, 2013. DOI: 10.1111/jace.12385.
- [57] B. O'Regan and M. Grätzel, "A low-cost, high-efficiency solar cell based on dye-sensitized colloidal TiO₂ films," *Nature*, vol. 353, no. 6346, pp. 737–740, 1991. DOI: 10.1038/353737a0.
- [58] J. Halme, P. Vahermaa, K. Miettunen, and P. Lund, "Device physics of dye solar cells" *Adv. Mater.*, vol. 22, no. 35, 2010. DOI: 10.1002/adma.201000726.

- [59] LumiPress Art - Technical data sheet, Stora Enso Paper, Finland, <http://printingandreading.storaenso.com/products-brands/for-print-media/coated-papers/LumiPress-Art>, accessed on 25.05.2017.
- [60] ISO535:1991(E), Paper and board - Determination of water, absorptiveness - Cobb method, International Organization for Standardization.
- [61] K. Miettunen, M. Toivola, G. Hashmi, J. Salpakari, I. Asghar, and P. Lund, "A carbon gel catalyst layer for the roll-to-roll production of dye solar cells," *Carbon* N. Y., vol. 49, no. 2, pp. 528–532, 2011. DOI: 10.1016/j.carbon.2010.09.052.
- [62] C. Punckt, J. D. Roy-Mayhew, D. J. Bozym, C. Punckt, and I. A. Aksay, "Functionalized graphene as a catalytic counter electrode in dye-sensitized solar cells" *ACS Nano*, 4 (10), pp 6203–6211, 2010. DOI: 10.1021/nn1016428.
- [63] M. M. Voigt, R. C. I. MacKenzie, S. P. King, C. P. Yau, P. Atienzar, J. Dane, P. E. Keivanidis, I. Zadrazil, D. D. C. Bradley, and J. Nelson, "Gravure printing inverted organic solar cells: The influence of ink properties on film quality and device performance," *Sol. Energy Mater. Sol. Cells*, vol. 105, pp. 77–85, 2012. DOI: 10.1016/j.solmat.2012.04.025.
- [64] L. Kavan, J.H. Yum, M. Grätzel, "Optically transparent cathode for dye-sensitized solar cells based on graphene nanoplatelets", *ACS Nano* 5, 165, 2011. DOI: 10.1021/nn102353h.
- [65] L. Kavan, J.-H. Yum, M. Grätzel, "Graphene-based cathodes for liquid-junction dye sensitized solar cells: Electrocatalytic and mass transport effects", *Electrochim. Acta* 128, 349, 2014. DOI: 10.1016/j.electacta.2013.08.112.
- [66] X. Fang, T. Ma, G. Guan, M. Akiyama, T. Kida, E. Abe, "Effect of the thickness of the Pt film coated on a counter electrode on the performance of a dye-sensitized solar cell", *J. Electroanal. Chem.* 570, 2, 257–263, 2004, DOI: 10.1016/j.jelechem.2004.04.004.
- [67] D. Fu, P. Huang, and U. Bach, "Platinum coated counter electrodes for dye-sensitized solar cells fabricated by pulsed electrodeposition-Correlation of nanostructure, catalytic activity and optical properties", *Electrochim. Acta* 77, 121-127, 2012. DOI: 10.1016/j.electacta.2012.05.158.

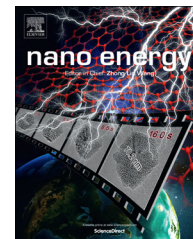
APPENDIX 1



Available online at www.sciencedirect.com

ScienceDirect

journal homepage: www.elsevier.com/locate/nanoenergy



RAPID COMMUNICATION

Highly conductive, non-permeable, fiber based substrate for counter electrode application in dye-sensitized solar cells



Syed Ghufran Hashmi^{a,*}, Merve Ozkan^b, Janne Halme^a,
Jouni Paltakari^b, Peter D. Lund^a

^aNew Energy Technologies Group, Department of Applied Physics, Aalto University, P.O. Box 15100, FI-00076 Aalto, Espoo, Finland

^bDepartment of Forest Products Technology, Aalto University School of Chemical Technology, Espoo, Finland

Received 1 June 2014; received in revised form 18 July 2014; accepted 19 July 2014
Available online 1 August 2014

KEYWORDS

Dye sensitized solar cells;
Counter electrode;
Carbon nanotubes;
Adhesion;
PEDOT

Abstract

3rd Generation photovoltaic systems such as dye-sensitized solar cells offer almost limitless material base that can be tested in variety of combinations with unique cell designs. One of the key challenges that remains with the dye-sensitized solar cells is to reduce their fabrication cost without compromising the performance. Such a target can only be achieved by fabricating inexpensive and abundantly available materials with simple and rapid preparatory methods that could deliver robust characteristics within the cell. With this motivation, we report here successful implementation of a highly conductive flexible fiber based substrate in dye-sensitized solar cell which is fabricated by coating a low temperature single walled carbon nanotube ink over a laminated fiber sheet. The substrate exhibited extraordinary durability under severe mechanical stability test conditions, reasonable overall efficiency ($6.0 \pm 0.3\%$) and charge transfer resistance ($3.3 \pm 1.6 \Omega \text{ cm}^2$).

© 2014 Elsevier Ltd. All rights reserved.

*Corresponding author. Tel.: +358 505952671;
fax: +358 451199233.

E-mail addresses: ghufran.hashmi@aalto.fi,
sghufranh28@gmail.com (S.G. Hashmi).

Dye-sensitized solar cells can be potentially fabricated through a high speed, roll to roll fabrication line by implementing flexible substrates such as transparent conducting oxide (TCO) coated flexible polymer sheet e.g. indium doped tin oxide polyethyleneterephthalate (ITO-PET) and indium doped tin oxide polyethylenaphtalate (ITO-PEN) or flexible metallic

sheets such as titanium (Ti) or stainless steel (StS) [1]. For transferring the traditional glass based geometry to the flexible DSSC, most of the experiments have been performed on these afore mentioned substrates [2-11]. However, each type of these flexible substrates have their pros and cons. For example, the opaque metallic sheets can be used as a photoelectrode (PE) because they can handle high temperature sintering process that is critically required to obtain high quality TiO_2 film [12] whereas the disadvantage associated with implementing a metal photoelectrode is the reverse illumination which affects the overall efficiency due to the absorption of light by the semitransparent catalyst layer and electrolyte [1]. Another drawback of using inexpensive metal sheets such as StS is their corrosion in the presence of iodine based redox couple either used as PE or counter electrodes (CE) [13-15]. Hence one of the immediate needs for this technology is to find alternative choices for substrates that could be composed of inexpensive and abundantly available materials similar to the cheap metals and could give high conductivities as well as robust mechanical characteristics. With this motivation, we report here about successful implementation of a non-permeable and highly conductive fiber based substrate (FBS) in dye-sensitized solar cell which is fabricated by coating a low temperature curable single walled carbon nanotube ink over a laminated fiber sheet. The substrate exhibited extraordinary durability against liquid penetration as well as severe mechanical stress, reasonable efficiency ($6.0 \pm 0.3\%$) and low charge transfer resistance ($3.3 \pm 1.6 \Omega \text{ cm}^2$) when tested as counter electrode in dye-sensitized solar cells.

The examined fiber based substrate (FBS), known as 'Encocard Pharma TR', supplied by Stora Enso Oy (Figure 1a) was identified through a wide series of tests (see Experimental methods section) that established its high

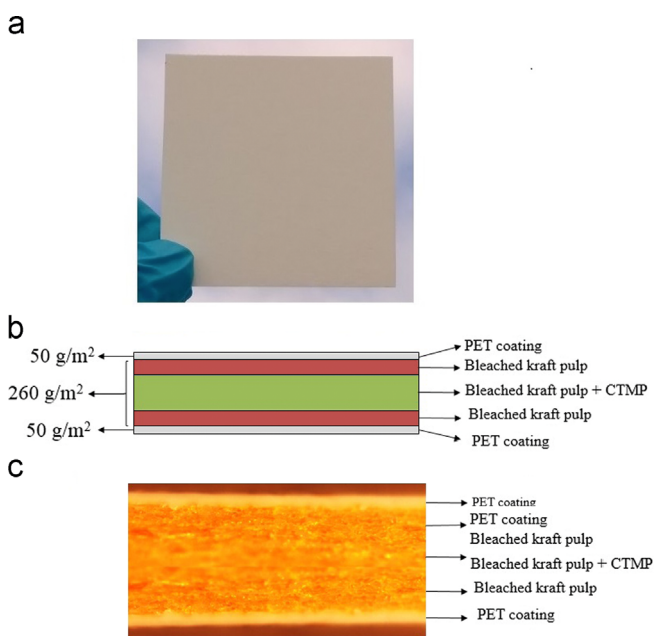


Figure 1 (a) Fiber based substrate 'Encocard Pharma TR'. (b) Illustration of the components of the substrate. (c) Optical microscope image. Fiber layers were stained with Arcidine Orange (N,N,N',N'-tetramethylacridine-3,6-diamine).

resistance against the liquid penetration. The basic structure of FBS is illustrated in Figure 1b whereas its composition was explored through optical micrograph (Figure 1c). The FBS is composed of three layers of bleached fibers kraft pulp (Sulfate pulp) [16] along with the chemi thermo mechanical pulp [17,18] which are sandwiched by compressing between two very thin layers of PET polymer coatings (Figure 1b and c). The fiber layers provide mechanical strength and necessary stiffness and at the same time good flexibility to the composite whereas the double sided polymer coating ensures high stability against water or moisture and does not allow them to penetrate inside the substrate.

Like the ITO-PET or ITO-PEN polymer sheets, the FBS can withstand only up to around 160 °C which restricts the use of high temperature based ink or paste of the desired materials over this FBS substrate as well. Therefore a low temperature based aqueous SWCNT ink was applied [19] (see Experimental methods section). The deposition scheme is shown in Figure 2(a-d) where the active area (patterns) was defined through tape mask (Figure 2a) and the aqueous SWCNT ink was spread over the active area of the substrate through a disposable pipette (Figure 2b). Then the substrate was placed over the preheated (120 °C) hotplate and in less than 5 min, upon solvent drying (Figure 2c), the FBS was transformed into a highly conductive substrate (Figure 2d). The sheet resistance of the deposited SWCNT film could be easily reduced from 30 Ω /sq to 5 Ω /sq by decreasing the concentration of surfactant particles from 0.1 to 0.05 g respectively, without compromising the adhesion of the film on the substrate (see Experimental methods section).

One of the major challenges associated with low temperature carbon compounds based inks/paste is their mechanical stability over the deposited substrates which is also rarely reported in the literature [8,19,20]. Therefore for this study, the mechanical durability of the deposited SWCNT film was examined through the substrate bending and tape adhesion tests.

SWCNT coated FBS stripe, as shown in Figure 3(a), was bended (10 times each) over very small bending radii (ranged from 2.5 cm to 1.5 cm) and its sheet resistance (R_{SH}) was regularly measured. These results are summarized in Figure 3(b-d). Marginal changes i.e. (1.4%) in the R_{SH} was observed when the substrate was exposed to 2.5 cm and 2 cm bending radii (Figure 3b and c). Slightly higher (2.3%) change in R_{SH} was observed when the substrate was further bended over severely lower bending radius (1.5 cm, Figure 3d). Moreover, the net change in R_{SH} from the very first relaxed value (of 2.5 cm bending radius) to very last relaxed value (of 1.5 cm bending radius) was only 5.2%. Additionally no visual cracks in SWCNT film were appeared ensuring the high adhesion of deposited SWCNT film.

The mechanical stability of deposited SWCNT film was further examined through severe tape adhesion tests where the layer was subjected under the heavy (2 kg) rolling through a round metallic disk under two types of pressure sensitive tapes (3M Removable i.e. Tape 1 and 3M Magic i.e. Tape 2, Figure 4a-d). The initial sheet resistance ($R_{SH}=6.2 \Omega$ /sq) was marginally (1.6%) increased upon first time tape removal (Figure 4b). This increment was almost maintained in further three consecutive tape adhesions and pulls and was again further changed to 1.6%. Hence the

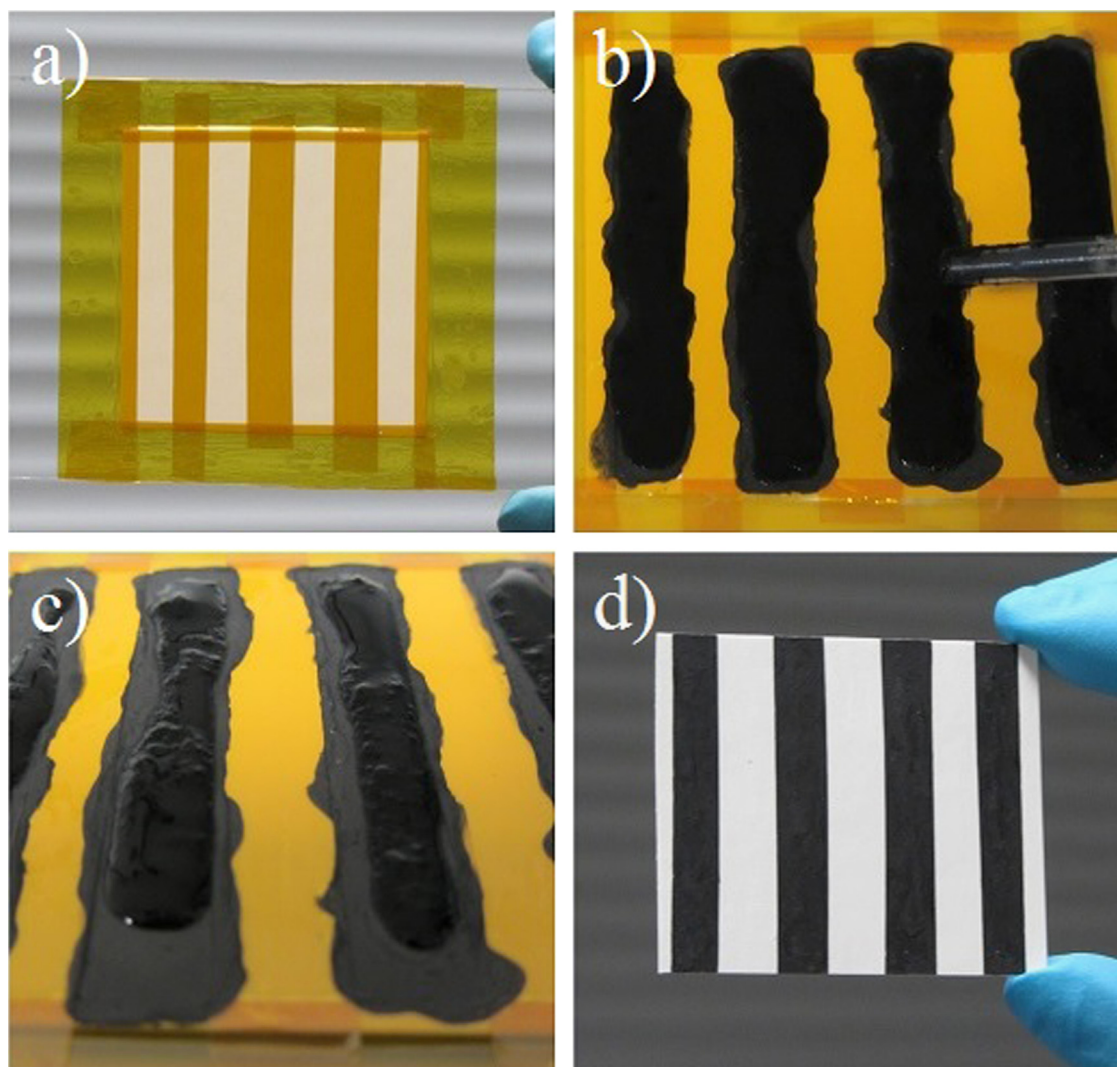


Figure 2 Deposition scheme of low temperature SWCNT ink (a) masking for active area through the tape, (b) ink spread through disposable pipette over the defined area, (c) solvent drying at 120 °C and (d) highly conductive substrate.

deposited SWCNT film exhibited minimal overall change (3.2%) in the sheet resistance with the Tape 1 confirming its remarkable adhesion.

This high adhesion over the nonconductive substrate of the SWCNT film was achieved due to significant enhancement in wetting properties of the low temperature ink [19]. The added surfactant (SDBS) is actively participating to a significant increase in the solubility of SWCNT into water [21,22], reducing the surface tension of the ink presumably by forming micelles around the hydrophobic surface of the carbon nanotube [23] as well as by increasing the viscosity of the end fluid [19] thus increasing the interaction forces between the SWCNT and the FBS.

This strong adhesion was further examined with more adhesive tape (i.e. 3M Magic, Tape 2, Figure 4c) and its R_{SH} was regularly measured (Figure 4d). The deposited SWCNT film unveiled high mechanical stability and maintained the initial R_{SH} (6.4 Ω /sq) under three initial tape pulls (Figure 4c) whereas a slight increase (1.6%) in R_{SH} with further two more tape adhesions and pulls. Hence the overall net change in R_{SH} after 10 consecutive tape

adhesions and pulls was less than 5% as very few particles from the deposited layer were detached (Figure 4a and c) certifying the robust adhesion over the FBS substrate.

Hence this highly conductive SWCNT coated FBS was tested as an alternative substrate for DSSC application where the typical requirement for the conductivity ranges in between 5 and 60 Ω /sq [10]. However the substrate requires an additional catalyst layers as the CNT were not found enough catalytic to obtain the desired results [24,25]. Therefore thin film of PEDOT:TsO to work as a catalyst layer was deposited through spin coating. The morphology of deposited films are depicted in the SEM image (Figure 5) which discloses a uniform coverage of PEDOT catalyst layer over the randomly distributed SWCNT network.

Finally, the FBS CE based DSSCs were assembled as shown in Figure 6(a) and their *IV* curves were recorded in the solar simulator. The average photovoltaic performance of three cells of each type are presented in Table 1 whereas Figure 6b represents the typical *IV* curve of the best cell of each type of DSSC. The FBS CE based DSSC exhibited $6.0 \pm 0.3\%$ (Table 1) overall cell efficiency in comparison

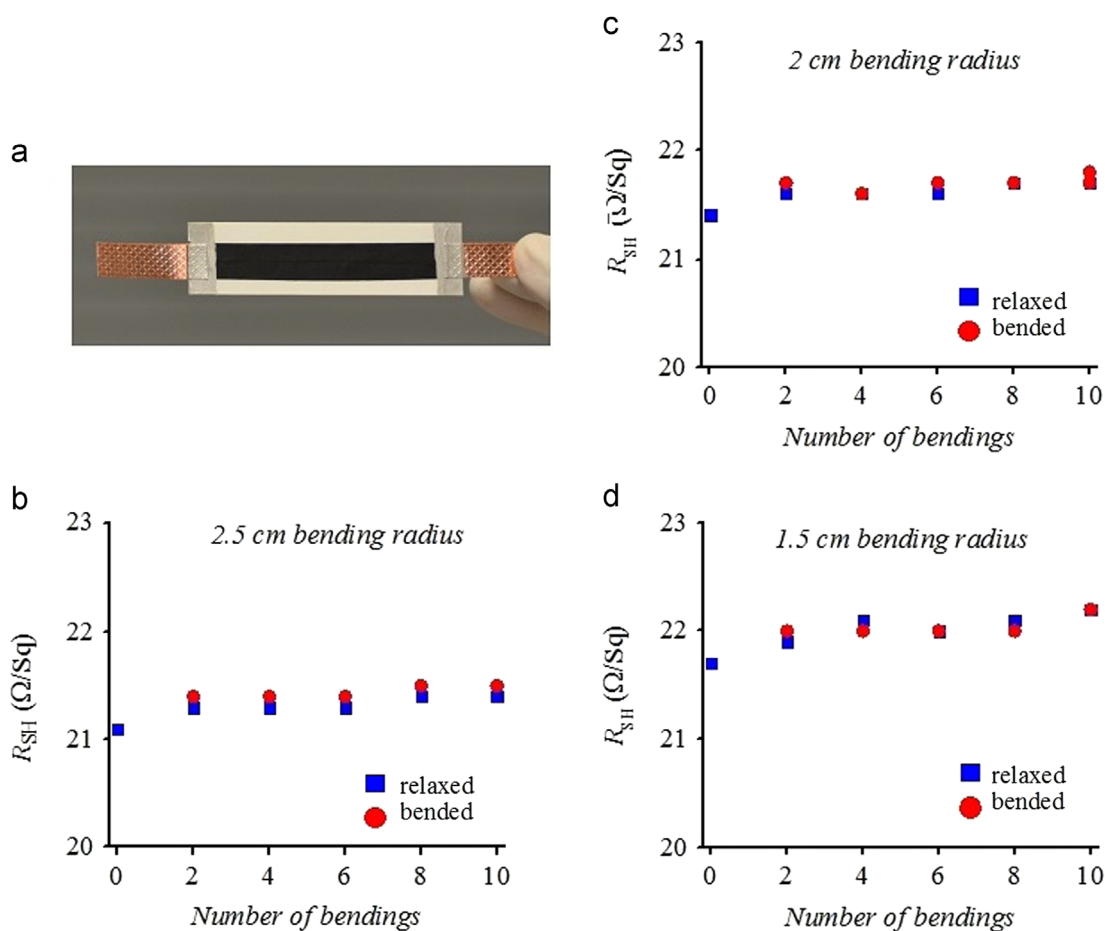


Figure 3 (a) SWCNT coated FBS substrate stripe was used for bending tests. SWCNT coated FBS substrate's mechanical bending tests of sheet resistance (R_{SH}) on (b) 2.5 cm bending radius, (c) 2 cm bending radius and (d) 1.5 cm bending radius.

with the reference $7.7 \pm 0.3\%$ (Table 1) thermally platinized counter electrode (TPCE) based DSSC due to lower open circuit voltage ($V_{OC} = 718 \pm 12$, Table 1) and short circuit current density ($J_{SC} = 14 \pm 1$, Table 1) as well as slightly higher cell resistance ($R_{CELL} = 29 \pm 4$, Table 1) than the reference ($27 \pm 5 \Omega$, Table 1). R_{CELL} depends upon several factors for instance resistance of photoelectrode or recombination resistance (R_{REC}), charge transfer resistance at the counter electrode (R_{CT}) or diffusion resistance (R_D). The information about these parameters can be obtained through electrochemical impedance spectroscopy (EIS) measurements which is discussed in the next section. The slightly lower value of short circuit current density ($J_{SC} = 14 \pm 1 \text{ mA/cm}^2$) for FBS CE based DSSC compared to the reference DSSC ($15 \pm 1 \text{ mA/cm}^2$) is consistent with our previous reports for PEDOT catalyst based metal free CEs [24]. The already discussed possible hypotheses associated with lower current densities in these types of metal free counter electrodes are the migration of iron particles (4-8% metal contents were present in these SWCNT according to the data sheet) which remain present in CNT [25] or the detachment of PEDOT catalyst particles and their settlement over the PE [10]. However, discussing them in detail is not the objective of this study. Nevertheless, these limitations can be potentially reduced by producing more cleaned

CNTs or by using an alternative low temperature deposited catalyst such as a carbon composite paste [8]. Also the slightly higher R_{CELL} of FBS CE based DSSC resulted a comparatively lower ($61 \pm 3\%$, Table 1) fill factor than the reference ($66 \pm 3\%$, Table 1) DSSC. To get more concrete information about the aforementioned causes, the EIS measurement was performed for each type of DSSC and the results are discussed in the following.

Figure 7(a and b) represents the typical EIS spectra of the best reference TPCE (in red) and best FBS/SWCNT/PEDOT CE (in blue) based DSSCs whereas the average EIS parameters of each type of DSSCs are summarized in Table 2. These measurements were performed under 1000 W/m^2 light intensity of a solar simulator (at open circuit voltage). The measured frequency range was from 100 mHz to 100 kHz. Glass/Pt CE based DSSC, in this frequency range, exhibits two low frequency peaks and one high frequency peak (Figure 7b) [8,26]. The high frequency (1-10 kHz, Figure 7b) peak corresponds to the charge transfer resistance ($R_{CT} = 1.4 \Omega \text{ cm}^2$, Figure 7a) at the counter electrode where as one of the low frequency peaks which ranges in between 10 and 100 Hz corresponds to recombination resistance ($R_{REC} = 2.7 \Omega \text{ cm}^2$, Figure 7a) [8,26]. The second low frequency peak that falls in between ~ 1 and 10 Hz comes from the diffusion resistance ($R_D = 0.3 \Omega \text{ cm}^2$, Figure 7a) [8,26].

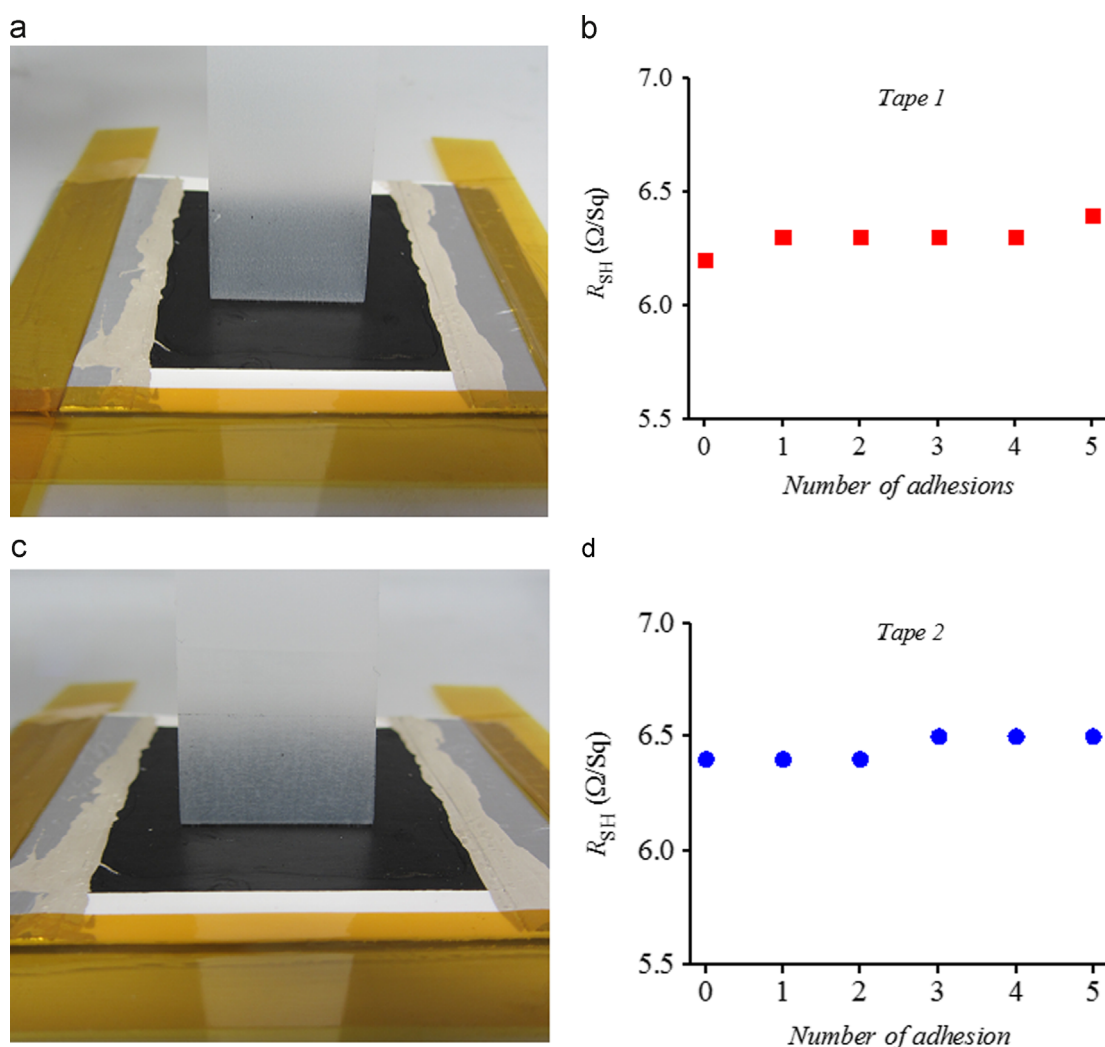


Figure 4 Tape adhesion test results (a and b) performed with pressure sensitive tape 3M Removable (Tape1), (c and d) performed with pressure sensitive tape 3M Magic (Tape 2).

The case is slightly different for FBS/SWCNT/PEDOT CE based DSSC (blue curve) where a large semicircle is obtained due to the overlapping of the responses of both PE and CE within the same low frequency range (10-100 Hz, Figure 7b) [10] and makes it difficult to get a correct estimation of its R_{CT} [10]. A reasonable approximation can be obtained by subtracting the R_{REC} value of the reference TPCE based DSSC from the total resistance ($R_{CT}+R_{REC}$) since the same PEs were used in fabrication of each type of solar cells [8,10]. Moreover, with FBS/SWCNT/PEDOT CE, there is an additional frequency peak which appears at very high frequency (i.e. 10-100 kHz, Figure 7b) and corresponds to a very small semicircle (i.e. the first semicircle from origin, Figure 7a) which has been hypothesized as in-pore diffusion resistance ($R_{PORE}=0.7 \Omega cm^2$, Figure 7b) or contact resistance [8,27,28].

The EIS spectra revealed lower series resistance ($R_S \sim 5.5 \pm 1.2 \Omega cm^2$, Table 2), i.e. the distance from origin to the first semicircle for both types of DSSC, in the FBS/SWCNT/PEDOT CE based DSSC than in the reference Glass/Pt CE ($5.6 \pm 1.3 \Omega cm^2$, Table 2) which confirms the high conductivity of the FBS substrate. Here the R_S mainly originates

from the R_{SH} of the substrates which was lower ($\sim 5-10 \Omega/Sq$) than in the reference FTO-Glass ($15 \Omega/sq$). Moreover the FBS/SWCNT/PEDOT CE exhibited lower R_{CT} ($2.3 \pm 1.3 \Omega cm^2$, Table 2) than the reference TPCE ($2.7 \pm 1.3 \Omega cm^2$, Table 2). The good catalytic performance of PEDOT catalyst has already been established in the literature [25,29]. The total charge transfer resistance ($R_{CT-TOTAL}=3.3 \pm 1.6 \Omega cm^2$, Table 2) [8] for FBS/SWCNT/PEDOT CE was finally calculated by adding the in-pore diffusion resistance ($R_{PORE}=1.0 \pm 0.3 \Omega cm^2$, Table 2) in the R_{CT} value.

In conclusion, we successfully engineered a new type of highly conductive, non-permeable fiber based substrate by applying low temperature single walled carbon nanotube ink with a quick and easy deposition scheme. This conductive substrate showed remarkable durability when subjected to very severe bending and tape adhesion tests. As a proof of concept, it was integrated in dye-sensitized solar cells for counter electrode application by spinning PEDOT catalyst layer that exhibited charge transfer resistance ($3.3 \pm 1.6 \Omega cm^2$) comparable with the reference platinum counter electrode ($2.7 \pm 1.3 \Omega cm^2$) and showed reasonable efficiency ($6.0 \pm 0.3\%$). These are much improved results

compared to our earlier report where a higher concentration of surfactant (SDBS) was used in the ink. In this experiment, the surface adhesion of the deposited SWCNT film was not at all affected upon reducing the amount of the surfactant and but resulted only better catalytic properties in the DSSC. This conductive FBS substrate also offers an alternative to cheap metal substrates which suffer due to corrosion problem in the presence of iodine based electrolyte in the cell. The result is a step towards low cost fully flexible printed DSSCs. Further work is nevertheless needed

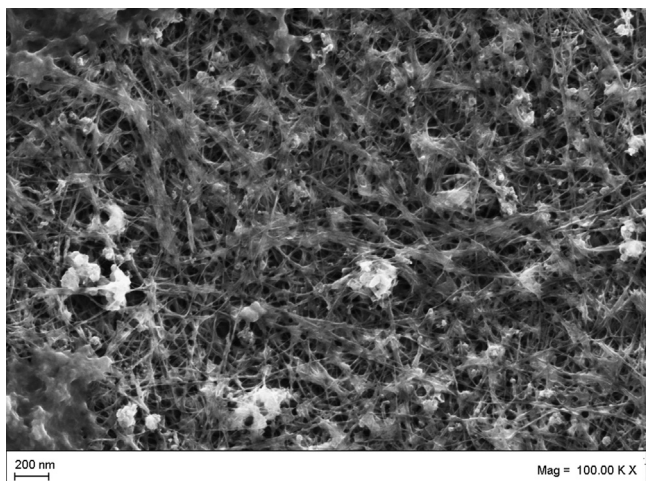


Figure 5 Scanning electron microscope images of PEDOT coated SWCNT on fiber based substrate.

to clarify the secondary effects that lead to lower V_{OC} and J_{SC} when FBS/SWCNT/PEDOT counter electrodes are used instead of the standard thermal Pt on FTO glass. These differences are not related to the conducting and catalytic properties of the CEs that affect only FF when they are sufficiently good, as was the case in the present work.

Experimental methods

Low temperature carbon nanotube ink

The low temperature SWCNT based aqueous ink was prepared by dispersing 0.05-1 g of surfactant sodium dodecyl benzene sulfonic acid sodium salt (SDBS, Fluka Chemika) and 0.05 g of SWCNT (Carbon solutions) in 10 ml of deionized water (DIW) with a tip sonicator (Branson model 450D) for 30 min followed by overnight aging at 40 °C in a water bath to complete the process.

Stability tests and selection of the substrate

Electrolyte leakage test

In the beginning, permeability of several types of commercially available fiber based flexible substrates was tested with drop test i.e. few drops of the electrolyte used in this study were dropped over these substrates and penetration of the drops were tested overnight. Among all the tested substrates, the 'Ensocard Pharma TR' supplied by Stora Enso (either bare or SWCNT coated) substrates showed no penetration or leakage of electrolyte.

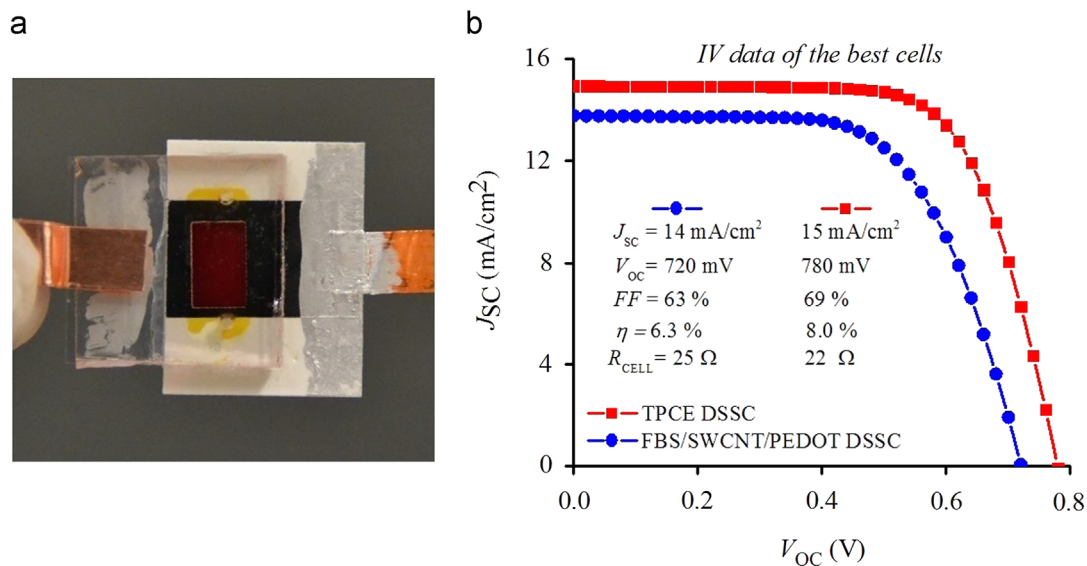


Figure 6 (a) FBS CE based DSSC. (b) IV curve of the best cell of each type of DSSC.

Table 1 Average photovoltaic performance of 3 cells of each type of DSSC along with their standard deviations.

Cell name	J_{SC} (mA/cm ²)	V_{OC} (mV)	FF (%)	η (%)	R_{CELL} (Ω)
FBS/SWCNT/PEDOT DSSC	14 ± 1	718 ± 12	61 ± 3	6.0 ± 0.3	29 ± 4
Glass/Pt DSSC	15 ± 1	788 ± 15	66 ± 3	7.7 ± 0.3	27 ± 5

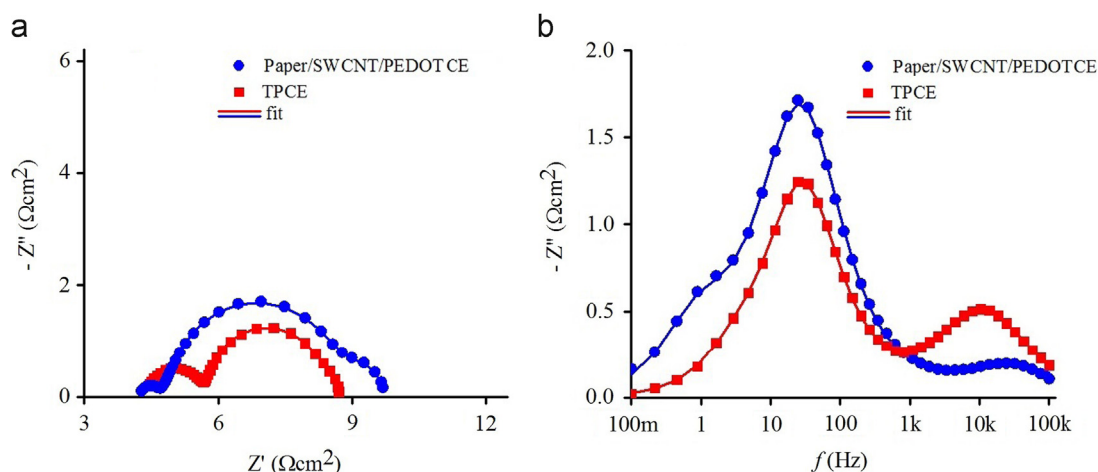


Figure 7 Typical EIS response of the DSSCs measured at V_{OC} under illumination represented as (a) Nyquist plot, as (b) imaginary impedance Z'' as a function of frequency (f). All solid lines correspond to the fitted data whereas the points represent the measured data.

Table 2 Average values of 3 cells of each type along with their standard deviations representing electrochemical impedance performances.

Cell type	R_S ($\Omega \text{ cm}^2$)	$R_{REC} + R_{CT}$ ($\Omega \text{ cm}^2$)	R_{REC} ($\Omega \text{ cm}^2$)	R_D ($\Omega \text{ cm}^2$)	R_{PORE} ($\Omega \text{ cm}^2$)	R_{CT} ($\Omega \text{ cm}^2$)	$R_{CT-TOTAL}$ ($\Omega \text{ cm}^2$)
FBS/SWCNT/PEDOT DSSC	5.5 ± 1.2	5.0 ± 1.4	-	2.4 ± 0.4	1.0 ± 0.3	2.3 ± 1.3	3.3 ± 1.6
Glass/Pt DSSC	5.6 ± 1.3	-	2.7 ± 0.1	1 ± 0.2	-	2.7 ± 1.3	-

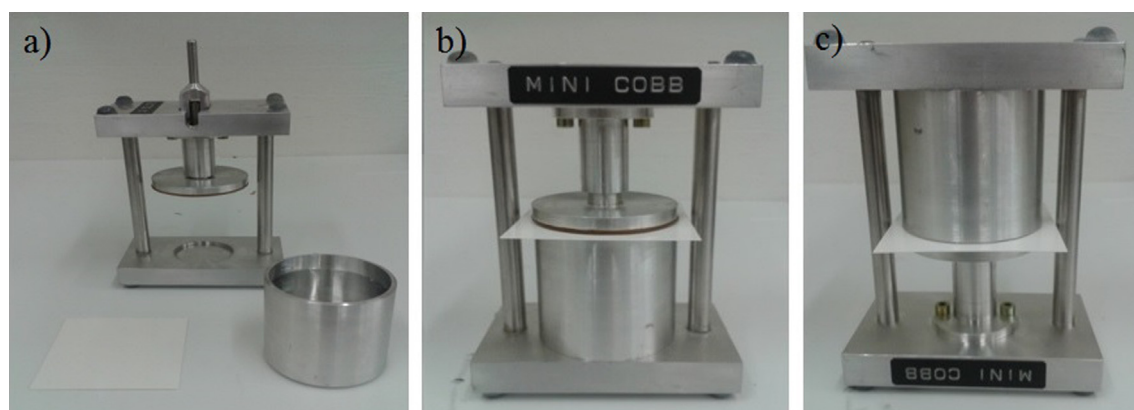


Figure E1 Cobb test for water absorptiveness (a) Mini Cobb with its ring filled with DI water and $7 \times 7 \text{ cm}^2$ substrate. (b) The substrate is fastened. (c) The substrate is exposed to water for one day by keeping Mini Cobb test device upside down.

Water absorption test

Liquid absorption resistance of the substrates was tested with a Cobb water absorption test. The Cobb test determines the amount of water absorbed by the surface of the substrate (typically sized or coated paper, paperboard or corrugated board) in a set period of time, usually 30, 60 or 120 s [30]. Water absorbance can be expressed as g/m^2 . The idea was adopted from the standard (ISO 535, EN 20535) tests and the fiber substrate ($7 \times 7 \text{ cm}^2$) was exposed to water for 24 h (Figure E1) with a smaller test cup (having inner diameter of

55 mm) for 24 h. No change in the weight of the fiber substrate was observed. The water absorption rate was less than the measurement sensitivity i.e. 0.42 g/m^2 .

Heat test

The droplets loaded fiber substrate (either bare or SWCNT coated) was then placed on a preheated ($80 \text{ }^\circ\text{C}$) hotplate for 2-3 h. No visible changes or signs of electrolyte leakage at the backside of the substrate were observed.

Light soaking test of dummy cells

The sandwich type dummy cell assembly was fabricated by separating the SWCNT coated fiber substrates and FTO coated glass through the Bynel frame foil (30 μm) and the electrolyte was injected through the drilled holes over the FTO glass substrate. The holes were then sealed with the Surlyn foil (20 μm) and a thin glass cover. These electrolyte containing dummy cells were then soaked in an artificial light soaking system under 1000 W/m^2 light intensity equivalent to 1 Sun illumination for 3 days and were then examined. No signs of electrolyte leakage were observed.

Metal free counter electrodes on FBS substrate

The prepared aqueous SWCNT ink was directly spread over the FBS (Ensocard Pharma TR supplied by Stora Enso) through a disposable plastic pipette and the substrate were then placed on a preheated oven at 120 $^{\circ}\text{C}$. Upon solvent drying in 5 min or less, the nonconductive FBS sheet was transformed into highly conductive substrate. The catalytic properties of deposited SWCNT were enhanced by spin coating (500 rpm for 30 s, 1000 rpm for 30 s) the conducting polymer poly(3,4-ethylenedioxythiophene doped with p-toluenesulphonate (PEDOT:TsO, Sigma Aldrich). The substrates were then heated at 100 $^{\circ}\text{C}$ for 30 min before assembly.

Thermal platinization on FTO glass

Platinum counter electrodes for the reference cell were fabricated by spreading 5 mM solution (4 μl) of chloroplatinic acid hydrate ($\text{H}_2\text{PtCl}_4 \cdot 6\text{H}_2\text{O}$) in 2-propanol on FTO coated glass substrates and fired at 410 $^{\circ}\text{C}$ in a preheated oven for 20 min. The substrates were then cooled down to room temperature and were kept in a sealed plastic box before use.

Photoelectrodes (PE)

The photoelectrodes for this study were prepared as follows.

In short three layers of nanocrystalline (18-NRT, Dyesol, 12 μm) and (4 μm) of scattering layer (WER2-0, Dyesol) of TiO_2 particles were sequentially deposited on pre-cleaned, TiCl_4 treated FTO glass substrate. These layers were then sintered at 500 $^{\circ}\text{C}$ for 40 min and were cooled down to room temperature followed by second time TiCl_4 treatment. The substrates were re-sintered at 500 $^{\circ}\text{C}$ and were again cooled down to room temperature. Finally the PEs were sensitized with 0.32 mM cis bis (isothiocyanato) bis (2,20-bipyridyl-4,40-dicarboxylato)-ruthenium (II) bis tetrabutylammonium (N-719, Solaronix) in ethanol (99.5 wt%) for 18 h to complete the process.

Cell assemblies

The PE and CE were separated with 25-50 μm thick Bynel foil (Dupont) in sandwich type assembly. Acetonitrile based electrolyte (0.06 M I_2 , 0.5 M PMII, 0.5 M TBP, 0.1 M GuSCN) was injected via drilled holes at PE. After that 20 μm thick Surlyn foil (Dupont) and thin glass cover were used to seal

the drilled holes via hot press. The contacts were then fabricated with copper tape and silver ink over the non-active area of the cell.

Measurements

The photovoltaic performance (*IV* curves) of fabricated DSSCs was recorded in a solar simulator under 1000 W/m^2 light intensity equivalent to 1 Sun. The active area of measured devices was 0.4 cm^2 . An electrochemical impedance spectrum analyzer (Zahner-Elektrik IM6 Potentiostat) was used to measure the electrochemical impedance spectra (EIS) of the samples. The samples for SEM imaging were prepared over FBS substrate and their images were recorded with Zeiss Ultra 55 FEG-SEM scanning electron microscope. The layered structure of the substrate was recorded with optical microscope Leica DM750 after staining the fibers with Arcidine Orange (N,N,N',N'-tetramethylacridine-3,6-diamine).

Mechanical stability test setup

Bending test

SWCNT coated FBS substrate ($L=6$ cm, $W=1$ cm, $T=3-5$ μm) was consecutively bent and relaxed over different bending radii and its resistance (R) was regularly measured [19]. Then given formula was used to calculate the sheet resistance (R_{SH}) of the stripe i.e. $R_{\text{SH}}=(RW)/L$ where W and L are the width and length of the SWCNT film respectively in between the electrical connections.

Tape adhesion test

The tape adhesion tests for this study were performed with two different types of pressure sensitive tapes (3M Removable and 3M Magic) [31]. SWCNT coated FBS substrate ($L=4$ cm, $W=3.3$ cm) was rolled down under the pressure sensitive tapes with a round metallic disk (2 kg). After that the tape was pulled at 90 $^{\circ}$ and the resistance (R) of the substrate was measured. Then its R_{SH} was calculated with the formula as described earlier (in section bending test).

Acknowledgments

This work was financed through Aalto University (Project # 91701904) (Renewable) and SELECT+ Erasmus Mundus Programme. Ghufuran Hashmi thanks Mr. Tapio Saukkonen for recording the SEM image for this study.

References

- [1] G. Hashmi, K. Miettunen, T. Peltola, J. Halme, I. Asghar, K. Aitola, M. Toivola, P. Lund, *Renew. Sustain. Energy Rev.* 15 (2011) 3717-3732.
- [2] T. Yamaguchi, N. Tobe, D. Matsumoto, T. Nagai, H. Arakawa, *Sol. Energy Mater. Sol. Cells* 94 (2010) 812-816.
- [3] S. Ito, N.C. Ha, G. Rothenberger, P. Liska, P. Comte, S. M. Zakeeruddin, et al., *Chem. Commun.* 38 (2006) 4004-4006.
- [4] J.H. Park, Y. Jun, H. Yun, S. Lee, M.G. Kang, *J. Electrochem. Soc.* 155 (2008) F145-F149.
- [5] S.K. Balasingam, M.G. Kang, Y. Jun, *Chem. Commun.* 49 (2013) 11457-11475.

- [6] D. Zhang, T. Yoshida, K. Furuta, H. Minoura, J. Photochem. Photobiol. A 164 (2004) 159-166.
- [7] L. Chen, W. Tan, J. Zhang, X. Zhou, X. Zhang, Y. Lin, Electrochim. Acta 55 (2010) 3721-3726.
- [8] S.G. Hashmi, J. Halme, T. Saukkonen, E.L. Rautama, P. Lund, Phys. Chem. Chem. Phys. 15 (2013) 17689-17695.
- [9] H. Lindstrom, A. Holmberg, E. Magnusson, S. Lindquist, L. Malmqvist, A. Hagfeldt, Nano Lett. 1 (2001) 97-100.
- [10] G. Hashmi, K. Miettunen, J. Halme, I. Asghar, H. Vahlman, T. Saukkonen, Z. Huaijin, P. Lund, J. Electrochem. Soc. 159 (2012) H656-H661.
- [11] T. Ma, X. Fang, M. Akiyama, K. Inoue, H. Noma, E. Abe, J. Electroanal. Chem. 574 (2004) 77-83.
- [12] M. Toivola, J. Halme, K. Miettunen, K. Aitola, P.D. Lund, Int. J. Energy Res. 33 (2009) 1145-1160.
- [13] K. Miettunen, X. Ruan, T. Saukkonen, J. Halme, M. Toivola, H. Guangsheng, et al., J. Electrochem. Soc. 157 (2010) B814-B819.
- [14] K. Miettunen, M.I. Asghar, X. Ruan, T. Saukkonen, J. Halme, P. Lund, J. Electroanal. Chem. 653 (2011) 93-99.
- [15] K. Miettunen, J. Halme, P. Lund, J. Phys. Chem. C 113 (2009) 10297-10302.
- [16] Chemical Pulping, Book 6, Updated second edition of Part 1, Pedro Fardim (Ed.), Paper Engineers' Association/Paperi ja Puu Oy, Porvoo, 2011, 748 p., ISBN:978-952-5216-41-7.
- [17] C.-A. Lindholm, Chemimechanical pulping, Chapter 8 in Book 5 Mechanical Pulping, Bruno Lönnberg (Ed.), Paper Engineers' Association/Paperi ja Puu Oy, Jyväskylä, 2009, pp. 248-281, ISBN:978-952-5216-35-6.
- [18] J. Sundholm, Idea of mechanical pulping, Chapter 2 in Book 5 Mechanical Pulping, Bruno Lönnberg (Ed.), Paper Engineers' Association/Paperi ja Puu Oy, Jyväskylä, 2009, pp. 18-22, ISBN:978-952-5216-35-6.
- [19] S.G. Hashmi, J. Halme, Ying Ma, T. Saukkonen, P. Lund, Adv. Mater. Interfaces 1 (2014) 1300055.
- [20] M. Wu, T. Ma, ChemSusChem 5 (2012) 1343-1357.
- [21] M.J. Rosen, Surfactants and Interfacial Phenomenon, John Wiley & Sons, New York 243.
- [22] M.F. Islam, E. Rojas, D.M. Bergey, A.T. Johnson, A.G. Yodh, Nano Lett. 3 (2003) 269.
- [23] M.J. Rosen, Surfactants and Interfacial Phenomenon, John Wiley & Sons, New York 105.
- [24] K. Aitola, A. Kaskela, J. Halme, V. Ruiz, A.G. Nasibulin, E. I. Kauppinen, P.D. Lund, J. Electrochem. Soc. 157 (2010) B1831.
- [25] K. Aitola, M. Borghei, A. Kaskela, E. Kemppainen, A.G. Nasibulin, E.I. Kauppinen, P.D. Lund, V. Ruiz, J. Halme, J. Electroanal. Chem. 683 (2012) 70.
- [26] J. Halme, P. Vahermaa, K. Miettunen, P. Lund, Adv. Mater. 22 (2010) E210-E234.
- [27] K. Miettunen, M. Toivola, G. Hashmi, J. Salpakari, I. Asghar, P. Lund, Carbon 49 (2011) 528-532.
- [28] J.D. Roy-Mayhew, D.J. Bozym, C. Punckt, I.A. Aksay, ACS Nano 4 (2010) 6203.
- [29] S. Ahmad, J. Yum, Z. Xianxi, M. Gratzel, H. Butt, M. K. Nazeeruddin, J. Mater. Chem. 20 (2010) 1654-1658.
- [30] ISO535:1991(E), Paper and Board - Determination of Water Absorptiveness - Cobb Method, International Organization for Standardization.
- [31] (a) Association Connecting Electronics Industries, Tape Testing Methods Manual. (<http://www.ipc.org/TM/2.4.1E.pdf>), (accessed 17.07.14); (b) Peel Adhesion of Pressure Sensitive Tape. (<http://www.pstc.org/files/public/101.pdf>), 2007, (accessed 17.07.14).



Mr Ghufuran Hashmi is researcher at Aalto University (Former Helsinki University of Technology) and has been associated with the fabrication and up-scaling of nano-structured Dye-sensitized solar cells (DSSC) and recently developed Perovskite Solar Cells by implementing modern printing techniques and their stability. He recently finished his PhD work under the supervision of Professor Peter. D. Lund and will be receiving the DSc degree in August 2014. He received his MSc degree in Micro and Nanotechnology from Helsinki University of Technology in 2009 and BS degree in Bio-medical Engineering from Sir Syed University of Engineering and Technology in 2002. He is also actively involved in fabrication of both low and high temperature inks and pastes and their applications in energy and printed electronics.



M.Sc. Merve Özkan was graduated in 2009 from Information and Automation Engineering in University of Bremen. She has continued as a doctoral student and researcher in the Select+ doctoral programme (Environmental Pathways for Sustainable Energy Services) at Aalto University under supervision of professor Jouni Paltakari. Her research work focuses on development of solar cell applications onto flexible fibre based substrates.



Dr Janne Halme is university lecturer at Aalto University and has been an expert of modeling and device characterization of nanostructured dye-sensitized solar cells since 2002. His other interests include device stability and upscaling of dye-solar cells on flexible substrates. He received his DSc degree in Engineering Physics from Helsinki University of Technology in 2009.



Professor Jouni Paltakari (D.Sc. Tech) has a chair in paper converting and packaging technology at Aalto University. His research group focuses on unit operations and technologies for adding value for fibre based substrates in converting processes and packaging applications. Pigment coating solutions and new material combinations consisting e.g. nano-cellulose as a renewable biomaterial are of great interest in research and education. In addition, functional and intelligent solutions and products are also covered.



Dr Peter. D. Lund is a Professor of Applied Physics at Aalto University. His research interests include fuel cells, Perovskite solar cells, dye-sensitized solar cells and micro and nanotechnology for energy applications. He holds numerous positions of trusts and has been an advisor for research and development policy in Finland. He is also board member of several journals of science and has received several awards.

APPENDIX 2



Rheological characterization of liquid electrolytes for drop-on-demand inkjet printing



Merve Özkan ^{a,*}, Katarina Dimic-Misic ^a, Alp Karakoc ^{a,c}, Syed Ghufan Hashmi ^b, Peter Lund ^b, Thad Maloney ^a, Jouni Paltakari ^a

^a Department of Forest Products Technology, School of Chemical Technology, Aalto University, Finland

^b New Energy Technologies Group, Department of Applied Physics, Aalto University, Finland

^c Department of Civil and Environmental Engineering, University of California Los Angeles, Finland

ARTICLE INFO

Article history:

Received 31 May 2016

Received in revised form

2 September 2016

Accepted 3 September 2016

Available online 12 September 2016

Keywords:

Inkjet printing

Rheology

Dilatancy

Electrolyte

Dye-sensitized solar cells

ABSTRACT

Physico-chemical properties of inkjet printing liquids significantly affect the quality of print-out, thus being the key parameter in the performance of printed electronic device (PEDs). Complex hydrodynamic interactions that inks are subjected to in an inkjet printing device has an influence on their rheological response, thus final drop formation, jetting, and drying kinetics. This paper provides a systematic comparison of three PED electrolytes based on different solvents i.e. Sulfolane, 3-Methoxypropionitrile and Acetonitrile that gave them different physico-chemical properties. Rheological properties of printed electrolytes were found to strongly influence the quality of print-outs, which is investigated both optically and morphologically. Best printing results were obtained with the sulfolane-based electrolyte that has the most uniform temperature and shear rate dependent rheological behavior as well as the lowest evaporation rate. By carefully controlling the printing temperature window, it is possible to subject PED electrolytes to higher shearing viscosity profiles while avoiding undesirable dilatant behavior which results in clogged printing nozzles and disrupted droplet trajectory.

© 2016 Elsevier B.V. All rights reserved.

1. Introduction

As the most mature practice of direct writing (DW) technology [1], inkjet printing offers mask-free material deposition with micrometer accuracy and cost saving of the materials [2]. For the last decades drop-on-demand (DoD) inkjet printing has been extensively used in lab-scale research and it has been one of the most promising technique for massive production of printed electronic devices (PEDs), in particular integrated circuits, small antennas, solar cells, batteries, thin-film transistors and light-emitting diodes [3–8]. Development of PED sets an on-going demand for improved resolution and printability on different substrates. Such a target can be achieved only by optimal, reliable, and sustainable droplet formation, jetting and substrate-drop interaction which depend on the physical characteristics of the inks such as surface tension and viscosity [9].

Upon applying a sufficient voltage to the piezoelectric actuator

in the microchannel of the printer nozzle, the ink flows through the channel depending on its viscosity [10]. Once kinetic energy and surface energy of the ink overcomes the energy required for ejection of a spherical droplet, with the help of contraction within the chamber, a droplet is formed and gets ejected from the nozzle [9,11]. Printing inks are semi-diluted suspensions consisting of the complex mix of particles which are segregated due to the mutual immiscibility and cross-material repulsive forces in the stationary state, such that the system remains de-mixed [12–14]. After strain and shear are applied, ink may first exhibit an induced elasticity as the resistance to mixing reaches a maximum, which induces dilatancy [15,16]. Dilatancy induced in high shear rate jetting conditions accompanied with rapid evaporation upon ejection leads to undesirable clogging of nozzles [17,18]. By determining the viscosity dependence over a broad shear rate range that affect droplet formation, ink recovery rate and trajectory formation that affect droplet setting, it is possible to correlate the flow parameters with print-out performance [19–21].

In this paper we provide investigation of different rheological and printing performance of three dye-sensitized solar cell inks based on three different solvents (sulfolane, 3-

* Corresponding author.

E-mail addresses: merve.ozkan@aalto.fi, merve.ozkan85@gmail.com (M. Özkan).

methoxypropionitrile and acetonitrile). Using the same inks for different printing temperature conditions using the paper as printing substrate, we correlate the change of rheological parameters with the printing performance. Rheological behavior of ink accompanied with the evaporation rate of electrolyte has an important effect on the printing results, and for suboptimal electrolytes it can be tuned by changing the temperature conditions, to improve the complex set of parameters that affect the end up performance.

2. Experimental

2.1. Materials

The electrolytes were prepared in the similar way as reported in the literature, with sulfolane, 3-methoxypropionitrile and acetonitrile as liquid ink vehicles and labeled as SFN, MPN and ACN respectively [22–24]. Table 1 lists the components of the electrolytes used in this study along with their molar ratios and the corresponding abbreviations can be found at the end of Table 1.

DMII, PMII (>98% purity), EMII (>98% purity) were purchased from Io-Li-Tec and EMITCB and anhydrous LiI was obtained from Merck. GuSCN (purity > 99%), NMBI (purity 99%), TBP (purity 96%), I₂, NBB and all the solvents (Sulfolane 99% purity, Acetonitrile 99.8% anhydrous, 3-Methoxypropionitrile 98% purity) were supplied by Sigma Aldrich.

2.2. Characterization of inks

For an ideal print outcome, a high-performance jetting ink should meet certain demands regarding its physical properties (28–42 mN/m surface tension; 10–12 mPa s viscosity; <100 °C boiling point; >1 g/cm³ density; <0.2 μm particle size; 4–9 pH) [25]. Being the key parameter for the volatility of the ink at the nozzle orifice, solvent boiling temperatures are 285 °C, 164 °C and 82 °C for SFN, MPN and ACN electrolytes, respectively. Surface tension values of 24.5 ± 0.6, 33.9 ± 0.14, 42.7 ± 0.09 mN/m, respectively, were measured using an optical tensiometer (CAM 200 from KSV instruments) in pendant drop mode at room temperature and the inks were more characterized at elevated temperatures as mentioned in the results part. In order to characterize substrate-ink interaction, contact angle measurements were conducted in sessile drop mode at room temperature in 65% relative humidity with optical tensiometer.

A sub-optimal ink might cause clogging of the nozzles or drops deviating from the expected flying direction due to ambient interaction while spherical are anticipated [26]. Drop formation and performance characteristics of inkjet printing inks have been benchmarked using a set of non-dimensional parameters consisting of inverse Ohnesorge number ($Oh^{-1} = Z$), Reynolds number (Re) and Weber number (We) given by Equations (1)–(4) [27,28].

$$Z = \sqrt{(d\rho\gamma)} / \eta \quad (1)$$

$$Re = \rho v d / \eta \quad (2)$$

$$We = \rho d v^2 / \gamma \quad (3)$$

$$Z = Oh^{-1} = Re / \sqrt{We} \quad (4)$$

Where d , ρ , γ , η and v refer to nozzle radius, density, surface tension, dynamic viscosity measured at low shear and drop velocity, respectively. By virtue of being mostly experimental, the correlation of non-dimensional parameters with printing results has been determined within different limits. Defined as the equilibrium indicator of viscous forces to surface tension forces of the ink Z was experimentally demonstrated to be $1 < Z < 10$ for jettable fluids [29]. On the other hand many researchers challenged this defined range as presented in Ref. [30] as $2 < Z < 40$ or in Ref. [31] as $0.67 < Z < 50$. Re and We, being indicators of drop formation, impact and spreading, represent the ratio of inertial forces to viscous and surface tension forces, respectively and they are characteristically fall into 1–100 for inkjet printers [32].

2.3. Inkjet printing process

In this study, we carried out a proof-of-concept study using a lab scale, DoD and piezoelectric based materials printer (DMP-2831, Fujifilm Dimatix, Inc., CA, USA) [25]. In order to obtain uniformity of factors affecting printability, droplet jetting frequency of 1 kHz was used for all inks, whilst paper substrate was kept the same. Jetting temperature was chosen as to correlate with temperature set up for rheological tests, and apart from room temperature (23 °C), it was increased to 40 °C and 60 °C, by adjusting the heating system in the printer.

Jetting trajectories and velocity of the ejected drops were determined by embedded stroboscopic drop watcher camera. Deviation of the drop trajectory and a drop travelling velocity different than optimal value (7–9 m/sec for this printer geometry) are highly detrimental for the printing results and might give rise to shorter cartridge life cycle by clogging the nozzles due to possible agglomeration on the orifice [33]. In many studies the complicated response of the non-Newtonian fluids during the dispensing process was highlighted [34] and the drop velocity adjustment was proposed in order to improve the printing results [35].

In this study an in-house algorithm written in Mathematica technical computing software was applied to the captured images by embedded stroboscopic drop watcher camera in order to obtain detailed data to identify the tail and filament structures along with the final drop formation process of medium dilatant MPN electrolyte as an example [36]. The algorithm had two main functions: image processing and regression analysis. The image processing function was designed to binarize and categorize the pixels based on their color functions. For binarization threshold, Otsu method

Table 1
Electrolytes used in this study.

Electrolyte	Components	Molar ratio	Reference
SFN	DMII:EMII:EMITCB:I ₂ :NBB:GuSCN	12:12:16:1.67:3.33:0.67	[22]
MPN	I ₂ :GuSCN:NMBI:PMII	0.06:0.1:0.5:0.5	[23]
ACN	DMII:I ₂ :LiI:TBP:GuSCN	1:0.03:0.05:0.5:0.1	[24]

DMII: 1, 3-dimethylimidazolium iodide, EMII: 1-ethyl-3-methylimidazolium iodide, EMITCB: 1-ethyl-3-methylimidazolium tetracyanoborate, I₂: Iodine, NBB: N-butylbenzimidazole, GuSCN: Guanidine Thiocyanate, PMII: 1-methyl-3 propylimidazolium iodide, LiI: lithium iodide, TBP: 4-tertbutylpyridine.

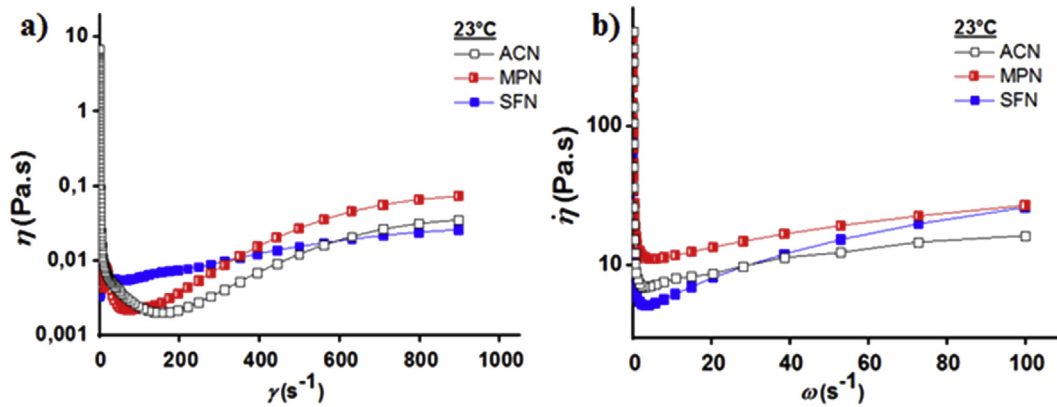


Fig. 1. Rheological behavior of inks: a) shear dynamic viscosity (η) and b) complex (η^*) viscosity.

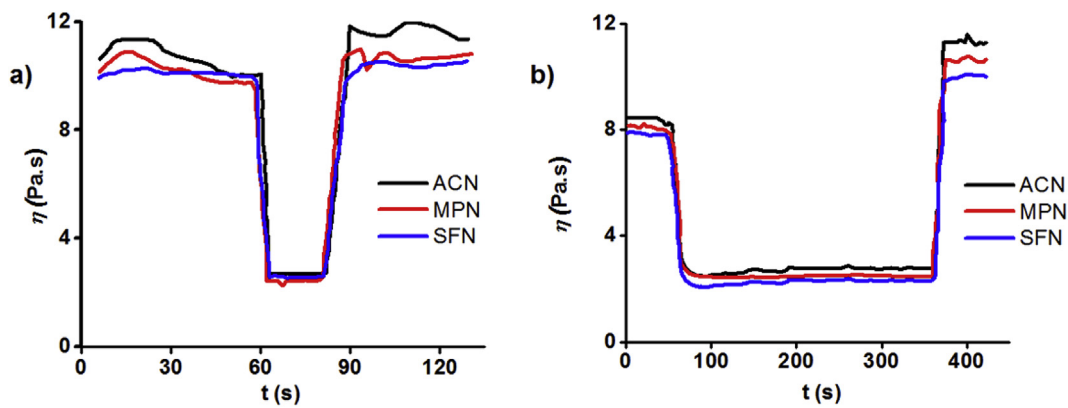


Fig. 2. 3ITT tests under: a) step wise increase of shear, with high shear rate of 50s^{-1} , b) linearly increasing shear in second interval.

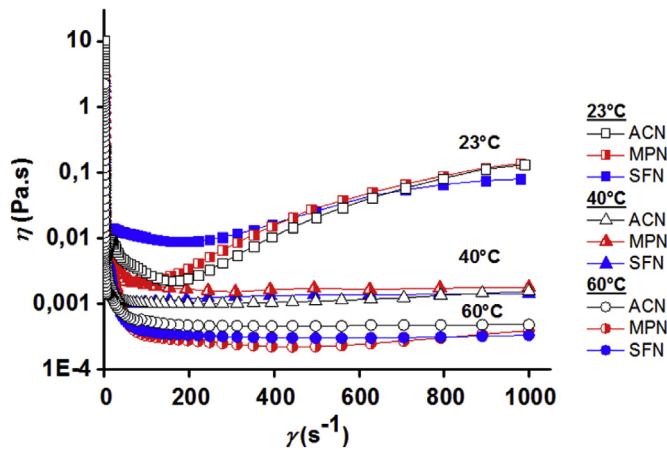


Fig. 3. Dynamic viscosity (η) and strain deformation at different temperatures 23°C (room temperature), 40°C and 60°C .

was used, which minimizes the combined spread of foreground and background pixels. As a result of binarization, ink droplet region was represented with white color referring to foreground pixels whereas the background was represented with black color referring to background pixels. Following the binarization, coordinate data of the foreground pixels were computed and averaged to determine the droplet centroid coordinates. Thereafter linear regression analysis, which was explained in the jet trajectory

verification section, was conducted to determine the jet trajectory and jetting angle.

2.4. Rheological tests

Three popular ionic electrolytes were studied in terms of their viscoelastic rheological behavior by using a rotational rheometer (Physica MCR 301, Anton Paar, Graz, Austria). In order to obtain more in-depth characterization, the measurements were carried out under altered temperature and shear conditions.

2.4.1. Pre-shearing

The samples were inserted between two parallel plates (top: serrated and bottom: smooth configuration to avoid wall-slip formation) at 23°C and the upper plate was lowered until distance between two plates is 0.5 mm . As a mean to even out heterogeneities within the samples, the samples were subjected to mild pre-treatment with oscillation set up of $\omega = 1\text{ (rad)s}^{-1}$ and strain deformation $\gamma = 0.01\%$ for 10 min after which they were left to equilibrate for 2 min before conducting the measurements. All the measurements were repeated three times, the precision of the results was better than 5%. A silicone oil was spread around the samples to eliminate evaporations of solvents.

2.4.2. Oscillatory rheology profiling and viscoelastic characterization

Viscosities of inks, complex viscosity (η^*) dependence of intact samples on angular frequency (ω) in range $0.1\text{--}100\text{ (rad)s}^{-1}$ and dynamic viscosity (η) dependence on three decades of shear rates

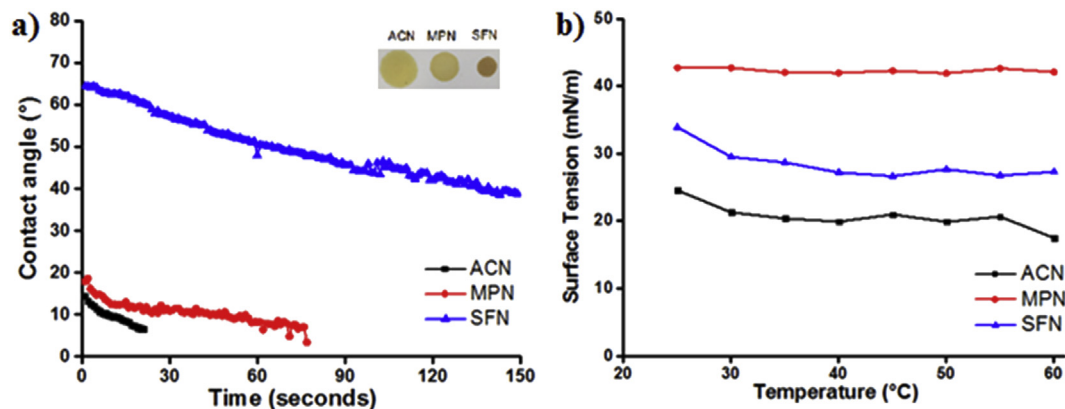


Fig. 4. Sessile and pendant drop behavior of electrolytes: a) Contact angle of electrolytes as a function of time for inkjet printing substrate, inset 2 μL drop spreading on printing paper, b) Surface tension of the inks with elevated temperatures.

Table 2

Velocity of ejected drops ejected from the nozzles and non-dimensional parameter set for inkjet printing performance prediction at different temperature settings. Z , Re and We are inverse Ohnesorge, Reynolds and Weber numbers, respectively, and v is the drop velocity.

Electrolyte	Parameter							
	40 °C				60 °C			
	Z	Re	We	v	Z	Re	We	v
ACN	8.5	41.5	23.7	5	12.5	0	0	0
MPN	5.5	21.7	15.8	6	3.1	16.6	28.1	7
SFN	3.8	22.2	34.1	7	9.6	72.1	56.4	9

(0.01 and 1000 s^{-1}), gave information about the samples when structure was intact (within linear viscoelastic region, LVE) and when broken with shearing, η and η^* , respectively. Prior to frequency sweep test, amplitude sweep oscillatory test were performed with strain $\gamma = 0.01$ –100% and $\omega = 1$ (rad) s^{-1} .

2.4.3. Three interval thixotropic test (3ITT)

In order to obtain information about the viscosity (η) response of inks after high shear application, two different variations of a Three Interval Thixotropic Tests (3ITT) were conducted, applying the 3-interval test, with low shear in the first and third interval and high shear in the second interval. During the first and third intervals, the sample was sheared at a low shear rate (0.1 s^{-1}), and second interval was performed with both constant intermediate shear rate of 500 s^{-1} and step-wise increase of shear rate = 0.1–500 s^{-1} [18].

2.5. Characterization of printouts

Printing papers were provided by Stora Enso (Lumipress, 170 g/ m^2 substance) [37]. The information about uniformity and surface morphology of printed electrolyte patterns were determined with optical light microscope (Leica Microsystems) and MultiMode 8 atomic force microscope (AFM) having a NanoScope V controller (Bruker Corp.) in tapping mode in air. The image analysis was performed using NanoScope 1.5 software (Bruker Corp.) without any image processing except flattening.

3. Results and discussion

3.1. Rheological properties of printing liquids

Viscoelastic behavior of the inks is crucial for the jetting

performance of the drops in inkjet printing applications. Although in many inkjet printing studies only zero-shear rate viscosity of the inks has been presented [42] more measurement points need to be added into the experiments in case of non-Newtonian fluids [38]. Viscoelastic profile of printing inks including complex and dynamic flow was presented in Fig. 1. Being much larger than the dynamic flow, complex viscosity presents the structural deformation response of the inks. Dynamic viscosity measurements of the liquids indicated a shear thinning behavior at low to medium shear rates, and thickening behavior (dilatancy) at higher shear rates, as expected for semi-diluted hydrophobic particle suspensions [12,17,18]. Viscoelastic measurements also reveal shear thinning behavior of η^* for low to medium angular frequencies, with dilatant behavior at higher frequencies. The more uniform viscosity response to shearing was observed in the sulfolane based electrolyte whereas both ACN and MPN have pronounced shear related viscosity increase (Fig. 1).

At low shear rates all electrolytes have shear thinning dynamic viscosity response, but at the higher shear rates and angular frequencies, since they are complex semi diluted suspensions consisting of different particles, their viscosity increases due to the complex inter-particle forces and rearrangements from two to three-dimensional arrangement of flow lamellae under high shear rates, they have shear thickening viscosity response at high shear rates (dilatant) [12–18]. As presented in Fig. 1, the electrolytes display dilatant behavior, and therefore it is important to define the degree of viscosity increase during the high shear period. As illustrated in Fig. 2, the viscosity increase after the high shear rate interval is lowest for the SFN ink, which is prominent when the dilatant behavior is undesirable as it can result in clogging of nozzles especially if accompanied with immediate solvent evaporation upon droplet contact with air. Fig. 2 a shows a typical plot of viscosity at low shear rates, but as the shear rate increases in the second 3ITT interval, the viscosity decreases to very low value. Upon cessation of high shear, the shear force is decreased again in the third interval, and the viscosity increases again, to a higher value than in the first interval, typical for dilatant behavior. Fig. 2 b shows the dilatant behavior of the electrolytes in the third interval, when the shear rate is linearly increased between 0.1 and 500 s^{-1} . As seen from Fig. 2 a–b, SFN electrolyte exhibits much less viscosity fluctuation compared to other inks under not only constant shear, but also increasing shear.

Flow curves of dynamic viscosity at different temperatures, 23 °C, 40 °C and 60 °C (Fig. 3) show that increasing of temperature results a reduction in the high-shear rate induced dilatant behavior. Even with a slight dilatancy at higher temperatures (40 °C and

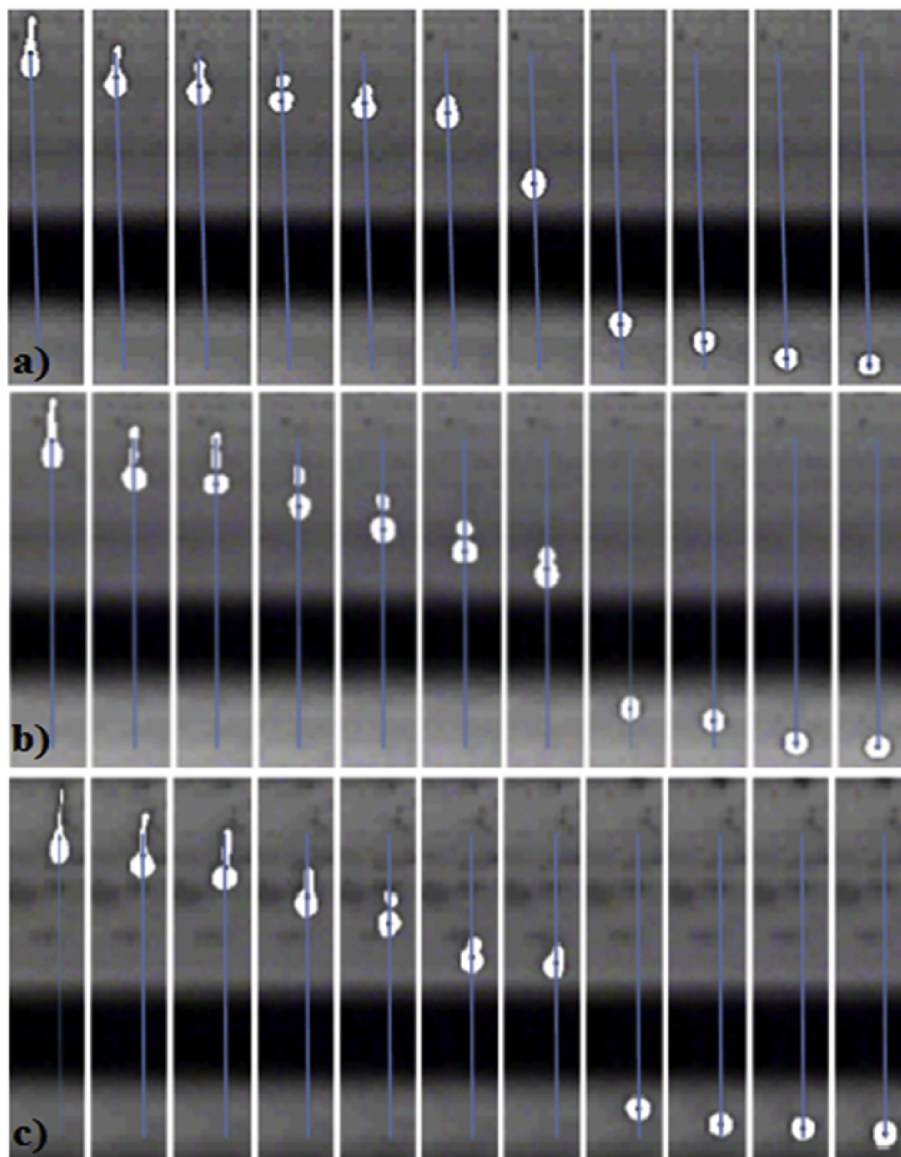


Fig. 5. Trajectory determination of MPN electrolyte jetted at: a) room temperature, b) 40 °C, c) 60 °C.

60 °C), the viscosity of all three electrolytes are seen to stay at reduced viscosity after shear thinning period, which are below the room temperature values, exhibiting almost Newtonian behavior through the shear rate range. Heating the electrolytes leads to a higher mobility within the particles in the ink matrix and improvement of jettability. However, an increase of temperature leads to faster evaporation of the solvent from the ink, and even though the rheological profile is more uniform, the heating of ink might not deliver the desired improvement due to evaporative build-in despite improved rheological behavior.

3.2. Surface tension and contact angle

In Fig. 4, the contact angle of sessile drops on printing substrate and surface tension of pendant drops is presented. SFN electrolyte exhibited more stable and less uneven spreading pattern compared to ACN and MPN electrolytes maintaining its contact angle for long period (Fig. 4a). Such a slow drying routine of a drop has been attributed to lead better self-organization of the components in the

ink [9,40]. Being one of the major determinant factors in pattern resolution for liquid-based printing applications, a smaller drop impact of SFN ink was observed due to the high boiling point. Determined with the same goniometric set-up including a heating chamber surface tension values of the inks are measured starting from room temperature up to 60 °C for ACN, MPN and SFN respectively (Fig. 4b). At elevated temperatures all surface tension values reduced as expected, however, SFN surface tension changed less during the thermal alteration.

3.3. Inkjet printing

After adjusting the optimal signal, which induces the jetting of nozzles, the assessment of the inkjet printing behavior was determined by calculating the non-dimensional drop-jetting parameter set at 40 °C and 60 °C, assuming Newtonian-like behavior (Fig. 3) [39]) (Table 2). The parameter values were in the drop-formation range and practically the drop formation from all the inks was successful at all temperature points except ACN at 60 °C due to

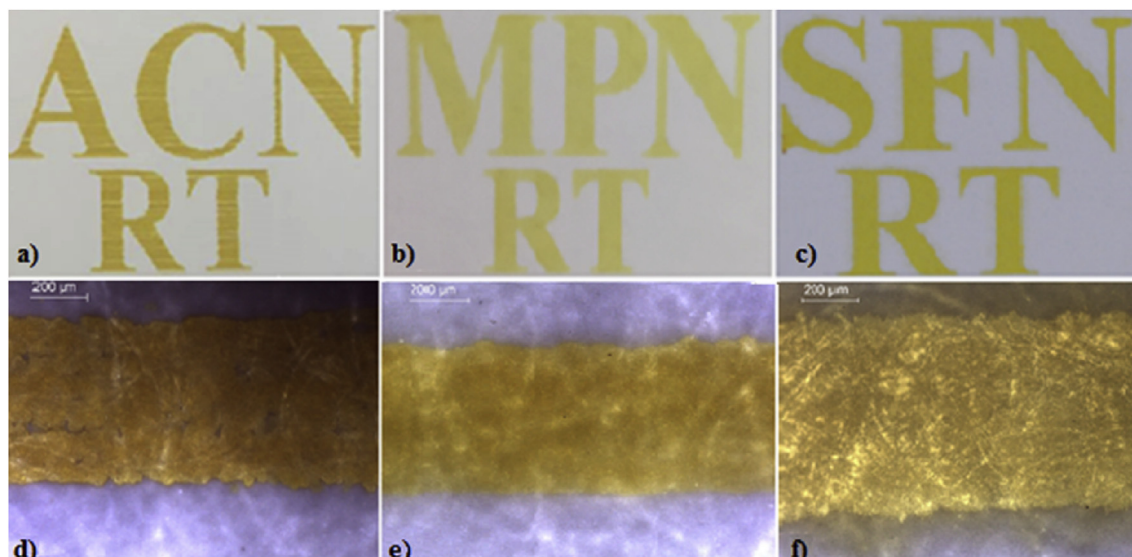


Fig. 6. Inkjet print-outs at room temperature: a, b and c) 4×3 cm size ACN, MPN and SFN electrolytes, d, e and f) Micrographs of ACN, MPN and SFN electrolytes, respectively.

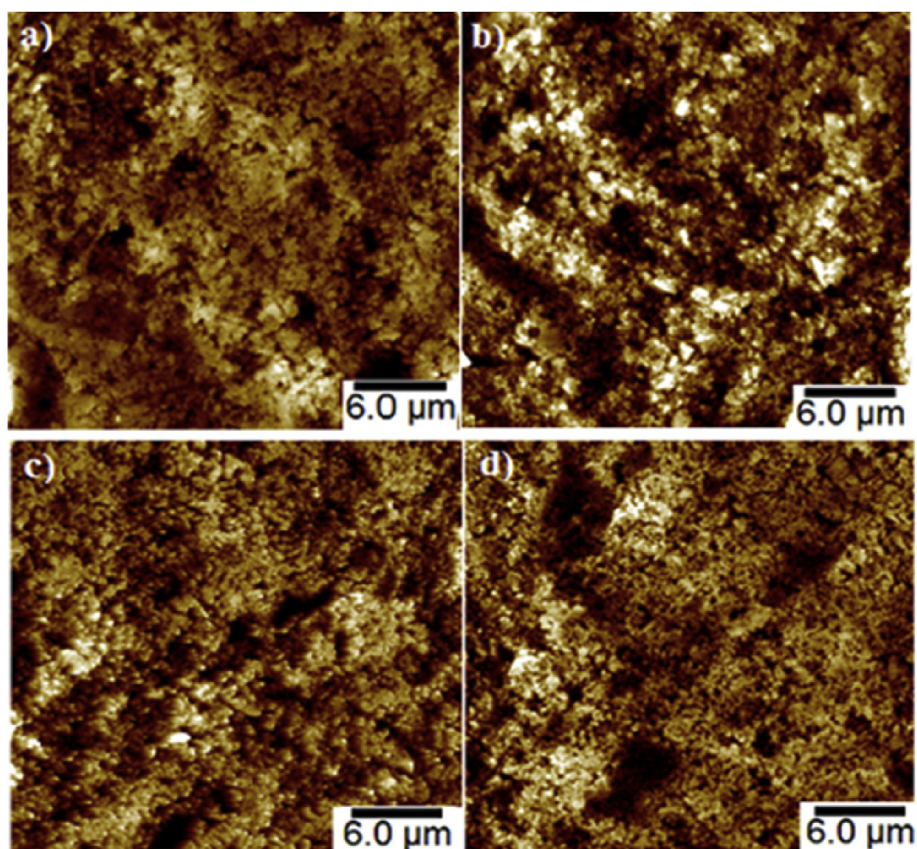


Fig. 7. AFM images of printouts produced at room temperature for all three inks: a) unprinted surface used as a reference, b-d) room temperature inkjet printed substrates (ACN, MPN and SFN respectively).

extreme evaporation rate on the nozzle orifice. Since the velocity values of ejected drops at 40°C and 60°C (Table 2) are closer to the optimal value determined by the manufacturer compared to the drops generated in room temperature (3.5, 4 and 5 m/s for ACN, MPN and SFN inks, respectively), enhanced printing quality would be expected at elevated temperatures. Increased proportion of inertial forces over viscous and surface tensions forces, that once the

drop arrives on the substrate surface, splashing would be avoided, viscosity staying within desired operating window [40,41].

3.4. Jet trajectory verification

Initially detailed analysis for the trajectory determination of MPN was carried out at room temperature (Fig. 5a–c) based on the

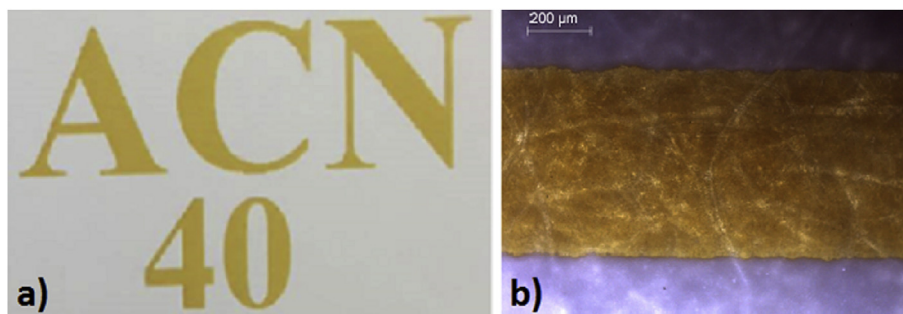


Fig. 8. Inkjet print-outs of ACN electrolyte printed at 40 °C: a) 4 × 3 cm size and b) Micrograph.

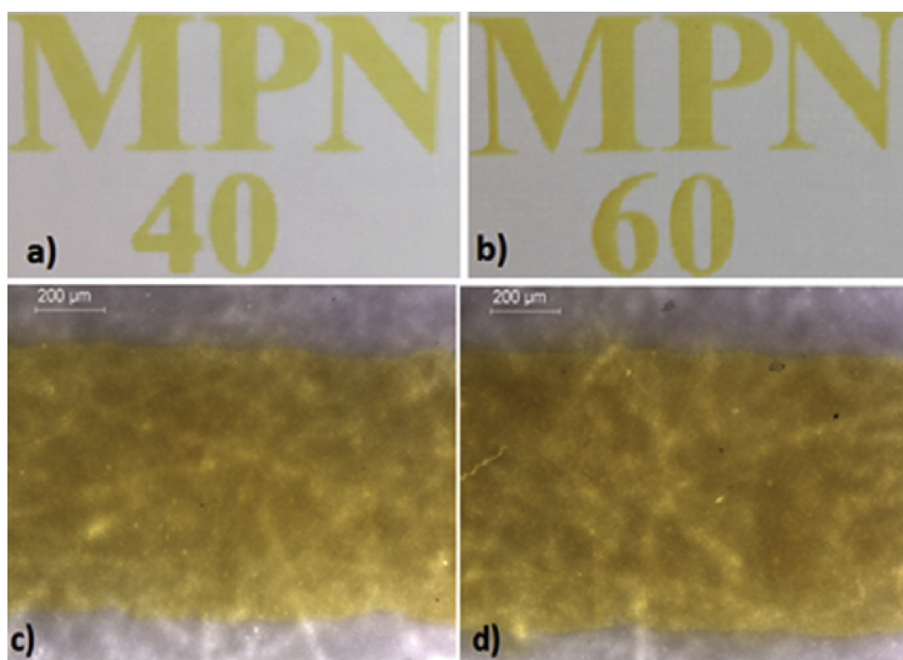


Fig. 9. Inkjet print-outs of MPN electrolyte printed at: a) 40 °C, 4 × 3 cm size, b) 60 °C, 4 × 3 cm size, c) 40 °C micrograph and d) 60 °C micrograph.

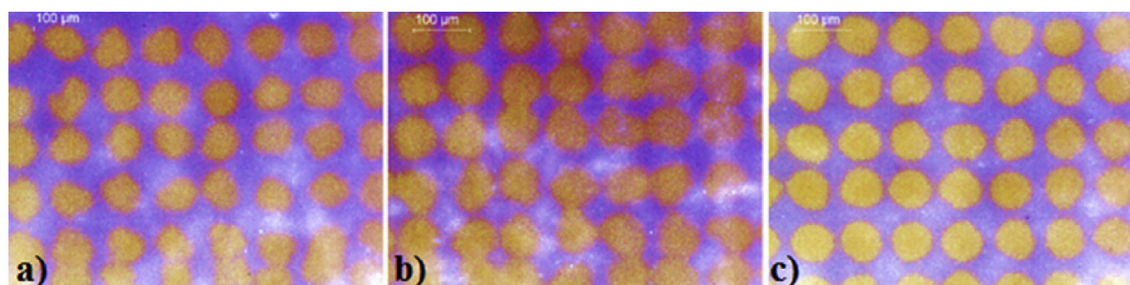


Fig. 10. Micrographs of MPN electrolyte inkjet print-outs printed with 90 μm drop spacing at: a) room temperature, b) 40 °C, c) 60 °C.

previously described method [36]. The frames shown in Fig. 5 were first binarized to obtain foreground and background pixel and thereafter, morphological analysis was performed on the foreground pixels to define droplet centroid coordinate in each frame. Eventually, least squares estimator of the linear regression model $y = C_0 + C_1x$ through the coordinate data was used to determine the trajectory and jetting angle of the droplet, $\arccot(C_1)$.

Followed by pinching off from the ligament and resulting the

drop creation, primarily filament formation with 50 μm length was observed. Satellite drop eventually joined to the main drop and geometrical stabilization of the main drop was observed after the drop travels 160 μm from the orifice. The major problem related to the jetting behavior of the MPN is the low velocity at room temperature jetting process which increases the ambient interaction of the drop resulting in the wide 1.4° jetting angle. At elevated temperatures longer filament formation and slower coalescence of the

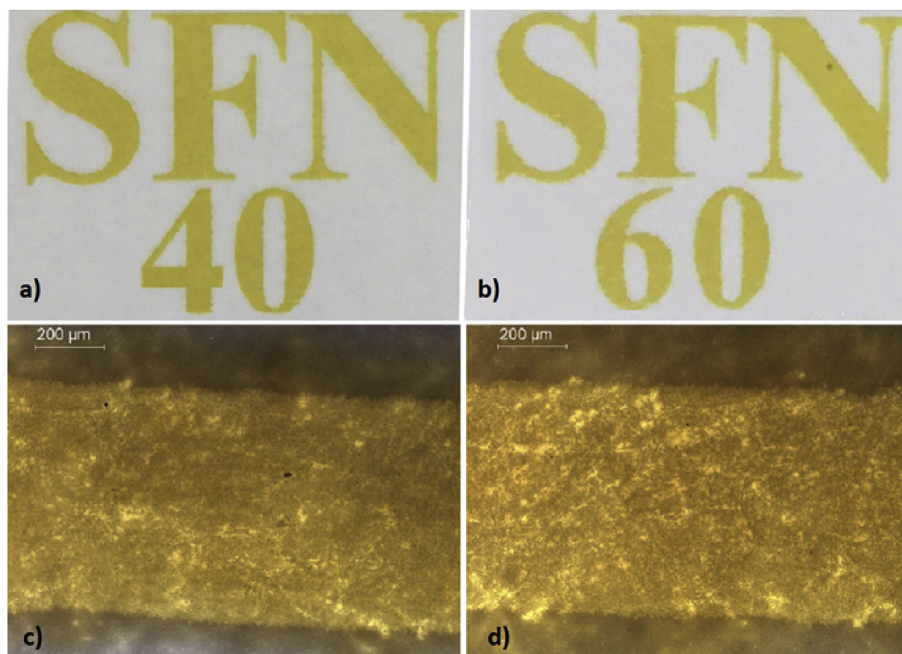


Fig. 11. Inkjet print-outs of SFN electrolyte: printed at a) 40 °C, 4 × 3 cm size, b) 60 °C, 4 × 3 cm size, c) 40 °C, micrograph and d) 60 °C, micrograph.

satellite drop with the main drop were observed (Fig. 5b and c). As a result of improved velocity, low jetting angle (0.2° for both trajectories) value and axis-symmetry of the ligament (at 40 °C jetting) better printing results in concert with better placement inaccuracy is expected. Such an improvement pattern can be predicted from the physico-chemical properties of the ink (lower viscosity and surface tension) profiled in the previous sections. Additionally less dilatant profile at 40 °C resulting more convenient viscoelastic characteristics of the MPN electrolyte can contribute to more sustainable inkjet printing process during the high temperature experiments.

3.5. Printing at different temperature regimes

All the inks created a drop impact of 50–70 µm on the special printing paper. Therefore during the printing process 30 µm drop spacing was applied due to the requirement of continuous films in electronics applications. As an overall printing quality, the best performance was obtained with SFN electrolyte: no failed jets even after long hours of printing process (more than 1000 h) at room temperature (Fig. 6 c and f). MPN, a less shear-thickening electrolyte comparing to ACN ink, exhibited better print-out results than ACN.

The AFM images of the bare and room temperature inkjet printed substrates presented in Fig. 7 were used to further investigate the printouts. As revealed from Fig. 7 d printout morphology of SFN inks has the best uniformity and homogeneity.

In order to evaluate influence of improved rheological uniformity with increased temperatures (Fig. 8), we have performed printing at 40 °C and 60 °C. Staying within the Z, Re and We limits, having the reduced dilatancy profile and higher velocity at 40 °C the ACN electrolyte printing result was ameliorated. Interestingly, even though the surface tension of the electrolyte was far lower than the minimum limit defined by the manufacturer (20 mN/m) a finer structure with almost no spikes on the border was achieved comparing to the room temperature printing.

Similarly the MPN electrolyte provided superior performance

during the high temperature printing process (Fig. 9) despite displaying slightly lower surface tension than optimal range (27 mN/m). Even that viscosity profiles are more uniform at higher temperatures, they can induce faster solvent evaporation rate, which acts to initiate nozzle clogging.

The effect of the temperature increase was further investigated by micrographs of the printouts. Jetting related accuracy was evaluated by printing with 90 µm drop spacing and a clear improvement was observed at 60 °C (Fig. 10).

As can be seen from Fig. 11, and as presented from rheological observations, SFN based ink has advantageous temperature dependent rheological and printing performance. The major reason for such observation was the improved viscosity profile and minor variation in the rest of the physicochemical properties of SFN driven by the thermal changes giving the opportunity to employ this electrolyte in a broader range of operational conditions. Furthermore the rheological profiling data suggest a remarkable stability of printing results at different operating temperatures for SFN electrolyte.

4. Conclusion

We investigated the effect of physico-chemical properties related to printability using the DoD process of three popular DSSC electrolytes at different temperatures. We found that the viscosity profile of the printing ink has a major impact on the printing results. Rheological properties of inks are shear rate and temperature dependent, which accompanied with the different evaporation properties of solvent, influence the drop formation, trajectory, and setting on substrate. Increasing the printing temperature decreases the dilatant behavior of inks, and subsequently reduces accumulation of ink on nozzle edges upon increased viscosity and solvent evaporation. A novel image processing was applied to investigate the jetting characteristics of the medium dilatant electrolyte from which faster drops following a jetting trajectory with almost zero angle were obtained at higher temperatures than room temperature due to the lower viscosity, surface tension and dilatancy. The

least dilatant electrolyte exhibited remarkably the best results at all printing temperatures.

Acknowledgments

This research was funded by SELECT+(Environmental pathways for sustainable energy services) with 602163 project number. Alp Karakoc is grateful to acknowledge the financial support of Tekniikan edistämissäätiö TES through Foundations' Post Doc Pool, Finland. Ghufuran Hashmi is grateful to Academy of Finland for Post-doctoral research fellowship (287641 grant number). Bio economy infrastructure is acknowledged for the use of the equipment.

References

- [1] K.K.B. Hon, L. Li, I.M. Hutchings, Direct writing technology—Advances and developments, *CIRP Ann. Manuf. Technol.* 57 (2008) 601–620, <http://dx.doi.org/10.1016/j.cirp.2008.09.006>.
- [2] H. Kang, D. Soltman, V. Subramanian, Hydrostatic optimization of inkjet-printed films, *Langmuir* 26 (2010) 11568–11573, <http://dx.doi.org/10.1021/la100822s>.
- [3] J. Kwon, Y. Takeda, K. Fukuda, K. Cho, S. Tokito, S. Jung, Vertically stacked complementary organic field-effect transistors and logic circuits fabricated by inkjet printing, *Adv. Electron. Mater.* (2016) 2–7, <http://dx.doi.org/10.1002/aem.201600046>.
- [4] S. Ahmed, F.A. Tahir, A. Shamim, H.M. Cheema, A compact Kapton-based inkjet-printed multiband antenna for flexible wireless devices, *IEEE Antennas Wirel. Propag. Lett.* 14 (2015) 1802–1805, <http://dx.doi.org/10.1109/LAWP.2015.2424681>.
- [5] S.G. Hashmi, M. Ozkan, J. Halme, K.D. Misic, S.M. Zakeeruddin, J. Paltakari, M. Gratzel, P.D. Lund, High performance dye-sensitized solar cells with inkjet printed ionic liquid electrolyte, *Nano Energy* 17 (2015) 206–215, <http://dx.doi.org/10.1016/j.nanoen.2015.08.019>.
- [6] T. Janoschka, A. Teichler, B. Häupler, T. Jähnert, M.D. Hager, U.S. Schubert, Reactive inkjet printing of cathodes for organic radical batteries, *Adv. Energy Mater.* 3 (2013) 1025–1028, <http://dx.doi.org/10.1002/aenm.201300036>.
- [7] E. Sowadea, K.Y. Mittra, E. Ramonb, C. Martinez-Domingob, F. Villanic, F. Loffredoc, H.L. Gomesd, R.R. Baumanna, Up-scaling of the manufacturing of all-inkjet-printed organic thin-film transistors: device performance and manufacturing yield of transistor arrays, *Org. Electron.* 30 (2016) 237–246, <http://dx.doi.org/10.1016/j.orgel.2015.12.018>.
- [8] J. Ha, J. Park, J. Ha, D. Kim, S. Chung, C. Lee, Y. Hong, Selectively modulated inkjet printing of highly conductive and transparent foldable polymer electrodes for flexible polymer light-emitting diode applications, *Org. Electron.* 19 (2015) 147–156, <http://dx.doi.org/10.1016/j.orgel.2015.01.017>.
- [9] B. Derby, Inkjet printing of functional and structural materials: fluid property requirements, feature stability, and resolution, *Annu. Rev. Mater. Res.* 40 (2010) 395–414, <http://dx.doi.org/10.1146/annurev-matsci-070909-104502>.
- [10] H. Yoo, C. Kim, Generation of inkjet droplet of non-Newtonian fluid, *Rheol. Acta* 52 (2013) 313–325, <http://dx.doi.org/10.1007/s00397-013-0688-4>.
- [11] D. Cibis, K. Krüger, System analysis of a DoD print head for direct writing of conductive circuits, *Int. J. Appl. Ceram. Technol.* 4 (2007) 428–435, <http://dx.doi.org/10.1111/j.1744-7402.2007.02160.x>.
- [12] H.A. Barnes, Shear-thickening (“dilatancy”) in suspensions of nonaggregating solid particles dispersed in Newtonian liquids, *J. Rheology* 33 (1999) 329–366, <http://dx.doi.org/10.1122/1.550017>.
- [13] W.J. Frith, P.d. Haene, R. Buscall, Shear thickening in model suspensions of sterically stabilized particles, *J. Rheology* 40 (1996) 531–548, <http://dx.doi.org/10.1122/1.550791>.
- [14] W.H. Boersma, J. Laven, H.N. Stein, Shear thickening (dilatancy) in concentrated dispersions, *AIChE J.* 36 (3) (1990) 321–332, <http://dx.doi.org/10.1002/aic.690360302>.
- [15] W.W.D. Teng, M.J.M. Edirisinghe, J.J.R.G. Evans, Optimization of dispersion and viscosity of a ceramic jet printing ink, *J. Am. Ceram. Soc.* 80 (1997) 486–494, <http://dx.doi.org/10.1111/j.1151-2916.1997.tb02855.x>.
- [16] P.S.R.K. Prasad, A.V. Reddy, P.K. Rajesh, P. Ponnambalam, K. Prakasan, Studies on rheology of ceramic inks and spread of ink droplets for direct ceramic ink jet printing, *J. Mater. Process. Technol.* 176 (2006) 222–229, <http://dx.doi.org/10.1016/j.jmatprotec.2006.04.001>.
- [17] B. Derby, N. Reis, Inkjet printing of highly loaded particulate suspensions, *MRS Bull.* 28 (2003) 815–818, <http://dx.doi.org/10.1557/mrs2003.230>.
- [18] M.M. Voigt, R.C.L. MacKenzie, S.P. King, C.P. Yau, P. Atienzar, J. Dane, P.E. Keivanidis, I. Zadrzil, D.D.C. Bradley, J. Nelson, Gravure printing inverted organic solar cells: the influence of ink properties on film quality and device performance, *Sol. Energy Mater. Sol. Cells* 105 (2012) 77–85, <http://dx.doi.org/10.1016/j.solmat.2012.04.025>.
- [19] T.M. Lee, T.G. Kang, J.S. Yang, J. Jo, K.Y. Kim, B.O. Choi, D.S. Kim, Drop-on-demand solder droplet jetting system for fabricating microstructure, *IEEE Trans. Electron. Packag. Manuf.* 31 (2008) 202–210, <http://dx.doi.org/10.1109/TEPM.2008.926285>.
- [20] C.J. Brabec, N.S. Sariciftci, J.C. Hummelen, Plastic solar cells, *Adv. Funct. Mater.* 11 (2001) 15–26, [http://dx.doi.org/10.1002/1616-3028\(200102\)11:1<15::AID-ADFM15>3.0.CO;2-A](http://dx.doi.org/10.1002/1616-3028(200102)11:1<15::AID-ADFM15>3.0.CO;2-A).
- [21] F.C. Krebs, Fabrication and processing of polymer solar cells: a review of printing and coating techniques, *Sol. Energy Mater. Sol. Cells* 93 (2009) 394–412, <http://dx.doi.org/10.1016/j.solmat.2008.10.004>.
- [22] M. Marszalek, F.D. Arendse, J.D. Decoppet, S.S. Babkair, A.A. Ansari, S.S. Habib, M. Wang, S.M. Zakeeruddin, M. Gratzel, Ionic liquid-sulfonate composite electrolytes for high-performance and stable dye-sensitized solar cells, *Adv. En. Mater.* 4 (2014) 1–8, <http://dx.doi.org/10.1002/aenm.201301235>.
- [23] A. Tiihonen, K. Miettunen, S. Rendon, D. Mavrynsky, J. Halme, R. Leino, P. Lund, The effect of electrolyte purification on the performance and long-term stability of dye-sensitized solar cells, *J. Electrochem. Soc.* 162 (2015) H661–H670, <http://dx.doi.org/10.1149/2.0671509jes>.
- [24] S.G. Hashmi, T. Moehl, J. Halme, Y. Ma, T. Saukkonen, A. Yella, F. Giordano, J.D. Decoppet, S.M. Zakeeruddin, P. Lund, M. Gratzel, A durable SWCNT/PET polymer foil based metal free counter electrode for flexible dye-sensitized solar cells, *J. Mater. Chem. A* 2 (2014) 19609–19615, <http://dx.doi.org/10.1039/c4ta03730h>.
- [25] Dimatix Materials Printer DMP-2800 Series User Manual, FUJIFILM Dimatix, 2008. http://www.fujifilmusa.com/products/industrial_inkjet_printheads/deposition-products/dmp-2800/, accessed on 25.05.16.
- [26] G. Cummins, R. Kay, J. Terry, M.P.Y. Desmulliez, A.J. Walton, Optimization and characterization of drop-on-demand inkjet printing process for platinum organometallic inks, *IEEE 13th Electron. Packag. Technol. Conf. (EPTC)* (2011) 256–261, <http://dx.doi.org/10.1109/EPTC.2011.6184427>.
- [27] J.E. Fromm, Numerical calculation of the fluid dynamics of drop-on-demand jets, *IBM J. Res. Dev.* 28 (3) (1984) 322–333, <http://dx.doi.org/10.1147/rd.283.0322>.
- [28] N. Reis, B. Derby, Ink Jet Deposition of Ceramic Suspensions: Modeling and Experiments of Droplet Formation, in: *MRS Proceedings* Cambridge University Press vol. 625, 2000, <http://dx.doi.org/10.1557/PROC-625-117>.
- [29] B. Derby, Inkjet printing ceramics: from drops to solid, *J. Eur. Ceram. Soc.* 31 (2011) 2543–2550, <http://dx.doi.org/10.1016/j.jeurceramsoc.2011.01.016>.
- [30] L. Wong, G. Lim, T. Ye, F.B.S. Silva, J. Zhuo, R. Png, S. Chua, P.K.H. Ho, Jettable fluid space and jetting characteristics of a microprint head, *J. Fluid Mech.* 713 (2012) 109–122, <http://dx.doi.org/10.1017/jfm.2012.440>.
- [31] J. Tai, H. Yap Gan, Y.N. Liang, B.K. Lok, Control of droplet formation in inkjet printing using Ohnesorge number category: materials and processes, in: *10th Electronics Packaging Technology Conference*, 2008, pp. 761–766, <http://dx.doi.org/10.1109/EPTC.2008.4763524>.
- [32] A. Kosmala, Q. Zhang, R. Wright, P. Kirby, Development of high concentrated aqueous silver nanofluid and inkjet printing on ceramic substrates, *Mater. Chem. Phys.* 132 (2012) 788–795, <http://dx.doi.org/10.1016/j.matchemphys.2011.12.013>.
- [33] F. Torrisi, T. Hasan, W. Wu, Z. Sun, A. Lombardo, T.S. Kulmala, G.-W. Hsieh, S. Jung, F. Bonaccorso, P.J. Paul, D. Chu, A.C. Ferrari, Inkjet-printed graphene electronics, *ACS Nano* 6 (2012) 2992–3006, <http://dx.doi.org/10.1021/nn2044609>.
- [34] C. Clasen, P.M. Phillips, L. Palangetic, J. Vermant, *Dispens. rheologically complex fluids map misery.* *AIChE J.* 58 (10) (2012) 3242–3255.
- [35] S.D. Hoath, S. Jung, W.-K. Hsiao, I.M. Hutchings, How PEDOT: PSS solutions produce satellite-free inkjets, *Org. Electron.* 13 (12) (2012) 3259–3262, <http://dx.doi.org/10.1016/j.orgel.2012.10.004>.
- [36] A. Karakoc, J. Freund, A direct simulation method for the effective in-plane stiffness of cellular materials, *Int. J. Appl. Mech.* 5 (3) (2013) 1350034, <http://dx.doi.org/10.1142/S1758825113500348>.
- [37] LumiPress Art, Stora Enso, Finland, <http://printingandreading.storaenso.com/products-brands/for-print-media/coated-papers/LumiPress-Art>, accessed on 25.05.16.
- [38] M.A. Sukeshini, R. Cummins, T.L. Reitz, R.M. Miller, Ink-jet printing: a versatile method for multilayer solid oxide fuel cells fabrication, *J. Am. Ceram. Soc.* 92 (2009) 2913–2919, <http://dx.doi.org/10.1111/j.1551-2916.2009.03349.x>.
- [39] T.R. Tuladhar, M.R. Mackley, Filament stretching rheometry and break-up behaviour of low viscosity polymer solutions and inkjet fluids, *J. Newt. Fluid Mech.* 148 (1) (2008) 97–108, <http://dx.doi.org/10.1016/j.jnnfm.2007.04.015>.
- [40] D. Soltman, V. Subramanian, Inkjet-printed line morphologies and temperature control of the coffee ring effect, *Langmuir* 24 (2008) 2224–2231, <http://dx.doi.org/10.1021/la7026847>.
- [41] D. Gardini, M. Blosi, C. Zanelli, M. Dondi, Ceramic ink-jet printing for digital decoration: physical constraints for ink design, *J. Nanosci. Nanotechnol.* 15 (5) (2015) 3552–3561, <http://dx.doi.org/10.1166/jnn.2015.9857> (2015).
- [42] X. Wang, W.W. Carr, D.G. Bucknall, J.F. Morris, High-shear-rate capillary viscometer for inkjet inks, *Rev. Sci. Instrum.* 81 (2010) 065106, <http://dx.doi.org/10.1063/1.3449478>.

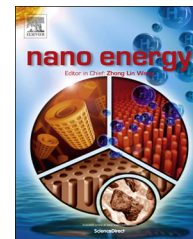
APPENDIX 3



Available online at www.sciencedirect.com

ScienceDirect

journal homepage: www.elsevier.com/locate/nanoenergy



RAPID COMMUNICATION

High performance dye-sensitized solar cells with inkjet printed ionic liquid electrolyte



Syed Ghufuran Hashmi^{a,*}, Merve Ozkan^b, Janne Halme^a,
Katarina Dimic Misic^b, Shaik Mohammed Zakeeruddin^c,
Jouni Paltakari^b, Michael Grätzel^c, Peter D. Lund^a

^aNew Energy Technologies Group, Department of Applied Physics, Aalto University School of Science, P.O. Box 15100, FI-00076 Aalto (Espoo), Finland

^bDepartment of Forest Products Technology, Aalto University School of Chemical Technology, Finland

^cLaboratory of Photonics and Interfaces, Ecole Polytechnique Federale de Lausanne (EPFL), CH G1 551, Station 6, CH-1015 Lausanne, Switzerland

Received 9 June 2015; received in revised form 4 August 2015; accepted 24 August 2015
Available online 2 September 2015

KEYWORDS

Dye sensitized solar cells;
Inkjet printing;
Ionic liquid electrolyte;
Stability;
Viscosity;
Sealing

Abstract

We successfully inkjet printed an ionic liquid electrolyte in the dye-sensitized solar cell (DSSC) as a part of a new cell fabrication sequence that eliminates drilling holes in the DSSC substrates. The inkjet printing of ionic liquid electrolyte does not only reduce the overall fabrication cost since no additional thermoplastic sealant and glass cover are required to seal the cells, but also removes one extra cell sealing step present in the traditional cell sealing process. The dye-sensitized DSSCs fabricated with printed electrolyte exhibited 6% enhancement in overall cell conversion efficiency compare to the reference cells. More significantly, the printed electrolyte based solar cells maintained 100% of the initial performance in an accelerated ageing test for 1120 h that was performed under full sun light intensity at 35 °C. These results provide a solid base to develop this process further for the production of cheaper, more robust, large area DSSC solar panels.

© 2015 Elsevier Ltd. All rights reserved.

Dye sensitized solar cell (DSSC) technology provides an economical pathway to promote 3rd generation PV technologies while showing conversion efficiencies up to 13% [1]. The production cost of these solar cells may be significantly reduced by not only introducing cost efficient materials but

also implementing fast and continuous industrial production models [2–4]. More robust DSSCs devices are expected in near future by resolving the key challenges that have been associated to materials development as well as the compatibility of their deposition through established printing techniques for a complete printable solar cell.

Currently among all associated materials and fabrication steps for DSSC, the composition of electrolyte and its deposition has been considered as one of the key factors that

*Corresponding author.

E-mail addresses: ghufuran.hashmi@aalto.fi,
sghufranh28@gmail.com (S.G. Hashmi).

strongly affect its overall performance [5]. Volatile solvents such as acetonitrile based electrolytes have been utilized in fabricating high efficiency cells frequently [1,6] but they were not found suitable for long term and stable operation due mainly to sealing issues [7]. The problem was mitigated by introducing relatively high boiling point solvent based electrolytes which have shown good stability in accelerated aging tests [8,9]. One of the best electrolyte formulations both in terms of performance and stability that have recently been reported is a mixture of an ionic liquid with sulfolane (Z988-EL) that maintained more than 92% and 80% of the initial ca. 8.2% cell efficiencies over a 2230 h long light soaking test at 60 °C and a 1065 h long thermal stability test in the dark at 80 °C, respectively [10]. The merits of this electrolyte are in large part due to the high boiling point solvent, sulfolane, that exhibits excellent properties as a DSSC solvent with favorable interaction with the I^-/I_3^- redox couple [11], enhancing simultaneously both the performance and stability of DSSCs when used as an additive in ionic liquid electrolytes [12].

Compared to the optimization of the electrolyte formulations, development of better electrolyte application methods has received little attention. For instance, the traditional electrolyte filling step for laboratory-sized small area DSSC utilizes one drilled hole mostly on the counter electrode (CE) side requiring a vacuum back filling method (Figure 1a) [13]. The filling can also be accomplished by capillary action using two drilled holes i.e. one for electrolyte insertion and the other to release the trapped air within the cell channel (Figure 1b) [14]. However in both the aforementioned cases, the amount of electrolyte is difficult to control as it fills the entire cell channel which needs to be larger than the active area to avoid overlap between the filling holes and the photoelectrode which would reduce the active area of the cell. This extra amount of electrolyte within the filling channel is undesirable as it may increase the dark current from the photoelectrode substrate [15], causes current driven edge effects that redistribute the redox pair laterally when the cell is operated [16], lowers the geometric filling factor, i.e. the active vs. total area, and thus the efficiency of a DSSC module [17]. In addition to these geometrical disadvantages, the filling step itself can be problematic. For instance, the pumping of viscous ionic liquid electrolytes through the long channels of a large area DSSC module cannot be realized at room

temperature but requires an additional heating setup [18]. Furthermore, when the electrolyte flows through the nanoporous photoelectrode layer, some of the electrolyte components distribute unevenly in the nanopores due to a molecular filtration effect, which leads to spatial variations in the performance characteristics and overall decrease in cell efficiency [19].

Ideally, the electrolyte would be deposited directly over the photoelectrode or counter electrode followed by sealing of the device without holes in the substrates. Until now, this has been possible only by changing considerably either the cell design or the electrolyte composition. Examples are screen printing of the electrolyte over the porous multilayers in a monolithic design [20], solid state hole conductors that need not to be filled in the cell as a liquid [11], inorganic-organic silica nanocomposite electrolytes that glue the electrodes together [21], electrolyte-wetted porous separator foils that can be cut to a desired size and placed between the electrodes [22], and application of the electrolyte over a sponge-like layer made of cellulose aerogel that withholds the electrolyte during the sealing step [23]. Introducing new materials in DSSC is always risky from the point-of-view of both efficiency and long-term stability. Here, we show that direct electrolyte deposition and hole free sealing is possible by inkjet-printing a state-of-the-art ionic liquid sulfolane electrolyte without adding any new cell materials. In fact, the new hole free electrolyte filling method gives higher efficiency and equal stability with fewer components and preparation steps while minimizing the amount of extra electrolyte in the cell.

More specifically, we used inkjet printing to deposit an ionic liquid sulfolane electrolyte (coded as Z988-EL, see experimental section) directly onto the sensitized mesoporous TiO_2 films. This composition of the electrolyte is similar to the stable, high performance formulations used before [10,24]. The precisely printed electrolyte remains stable over the porous TiO_2 film during the printing step and does not spread substantially when it is contacted by the catalyst loaded surface of the counter electrode, even when the thermoplastic edge sealant is melted at 120-130 °C.

The inkjet printing of the electrolyte was performed through Fujifilm's drop on demand Dimatix materials printer (DMP-2831, Figure 2a). The printer utilizes a disposable silicon based piezoelectric inkjet cartridge that was loaded

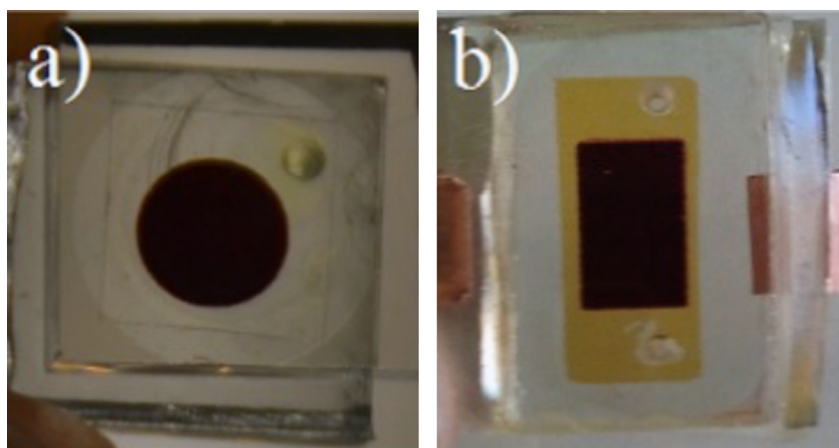


Figure 1 (a) Vacuum back filled electrolyte based DSSC with one drilled hole (b) DSSC with two drilled holes on substrate.

with the electrolyte (Figure 2b) after filtering through a 0.2 μm filter. During the printing cycle, the print head of the cartridge (which consists of 16 nozzles, 254 μm apart from each other) dispense the loaded fluid in the form of droplets through the applied voltage and time controlled signal to its piezoelectric element on the nozzle channels. Therefore depending on the requirements of the application, the droplets with different size and velocity can be produced by adjusting the voltage and printing waveform.

The characteristics of a printable ink and its optimal range required to produce efficient jetting of the material (recommended by the manufacturer) include surface tension (28–42 dynes/cm), boiling point ($B.P > 100^\circ\text{C}$) and specific gravity (>1) which were obtained for each electrolyte through the established fluid characterization techniques (see experimental section) and are summarized in Table 1.

In the very beginning, the fluid-substrate interaction was explored through the contact angle measurements by pipetting out a drop (4 μl) through a controlled dispenser on the sensitized TiO_2 coated glass substrate (Figure 3a–d). For comparison, contact angle measurements and printing trials were performed also with traditional electrolyte formulations based on 3-methoxypropionitrile (MPN-EL) and acetonitrile (ACN-EL) as the solvent (see experimental section). Both the MPN-EL and ACN-EL spread rapidly over the substrates (Figure 3b–c) and their corresponding contact angles were quickly reduced to 0° . The Z988-EL, on the contrary, produced more stable drop pattern on the light scattering TiO_2 film (Figure 3d) and maintained the equilibrium contact angle (10°). Even higher contact angles of various solvents have been reported previously [21], however, in general, the wetting properties of complete electrolyte solutions are complex resulting from the interaction between all the electrolyte components, the TiO_2 particles and the dye [25], and cannot be readily predicted beforehand. Interestingly, Z988-EL drop was able to maintain its shape even over four weeks after the deposition of the drop on the TiO_2 . After the initial drop tests, a precise amount of Z988-EL was printed onto the dyed TiO_2 layers deposited on FTO Glass with a light scattering TiO_2 layer as the top-most layer (Figure 3e). The printed Z988-EL layer did not spread over the substrate or evaporate when exposed to air for several weeks. All three electrolytes were also tested on platinum (Pt) coated FTO-Glass (Counter electrodes), however, rapid and uneven drop spreading was found which ruled out the possibility of printing the electrolyte over the counter electrodes.

In the second phase, the inkjet printing of each electrolyte was tested over commonly available Xerox paper as shown

in Figure 4. Among them, MPN-EL and Z988-EL layers were printed smoothly (Figure 4a–b) whereas ACN-EL could not be printed properly due to fast evaporation of its solvent acetonitrile, ($B.P=82^\circ\text{C}$, Figure 4c). This result is in complete agreement with the desirable electrolytes characteristics which are summarized in Table 1 where the recommended boiling point of the solvent was more than 100°C .

Finally, DSSCs with inkjet printed electrolyte layers were assembled using a new sequence of fabrication (Figure 5a) along with reference DSSCs made for comparison by the traditional scheme (Figure 5b). The amount of printed electrolyte was controlled by the ink-jet printer settings, such as voltage and printing waveform (See Figure S1 in the Supporting information). These settings can be routinely adjusted by the experimenter to obtain the desired printing quality. The optimum amount was able to completely wet the photoelectrode and to make a contact with the counter electrode without spreading too much when the cell was assembled and sealed. This is important since if the electrolyte makes a contact with the sealant before the heat sealing step, the adhesion of the sealant on the substrates might be compromised.

A hole-free DSSC device fabricated with the printed electrolyte layer is also shown in Figure 6. The current-voltage (J - V) characteristics (measured under full sun light intensity) of the fabricated DSSCs are summarized in Table 2 whereas Figure 7 represents the J - V curves of the best performing DSSCs of each type.

The hole-free DSSC exhibited very impressive performance by revealing similar initial short circuit current densities ($J_{SC}=14.9\pm 0.5\text{ mA/cm}^2$, Table 2, Batch 2) and open circuit voltage ($V_{OC}=675\pm 3\text{ mV}$) as well as higher ($\sim 5\%$) fill factors which corresponds to a clear increase ($\sim 6\%$, $7.4\pm 0.3\%$) in the overall efficiency compared to the reference DSSC ($7.0\pm 0.2\%$). There was also significant reduction ($\sim 14\%$) of

Table 1 Characteristics of different electrolytes MPN-EL, ACN-EL, and Z988-EL: ρ =density of the electrolyte, γ =surface tension of the electrolyte, BP=boiling point of the solvent, and their optimal values specified by the manufacturer of the inkjet printer.

Characteristics	MPN-EL	ACN-EL	Z988-EL	Optimal value
ρ (kg/m^3)	980	880	1360	> 1000
γ (dynes/cm)	27	24	40	28–42
BP ($^\circ\text{C}$)	164	82	285	> 100

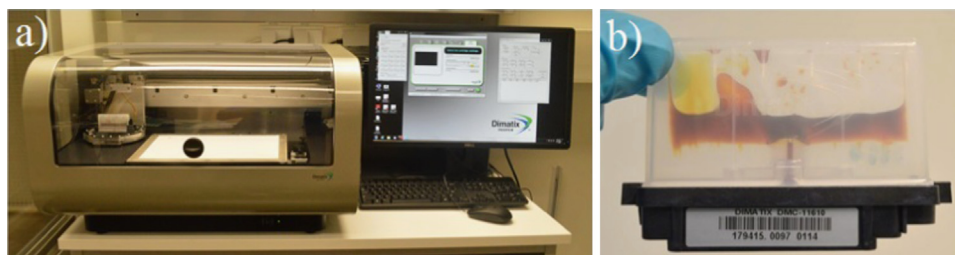


Figure 2 (a) Fujifilm's Dimatix materials printer DMP-2831 (b) A printer cartridge filled with Z988 electrolyte.

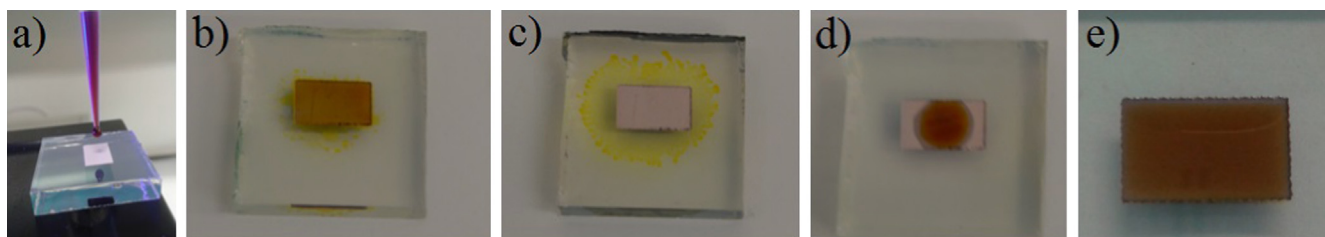


Figure 3 (a) CAM sessile electrolyte drop experiment over TiO_2 ($8 \times 5 \text{ mm}^2$) coated FTO glass (b) spreading of MPN-EL over the substrate (c) spreading of ACN-EL over the substrate. Acetonitrile based electrolyte drop was completely evaporated from TiO_2 and left impressions around the surroundings of the active area thus making the TiO_2 film appear white again due to the light scattering layer. (d) Incomplete drop wetting of electrolyte Z988-EL over TiO_2 . The droplet's contact angle stabilized to 10° after initial spreading. (e) Electrolyte Z988-EL inkjet-printed precisely over the whole dye-sensitized TiO_2 photoelectrode layer. The printed layer kept its shape up to weeks and did not spread from the mesoporous TiO_2 layer to the FTO layer of the substrates.

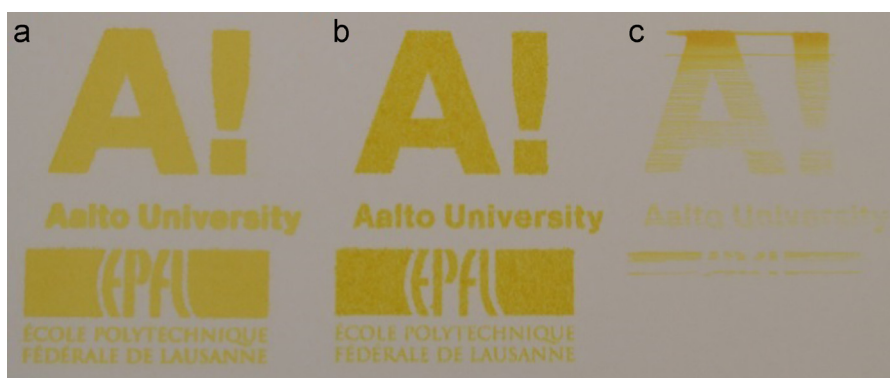


Figure 4 Inkjet printed electrolytes on common paper [27] (a) MPN-EL (b) Z988-EL (c) ACN-EL.

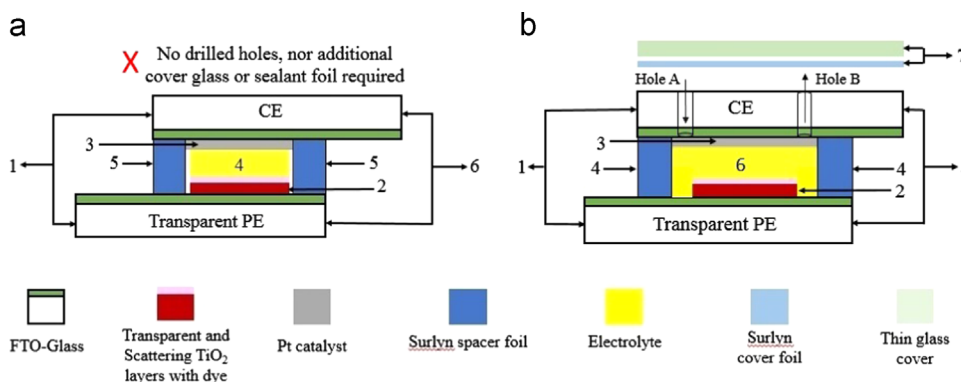


Figure 5 Device designs and fabrication sequences of (a) hole-free DSSC: 1. FTO-Glass substrate cleaning, 2. Sequential TiCl_4 treatments, screen printing and sintering of nanocrystalline and scattering TiO_2 particles, and dye sensitization, 3. Thermal platinization on FTO-Glass counter electrode, 4. Inkjet printing of Z988-EL over sensitized photoelectrodes, 5. Placement of Surlyn spacer foil over photoelectrode, 6. Photoelectrode and counter electrode fusing at $130\text{--}135^\circ\text{C}$. (b) traditional DSSC: 1. FTO-Glass substrates cleaning 2. Sequential TiCl_4 treatments, screen printing and sintering of nanocrystalline and scattering TiO_2 particles, and dye sensitization, 3. Thermal platinization on FTO-Glass counter electrode, 4. Placement of Surlyn spacer foil on FTO-Glass CE, 5. Photoelectrode and counter electrode fusing at $130\text{--}135^\circ\text{C}$, 6. Electrolyte insertion from counter electrode through hole A by releasing trapped air in the cell channel through hole B, 7. Sealing of the drilled holes by applying a Surlyn cover foil and glass cover through hot press at the counter electrode.

the overall cell resistance ($R_{\text{Cell}}=27.4 \pm 1.4 \Omega$) in the hole-free DSSC compared to the traditional design, in agreement with the increased FF . This performance improvement is noteworthy since the purpose of the electrolyte printing and hole-free cell design was not to enhance the cell performance, but to decrease the *inactive* area in the device as

well as to simplify the cell preparation. It should be noted that same DSSC materials, including same thickness ($25 \mu\text{m}$) of spacer foil, was used in both types of DSSC embodiments. In other words, there were no apparent differences in the active materials and components. These results therefore reveal a surprising performance superiority of the hole-free

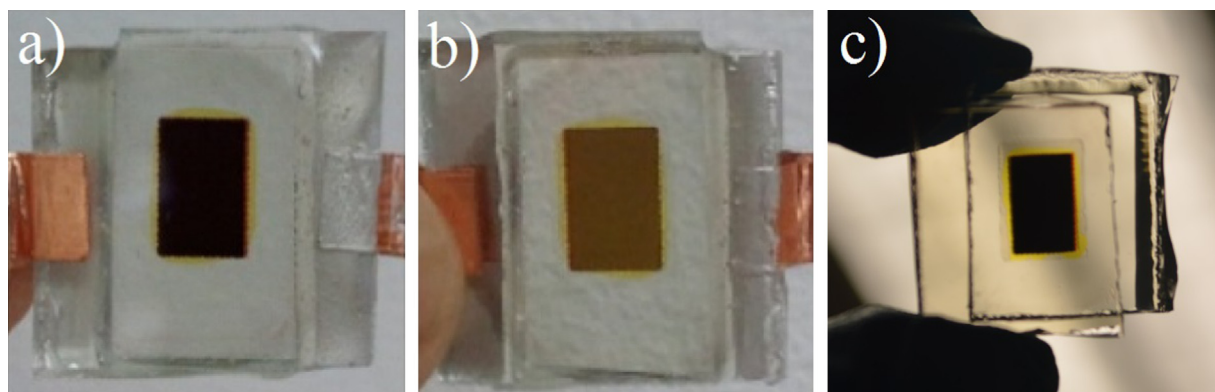


Figure 6 A hole-free DSSC with printed electrolyte layer. The electrolyte does not spread substantially around the electrode area ($8 \times 5 \text{ mm}^2$) during the cell sealing process. (a) front view, (b) rear view, (c) view with rear illumination to show the edges of the sealant (Surllyn).

Table 2 Photovoltaic characteristics of two independent batches of solar cells prepared on consecutive days (initial data without aging), and performance of the Batch 2 after 1120 h light soaking at open circuit voltage conditions: number of cells in each series (N), average \pm standard deviation of the photovoltaic metrics, and relative difference in the average (printed vs. reference cells), and p -value (two-tailed two-sample t -test with unequal variances). p -values less than $\alpha=0.05$ and differences more than 5% are underlined to signify statistically significant and practically relevant differences, respectively. Total cell resistance (R_{cell}) was calculated as the inverse slope of the J - V curve at V_{OC} . The active area of cells was 0.17 cm^2 in all cases, defined by the aperture area of a black tape mask. Photovoltaic metrics of the individual cells are provided as Supporting Information.

	N	J_{SC} (mA/cm^2)	V_{OC} (mV)	FF (%)	η (%)	R_{cell} (Ω)
Batch 1						
Hole free DSSC	5	14.7 ± 0.3	668 ± 8	73.7 ± 0.7	7.26 ± 0.18	29 ± 3
Reference DSSC	3	15.1 ± 0.2	669 ± 1	71.1 ± 0.7	7.19 ± 0.03	33 ± 1
Difference		-2.4%	-0.2%	3.7%	1.0%	-14%
p -value		0.09	0.68	<u>0.008</u>	0.43	<u>0.03</u>
Batch 2						
Hole free DSSC	7	14.9 ± 0.5	675 ± 3	73.7 ± 0.4	7.39 ± 0.26	27 ± 1
Reference DSSC	5	14.9 ± 0.5	667 ± 11	70.3 ± 0.7	6.98 ± 0.15	32 ± 1
Difference		-0.2%	1.2%	4.8%	5.9%	-14%
p -value		0.92	0.19	<u>0.0002</u>	<u>0.006</u>	<u>0.0001</u>
Batch 2 aged 1120 h						
Hole free DSSC	7	17.1 ± 0.3	624 ± 9	69.9 ± 1.7	7.47 ± 0.21	29 ± 2
Reference DSSC	5	14.7 ± 0.3	649 ± 9	72.3 ± 0.6	6.91 ± 0.08	30 ± 2
Difference		16%	-3.7%	-3.3%	8.1%	-2.2%
p -value		<u>0.0000002</u>	<u>0.002</u>	<u>0.008</u>	<u>0.0002</u>	0.58

over the traditional design, which adds to the other benefits already mentioned.

We emphasize that the surprising performance improvement was statistically significant (Batch 2, Table 2), and occurred due to decrease in the cell resistance which led to improved fill factor. The decrease of R_{Cell} and increase of FF were also *reproducible*: similar result was obtained from a batch prepared on the previous day (Batch 1, Table 2), although it did not translate to a statistically significant difference in efficiency in that case.

The individual contributions to the overall R_{Cell} , i.e. series resistance (R_s), recombination resistance (R_{REC}), charge transfer resistance at the counter electrode (R_{CT}) and diffusion resistance in the electrolyte (R_D), of each type of DSSC were investigated through electrochemical

impedance spectroscopy (EIS). Figure 8 represents the electrochemical performance of the best DSSC of each type whereas the average EIS values along with their standard deviations and statistical analysis are summarized in Table 3.

As expected, the reference DSSCs exhibited three semi-circles (Figure 8a, red squares) in the measured frequency range (100 mHz-100 kHz), as has been reported in our earlier studies, and which can be identified according to their unique peak positions [14,26]. The distance from origin to the first semi-circle in the Nyquist plots (Figure 8a) represents the series resistance (R_s) which mainly originates from the sheet resistance (R_{SH}) of the substrates. The first characteristic peak from right (Figure 8b, red squares) which appeared at high frequency (1-10 kHz) corresponds to charge

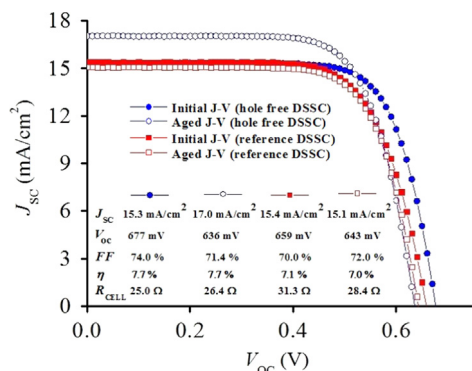


Figure 7 J-V curves of the best performing initial and 1120 h aged DSSCs measured under 1 Sun light intensity. Active area of the cells was 0.17 cm², defined by the aperture area of a black tape mask.

transfer resistance (R_{CT}) at the counter electrode of DSSC whereas the second characteristic peak from right at low frequency (10-100 Hz, Figure 8b) represents the recombination resistance (R_{REC}) or also known as resistance of the photoelectrode (R_{PE}). Moreover, the electrolyte diffusion resistance (R_D) appears at very low frequency (100 mHz-1 Hz, Figure 8b).

Surprisingly, a different Nyquist plot (in blue, Figure 8a) was obtained in case of hole-free DSSC in which the first characteristic peak from the right (Figure 8b, blue circles), which is normally associated with the charge transfer resistance at the counter electrode, is significantly smaller and appears at higher frequencies (10-100 kHz) than in the reference cells. Since the characteristic frequency f^* is related the RC time constant of the electrode as $\tau = (2\pi f^*)^{-1} = R_{CT}C_{CE}$ the electrochemical double layer capacitance of each type of CE was calculated from the constant phase element (CPE) values obtained by equivalent circuit curve fitting [27]. The capacitance values differed only by 18% ($C_{CE} = 6.2 \pm 0.8 \mu F$ for the hole-free DSSCs and $C_{CE} = 7.7 \pm 0.9 \mu F$ for the reference DSSCs, Table 3, Batch 2), whereas the difference in R_{CT} was as high as 71% ($R_{CT} = 1.0 \pm 0.1 \Omega$ for the hole-free DSSCs and $R_{CT} = 3.6 \pm 0.4 \Omega \text{ cm}^2$ for reference DSSCs). This means that the lower CE time constant ($\tau_{CE} = 6.4 \pm 0.4 \mu s$) in the case of the hole-free DSSCs compared to the reference DSSCs ($\tau_{CE} = 27 \pm 4 \mu s$), which made the peak appear at higher frequency (Figure 8b), is mainly due to lower R_{CT} of hole-free DSSC. Since C_{CE} is generally less sensitive to changes in the electrolyte composition and catalyst surface properties than R_{CT} , as it depends mainly on the surface area of the electrode, we take the similar C_{CE} as an indication that the high frequency arc can still be assigned to the charge transfer at the counter electrode. Moreover, we expect the measured C_{CE} value of the reference DSSCs to include additional contributions from the regions where the excess electrolyte is in contact with the counter electrode (Figure 1b). This may explain the $\sim 18\%$ lower C_{CE} of the hole-free DSSCs where such regions hardly exist (Figure 6). However, the same does not explain the lower R_{CT} of these cells, since smaller electrode surface area should have the opposite effect: it should give higher R_{CT} . It should also have no effect on the characteristic frequency. Since this was not the case, the R_{CT} must be lower in the hole-free cells due to other reasons. The hole-free DSSCs exhibited also

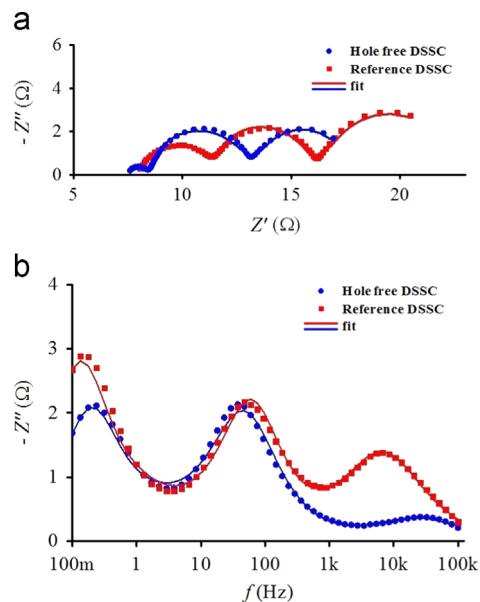


Figure 8 Typical EIS response of the best DSSCs measured at V_{oc} under 1 Sun illumination represented as (a) Nyquist plot (b) imaginary impedance Z'' as a function of frequency (f). All solid lines correspond to the fitted data whereas the points represent the measured data. (For interpretation of the references to color in this figure legend, the reader is referred to the web version of this article)

markedly lower ($\sim 29\%$) electrolyte diffusion resistance ($R_D = 4.8 \pm 0.1 \Omega$ Table 3, Batch 2) than the reference DSSC ($R_D = 6.8 \pm 0.6 \Omega$), and similar relative difference ($\sim 32\%$) in the diffusion time constant τ_D . The latter would suggest that there is difference either in the diffusion coefficient (D) of the redox couple or in the effective diffusion path length (δ), since $\tau_D \propto \delta^2/D$, but the present data alone does not allow separating their contributions.

The other differential cell resistances, R_S and R_{REC} , were similar in both types of cells. This means that the total differential resistance R_{TOT} , which was $\sim 18\%$ lower in hole-free DSSCs (Table 3, Batch 2), and agrees well with the $\sim 14\%$ lower R_{cell} derived from the J-V curve (Table 2), is explained mainly by the abovementioned differences in R_{CT} and R_D . These main differences were also reproducible (Batch 1, Table 3).

It should be again noted that similar materials were used in the whole experiment. In fact, we can think of only the following main differences between the two types of cells: 1) the electrolyte application method, 2) the sealing procedure, and 3) smaller inactive area exposed to the electrolyte. However, as the focus of this study was not to explore which of these differences would be responsible for the performance improvement, nor to determine the underlying mechanism causing it, we shall address the question in future investigations.

Finally, all the fabricated DSSCs of each type (Batch 2) were subjected to a continuous 35 °C light soaking stress test for a period of 1120 h under open circuit voltage (V_{oc}) conditions. The results are depicted in Figure 9a-d and the average values are summarized in Table 2. Both type of cells showed remarkably stable performance: relative changes in their average efficiency were both marginal ($\sim 1\%$) and

Table 3 Impedance characteristics of Batches 1 and 2 representing the initial data without aging: number of cells in each series (N), average \pm standard deviation of the EIS characteristics, relative difference in the average (printed vs. reference cells), and p -value (two-tailed two-sample t -test with unequal variances). p -values less than $\alpha=0.05$ and differences more than 20% are underlined to signify statistically significant and practically relevant differences, respectively. The total resistance was calculated as $R_{TOT}=R_S+R_{PE}+R_{CT}+R_D$. The PE and CE time constants were calculated from their resistance and capacitance as $\tau=RC$. The active area of cells was 0.4 cm^2 in all cases, defined by the photoelectrode dimensions (a tape mask was not used). EIS data of the individual cells and their complete EIS characteristics are provided as Supporting information.

	N	R_S (Ω)	R_{PE} (Ω)	R_{CT} (Ω)	C_{CE} (μF)	τ_{CE} (μs)	R_D (Ω)	τ_D (s)	R_{TOT} (Ω)
Batch 1									
Hole free DSSC	5	8.7 ± 0.7	4.6 ± 0.3	0.91 ± 0.11	5.4 ± 0.8	4.8 ± 0.3	4.82 ± 0.06	2.11 ± 0.05	19 ± 0.9
Reference DSSC	3	8.9 ± 1.1	3.9 ± 0.2	3.31 ± 0.24	6.6 ± 0.2	21.8 ± 2.2	7.36 ± 0.44	3.11 ± 0.42	23.4 ± 1.5
Difference		-1.8%	18%	<u>-73%</u>	-18%	<u>-78%</u>	<u>-34%</u>	<u>-32%</u>	-19%
p -value		0.841	<u>0.011</u>	<u>0.001</u>	<u>0.023</u>	<u>0.005</u>	<u>0.009</u>	0.053	<u>0.021</u>
Batch 2									
Hole free DSSC	7	8.2 ± 0.6	4.3 ± 0.1	1.03 ± 0.09	6.2 ± 0.8	6.4 ± 0.4	4.82 ± 0.08	2.01 ± 0.05	18.4 ± 0.6
Reference DSSC	5	7.7 ± 0.5	4.4 ± 0.3	3.58 ± 0.37	7.7 ± 0.9	27.4 ± 4.4	6.78 ± 0.61	2.97 ± 0.43	22.4 ± 0.6
Difference		7.2%	-2.3%	<u>-71%</u>	-18%	<u>-77%</u>	<u>-29%</u>	<u>-32%</u>	-18%
p -value		0.114	0.546	<u>0.000</u>	<u>0.023</u>	<u>0.000</u>	<u>0.002</u>	<u>0.008</u>	<u>0.000</u>

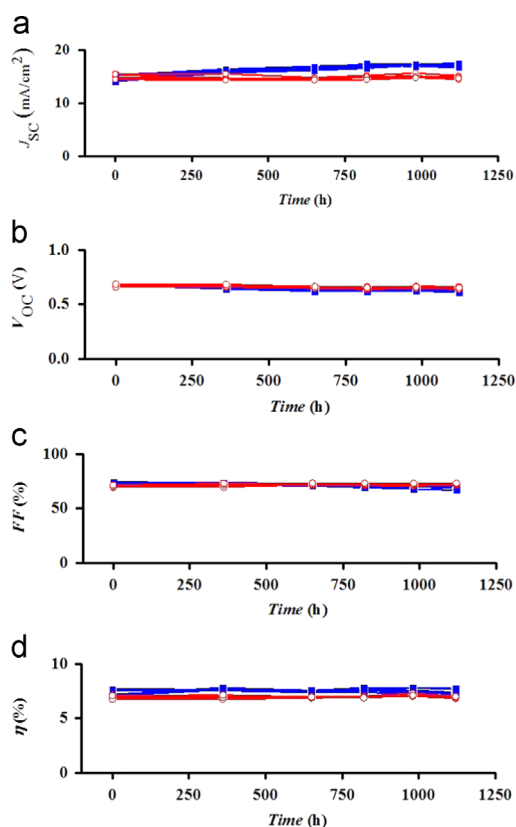


Figure 9 Result of 1 Sun light soaking test at $35\text{ }^\circ\text{C}$ of hole-free DSSC (7 samples, blue closed markers) and reference DSSC (5 samples, red open markers). (For interpretation of the references to color in this figure legend, the reader is referred to the web version of this article)

statistically insignificant. (Statistical analysis of the aging results is provided as Supporting information.). This shows that there is apparently no harmful effect neither to the electrolyte from the inkjet printing, which could happen e.g.

if impurities were picked up in the process, nor to the quality of the sealing, which could happen if the electrolyte crept under the sealant frame. Note that, although the efficiency of the hole-free DSSCs remained stable, their other J - V characteristics did change somewhat during the aging, as can be clearly seen from the J - V curves in Figure 7, and the data in Table 2: their J_{SC} increased by $\sim 15\%$, V_{OC} decreased by $\sim 7\%$ and FF decreased by $\sim 5\%$. The reference DSSCs exhibited much smaller changes, of which only the decrease of R_{cell} by ca. 7% was statistically significant. The original $\sim 14\%$ difference of in R_{cell} disappeared in the aging due to a simultaneous small increase of R_{cell} in the hole-free cells. It therefore seems that the electrolyte printing and hole-free sealing may have caused subtle changes in the electrolyte composition which made the J - V characteristics evolve differently over time, without affecting the efficiency.

Overall, the results presented here reveal the potential and advantage of adopting simpler and more economical fabrication step of dye sensitized solar cells. One of the advantages of this approach is that the electrolyte is protected from the ambient air, unlike in screen printing where the ink is first spread to the mesh and stays on for long until either being printed on the substrate or collected for re-use. Although screen printing is popular for homogenous material deposition it is unclear from the published reports how the distribution of the electrolyte ink on the substrate during printing and sealing has been managed [20]. The other benefits of our approach propose omitting glass drilling that is associated with a risk of glass breaking and the need for extra sealing components and an additional sealing step that contribute to the overall fabrication cost.

In conclusion, we successfully inkjet-printed an ionic liquid sulfolane electrolyte in the dye-sensitized solar cell as a part of a new cell fabrication sequence that eliminates drilling holes in the DSSC substrates. This finding was mainly based on a simple drop test experiment that was performed over the mesoporous TiO_2 layer which showed highly stable drop pattern in case of sulfolane based ionic liquid electrolyte.

Additionally, the high boiling point of the sulfolane solvent corresponded well to the inkjet printer characteristic and played a key role along with the higher surface tension of the ionic liquid electrolyte in preventing it from spreading during the cell sealing process at 130-135 °C. These results provide a solid base to develop this process further for the production of cheaper, more robust, large area DSSC solar panels.

Experimental methods

Materials

TiO₂ nanocrystalline paste (18-NRT, 20 nm) and TiO₂ scattering paste (WER2-0, 400 nm) were purchased from Dyesol. Chloroplatinic acid hydrate (H₂PtCl₄·6H₂O, purity 99.9%), Guanidine Thiocyanate (GuSCN, purity > 99%), 1 Methylbenzimidazole (NMBI, purity 99%), 4-tert-butylpyridine (TBP, purity 96%) and all the solvents (Sulfolane 99% purity, 2-Propanol 99.5% anhydrous, Acetonitrile 99.8% anhydrous, 3-Methoxypropionitrile 98% purity and N, N Dimethylformamide 99.8% purity) were obtained from Sigma Aldrich. Electrolyte 'Z988' and dye C101 were synthesized as reported earlier respectively [10,28]. 1, 3-dimethylimidazolium iodide (DMII), 1 Methyl-3-Propylimidazolium (PMII > 98% purity) and 1-ethyl-3-methylimidazolium iodide (EMII > 98% purity) were purchased from Io-Li-Tec and 1-ethyl-3-methylimidazolium tetracyanoborate (EMITCB) was purchased from Merck.

Electrolytes

The compositions of the electrolytes used in this experiment are as follows:

- MPN-EL: I₂ (0.06 M), GuSCN (0.1 M), NMBI (0.5 M), PMII (0.5 M) in 3-Methoxypropionitrile solvent.
- ACN-EL: I₂ (0.06 M), GuSCN (0.1 M), TBP (0.5 M), PMII (0.5 M) in Acetonitrile solvent.
- Z988-EL: DMII/EMII/EMITCB/I₂/NBB/GNCS (molar ratio 12:12:16:1.67:3.33:0.67) mixed and diluted with 50% of sulfolane (v/v).

Photoelectrodes (PE)

The photo electrodes for this experiment were prepared on fluorine doped tin oxide (FTO) coated Glass (NSG-10, R_{SH} 10 Ω/Sq). The conducting glass substrates were subsequently cleaned and sonicated with mild detergent and in acetone and ethanol solutions (15 min each) respectively and then dried with compressed air. These substrates were then treated in UV-O₃ cleaner (UVO-Cleaner, Model 256-220, Jelight Company Inc, USA) for 25 min to remove any possible impurity residues. After that all the substrates were heated in 40 mM TiCl₄ aqueous solution for 30 min in a preheated oven and were first sequentially rinsed with deionized water (DIW) and ethanol and were then dried with compressed air. Sequential printing of 8 μm and 5 μm thick layer of nano crystalline TiO₂ particles (20 nm) and scattering particles (400 nm) respectively was performed via screen printing. Each layer was heated to 110 °C for 5 min. These deposited layers were then sintered at 500 °C for 30 min and were

cooled down to room temperature. After that the sintered layers were re-treated in the 40 mM TiCl₄ aqueous solution and were re-sintered at 500 °C in the oven and were cooled down again to room temperature. These PE were finally sensitized with dye C-101 [28] to end the procedure.

Counter electrodes (CE)

10 mM chloroplatinic acid hydrate (H₂PtCl₄·6H₂O) solution (in 2-propanol) was drop casted over FTO coated glass substrates (TEC 7, R_{SH}=7 Ω/Sq) and was fired at 410 °C for 20 min. These substrate were then cooled down to room temperature and were kept in a sealed plastic box before use.

Inkjet printing of electrolyte

The inkjet printing of the electrolytes over mesoporous TiO₂ was performed by applying a maximum potential difference of 20 V to the print head nozzles with a printing waveform as shown in Figure S1. Approximately 50 s were spent to print over 8 × 5 cm² active area whereas 1.1 mg of electrolyte was consumed for the best performing devices.

Cell assembly

The printed electrolyte loaded PE and CE were faced together with a 25 μm thick Surlyn (1702) frame foil in between, and were carefully fused together over hotplate at 130-135 °C. After that, contacts were fabricated from copper tape and quick drying silver paste at the non-active area of the cell and were protected with a slow drying epoxy.

Measurements

The photovoltaic (*J-V* curves) measurement was performed in a Xenon lamp based solar simulator from Peccell Technologies under 1000 W/m² (1 Sun) illumination with a black tape mask with 0.17 cm² aperture area (the photoelectrode area was 0.4 cm²). The electrochemical impedance spectra (EIS) were recorded with Zahner-Elektrik IM6 electrochemical workstation whereas the curve fitting of the recorded data was performed with Zview2 software [29]. The EIS data were recorded at open circuit voltage condition, close to 1 Sun illumination, using a home-made solar simulator based on tungsten halogen lamps. The surface tension and contact angle of the fluids were measured by CAM 200 goniometer (KSV Instruments) in pendant and sessile drop modes respectively. The cells were aged at open circuit voltage conditions under 1 Sun light intensity at 35 °C in an artificial solar simulator with Halogen lamps (Philips 13117) and UV filter (Asmetetc GmbH, 400 nm cut-off) during which their *J-V* were measured periodically in the above-mentioned separate solar simulator.

Acknowledgment

Ghufran Hashmi thanks Academy of Finland (grant number 287641) for post-doctoral research grant and grateful to Dr S. M. Zakeeruddin and Professor Michael Gratzel for the useful discussions during the work and Armi Tiihonen for the help in cell ageing experiment. This work was also financed

from the European Research Council for an Advanced Research Grant (ARG 247404) funded under “Mesolight” project. M. O thanks Select+ (Environmental pathways for sustainable energy services) for doctoral research funding.

Appendix A. Supporting information

Supplementary data associated with this article can be found in the online version at <http://dx.doi.org/10.1016/j.nanoen.2015.08.019>.

References

- [1] S. Mathew, A. Yella, P. Gao, R.H. Baker, B.F.E. Curchod, N.A. Astani, I. Tavernelli, U. Rothlisberger, M.d. K. Nazeeruddin, M. Grätzel, *Nat. Chem.* 6 (2014) 242-247.
- [2] A. Fakharuddin, R. Jose, T.M. Brown, F.F. Santiago, J. Bisquert, *Energy Environ. Sci.* 7 (2014) 3952-3981.
- [3] G. Hashmi, K. Miettunen, T. Peltola, J. Halme, I. Asghar, K. Aitola, M. Toivola, P. Lund, *Renew. Sustain. Energy Rev.* 15 (2011) 3717-3732.
- [4] J. Kalowekamo, E. Baker, *Sol. Energy* 83 (2009) 1224-1231.
- [5] K. Miettunen, I. Asghar, S. Mastroianni, J. Halme, P.R. F. Barnes, E. Rikkinen, B. O'Regan, P. Lund, *J. Electroanal. Chem.* 664 (2012) 63-72.
- [6] A. Yella, H.W. Lee, N.H. Tsao, C. Yi, A.K. Chandiran, M.K. Nazeeruddin, E.W. Diau, C.Y. Yeh, S.M. Zakeeruddin, M. Grätzel, *Science* 334 (2011) 629-634.
- [7] M.I. Asghar, K. Miettunen, J. Halme, P. Vahermaa, M. Toivola, K. Aitola, *Energy Environ. Sci.* 3 (2010) 418-426.
- [8] A.G. Kontos, T. Stergiopoulos, V. Likodimos, D. Milliken, H. Desilvestro, G. Tulloch, P. Falaras, *J. Phys. Chem. Chem. Phys.* 117 (2013) 8636-8646.
- [9] N. Jiang, T. Sumitomo, T. Lee, A. Pellaroque, O. Bellon, D. Milliken, H. Desilvestro, *Sol. Energy Mater. Sol. Cells* 119 (2013) 36-50.
- [10] M. Marszalek, F.D. Arendse, J.D. Decoppet, S.S. Babkair, A.A. Ansari, S.S. Habib, M. Wang, S.M. Zakeeruddin, M. Grätzel, *Adv. Energy Mater.* 4 (2014) 1-8 1301235.
- [11] E. Stathatos, P. Lianos, A.S. Vuk, B. Orel, *Adv. Funct. Mater.* 14 (2004) 45-48.
- [12] H. Matsui, K. Okada, T. Kitamura., Electrolyte composition and photoelectric conversion element incorporating the same. U.S. Patent, 12/789, 135 (2010).
- [13] S. Ito, P. Chen, P. Comte, M.K. Nazeeruddin, P. Liska, P. Pechy, M. Grätzel, *Prog. Photovolt.: Res. Appl.* 15 (2007) 603-612.
- [14] S.G. Hashmi, M. Ozkan, J. Halme, J. Paltakari, P.D. Lund, *Nano Energy* 9 (2014) 212-220.
- [15] S. Ito, P. Liska, P. Comte, R. Charvet, P. Péchy, U. Bach, L.S. Mende, S.M. Zakeeruddin, A. Kay, M.K. Nazeeruddin, M. Grätzel, *Chem. Commun.* (2005) 4351-4353.
- [16] K. Miettunen, J. Halme, A.M. Visuri, P. Lund, *J. Phys. Chem. C* 115 (2011) 7019-7031.
- [17] R. Sastrawan, Photovoltaic modules of dye solar cells (PhD thesis 2006), <https://www.freidok.uni-freiburg.de/data/2623>.
- [18] R. Sastrawan, J. Beier, U. Belledin, S. Hemming, A. Hirsch, R. Kern, C. Vetter, F.M. Petrat, A.P. Schwab, P. Lechner, W. Hoffmann, *Sol Energy Mater Sol Cells* 90 (2006) 1680-1691.
- [19] K. Miettunen, J. Halme, P. Lund, *Electrochem. Commun.* 11 (2009) 25-27.
- [20] H. Pettersson, T. Gruszecki, L.H. Johansson, P. Johander, *Sol. Energy Mater. Sol. Cells* 77 (2003) 405-413.
- [21] E. Stathatos, P. Lianos, V. Jovanovski, B. Orel, *J. Photochem. Photobiol. A: Chem.* 169 (2005) 57-61.
- [22] J. Chen, H. Lin, X. Li, X. Zhao, F. Hao, S. Dong, *J. Power Sources* 222 (2013) 333-339.
- [23] K. Miettunen, J. Vapaavuori, A. Tiihonen, A. Poskela, P. Lahtinen, J. Halme, P. Lund, *Nano Energy* 8 (2014) 95-102.
- [24] J.D. Decoppet, T. Moehl, S.S. Babkair, R.A. Alzubaydi, A.A. Ansari, S.S. Habib, S.M. Zakeeruddin, H.W. Schmidt, M. Grätzel, *J. Mater. Chem. A* 2 (2014) 15972-15977.
- [25] A. Connell, P.J. Holliman, M.L. Davies, C.D. Gwenin, S. Weiss, M.B. Pitak, P.N. Horton, S.J. Coles, G. Cooke, *J. Mater. Chem. A* 2 (2014) 4055-4066.
- [26] S.G. Hashmi, J. Halme, T. Saukkonen, E.L. Rautama, P. Lund, *Phys. Chem. Chem. Phys.* 15 (2013) 17689-17695.
- [27] (<http://www.staples.co.uk/a4-multiuse-quickpack-a4-80gsm-2500-sheets/cbs/399037.html>).
- [28] F. Gao, Y. Wang, D. Shi, J. Zhang, M. Wang, X. Jing, R.H. Baker, P. Wang, S.M. Zakeeruddin, M. Grätzel, *J. Am. Chem. Soc.* 130 (2008) 10720-10728.
- [29] J. Halme, P. Vahermaa, K. Miettunen, P. Lund, *Adv. Energy Mater.* 22 (2010) E210-E234.



Ghufuran Hashmi completed his D.Sc. (Tech) degree in Advanced Energy Systems from Aalto University-Finland in 2014. He has recently been awarded a 3 year post-doctoral research grant from Academy of Finland to work on flexible dye sensitized solar cells and perovskite solar cells. He is keenly involved in development of advanced printable precursor solutions, inks and pastes for energy applications and their deposition through established printing techniques. His research interests include nano materials for energy applications, upscaling and long term stability of dye sensitized solar cells and perovskite solar cells.



Merve Özkan (M.Sc.) was graduated in 2012 from Information and Automation Engineering in University of Bremen. She has continued as a doctoral student in the SELECT+ doctoral programme (Environmental Pathways for Sustainable Energy Services) at Aalto University under supervision of Professor Jouni Paltakari. Her research work focuses on development of solar cells on flexible fiber based substrates.



Janne Halme has D.Sc. (Tech.) degree in engineering physics from Helsinki University of Technology and is currently a University Lecturer at the Aalto University School of Science. He has carried out both fundamental and applied research of dye-sensitized solar cells (DSSC) with a particular focus on flexible printed devices and their advanced performance characterization techniques. His current research interests are in electrochemical energy conversion and storage, building integrated photovoltaics and ambient energy harvesting.



Dr Katarina Dimic-Misic is currently working as post-doctoral researcher at the Department of Forest Product Technology, Aalto University-Finland. She received her D. Sc (Tech) degree in the field of rheology of complex suspensions from Aalto University in 2014. Her research interests include rheological properties of fluids and their processing at industrial scale.



Shaik M Zakeeruddin received his Ph.D. from Osmania University, India in 1989. He then joined Prof. Grätzel's group at the Swiss Federal Institute of Technology Lausanne (EPFL) as a post-doctoral fellow, remaining there as a senior scientist. The main areas of his research are nanomaterials, solar energy conversion, electrochromic displays, ionic liquids, lithium ion batteries, light-emitting diodes and biosensors. He has published over

280 peer-reviewed scientific papers and holds more than 20 patents. These contributions have often had a pioneering character and have been awarded a very large impact, with over 29,400 citations so far with h-index of 85. In a recently published top-100 chemist list of decade by Thomson Reuters, ranked 53rd for the chemist list and 29th for the material scientists list. (<http://sciencewatch.com/dr/sci/misc/Top100Chemists2000-10/>). Since March 2014 appointed as Distinguished Adjunct Professor at KAU, Jeddah, Saudi Arabia.



Professor Jouni Paltakari (D.Sc. Tech) has a chair in paper converting and packaging technology at Aalto University. His research group focuses on unit operations and technologies for adding value for fibre based substrates in converting processes and packaging applications. Pigment coating solutions and new material combinations consisting e.g. nano-cellulose as a renewable biomaterial are of great interest in

research and education. In addition, functional and intelligent solutions and products are also covered.



Professor Michael Grätzel of Physical Chemistry at the Ecole Polytechnique Fédérale de Lausanne, he directs there the Laboratory of Photonics and Interfaces. He pioneered research in the field of energy and electron transfer reactions in mesoscopic systems and their use for the solar generation of electricity and fuels as well as lithium ions batteries. He received numerous awards including the Albert Einstein

World Award of Science, the Paul Karrer Gold Medal, the 2010 Millennium Technology Grand Prize, and the 2009 Balzan Prize. Author of over 1300 publications, that received over 160'000 citations, and several books, he is a member of the German Academy of Science (Leopoldina) and other learned societies.



Peter D. Lund is Professor in Advanced Energy Systems at Aalto University-Finland. He is also Visiting Professor in Wuhan, China. His primary interest is on sustainable energy systems, including nanotechnology for energy applications, solar cells and fuel cells. Dr. Lund is active in senior roles with EU initiatives in energy: he chaired the Advisory Group Energy of E.C. 2002-06 and chairs the Energy Steering

Panel of European Academies Science Advisory Council (EASAC). He has served in advisory role in many energy programs world-wide. Dr. Lund is Co-Editor for Global Challenges, Interdisciplinary Reviews: Energy and Environment, and Energy Research.

High performance dye-sensitized solar cells with inkjet printed ionic liquid electrolyte

Syed Ghufran Hashmi ^{a}, Merve Ozkan ^b, Janne Halme ^a, Katarina Dimic Mistic, Shaik*

Mohammad Zakeeruddin ^c, Jouni Paltakari ^b, Michael Grätzel ^c, Peter D. Lund ^a

Supplementary information

Nomenclature:

<i>N</i>	number of samples
<i>ave</i>	average
<i>std</i>	standard deviation
<i>std/ave, Rel. stdev</i>	relative standard deviation compared to average
<i>sem</i>	standard error of the mean
<i>95% CI</i>	half of the full 95 % confidence interval based on Student's t-distribution
<i>Difference</i>	relative difference of average values: Printed vs reference, or Batch 2 vs Batch 1.
<i>p-value</i>	calculated with two-tailed two-sample t-test with unequal variances
<i>J_{sc}</i>	short circuit current density
<i>V_{oc}</i>	open circuit voltage
<i>FF</i>	fill factor
<i>η</i>	efficiency
<i>R_{cell}</i>	cell resistance (inverse slope of the IV curve at <i>V_{oc}</i>)

Photovoltaic data of individual cells corresponding to Table 2 of the paper

Table S1. Complete J-V data of Batches 1 and 2. Initial data without aging.

Batch 1		N				
Hole-free	5	J_{sc} (mA/cm²)	V_{oc} (V)	FF	η (%)	R_{cell} (Ω)
	P111	14.7	0.681	0.726	7.28	33.9
	P222	15.2	0.667	0.743	7.51	25.5
	P333	14.9	0.666	0.741	7.33	26.5
	P4444	14.6	0.661	0.736	7.12	28.6
	P555	14.4	0.664	0.740	7.07	28.9
	ave	14.7	0.668	0.737	7.26	28.7
	std	0.3	0.008	0.007	0.18	3.2
	std/ave	1.9 %	1.2 %	0.9 %	2.4 %	11.3 %
	sem	0.1	0.004	0.003	0.08	1.4
	95%CI	0.4	0.010	0.008	0.22	4.0
Reference	3	J_{sc} (mA/cm²)	V_{oc} (V)	FF	η (%)	R_{cell} (Ω)
	PR111	15.2	0.668	0.713	7.21	32.3
	PR222	15.3	0.670	0.703	7.20	34.7
	PR333	14.9	0.670	0.717	7.16	33.1
	ave	15.1	0.669	0.711	7.19	33.4
	std	0.2	0.001	0.007	0.03	1.2
	std/ave	1.4 %	0.2 %	1.1 %	0.4 %	3.7 %
	sem	0.1	0.001	0.004	0.02	0.7
	95%CI	0.5	0.003	0.019	0.07	3.1

Batch 2		N				
Hole-free	7	J_{sc} (mA/cm²)	V_{oc} (V)	FF	η (%)	R_{cell} (Ω)
G111		14.0	0.675	0.744	7.05	28.7
G222		14.5	0.670	0.737	7.15	27.7
G333		14.4	0.677	0.737	7.17	26.5
G555		15.2	0.675	0.732	7.51	29.3
G666		15.3	0.671	0.735	7.55	28.1
G777		15.3	0.679	0.737	7.66	26.5
G888		15.3	0.677	0.739	7.66	25.2
ave		14.9	0.675	0.737	7.39	27.4
std		0.5	0.003	0.004	0.26	1.4
std/ave		3.6 %	0.5 %	0.5 %	3.5 %	5.2 %
sem		0.2	0.001	0.001	0.10	0.5
95%CI		0.5	0.003	0.003	0.24	1.3
Reference	5	J_{sc} (mA/cm²)	V_{oc} (V)	FF	η (%)	R_{cell} (Ω)
GR333		14.7	0.668	0.707	6.94	31.9
GR444		14.5	0.663	0.699	6.74	33.3
GR555		15.5	0.658	0.696	7.08	30.5
GR777		15.4	0.659	0.700	7.10	31.3
GR888		14.4	0.686	0.715	7.06	32.5
ave		14.9	0.667	0.703	6.98	31.9
std		0.5	0.011	0.007	0.15	1.1
std/ave		3.3 %	1.7 %	1.1 %	2.2 %	3.3 %
sem		0.2	0.005	0.003	0.07	0.5
95%CI		0.6	0.014	0.009	0.19	1.3

Table S2. Complete *J-V* data of Batch 2 after 1120 hour aging.

Batch 2		N Aged 1120 hours				
Hole-free	7	J_{sc} (mA/cm²)	V_{oc} (V)	FF	η (%)	R_{cell} (Ω)
G13		17.0	0.636	0.714	7.74	26.4
G23		16.9	0.632	0.714	7.63	26.8
G33		17.1	0.631	0.710	7.67	27.4
G54		17.5	0.621	0.668	7.24	33.5
G63		17.3	0.617	0.690	7.35	29.9
G73		16.7	0.621	0.702	7.26	29.1
G83		17.2	0.613	0.698	7.35	29.0
ave		17.1	0.624	0.699	7.47	28.9
std		0.3	0.009	0.017	0.21	2.4
std/ave		1.5 %	1.4 %	2.4 %	2.8 %	8.4 %
sem		0.1	0.003	0.006	0.08	0.9
95%CI		0.2	0.008	0.015	0.19	2.2
Reference	5	J_{sc} (mA/cm²)	V_{oc} (V)	FF	η (%)	R_{cell} (Ω)
GR33		14.4	0.663	0.719	6.86	32.2
GR43		14.7	0.645	0.719	6.82	29.5
GR53		15.1	0.643	0.720	7.00	28.4
GR73		14.9	0.639	0.724	6.88	28.9
GR83		14.6	0.653	0.732	6.98	28.7
ave		14.7	0.649	0.723	6.91	29.5
std		0.3	0.009	0.006	0.08	1.6
std/ave		1.8 %	1.5 %	0.8 %	1.2 %	5.2 %
sem		0.1	0.004	0.003	0.04	0.7
95%CI		0.3	0.012	0.007	0.10	1.9

EIS Data of individual cells corresponding to Table 3 of the paper

Table S3. Complete EIS data of Batches 1 and 2. Initial data without aging.

Batch 1		N	SERIES R						PHOTOELECTRODE						COUNTER ELECTRODE						DIFFUSION			TOTAL R
Hole-free	5	R_S (Ω)	R_{PE} (Ω)	$Q_{CPE,PE}$	$\beta_{CPE,PE}$	C_{PE} (F) *	τ_{PE} (s) *	f_{PE}^* (Hz) *	R_{CE} (Ω)	$Q_{CPE,CE}$	$\beta_{CPE,CE}$	C_{CE} (F) *	τ_{CE} (s) *	f_{CE}^* (Hz) *	R_D (Ω)	τ_D (s)	f_D^* (Hz) *	R_{TOT} (Ω)						
P1		9.859	4.858	1.054E-03	0.954	8.174E-04	3.971E-03	40.08	0.859	2.278E-04	0.700	5.867E-06	5.041E-06	31573	4.813	2.133	7.462E-02	20.39						
P2		8.492	4.269	1.037E-03	0.964	8.448E-04	3.606E-03	44.13	0.902	2.874E-04	0.675	5.347E-06	4.822E-06	33008	4.729	2.096	7.593E-02	18.39						
P3		8.373	4.788	1.044E-03	0.953	8.018E-04	3.839E-03	41.46	0.755	2.564E-04	0.698	6.399E-06	4.833E-06	32928	4.829	2.040	7.802E-02	18.75						
P4		8.894	4.666	1.061E-03	0.955	8.267E-04	3.857E-03	41.26	0.973	3.363E-04	0.650	4.455E-06	4.336E-06	36709	4.848	2.103	7.568E-02	19.38						
P5		8.012	4.345	1.035E-03	0.961	8.338E-04	3.623E-03	43.93	1.048	1.590E-04	0.715	4.971E-06	5.210E-06	30549	4.896	2.166	7.348E-02	18.30						
ave		8.7	4.6	1.046E-03	0.957	8.249E-04	3.779E-03	42.2	0.91	2.534E-04	0.688	5.408E-06	4.848E-06	32954	4.82	2.11	7.554E-02	19.0						
std		0.7	0.3	1.115E-05	0.005	1.635E-05	1.587E-04	1.8	0.11	6.635E-05	0.026	7.576E-07	3.285E-07	2334	0.06	0.05	1.689E-03	0.9						
std/ave		8.1 %	5.8 %	1.1 %	0.5 %	2.0 %	4.2 %	4.2 %	12.3 %	2.6 %	3.7 %	14.0 %	6.8 %	7.1 %	1.3 %	2.2 %	2.2 %	4.5 %						
sem		0.3	0.1	4.988E-06	0.002	7.311E-06	7.096E-05	0.8	0.05	2.967E-05	0.011	3.388E-07	1.469E-07	1044	0.03	0.02	7.554E-04	0.4						
95% CI		0.9	0.3	1.385E-05	0.006	2.030E-05	1.970E-04	2.2	0.14	8.238E-05	0.032	9.407E-07	4.079E-07	2898	0.08	0.06	2.097E-03	1.1						
Reference	3	R_S (Ω)	R_{PE} (Ω)	$Q_{CPE,PE}$	$\beta_{CPE,PE}$	C_{PE} (F) *	τ_{PE} (s) *	f_{PE}^* (Hz) *	R_{CE} (Ω)	$Q_{CPE,CE}$	$\beta_{CPE,CE}$	C_{CE} (F) *	τ_{CE} (s) *	f_{CE}^* (Hz) *	R_D (Ω)	τ_D (s)	f_D^* (Hz) *	R_{TOT} (Ω)						
PR1		10.100	3.692	5.446E-04	1.052	7.402E-04	2.733E-03	58.24	3.505	6.853E-05	0.783	6.816E-06	2.389E-05	6662	7.854	3.591	4.432E-02	25.15						
PR2		8.607	3.814	6.086E-04	1.029	7.220E-04	2.754E-03	57.79	3.048	6.825E-05	0.782	6.398E-06	1.950E-05	8161	7.020	2.780	5.725E-02	22.49						
PR3		7.938	4.139	6.502E-04	1.022	7.385E-04	3.057E-03	52.07	3.384	6.524E-05	0.785	6.535E-06	2.211E-05	7197	7.191	2.970	5.359E-02	22.65						
ave		8.9	3.9	6.011E-04	1.034	7.336E-04	2.848E-03	56.0	3.3	6.734E-05	0.783	6.583E-06	2.184E-05	7340	7.36	3.11	5.172E-02	23.4						
std		1.1	0.2	5.320E-05	0.016	1.004E-05	1.812E-04	3.4	0.2	1.826E-06	0.002	2.132E-07	2.208E-06	760	0.44	0.42	6.664E-03	1.5						
std/ave		12.5 %	6.0 %	8.9 %	1.5 %	1.4 %	6.4 %	6.1 %	7.1 %	2.7 %	0.2 %	3.2 %	10.1 %	10.4 %	6.0 %	13.6 %	12.9 %	6.4 %						
sem		0.6	0.1	3.071E-05	0.009	5.794E-06	1.046E-04	2.0	0.1	1.054E-06	0.001	1.231E-07	1.275E-06	439	0.25	0.24	3.848E-03	0.9						
95% CI		2.7	0.6	1.322E-04	0.039	2.493E-05	4.502E-04	8.5	0.6	4.535E-06	0.005	5.297E-07	5.485E-06	1887	1.09	1.05	1.655E-02	3.7						

* Quantities marked with "*" are calculated from the values unmarked values in the previous columns. The unmarked values were obtained by fitting an equivalent circuit model to the measured EIS data.

Batch 2		N	SERIES R						PHOTOELECTRODE						COUNTER ELECTRODE						DIFFUSION			TOTAL R
Hole-free	7	R_S (Ω)	R_{PE} (Ω)	$Q_{CPE,PE}$	$\beta_{CPE,PE}$	C_{PE} (F) *	τ_{PE} (s) *	f_{PE}^* (Hz) *	R_{CE} (Ω)	$Q_{CPE,CE}$	$\beta_{CPE,CE}$	C_{CE} (F) *	τ_{CE} (s) *	f_{CE}^* (Hz) *	R_D (Ω)	τ_D (s)	f_D^* (Hz) *	R_{TOT} (Ω)						
G1		7.974	4.215	9.870E-04	0.956	7.669E-04	3.232E-03	49.24	1.080	1.670E-04	0.721	5.913E-06	6.386E-06	24922	4.787	2.041	7.798E-02	18.06						
G2		8.261	4.350	1.068E-03	0.949	8.002E-04	3.481E-03	45.72	0.939	1.576E-04	0.738	6.853E-06	6.438E-06	24722	4.913	2.070	7.689E-02	18.46						
G3		7.643	4.576	9.510E-04	0.956	7.391E-04	3.382E-03	47.06	1.000	2.193E-04	0.712	7.213E-06	7.213E-06	22065	4.904	2.005	7.938E-02	18.12						
G5		9.378	4.257	9.890E-04	0.957	7.749E-04	3.299E-03	48.25	1.166	1.242E-04	0.736	5.195E-06	6.058E-06	26273	4.747	1.967	8.091E-02	19.55						
G6		8.241	4.261	1.045E-03	0.956	8.140E-04	3.469E-03	45.89	1.134	2.427E-04	0.681	5.188E-06	5.883E-06	27052	4.713	2.077	7.663E-02	18.35						
G7		8.432	4.465	9.690E-04	0.953	7.387E-04	3.298E-03	48.26	0.917	3.418E-04	0.673	6.721E-06	6.162E-06	25828	4.755	1.941	8.200E-02	18.57						
G8		7.515	4.200	9.990E-04	0.954	7.691E-04	3.230E-03	49.27	1.008	1.005E-04	0.772	6.635E-06	6.688E-06	23798	4.886	2.002	7.950E-02	17.61						
ave		8.2	4.3	1.001E-03	0.954	7.718E-04	3.342E-03	47.7	1.03	1.933E-04	0.719	6.245E-06	6.404E-06	24951	4.82	2.01	7.904E-02	18.4						
std		0.6	0.1	4.142E-05	0.003	2.827E-05	1.043E-04	1.5	0.09	8.218E-05	0.034	8.179E-07	4.446E-07	1665	0.08	0.05	2.006E-03	0.6						
std/ave		7.5 %	3.3 %	4.1 %	0.3 %	3.7 %	3.1 %	3.1 %	9.2 %	4.2 %	4.8 %	13.1 %	6.9 %	6.7 %	1.7 %	2.5 %	2.5 %	3.3 %						
sem		0.2	0.1	1.565E-05	0.001	1.069E-05	3.940E-05	0.6	0.04	3.106E-05	0.013	3.091E-07	1.680E-07	629	0.03	0.02	7.584E-04	0.2						
95% CI		0.6	0.1	3.831E-05	0.003	2.615E-05	9.642E-05	1.4	0.09	7.600E-05	0.032	7.565E-07	4.112E-07	1540	0.08	0.05	1.856E-03	0.6						
Reference	5	R_S (Ω)	R_{PE} (Ω)	$Q_{CPE,PE}$	$\beta_{CPE,PE}$	C_{PE} (F) *	τ_{PE} (s) *	f_{PE}^* (Hz) *	R_{CE} (Ω)	$Q_{CPE,CE}$	$\beta_{CPE,CE}$	C_{CE} (F) *	τ_{CE} (s) *	f_{CE}^* (Hz) *	R_D (Ω)	τ_D (s)	f_D^* (Hz) *	R_{TOT} (Ω)						
GR3		8.060	4.632	6.320E-04	0.997	6.199E-04	2.871E-03	55.43	3.421	4.105E-05	0.853	8.922E-06	3.052E-05	5215	7.257	3.289	4.839E-02	23.37						
GR4		6.937	4.726	5.490E-04	1.012	5.892E-04	2.784E-03	57.16	4.016	3.800E-05	0.852	8.209E-06	3.297E-05	4827	7.048	3.043	5.230E-02	22.73						
GR5		7.367	4.648	5.720E-04	1.004	5.857E-04	2.722E-03	58.47	3.858	3.626E-05	0.845	7.103E-06	2.740E-05	5808	5.760	2.246	7.086E-02	21.63						
GR7		8.035	4.066	5.750E-04	1.014	6.252E-04	2.542E-03	62.61	3.516	3.713E-05	0.839	6.651E-06	2.338E-05	6806	6.675	2.950	5.395E-02	22.29						
GR8		7.867	4.089	5.900E-04	1.017	6.525E-04	2.668E-03	59.64812631	3.083	5.780E-05	0.808	7.428E-06	2.290E-05	6950	7.141	3.317	4.798E-02	22.18						
ave		7.7	4.4	5.836E-04	1.009	6.145E-04	2.718E-03	58.7	3.58	4.205E-05	0.839	7.663E-06	2.744E-05	5921	6.78	2.97	5.470E-02	22.4						
std		0.5	0.3	3.078E-05	0.008	2.767E-05	1.239E-04	2.7	0.37	8.989E-06	0.018	9.051E-07	4.391E-06	942	0.61	0.43	9.387E-03	0.6						
std/ave		6.4 %	7.4 %	5.3 %	0.8 %	4.5 %	4.6 %	4.6 %	10.3 %	21.4 %	2.2 %	11.8 %	16.0 %	15.9 %	9.0 %	14.6 %	17.2 %	2.9 %						
sem		0.2	0.1	1.376E-05	0.004	1.238E-05	5.543E-05	1.2	0.16	4.020E-06	0.008	4.048E-07	1.964E-06	421	0.27	0.19	4.198E-03	0.3						
95% CI		0.6	0.4	3.822E-05	0.010	3.436E-05	1.539E-04	3.4	0.46	1.116E-05	0.023	1.124E-06	5.452E-06	1170	0.76	0.54	1.166E-02	0.8						

* Quantities marked with "*" are calculated from the values unmarked values in the previous columns. The unmarked values were obtained by fitting an equivalent circuit model to the measured EIS data.

Statistical analysis of all EIS characteristics

Table S4. Complete EIS data of Batches 1 and 2. Initial data without aging.

	N	PHOTOELECTRODE							COUNTER ELECTRODE							DIFFUSION			TOTAL R
		SERIES R R_S (Ω)	R_{PE} (Ω)	$Q_{CPE,PE}$ ($\cdot 10^{-3}$)	$\beta_{CPE,PE}$	C_{PE} (mF) *	τ_{PE} (ms) *	f_{PE}^* (Hz) *	R_{CE} (Ω)	$Q_{CPE,CE}$ ($\cdot 10^{-3}$)	$\beta_{CPE,CE}$	C_{CE} (μ F) *	τ_{CE} (μ s) *	f_{CE}^* (kHz) *	R_D (Ω)	τ_D (s)	f_D^* (mHz) *	R_{TOT} (Ω)	
Batch 1																			
Hole-free	5	8.7 \pm 0.7	4.6 \pm 0.3	1.05 \pm 0.01	0.957 \pm 0.005	0.82 \pm 0.02	3.8 \pm 0.2	42 \pm 2	0.91 \pm 0.11	0.253 \pm 0.066	0.688 \pm 0.026	5.4 \pm 0.8	4.8 \pm 0.3	33 \pm 2.3	4.82 \pm 0.06	2.11 \pm 0.05	76 \pm 2	19 \pm 0.9	
Reference	3	8.9 \pm 1.1	3.9 \pm 0.2	0.6 \pm 0.05	1.034 \pm 0.016	0.73 \pm 0.01	2.8 \pm 0.2	56 \pm 3	3.31 \pm 0.24	0.067 \pm 0.002	0.783 \pm 0.002	6.6 \pm 0.2	21.8 \pm 2.2	7.3 \pm 0.8	7.36 \pm 0.44	3.11 \pm 0.42	52 \pm 7	23.4 \pm 1.5	
Difference		-1.8 %	18 %	<u>74 %</u>	-7.4 %	12 %	<u>33 %</u>	<u>-25 %</u>	<u>-73 %</u>	<u>276 %</u>	-12 %	-18 %	<u>-78 %</u>	<u>349 %</u>	<u>-34 %</u>	<u>-32 %</u>	<u>46 %</u>	-19 %	
p-value		0.841	<u>0.011</u>	<u>0.004</u>	<u>0.010</u>	<u>0.000</u>	<u>0.002</u>	<u>0.011</u>	<u>0.001</u>	<u>0.003</u>	<u>0.001</u>	<u>0.023</u>	<u>0.005</u>	<u>0.000</u>	<u>0.009</u>	0.053	<u>0.022</u>	<u>0.021</u>	
Batch 2																			
Hole-free	7	8.2 \pm 0.6	4.3 \pm 0.1	1 \pm 0.04	0.954 \pm 0.003	0.77 \pm 0.03	3.3 \pm 0.1	48 \pm 1	1.03 \pm 0.09	0.193 \pm 0.082	0.719 \pm 0.034	6.2 \pm 0.8	6.4 \pm 0.4	25 \pm 1.7	4.82 \pm 0.08	2.01 \pm 0.05	79 \pm 2	18.4 \pm 0.6	
Reference	5	7.7 \pm 0.5	4.4 \pm 0.3	0.58 \pm 0.03	1.009 \pm 0.008	0.61 \pm 0.03	2.7 \pm 0.1	59 \pm 3	3.58 \pm 0.37	0.042 \pm 0.009	0.839 \pm 0.018	7.7 \pm 0.9	27.4 \pm 4.4	5.9 \pm 0.9	6.78 \pm 0.61	2.97 \pm 0.43	55 \pm 9	22.4 \pm 0.6	
Difference		7.2 %	-2.3 %	<u>72 %</u>	-5.4 %	<u>26 %</u>	<u>23 %</u>	-19 %	<u>-71 %</u>	<u>360 %</u>	-14 %	-18 %	<u>-77 %</u>	<u>321 %</u>	<u>-29 %</u>	<u>-32 %</u>	<u>45 %</u>	-18 %	
p-value		0.114	0.546	<u>0.000</u>	<u>0.000</u>	<u>0.000</u>	<u>0.000</u>	<u>0.000</u>	<u>0.000</u>	<u>0.003</u>	<u>0.000</u>	<u>0.023</u>	<u>0.000</u>	<u>0.000</u>	<u>0.002</u>	<u>0.008</u>	<u>0.004</u>	<u>0.000</u>	

* Quantities marked with "*" are calculated from the values unmarked values in the previous columns. The unmarked values were obtained by fitting an equivalent circuit model to the measured EIS data.

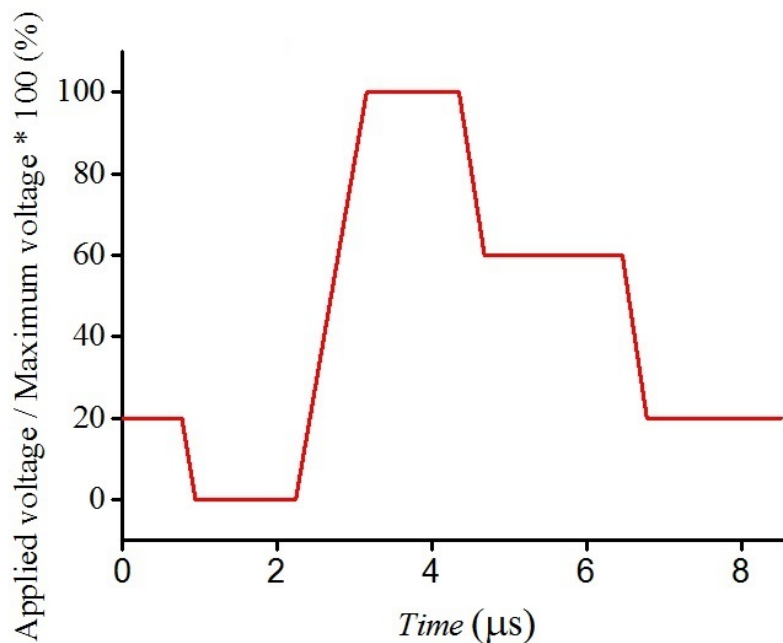


Figure S1: Inkjet printing waveform for electrolyte Z988-EL.

Statistical analysis of the aging results

Table S4 shows statistical analysis of the changes that occurred to the seven hole-free DSSCs and five reference DSSCs in the 1120 hour aging test (see the experimental section for details).

Neither of the cell types showed statistically significant difference in their efficiency before vs. after the aging. Both cell types can therefore be concluded equally stable within the experimental error: degradation or improvement of efficiency, if any, were smaller than the standard deviations which were less than 0.26 %-units for the seven hole-free cells and less than 0.15 %-units for the five reference cells.

Other photovoltaic parameters do however show statistically significant changes ($p < 0.05$) that are also practically significant (relative change $> 5\%$). Most notable of these is the 15 % increase in J_{SC} of the hole-free cells upon aging, which was compensated by the 7 % decrease in V_{OC} and 5 % decrease in η to yield an unchanged efficiency. In the case of the reference cells, all basic IV characteristics remained stable ($p > 0.05$ or relative change $< 5\%$). However, R_{cell} decreased by ca. 7 %, which was nevertheless not enough to cause significant decrease in FF .

Table S5. Statistical analysis of the aging changes in hole-free and reference DSSCs caused by 1120 h light soaking at open circuit voltage conditions, corresponding to the result in Table 2 of the paper. The p -value was calculated using two-tailed paired t-test. p -values less than $\alpha = 0.05$ and differences more than 5% are underlined to signify statistically significant and practically relevant differences, respectively.

	<i>N</i>	J_{SC} (mA/cm ²)	V_{OC} (mV)	FF (%)	η (%)	R_{cell} (Ω)
Hole-free						
Before aging	7	14.9 ± 0.5	675 ± 3	73.7 ± 0.4	7.39 ± 0.26	27 ± 1
Rel. stdev		3.6 %	0.5 %	0.5 %	3.5 %	<u>5.2 %</u>
After aging	7	17.1 ± 0.3	624 ± 9	69.9 ± 1.7	7.47 ± 0.21	29 ± 2
Rel. stdev		1.5 %	1.4 %	2.4 %	2.8 %	<u>8.4 %</u>
Difference		<u>15.0 %</u>	<u>-7.4 %</u>	<u>-5.2 %</u>	1.0 %	<u>5.4 %</u>
p -value		<u>0.00004</u>	<u>0.00001</u>	<u>0.0004</u>	0.70	0.15
Reference						
Before aging	5	14.9 ± 0.5	667 ± 11	70.3 ± 0.7	6.98 ± 0.15	32 ± 1
Rel. stdev		3.3 %	1.7 %	1.1 %	2.2 %	3.3 %
After aging	5	14.7 ± 0.3	649 ± 9	72.3 ± 0.6	6.91 ± 0.08	30 ± 2
Rel. stdev		1.8 %	1.5 %	0.8 %	1.2 %	<u>5.2 %</u>
Difference		-1.1 %	-2.7 %	2.8 %	-1.1 %	<u>-7.3 %</u>
p -value		0.34	<u>0.01</u>	<u>0.001</u>	0.19	<u>0.03</u>

APPENDIX 4



Cite this: *Energy Environ. Sci.*, 2016, 9, 2453

Dye-sensitized solar cells with inkjet-printed dyes†

Syed Ghufuran Hashmi,^a Merve Özkan,^b Janne Halme,^{*a} Shaik Mohammed Zakeeruddin,^c Jouni Paltakari,^b Michael Grätzel^c and Peter D. Lund^a

The slow process in which the light absorbing dye molecules are adsorbed from solution on the nanocrystalline TiO₂ photoelectrode film has been a handicap to the fast and cost-effective fabrication of dye-sensitized solar cells (DSSCs) using printing techniques. Here, we report a versatile dye sensitization process, achieved by inkjet printing a concentrated dye solution over the TiO₂ film, which produces solar cells with equal performance and stability as obtained using the popular dye drop casting method. In addition to allowing precise control of dye loading required for dispensing just the right amount of dye to achieve uniform and full coloration of the TiO₂ films without any need for washing off the excess dye, inkjet printing also makes it possible to freely adjust the amount and position of the dye to create DSSCs with tailored transparency, color density gradients, and patterns of one or more dyes on the same electrode. The method was confirmed to be applicable also for non-transparent, high-efficiency DSSC designs that employ a light scattering layer. The inkjet-dyed DSSCs exhibited high stability, retaining almost 100% of their conversion efficiency ($\eta = 6.4 \pm 0.2\%$) and short circuit current density ($J_{sc} = 14.2 \pm 0.6 \text{ mA cm}^{-2}$) when subjected to a 1000 h accelerated aging test under 1 Sun illumination at 35 °C, followed by additional 1154 hours under 0.5 Sun at 60 °C. These results overcome one of the main hurdles in realizing fully printed DSSCs and open opportunities for entirely new DSSC designs.

Received 18th March 2016,
Accepted 9th June 2016

DOI: 10.1039/c6ee00826g

www.rsc.org/ees

Broader context

Dye-sensitized solar cells (DSSCs) can be possibly produced at low cost using high throughput methods such as screen or inkjet printing, but to do so requires re-designing some of their conventional fabrication steps. One of them is the step where the light absorbing dyes are attached to the nanocrystalline TiO₂ photoelectrode. This is normally done on the laboratory scale by slowly soaking the TiO₂ film in a dye solution. Although methods exist to speed up the process from hours to minutes, it could be even quicker and consume less materials, if the dye could be simply printed on the TiO₂ film. We report here for the first time that this can in fact be done using inkjet printing, which at the same time brings about additional benefits. Inkjet dyeing not only simplifies the overall fabrication and consumes less solvents, but also opens new opportunities for creating multi-coloured solar cells with tailored transparency and decorative designs, which can be important attributes for the commercialization of DSSCs.

1. Introduction

Dye sensitized solar cells (DSSCs) have been considered as a promising photovoltaic technology because they can be produced from abundantly available raw materials on various substrates using fast printing processes,^{1–3} and have intrinsic features, such as semi-transparency and color,^{4,5} as well as good operation at low light intensity,⁶ which offer interesting product opportunities

for building integrated photovoltaics and energy harvesting for low power wireless electronics.^{5,7–9} However, in order to manufacture them at high speed and using the roll-to-roll printing methods, some of their conventional fabrication steps have to be re-designed.¹

In the conventional fabrication method of dye-sensitized solar cells, a monolayer of dye molecules is attached to the nanocrystalline TiO₂ photoelectrode film by soaking it for 16–24 hours in a dye bath containing the sensitizer molecules, usually the ruthenium complex N719, which is followed by rinsing off the excess dye.^{10,11} Although suitable for small-scale experiments, and therefore popular in the research labs, this process is too slow for high through-put manufacturing, which should ideally consist of only fast, additive material printing and deposition steps, each completed in the time frame of seconds to minutes, as already demonstrated for roll-to-roll fabrication of organic solar cells.^{12–17}

^a Department of Applied Physics, Aalto University School of Science, P.O. BOX 15100, FI-00076 Aalto (Espoo), Finland. E-mail: janne.halme@aalto.fi

^b Department of Forest Products Technology, Aalto University School of Chemical Technology, P.O. BOX 15100, FI-00076 Aalto (Espoo), Finland

^c Laboratory of Photonics and Interfaces, Ecole Polytechnique Federale de Lausanne (EPFL), CH G1 551, Station 6, CH-1015 Lausanne, Switzerland

† Electronic supplementary information (ESI) available. See DOI: 10.1039/c6ee00826g



Studies show that the time required for saturating the surface of TiO₂ with the N719 dye can be shortened down to three minutes¹⁸ either by using a more concentrated dye solution,^{18–20} performing the sensitization at higher temperature,^{20,21} or by facilitating the supply of the dye molecules from the solution into the mesoporous film by circulating^{20–22} or sonicating²³ the dye solution, by applying an electrical field,²⁴ or even by mixing the TiO₂ nanoparticles into the concentrated dye solution followed by spraying.²⁵ The adsorption kinetics depend also on the chemical conditions of the TiO₂ surface, which can be altered to be more favorable for dye adsorption by treating it with acidic solution.²⁶ For small area DSSCs, the fastest reported uptake of N719 through the soaking process was completed in 5–10 minutes using drop casting and pumping methods, which gave dyed TiO₂ photoelectrodes capable of producing 11–18 mA cm⁻² short circuit current density under the standard reporting conditions.^{18–20}

On the other hand, the sensitization studies of large surface area DSSC modules are few, and among them the popular scheme has been the dye circulation through a pump,^{21,22,27} however, the sensitization time through this circulation technique was long (more than two hours). In the case of the new concept of pre-sensitization of TiO₂ nanoparticles in the dye solution followed by spraying, reported recently for large area flexible DSSCs, material consumption may be an issue since a significant fraction of the sprayed material can be wasted over the non-active area, which can increase the overall production cost.²⁵

Since most of the active materials of DSSCs can be deposited by printing and coating,^{1,28} it would be advantageous from the point-of-view of manufacturing if the dye could also be simply printed on the TiO₂ films. The first steps toward this direction were taken by Nazeeruddin *et al.* who introduced a rapid sensitization technique, in which a known volume of a highly concentrated N719 dye solution is pipetted onto the TiO₂ electrode, or the electrode is immersed in it briefly.¹⁸ This process, which took only three minutes at the shortest,¹⁸ was thereafter followed by others who showed that a similar performance can be achieved

with fast sensitization as with the traditional sensitization technique.^{19,20,29} Nevertheless, in some of these studies, the excess, non-adsorbed dye was washed away afterwards,^{18,29} which suggests that the control of the applied amount of dye was not sufficiently accurate to dispense just enough dye to saturate the film, but not more. Clearly, the rapid sensitization could reach its full potential as a DSSC fabrication process only if it could be performed using a precise, automated and industrially scalable printing technique.

Here, we report a versatile dye sensitization process, achieved through the inkjet printing of concentrated dye solutions over the TiO₂ electrode films (Fig. 1), which allows accurate control of the printed amount of dye, while producing solar cells with equal performance and stability as obtained using the known drop casting process. Based on the piezo-electric ‘drop-on-demand’ deposition of nominal 10 picoliter sized droplets, inkjet printing not only allows dispensing the right amount of dye needed for uniform and full coloration of the TiO₂ films without the excess dye, but also makes it possible to freely adjust the dye loading to create solar cells with tailored transparency, color density gradients, and arbitrary patterns of one or multiple dyes on the same TiO₂ electrode (Fig. 1).

The dye was printed using an automated inkjet printer (Fuji Film’s Dimatix Material Printer, model DMP-2800 Series) by filling the concentrated dye solutions (10–16 mM in DMF or DMSO) into its polymer cartridge after passing them through a 0.2 μm filter (see the Experimental section for further details). In the following, we discuss first the results from semi-transparent DSSCs, obtained by the inkjet printing of a ruthenium sensitizer C101.³²

2. Results and discussion

The following discussion has been divided into two parts (Sections 2 and 3). In the first part, we demonstrated the

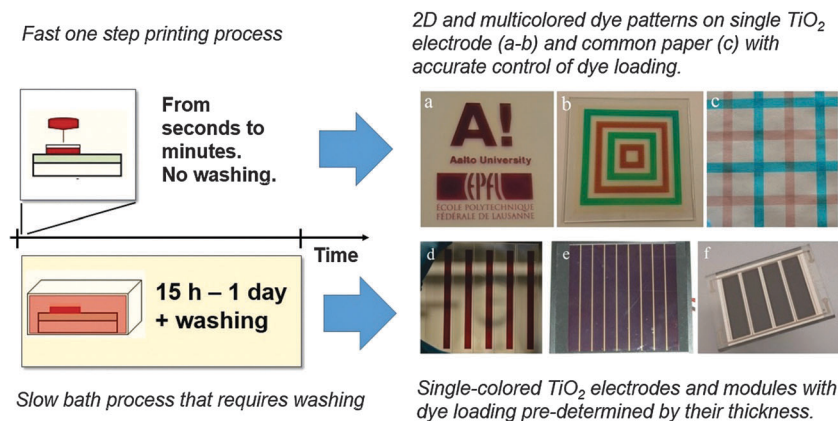


Fig. 1 An Illustration of DSSC fabrication using old and new dye sensitization methods (a) 2D patterning demonstration of Aalto University and EPFL University logos using the inkjet printing technique used in this study from a concentrated dye solution of C101 dye over a nanocrystalline TiO₂ layer (b) colorful patterns (SQ2 dye in green and Z907 dye in red) can be obtained on a single substrate which cannot be realized using the old dye bath technique (c) overlapping prints of SQ2 and Z907 dyes on a regular office paper as a demonstration of co-sensitization and color tuning (d–f) large area sensitized electrodes fabricated using the traditional dye bath methods.^{30,31}



potential capabilities of inkjet printing by using the semi-transparent DSSCs produced through efficient control of dye loadings on nanocrystalline mesoporous TiO₂ layers (no scattering layers were employed), whereas in the second part, the stability of printed dye is investigated in the standard DSSCs employing the scattering TiO₂ layers.

2.1. Demonstration of the capabilities of inkjet printing of the dye

2.1.1. Variable transparency, color density gradients and multi-dye patterns in a single DSSC. One of the advantages of inkjet printing is the controlled dispensing of fluid through which the dye loading of the photoelectrode can be accurately controlled. To demonstrate this capability, and to determine the printing parameters that yield full coloration, a 10 mM solution of C101 dye in DMF was inkjet-printed 1–5 times (1.1 $\mu\text{L cm}^{-2}$ per print) over a 7 μm thick TiO₂ electrode (0.4 cm², without a scattering layer) using 10 pL drop volume and 30 μm drop spacing, which corresponds to 11.3 nmol cm⁻² of dispensed dye per print. After a settling period of *ca.* 1 minute,

during which the dye attached on the TiO₂ surface from the printed solution, the films were rinsed with DMF (“washed” samples) to remove the possible non-adsorbed dye, or the rinsing step was omitted (“non-washed” samples). The photoelectrodes were then prepared for fully sealed solar cells (see the Experimental section) and their optical transmittance and absorbance (Fig. 2a–d), dye loading (Fig. 3a) and photovoltaic performance (Fig. 4a–f) were measured. Reference samples were prepared using the conventional “rapid sensitization” by spreading 70–80 μL (175–200 $\mu\text{L cm}^{-2}$) of the same dye solution on an identical TiO₂ film using a pipette (“drop-cast” samples), followed by the same 15 minute settling and final rinsing as done for the washed inkjet-printed samples.

According to the optical characterization, five printing cycles were enough to achieve the coloration of the films close to that of the drop-cast samples, which we consider to be fully saturated with the dye. With 1–5 printing cycles, the device transmittance could be varied systematically from 38% to 8% (at 550 nm), while the photoelectrode absorbance ranged correspondingly from 44% to 88% (Fig. 2a and d and Fig. S3 in ESI†). This immediately

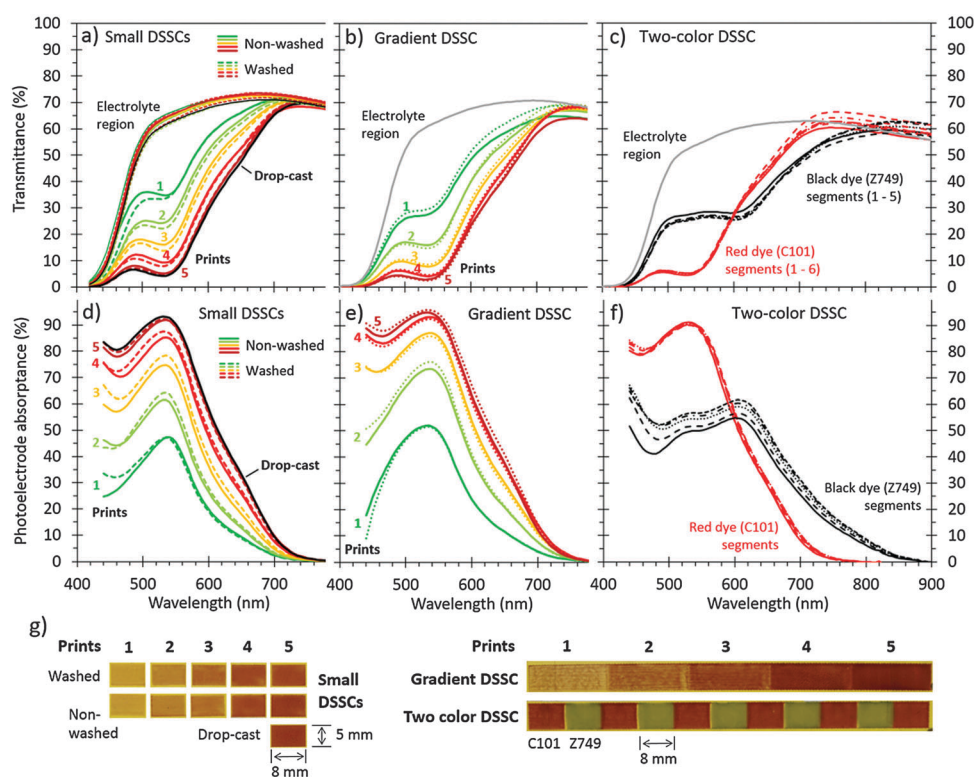


Fig. 2 Optical characteristics of semi-transparent DSSCs with inkjet-printed dyes: (a–c) transmittance, (d–f) photoelectrode absorbance, (g) photographs. (a and d) Small DSSCs dyed by inkjet-printing a dye solution (10 mM C101 in DMF) 1–5 times (1.1 $\mu\text{L cm}^{-2}$ per print) over a 7 μm thick TiO₂ electrode (0.4 cm², no scattering layer), followed by rinsing with DMF (“Washed”) or omitting the rinsing (“Non-washed”), compared with a reference sample dyed by drop-casting 70–80 μL of the same dye solution on an identical TiO₂ film using a pipette, followed by the same washing treatment (“Drop-cast”). (b and e) A DSSC with color density gradient made by inkjet-printing the C101 dye solution 1–5 times over different parts of the same TiO₂ electrode. (c and f) A two-color DSSC with ink-jet printed red (C101) and black (N749) dye segments on the same TiO₂ electrode. (d–f) Show the internal absorbance spectra of the photoelectrode layer calculated as the ratio of the transmittances through the photoelectrode and electrolyte regions of the same cell (a–c), normalized to zero at long wavelengths (at 800 nm for C101 and 900 nm for N749); (g) photographs of the photoelectrode regions of the measured DSSCs taken with white backlight. The printing was done in all the cases with a 10 pL drop volume and 30 μm drop spacing, using 10 mM C101 in DMF as the red dye ink and 10 mM N749 in DMF as the black dye ink (printed in 5 cycles). The small DSSCs spectra shown are examples from the complete data set consisting of three samples of each type. The complete data set and details of the calculation of figures (d–f) are available in the ESI.†



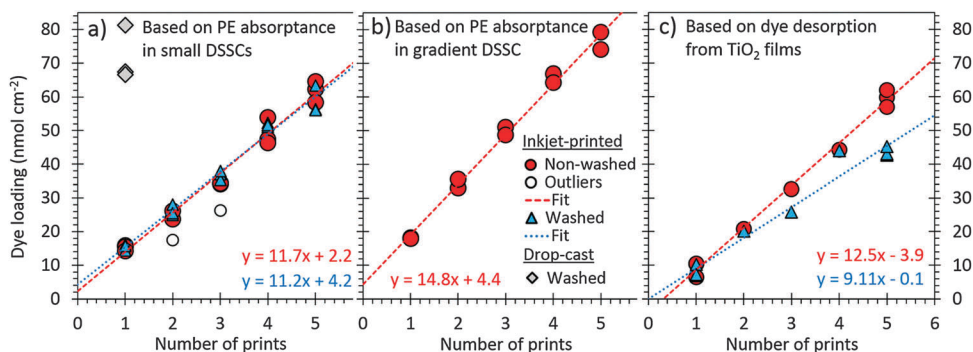


Fig. 3 Dye loading in the small DSSCs (a) and the gradient DSSC (b) determined from their photoelectrode absorbance spectra shown in Fig. 2, and confirmed by dye desorption from the TiO₂ films (c). The lines are linear fits to the data with equations shown. Note that many data points are overlapping. The number of data points are: (a) three for each 1–5 prints, (b) three for 1 and 3 prints and one for 2 to 4 prints, (c) two for each for each 1–5 prints. The data points marked as outliers in (a) correspond to the samples with less uniform coloration and are excluded from the fit. Details of the dye loading calculations are given in the ESI.†

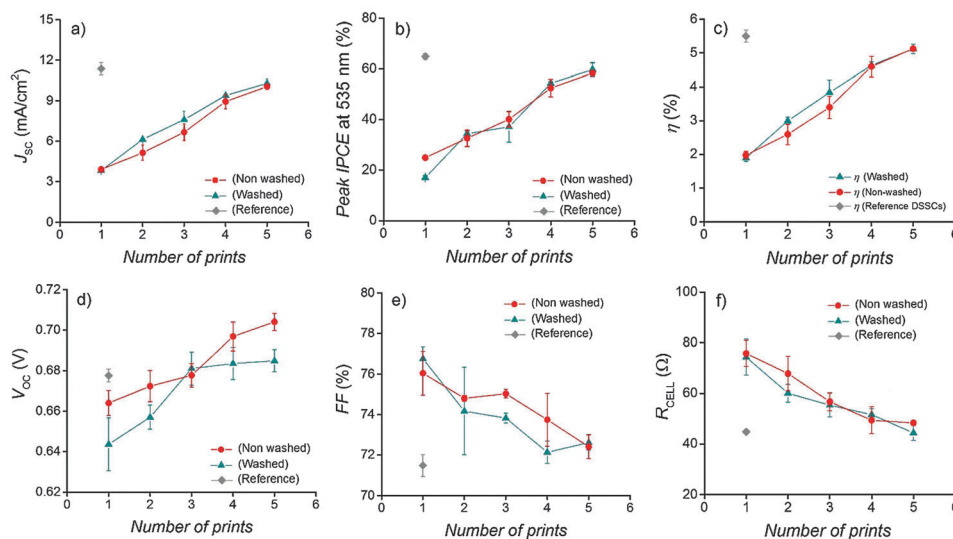


Fig. 4 (a–f) Photovoltaic parameters of one batch of DSSC devices with 1–5 time printed PEs. The points are average values of three cells and the error bars represent their standard deviation.

shows the unique feature of dye-sensitization using inkjet-printing that could be interesting for many applications of the semi-transparent DSSCs: the transparency of the devices can be fine-tuned by the dispensed amount of dye without changing the thickness of the TiO₂ film. This is exactly opposite to the conventional dyeing processes that produce fully dye-saturated films with transmittance dictated by their thickness.

The other interesting feature of inkjet printing already mentioned is that it allows printing almost arbitrary dye patterns (Fig. 1). Fig. 2g shows this capability in more detail by demonstrating the two most obvious opportunities it implies: the creation of dye patterns with varying color density (“gradient DSSC”) and combinations of multiple dyes (“two-color DSSC”) on the same photoelectrode. The optical characteristics of the five individual segments in the gradient DSSC, dyed with 1–5 prints of the C101 dye, are similar to those observed in the small individual DSSCs, but produced on the same long TiO₂ electrode stripe (Fig. 2b and e vs. Fig. 2a and d). In the two-color

DSSC, the characteristic absorbance spectra of the printed red (C101) or black (N749) dyes can be distinguished from the adjacent segments without any signs of mixing between them (Fig. 2c and f). This shows that inkjet printing accurately fixed the dyes in their own segments, allowing multicolored dye patterns to be produced on the same electrode. Note how uniform the coloration is in each segment of the two-color DSSC (Fig. 2g), and how repeatable the color density is between them, especially for the red dye (Fig. 2c and f). Although the coloration is less uniform in the gradient DSSC with 1–3 prints, it improves substantially with the successive 4th and 5th prints, and is remarkably good in the small DSSCs, even with a single print, so that practically no visual difference can be seen between the five-time printed and drop-cast samples (Fig. 2g).

2.1.2. Precise control of dye loading. Washing the TiO₂ films after printing the dye affected neither their optical absorbance nor visual appearance (Fig. 2d and g), and no traces of the dye could be seen in the transmittance spectra recorded from the



free electrolyte region of the cells (Fig. 2a–c). This indicates that all the printed dye had attached well to the TiO₂ film, leaving no excess or loosely bound dye that could be removed by washing or released into the electrolyte when built into a DSSC, even when the washing step had been omitted. The dye loading in the TiO₂ films, estimated from the photoelectrode absorbance spectra as detailed in the ESI,[†] confirms this by showing excellent agreement between the washed and non-washed samples (Fig. 3a). Moreover, the dye loading increases linearly with the number of prints, demonstrating good control and repeatability of the printing process. The average dye loading per print determined from the slope of the linear fits is 11.2 nmol cm⁻² in the washed and 11.7 nmol cm⁻² in the non-washed samples, which matches almost perfectly with the dispensed amount (11.3 nmol cm⁻²) determined by the printer settings (drop volume, spacing, and concentration). Note that the dye loading obtained with five prints (56–65 nmol cm⁻²) is only slightly below the values achieved by drop-casting (68–81 nmol cm⁻²), as one would expect if the loading does not exceed the saturation limit, but is close to it (Fig. 3a). Similar results with excellent linearity are also observed in the gradient DSSC, although at somewhat higher 14.8 nmol cm⁻² loading per print (Fig. 3b). The relatively high values with five prints (74–79 nmol cm⁻²), achieved without signs of saturation in the linear trend, indicate a somewhat higher film thickness in the gradient DSSC compared to the small DSSCs.

To confirm these results, some of the inkjet-dyed TiO₂ films from the same batch as those built into solar cells underwent a dye desorption experiment, where the printed dye was detached from the films to a desorption solution of known volume and then quantified using UV-VIS absorbance spectroscopy (see the Experimental section and ESI[†]). The results correspond well to those determined optically from the complete DSSCs: the dye loading increases linearly with the number of prints with slopes of 9.1 nmol cm⁻² per print in the washed and 12.5 nmol cm⁻² per print in the non-washed samples (Fig. 3c), and the values per film thickness obtained with five prints (6.5 and 8.9 nmol cm⁻² μm⁻¹, respectively) are close to the values reported for the same dye by others (8.8 to 11.4 nmol cm⁻² μm⁻¹).³³ Note that although the lower slope would suggest that washing had removed a significant amount of dye from the films in this case, only small amounts (<6 nmol cm⁻²) were detected in the five-time printed samples using UV-VIS spectroscopy, and none in the samples printed 1–4 times (data not shown). We therefore consider that these lower loadings, which deviate from the general trend more than the normal variation, resulted from occasionally failed printing cycles, which occurred in less than 4% of all the 174 printing cycles constituting the results of Fig. 3a–c. Indeed, only four of the nine washed samples in Fig. 3c show results below the linear trend of the non-washed ones, whereas the rest match well with it.

2.1.3. Photovoltaic performance of the semi-transparent DSSCs. Also the results from the photovoltaic characterization show clear trends without any significant differences between washed and non-washed samples (Fig. 4). The short circuit photocurrent density (J_{SC}) increases systematically with the

number of prints, reaching *ca.* ~10.1 mA cm⁻² with five prints (Fig. 4a), which is slightly lower than in the drop-cast samples (*ca.* ~11.4 mA cm⁻²), as expected from their lower dye loading (Fig. 3a). The peak value of incident-photon-to-collected-electron efficiency (IPCE) and the energy conversion efficiency (η) have similar trends to J_{SC} , reaching 59% and 5.1%, respectively with the fifth print, compared to 65% and 5.5% by drop-casting (Fig. 4b and c). This shows that dye loading (light absorption) was the main performance determining factor of these cells, which is also reflected in the other *JV* characteristics: When more dye is printed on the TiO₂ film of fixed thickness, the open circuit voltage (V_{OC}) increases (Fig. 4d), because more photocurrent is generated per unit volume of the film while the recombination rate ('dark current') remains more or less constant. The same would happen if the light intensity was increased instead.³⁴ Finally, the fill factor (FF) and cell resistance (R_{CELL}) follow qualitatively what is expected based on the evolution of J_{SC} and V_{OC} according to the electrochemical device model of DSSCs:³⁴ the decrease of FF (Fig. 4e) follows the increase of J_{SC} , because the voltage losses caused by the internal cell resistances at the maximum power increase proportionally to the current density, whereas the dependence of V_{OC} on the photocurrent is weaker (logarithmic). On the other hand, the observed reduction of R_{CELL} (Fig. 4f) with the increasing number of prints is expected based on the concomitant increase in V_{OC} (Fig. 4d), because the recombination resistance of the photoelectrode, which is the main contributor to R_{CELL} at the open circuit, is a decreasing function of voltage.³⁴

Short circuit current densities measured from the individual segments of the gradient and two-color DSSCs show a synergic operation that is expected from their electrical parallel connection in the cell: the lower J_{SC} of the more transparent segments are compensated by the higher J_{SC} from the darker segments, so that their average is close to the value measured for the solar cell as a whole (Fig. 5). Note that the J_{SC} values of the five-time printed red segments in both cells are lower than in the small DSSCs (Fig. 4a), although their optical absorption is similar (Fig. 2d–f). This is at least partly due to the difficulty of establishing comparable measurement conditions when most of the active area in the large cells has to be masked when the individual segments are measured. It also creates a situation where the results correspond to the parallel connection of illuminated and dark segments, making detailed *JV* analysis not feasible.

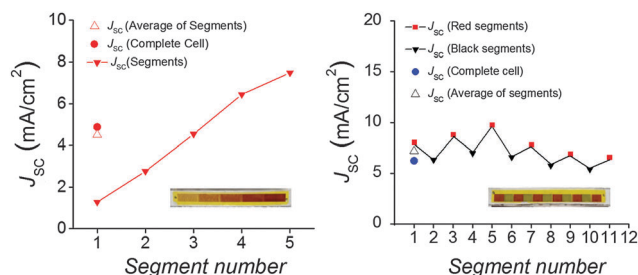


Fig. 5 J_{SC} characteristics of the gradient and two-color DSSCs.



2.2. Verification of high performance and stability of the inkjet-dyed DSSCs

Keeping all the above advantages and capabilities of dye-sensitization by inkjet printing in mind, it was confirmed that it is also entirely applicable for the preparation of traditional, non-transparent, high-efficiency DSSC designs. For this purpose, photoelectrodes consisting of an $\sim 12\ \mu\text{m}$ thick mesoporous TiO_2 layer and a $4\text{--}6\ \mu\text{m}$ thick light scattering TiO_2 layer ($0.8 \times 0.5\ \text{cm}^2$ PE area) were sensitized by dispensing $5 \pm 1\ \mu\text{L}$ volume through 5 prints, which exhibited very minor impressions of the excess dye over the TiO_2 scattering layer, and were not rinsed further with the solvent.

The complete DSSCs were fabricated with these dye-printed photoelectrodes by employing a sulfolane – ionic liquid electrolyte (coded as Z988)⁶ as the redox mediator along with platinum (Pt) counter electrodes, and their initial and long term stability performance was compared with the reference DSSCs, which were fabricated by drop casting the known volumes ($70\text{--}80\ \mu\text{L}$ with $20\text{--}25$ minute settling) of concentrated ($10\ \text{mM}$ in DMF) solution of the C101 dye over the similar PEs, followed by washing with DMF, using current-voltage (JV) analysis, electrochemical impedance spectroscopy (EIS) and incident photon to collected electron (IPCE) measurements.

Statistical analysis of the average initial performance of seven dye-printed DSSCs (efficiency $6.4 \pm 0.3\%$) and five reference DSSCs ($6.2 \pm 0.4\%$) showed no statistically significant difference between the two groups for any of the JV or EIS parameters (Tables S1 and S4 in the ESI[†], respectively). Most importantly, the two types of DSSCs showed almost equal short circuit current densities ($14.0 \pm 0.2\ \text{mA cm}^{-2}$ for printed dye and $13.8 \pm 0.3\ \text{mA cm}^{-2}$ for reference DSSCs), which confirms the successful sensitization process through inkjet printing.

The best performing devices among printed dye based DSSCs (five cells) and reference DSSCs (three cells) were then monitored through an accelerated ageing test at $35\ ^\circ\text{C}$ along with 1 Sun illumination over a period of 1000 hours (see the Experimental section and ESI[†] for further details). Fig. 6a–e shows the ageing trends of the photovoltaic parameters that were collected from periodic measurements during the 1000 h test, and the initial and aged JV and IPCE curves of the best DSSCs of each type are shown in Fig. 7 and 8, respectively. The results reveal highly stable performance retained at almost 100% of the initial conversion efficiency ($\eta = 6.4 \pm 0.2\%$) and short circuit current density ($J_{\text{SC}} = 14.2 \pm 0.6\ \text{mA cm}^{-2}$) values, with no statistically significant ageing of any of the JV parameters of each cell type, according to a paired Student's t -test at 95% confidence (see ESI[†]). This was also confirmed using periodic electrochemical impedance spectroscopy measurements performed throughout the ageing test, which revealed high stability with no statistically significant changes in any of the internal resistance components of the DSSC (Fig. 9a and b, see the ESI[†] for detailed results). The only statistically significant difference observed was a 5% lower V_{OC} in the printed cells compared to the reference cells at the end of the aging period (1000 h, ESI[†], Table S2), and the corresponding 14% lower recombination resistance in the printed cells, as measured by

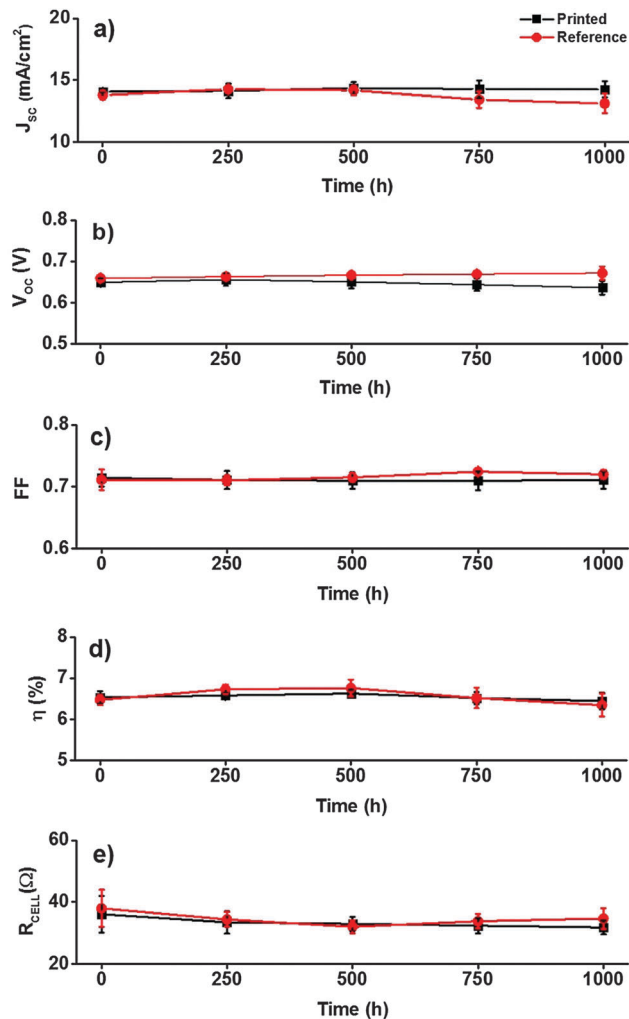


Fig. 6 (a–e) Photovoltaic parameters of fabricated devices of each type of DSSC obtained using periodical measurements during an accelerated ageing test (at $35\ ^\circ\text{C}$ under 1 Sun illumination) for a period of 1000 hours. The points are average values of five printed and three reference (drop-cast) cells, and the error bars represent standard deviation.

EIS at V_{OC} (Table S5, ESI[†]). This points to a small difference in the aging behavior of the TiO_2 /dye/electrolyte interface, which however, due to a compensating evolution of J_{SC} (Fig. 6d), resulted in no difference in the overall efficiency (Fig. 6d). Very small impressions of the excess dye that had remained over the scattering TiO_2 layer after the dye printing step, slowly dissolved into the electrolyte during the accelerated ageing test, which however caused no effects on the overall cell performance.

Encouraged by the first promising long term stability test, the same dye printed DSSCs (five cells) were further subjected to an additional accelerated test that was conducted under half Sun illumination at higher temperature ($60\ ^\circ\text{C}$) for 1154 more hours (to test if a higher temperature could affect the performance). Again, the solar cells exhibited stable performance retaining almost 100% of the initial conversion efficiency (Fig. 10a–d). Hence these two ageing tests certify the potential of inkjet printing as a new sensitization process for DSSCs which is expected to be developed further after these results.



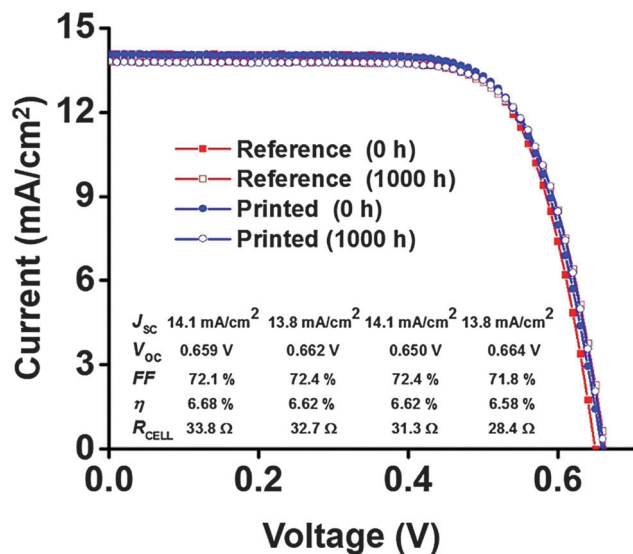


Fig. 7 Initial and aged (at 35 °C under 1 Sun illumination) JV curves of the best DSSCs of each type used in this study.

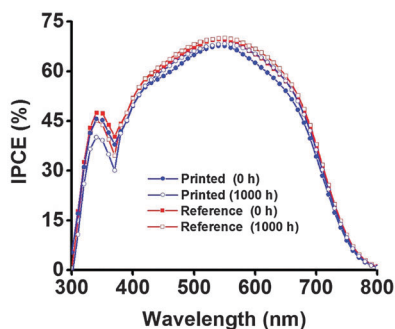


Fig. 8 Initial and aged (at 35 °C under 1 Sun illumination) IPCE spectra of the best DSSCs of each type used in this study.

In addition to the main capabilities of inkjet printing the dye discussed earlier, namely, the controlled dispensing and patterning of the dye, several other possible advantages can be mentioned. For instance, the highly pure dye solution can be

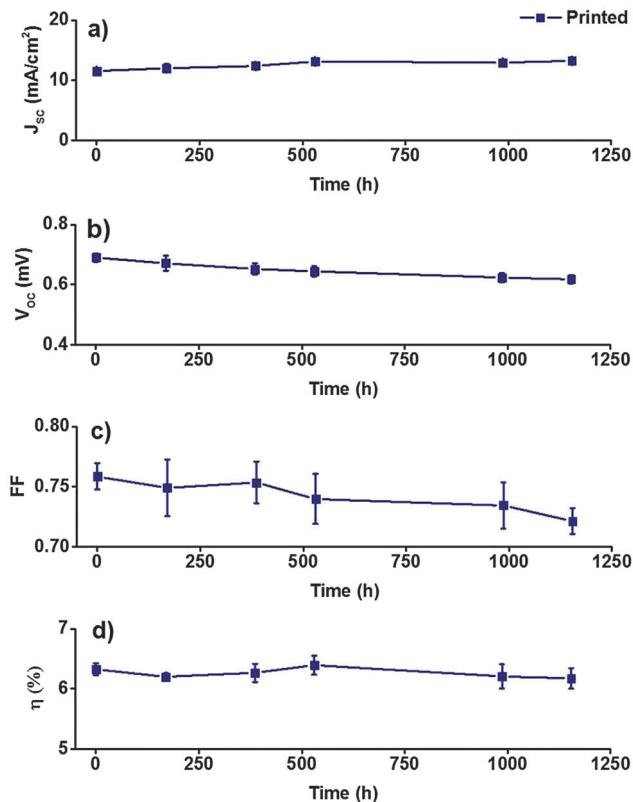


Fig. 10 (a–d) Average photovoltaic parameters of five printed DSSCs along with their standard deviations obtained by periodical measurements during an accelerated ageing test (at 60 °C and half Sun illumination) for 1184 hours.

contained in the printer cartridge until dispensed on the active layer, which protects it from contamination or degradation. Since the dye is printed only on the active layer, additional cleaning steps to remove the dye from the non-active area around it, before the application of the thermoplastic sealants, are not necessary. For the same reason, inkjet printing may also be potentially beneficial for plastic photoelectrodes, because it provides an opportunity to minimize the contact and interaction

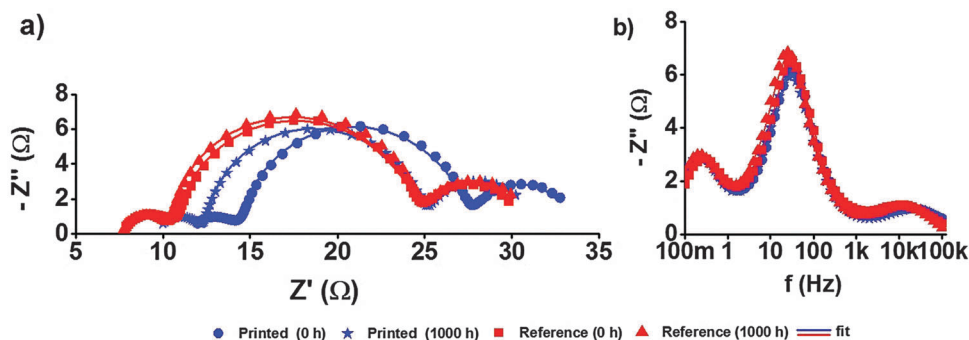


Fig. 9 Typical fresh and aged EIS spectra of complete DSSCs of the best devices of each type used in this study with a Pt counter electrode (a) Nyquist plots, (b) imaginary impedance (Z'') vs. frequency. The solid lines represent the fitted data, whereas the points represent the measured data. The shift of the Nyquist plot along the real axis in the case of printed dye DSSCs was due to a gradual decrease in the contact (series) resistance of the silver paint during the ageing test.



of possibly harsh solvents with plastic substrates, such as the commonly used indium doped tin oxide coated polyethylene terephthalate (ITO-PET) and polyethylene naphthalate (ITO-PEN) sheets. For example, ITO-PET might swell when exposed to certain solvents such as acetonitrile for long time periods required in the traditional dye bath soaking process. Hence, we also aim to apply and investigate this technique on flexible PEs in future. Again, unlike in the dye circulation process used for sensitizing the hermetically pre-sealed modules, in inkjet printing the dye solution never comes in contact with the Pt catalyst, which may help keep it clean of adsorbed dye molecules that could lower its catalytically active surface area. Moreover, the inkjet printing of dyes can also be potentially utilized for more accurate and controlled co-sensitization of TiO₂ layers by multiple dyes, by printing them at optimized amounts over the same electrode area, instead of controlling only the soaking time, which is the traditional approach.

3. Conclusion

In conclusion, the TiO₂ photoelectrodes of dye-sensitized solar cells (DSSCs) can be effectively stained by inkjet printing concentrated dye solutions on them. The unique feature of inkjet printing is that it allows accurate control of dye loading with respect to both the amount and position on the TiO₂ film. This offers several advantages over the conventional dye application methods. First, close to full coloration can be achieved without rinsing off any excess dye, which simplifies the DSSC fabrication process and reduces material consumption. Second, the color density of the films can be tuned without changing their thickness, which offers a new degree of freedom in the design of semi-transparent DSSCs, for example, for building integrated photovoltaics. Third, the high spatial resolution of inkjet printing makes it possible to create color density gradients and patterns of multiple dyes on the same photoelectrode, which suggests a new avenue for creating multi-colored DSSC designs attractive, for example, for stylish product integration of DSSCs. The inkjet printing of dyes is applicable with or without a light scattering TiO₂ layer, and yields stable devices with performance equal to those prepared using the manual drop casting sensitization process. Since inkjet printing is one of the most well-known, established and scalable techniques for manufacturing printed electronics, this new dye-sensitization process could be readily adopted in the industrial settings, possibly even in the high throughput roll-to-roll production of flexible DSSC devices. Combined with our previously reported inkjet printing of electrolytes,³⁶ the results presented here show a path towards fully inkjet-printed DSSCs.

4. Experimental

Materials

Chloroplatinic acid hydrate (H₂PtCl₄·6H₂O, purity 99.9%), guanidine thiocyanate (GuSCN, purity >99%), 1-methylbenzimidazole (NMBI, purity 99%), all the solvents (sulfolane 99% purity, 2-propanol 99.5% anhydrous, acetonitrile 99.8%

anhydrous, *N,N*-dimethylformamide (DMF) 99.8% purity) and the titanium(IV) chloride tetrahydrofuran complex were obtained from Sigma Aldrich. 1,3-Dimethylimidazolium iodide (DMII), 1-methyl-3-propylimidazolium (PMII >98% purity), 1-ethyl-3-methylimidazolium iodide (EMII >98% purity) and 1-ethyl-1-3-methylimidazolium tetracyanoborate (EMITCB) were purchased from Merck. TiO₂ nanocrystalline paste (18-NRT, 20 nm) and TiO₂ scattering paste (WER 2-0, 400 nm) were purchased from Dyesol. Dye C101 and electrolyte Z988 were produced as reported earlier.^{6,32,35} Dyes N749 and SQ2 were obtained from Solaronix, whereas dye Z907 was purchased from Dyesol. Solvent dimethyl sulfoxide (DMSO, ultra-pure grade) was purchased from Amresco.

TiO₂ photoelectrodes (PE)

The photoelectrodes for this experiment were prepared as follows. Fluorine doped tin oxide (FTO) coated NSG-Glass substrates (area = 1.6 cm × 2.0 cm and sheet resistance 10 Ω sq⁻¹) were first washed and sonicated with a detergent (10 minutes). The substrates were further washed and sonicated with acetone and ethanol solvents (5 minutes each) and were dried with compressed air. These substrates were then placed and cleaned (15 minutes) in a UV-O₃ cleaner (Bioforce Nanosciences USA). After cleaning in a UV-O₃ chamber, the substrates were immersed in 40 mM TiCl₄ solution and heated (30 minutes) in a preheated programmable oven and were sequentially rinsed with deionized water (DIW) and ethanol and were again dried with compressed air. The TiO₂ layers (12 μm of nanocrystalline TiO₂ particles, 20 nm and 4 μm thick layer of scattering particles, 400 nm) were sequentially screen printed and sintered at 450 °C for 30 minutes in the programmable oven and were cooled down to room temperature. Then, the photoelectrodes were re-heated in the 40 mM TiCl₄ aqueous solution and were washed again with DIW and ethanol and were dried with compressed air. Then, the photoelectrodes were again sintered at 450 °C in the programmable oven and were cooled down before the dye sensitization step. Note that the photoelectrodes for the dye desorption test (Fig. 3a and b) and for the dataset of DSSCs presented in Fig. 4(a-f) were not subjected to any TiCl₄ treatment and were not having any scattering layers, but only the semi-transparent TiO₂ layer (thickness 7 μm).

Dye solution formulations for inkjet printing

In the case of red C101 and black N749 (Fig. 1a and 2–10) the dye solution was 10 mM in DMF. In the case of blue SQ2 and red Z907 dyes (Fig. 1b and c), stock solutions were prepared (for individual dye) by dissolving 45 mg of dyes (SQ2 or Z907) in 3 mL of solvent dimethyl sulfoxide (DMSO). Both DMF and DMSO were found to be suitable solvents for inkjet printing these dyes.

Details of inkjet printing of dyes

Dye printing was achieved using an automated inkjet printer (Fuji Film's Dimatix Material Printer, Model DMP-2800 Series, see Fig. S4 in the ESI[†]) by filling the concentrated dye solutions



(dye C101 and N749) into its polymer cartridge. Additionally, the cartridge is equipped with a so-called 'print head' which consists of 16 micro-channels (orifices) through which the solution was dispensed. In order to get good printing results, the dye solution was passed through a 0.2 μm filter as recommended in the operating instructions of the printer. The TiO_2 layers (actual area = $0.8 \times 0.5 \text{ cm}^2$) without the scattering layer were sensitized with both dye solutions at 10 mM concentration using a 30 μm drop spacing leading 0.45 μL solution and 4.5 nmol of dye deposition per cycle. See Fig. 2 caption for more details. The cells which underwent the ageing study were assembled employing a scattering layer on nanocrystalline TiO_2 and they were processed with a 20 μm drop spacing corresponding to 1 μL solution and 16 nmol of dye per print from 16 mM solution. The printing process took around 3 and 2 minutes for 20 μm and 30 μm drop spacing respectively.

Photoelectrode sensitization for reference DSSCs

The TiO_2 layers of the photoelectrodes for the reference DSSCs were sensitized using a similar procedure as reported earlier for quick sensitization of dye C101.³³ In brief, the TiO_2 layers were completely covered by spreading the dye solution of known volumes (70 μL) with similar concentrations (10–16 mM of dye C101 dye in DMF) as used in the inkjet printing of the dye and were left for 20 minutes in a sealed plastic box. After that each photoelectrode was washed with DMF to remove the excess dye and was dried with compressed air before the cell assembly.

Counter electrodes (CE)

A drop (4 μL) of 10 mM chloroplatinic acid hydrate ($\text{H}_2\text{PtCl}_4 \cdot 6\text{H}_2\text{O}$) solution (in 2 propanol) was cast over pre-cleaned FTO coated glass substrates (TEC 7) and was fired at 410 $^\circ\text{C}$ for 20 minutes. After that all the electrodes were cooled down to room temperature and were placed in a tightly sealed plastic box prior to the final cell assembly.

Electrolyte composition

The ionic liquid electrolyte coded as Z988 with the following composition was used for this study: DMII/EMII/EMITCB/I₂/NMBI/GuSCN (molar ratio 12 : 12 : 16 : 1.67 : 3.33 : 0.67) mixed and diluted with 50% of sulfolane (v/v).

Cell assembly

The cell channel was defined by separating PE and CE through a thick (25 μm) Surllyn frame foil. The ionic liquid electrolyte was introduced into the cell channel through the drilled holes at the CE side. The cells were then sealed with 25 μm thick Surllyn foil and a thin glass cover. At last, the contacts were fabricated by applying the copper tape and quick drying silver paste at the non-active area of the electrodes.

Measurements

The *JV* curves of the DSSCs were recorded in a xenon lamp based solar simulator (Pecell Technologies, Japan, Model PEC-L01) under 1000 W m^{-2} light intensity calibrated to equivalent 1 Sun conditions using a reference solar cell (PV Measurements Inc.),

by using a black tape mask (aperture area 0.17 cm^2). The electrochemical impedance spectra were recorded from 100 mHz to 100 kHz under open circuit conditions at 1000 W m^{-2} light intensity on a Zahner-Elektrik IM6 electrochemical workstation, and analyzed using Zview2 software (Scribner Associates Inc.) using the well-known equivalent circuit model of DSSCs.³⁴ The incident photon to collected electron efficiency (IPCE) and transmittance spectra were measured using a QEX7 spectral response measurement unit (PV Measurements Inc.) at near normal incidence without bias light. The first stability test of the solar cells was performed by keeping them for 1000 hours under open circuit conditions at 35 $^\circ\text{C}$ in a self-made solar simulator under 1 Sun light intensity provided through halogen lamps (Philips 13117) and a UV filter (Asmetec GmbH, 400 nm cut-off), while recording their *JV* curves periodically in the above-mentioned separate solar simulator (Pecell Technologies, Japan). The second stability test was executed in the Suntest CPS Plus system at 60 $^\circ\text{C}$ under half Sun light illumination and similar periodic measurements as mentioned above were performed to record the *JV* curves in the solar simulator. The dye loading (mol cm^{-2}) in complete solar cells was determined based on two transmittance measurements from each cell: one taken through the photoelectrode and one through the electrolyte filled edge region next to it. The dye loading in freshly sensitized TiO_2 films was determined by desorbing the dye in a mixed solution of TMAOH and DMF (50/50 by volume). The decadic molar attenuation coefficient of C101 dye ($17.5 \times 10^3 \text{ M}^{-1} \text{ cm}^{-1}$) used in the calculations was taken from ref. 33. The details of both methods are given in the ESI.†

Acknowledgements

G. H. gratefully acknowledges the Academy of Finland for the post-doctoral research fellowship (Grant number: 287641). J. H. acknowledges the financial support from the Technology Industries of Finland Centennial Foundation (NIR-DSC project). M. G. acknowledges financial support from Swiss National Science Foundation and CTI 17622.1 PFMN-NM, glass2energy SA (g2e), Villaz-St-Pierre, Switzerland. This work was also supported by the SELECT + (Environmental pathways for sustainable energy services). Bioeconomy infrastructure is also acknowledged for the use of the equipment.

References

- 1 G. Hashmi, K. Miettunen, T. Peltola, J. Halme, I. Asghar, K. Aitola, M. Toivola and P. Lund, *Renewable Sustainable Energy Rev.*, 2011, **15**, 3717–3732.
- 2 A. Feltrin and A. Freundlich, *Ren. Energy*, 2006, **33**, 180–185.
- 3 C. S. Tao, J. Jiang and M. Tao, *Sol. Energy Mater. Sol. Cells*, 2011, **95**, 3176–3180.
- 4 A. Hinsch, W. Veurman, H. Brandt, K. Flarup Jensen and S. Mastroianni, *ChemPhysChem*, 2014, **15**, 1076–1087.
- 5 K. Zhang, C. Qin, X. Yang, A. Islam, S. Zhang, H. Chen and L. Han, *Adv. Energy Mater.*, 2014, **4**, 1301966.



- 6 M. Marszalek, F. D. Arendse, J. D. Decoppet, S. S. Babkair, A. A. Ansari, S. S. Habib, M. Wang, S. M. Zakeeruddin and M. Grätzel, *Adv. Energy Mater.*, 2014, **4**, 1301235.
- 7 Z. L. Wang and W. Wu, *Angew. Chem.*, 2012, **51**, 2–24.
- 8 F. De Rossi, T. Pontecorvo and T. M. Brown, *Appl. Energy*, 2015, **156**, 413–422.
- 9 S. Vignati, MSc thesis, Comm. Syst. Dept., KTH, 2012.
- 10 S. Ito, T. N. Murakami, N. Takuro, P. Comte, P. Liska, C. Graetzel, M. K. Nazeeruddin and M. Graetzel, *Thin Solid Films*, 2008, **516**, 4613–4619.
- 11 M. K. Nazeeruddin, A. Kay, I. Rodicio, R. Humphry-Baker, E. Mueller, P. Liska, N. Vlachopoulos and M. Graetzel, *J. Am. Chem. Soc.*, 1993, **115**, 6382–6390.
- 12 M. Hösel, H. F. Dam and F. C. Krebs, *Energy Technol.*, 2015, **3**, 293–304.
- 13 J. E. Carle, M. Helgesen, M. V. Madsen, E. Bundgaard and F. C. Krebs, *J. Mater. Chem. C*, 2014, **2**, 1290–1297.
- 14 D. Angmo, S. A. Gevorgyan, T. T. L. Olsen, R. R. Søndergaard, M. Hösel, M. Jørgensen, R. Gupta, G. U. Kulkarni and F. C. Krebs, *Org. Electron.*, 2013, **14**, 984–994.
- 15 J. S. Yu, I. Kim, J. S. Kim, J. Jo, T. T. L. Olsen, R. R. Søndergaard, M. Hösel, D. Angmo, M. Jørgensen and F. C. Krebs, *Nanoscale*, 2012, **4**, 6032–6040.
- 16 J. Adams, G. D. Spyropoulos, M. Salvador, N. Li, S. Strohm, L. Lucera, S. Langner, F. Machui, H. Zhang, T. Ameri, M. M. Voigt, F. C. Krebs and C. J. Brabec, *Energy Environ. Sci.*, 2015, **8**, 169–176.
- 17 K. Liu, T. T. Larsen-Olsen, Y. Lin, M. Beliatas, E. Bundgaard, M. Jørgensen, F. C. Krebs and X. Zhan, *J. Mater. Chem. A*, 2016, **4**, 1044–1051.
- 18 M. K. Nazeeruddin, R. Splivallo, P. Liska, P. Comte and M. Grätzel, *Chem. Commun.*, 2003, 1456–1457.
- 19 I. Concina, E. Frison, A. Braga, S. Silvestrini, M. Maggini, G. Sberveglieri, A. Vomiero and T. Carofiglio, *Chem. Commun.*, 2011, **47**, 11656–11658.
- 20 P. J. Holliman, M. L. Davies, A. Connell, B. V. Velasco and T. M. Watson, *Chem. Commun.*, 2010, **46**, 7256–7258.
- 21 M. Späth, P. M. Sommeling, J. A. M. van Roosmalen, H. J. P. Smit, N. P. G. van der Burg, D. R. Mahieu, N. J. Bakker and J. M. Kroon, *Prog. Photovoltaics*, 2003, **11**, 207–220.
- 22 R. Sastrawan, J. Beier, U. Belledin, S. Hemming, A. Hirsch, R. Kern, C. Vetter, F. M. Petrat, A. P. Schwab, P. Lechner and W. Hoffmann, *Sol. Energy Mater. Sol. Cells*, 2006, **90**, 1680–1691.
- 23 Y. Seo and J. H. Kim, *J. Ind. Eng. Chem.*, 2013, **19**, 488–492.
- 24 H. Seo, M. K. Son, I. Shin, J. K. Kim, K. J. Lee, K. Prabakar and H. J. Kim, *Electrochim. Acta*, 2010, **55**, 4120–4123.
- 25 H. G. Han, H. C. Weerasinghe, K. M. Kim, J. S. Kim, Y. B. Cheng, D. J. Jones, A. B. Holmes and T. H. Kwon, *Sci. Rep.*, 2015, **5**, 14645.
- 26 B. Kim, S. W. Park, J. Y. Kim, K. Yoo, J. Ah Lee, M. W. Lee, D. K. Lee, J. Y. Kim, B. S. Kim, H. Kim, S. Han, H. J. Son and M. J. Ko, *ACS Appl. Mater. Interfaces*, 2013, **5**, 5201–5207.
- 27 R. Sastrawan, J. Beier, U. Belledin, S. Hemming, A. Hirsch, R. Kern, C. Vetter, F. M. Petrat, A. P. Schwab, P. Lechner and W. Hoffmann, *Prog. Photovoltaics*, 2006, **14**, 697–709.
- 28 S. G. Hashmi, T. Moehl, J. Halme, Y. Ma, T. Saukkonen, A. Yella, F. Giordano, J. D. Decoppet, S. M. Zakeeruddin, P. Lund and M. Grätzel, *J. Mater. Chem. A*, 2014, **2**, 19609–19615.
- 29 S. C. Yeh, P. H. Lee, H. Y. Liao, Y. Y. Chen, C. T. Chen, R. J. Jeng and J. J. Shuye, *ACS Sustainable Chem. Eng.*, 2015, **3**, 71–81.
- 30 Fig. 1e is reprinted from, H. Arakawa, T. Yamaguchi, T. Sutou, Y. Koishi, N. Tobe, D. Matsumoto and T. Nagai, Efficient dye-sensitized solar cell sub-modules, *Curr. Appl. Phys.*, 2010, **10**(2), S157–S160, with permission from Elsevier.
- 31 Fig. 1f is reprinted from, H. Pettersson, T. Gruszecki, C. Schnetz, M. Streit, Y. Xu, L. Sun, M. Gorlov, L. Kloo, G. Boschloo, L. Haggman and A. Hagfeldt, Parallel-connected monolithic dye-sensitized solar modules, *Prog. Photovoltaics*, 2010, **18**, 340–345, with permission from John Wiley and Sons.
- 32 F. Gao, Y. Wang, D. Shi, J. Zhang, M. Wang, X. Jing, R. H. Baker, P. Wang, S. M. Zakeeruddin and M. Grätzel, *J. Am. Chem. Soc.*, 2008, **130**, 10720–10728.
- 33 M. Wang, S. Plogmaker, R. H. Baker, P. Pechy, H. Rensmo, S. M. Zakeeruddin and M. Grätzel, *ChemSusChem*, 2012, **5**, 181–187.
- 34 J. Halme, P. Vahermaa, K. Miettunen and P. Lund, *Adv. Mater.*, 2010, **22**, E210–E234.
- 35 J. D. Decoppet, T. Moehl, S. S. Babkair, R. A. Alzubaydi, A. A. Ansari, S. S. Habib, S. M. Zakeeruddin, H. W. Schmidt and M. Grätzel, *J. Mater. Chem. A*, 2014, **2**, 15972–15977.
- 36 S. G. Hashmi, M. Ozkan, J. Halme, K. Dimic-Misic, S. M. Zakeeruddin, J. Paltakari, M. Grätzel and P. D. Lund, *Nano Energy*, 2015, **17**, 206–215.



Electronic Supplementary Information

Dye-sensitized solar cells with inkjet-printed dyes

Syed Ghufran Hashmi ^a, Merve Özkan ^b, Janne Halme* ^a, Shaik Mohammad Zakeeruddin ^c,
Jouni Paltakari ^b, Michael Grätzel ^c, Peter. D. Lund ^a

Estimation of the dye loading from the transmittance of complete DSSC

The *absorptance* of the dyed TiO₂ photoelectrode film in a complete DSSC was approximated as

$$A_{\text{PE}} = 1 - T_{\text{PE}} = 1 - f \frac{T_{\text{cell,PE}}}{T_{\text{cell,EL}}} \quad (\text{SE1})$$

where $T_{\text{cell,PE}} = T_{\text{PE-sub}} T_{\text{PE}} T_{\text{EL}} T_{\text{Pt}} T_{\text{CE-sub}}$ and $T_{\text{cell,EL}} = T_{\text{PE-sub}} T_{\text{EL}} T_{\text{Pt}} T_{\text{CE-sub}}$ are respectively the transmittance measured through the photoelectrode and the electrolyte edge region next to it (**Figures S1 and S2 a-c**), each modeled as the product of the transmittances of the cell components through which the light beam goes in each measurement (“PE” stands for photoelectrode, “sub” for substrate, “EL” for electrolyte, “Pt” for the Pt catalyst layer, and “CE” for counter electrode). See ¹ for a similar optical model.

Note that, because in equation SE1 $T_{\text{cell,PE}}$ is divided with the ‘background’ measurement $T_{\text{cell,EL}}$ taken from the same sample, the division not only factors out the transmittance of the electrolyte (T_{EL}), substrate ($T_{\text{PE-sub}}$, $T_{\text{CE-sub}}$) and platinum (T_{Pt}), but also compensates for the sample-to-sample variations in them. In addition to this, the correction factor f , defined as

$$f = \frac{T_{\text{cell,EL}}(\lambda = 800 \text{ nm})}{T_{\text{cell,PE}}(\lambda = 800 \text{ nm})} \quad (\text{SE2})$$

is used to compensate for spatial variations in the amount of Pt (T_{Pt}) and presence of air bubbles and other possible imperfections in the Surlyn sealing at the CE side ($T_{\text{CE-sub}}$), by normalizing the absorbance to zero at 800 nm (900 nm in the case of the black dye) where the absorptance by the dye is known to be non-existent.

Equation (1) neglects reflectance at the material layer interfaces, which are low due to relatively good refractive index matching, as well as the reflectance of the photoelectrode layer, which is negligible near the absorption maximum at 535 nm, where the already low back scattering of light

¹ J. Halme, P. Vahermaa, K. Miettunen, P. Lund, *Adv. Mater.*, 2010, **22**, E210–E234.

form the film (due to absence of scattering particles) is further attenuated by the intense light absorption².

The photoelectrode absorptance spectra obtained this way are shown in **Figure S2 d-f**. Example spectra were selected from it to the Figure 3 of the paper.

The *dye loading* (mol cm⁻²) in photoelectrode film was calculated as

$$n_{\text{dye}} = \frac{Abs_{\text{PE}}(\lambda = 535 \text{ nm})}{\varepsilon_{\text{dye}}(\lambda = 535 \text{ nm})} \quad (\text{SE3})$$

where ε_{dye} is the molar attenuation coefficient of the dye ($\varepsilon_{\text{dye}} = 1.75 \times 10^3 \text{ m}^2 \text{ mol}^{-1} = 17.5 \times 10^3 \text{ M}^{-1} \text{ cm}^{-1}$, taken from ³, and assumed to correspond to decadic attenuation, at the absorption maximum of the dye at 535 nm, and Abs_{PE} is the decadic *absorbance* (**Figure S2 g-i**) of the photoelectrode calculated from the *absorptance* of equation SE1 as

$$Abs_{\text{PE}} = -\log_{10}(T_{\text{PE}}) = -\log_{10}(1 - A_{\text{PE}}) \quad (\text{SE4})$$

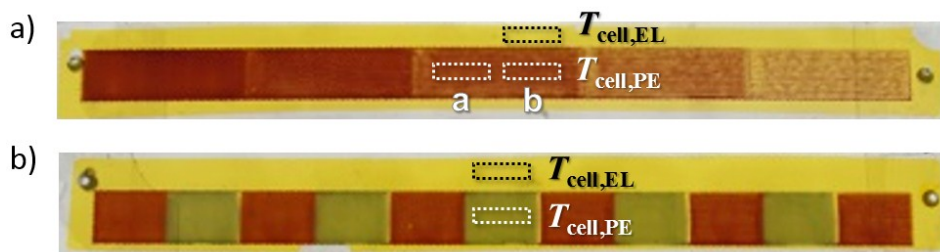


Figure S1. Photographs of the gradient (a) and two-color (b) DSSCs showing approximate positions and size of the light beam when measuring the transmittance through the center of each photoelectrode segment ($T_{\text{cell,PE}}$) and the free electrolyte region next to it ($T_{\text{cell,EL}}$). Two photoelectrode measurement (“a” and “b”) were taken from each segment of the gradient DSSC and one from the two-color DSSC.

² J. Halme, G. Boschloo, A. Hagfeldt, P. Lund, *J. Physic. Chem. C.*, 2008, **112**, 5623-5637.

³ M. Wang, S. Plogmaker, R. H. Baker, P. Pechy, H. Rensmo, S. M. Zakeeruddin, M. Gratzel, *Chem Sus Chem.*, 2012, **5**, 181 – 187.

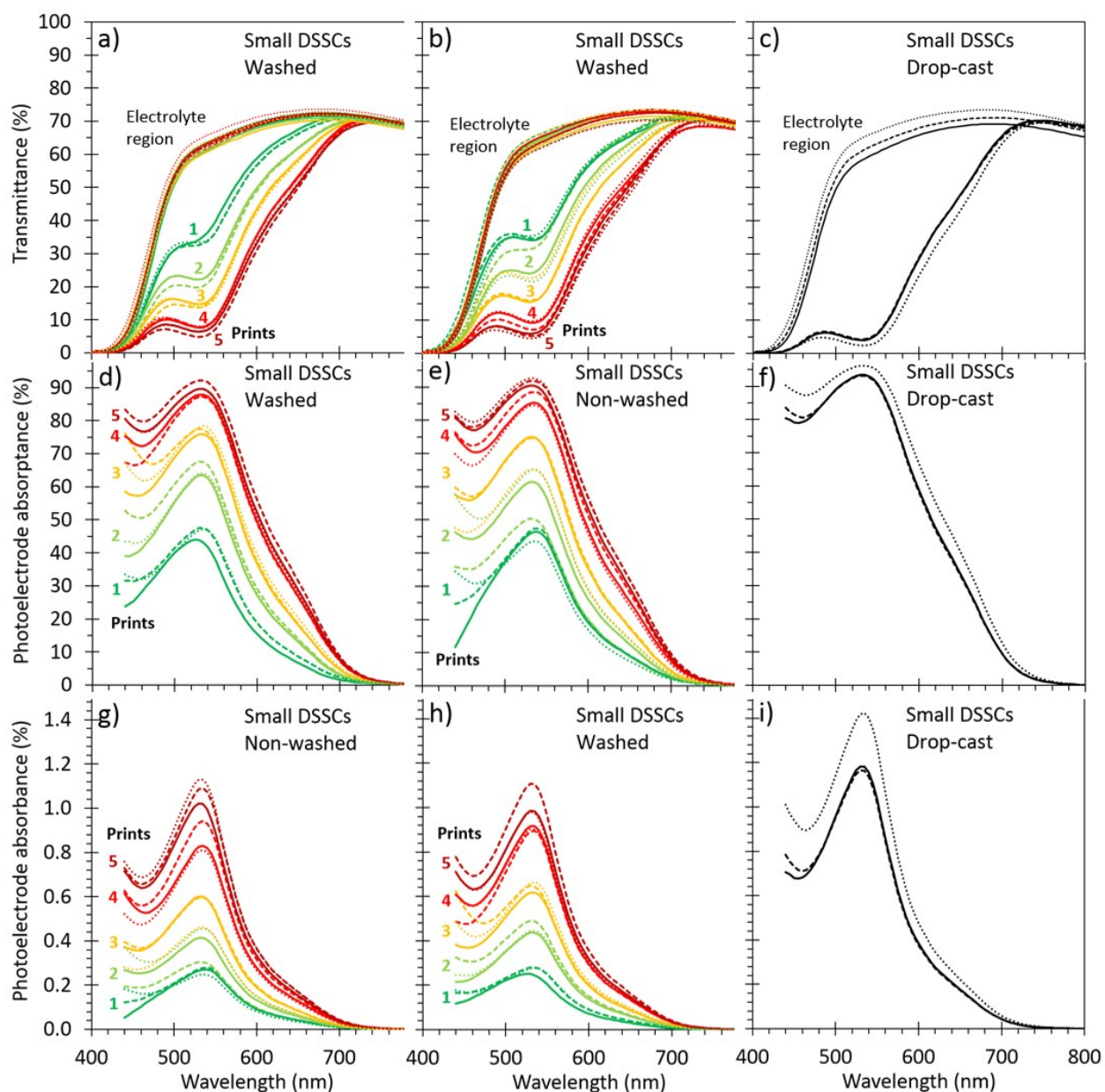


Figure S2. (a – c) Measured UV-VIS transmittance spectra ($T_{\text{cell,PE}}$ and $T_{\text{cell,EL}}$) of the small complete DSSCs, and calculated photoelectrode absorbance (d – f, equation SE1) and absorbance (g – i, equation SE4) spectra of their 7 μm thick TiO_2 photoelectrodes dyed with inkjet printing (C101 dye) with (a, d, g) or without (b, e, h) washing with DMF after printing, and the same for reference cells dyed by drop-casting the same dye solution in identical TiO_2 films (c, f, i). The absorbance data in figures (g – i) were used for calculating, with equation SE3, the dye loading shown in Figure 4 of the paper.

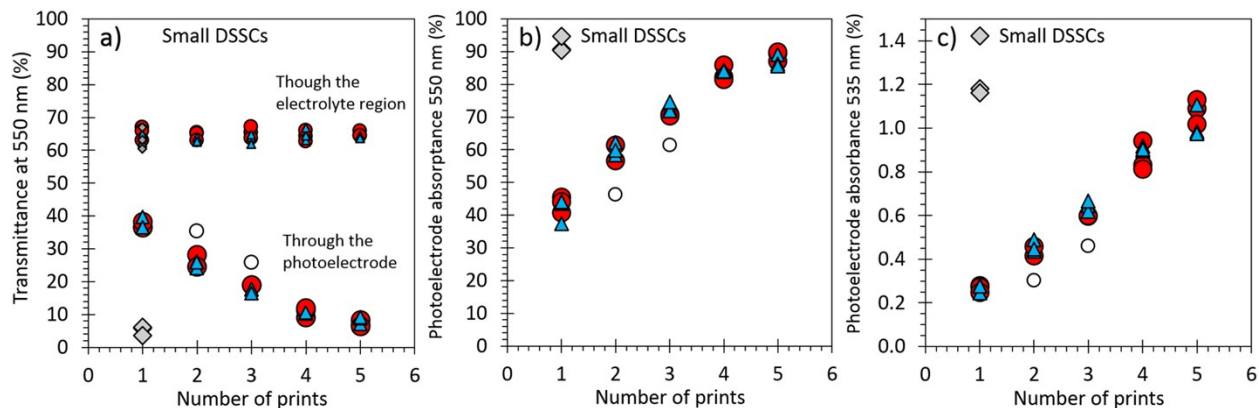


Figure S3. a) Device *transmittance* and b) photoelectrode *absorbance* values of the small semi-transparent DSSCs at 550 nm wavelength (used as a reference for visible transparency), and c) the corresponding photoelectrode *absorbance* at 535 nm peak absorption wavelength (used for calculating the dye loading with equation SE3), corresponding to the spectra shown in Figures S2a, d, and g. Figures a and b also show the overall small sample-to-sample variation (three samples of each type) in the data, not discernible from selected spectra shown in the Figures 3a and d in the paper.



Figure S4. The inkjet-printer used in this study. a) Fuji Film's Dimatix Material Printer, Model DMP-2800, and b) printer cartridge filled with dye C101 solution.

Estimation of the dye loading with dye desorption from the TiO₂ films

The *absorbance of the dye desorption* solutions was calculated by subtracting the background level $Abs_{sol,meas,bg}$ from the measured absorbance $Abs_{sol,meas}$

$$Abs_{sol} = Abs_{sol,meas} - Abs_{sol,meas,bg} \quad (SE5)$$

The background level $Abs_{sol,meas,bg}$ was determined separately for each absorbance spectrum as the average absorbance between 780 nm and 860 nm, where the dye is known to have negligible absorption. This corresponds to the similar correction made for solar cell transmittance data in equation (SE1). The resulting absorbance spectra are shown in **Figure S5**.

The dye loading (mol cm⁻²) in the photoelectrode film (Figure 4c in the paper) was calculated as

$$n_{dye} = \frac{Abs_{sol}(\lambda = 535 \text{ nm}) \cdot V_{sol}}{\epsilon_{dye}(\lambda = 535 \text{ nm}) \cdot L \cdot A_{film}} \quad (SE6)$$

where V_{sol} is the volume of the desorption solution ($V_{sol} = 4$ ml), L is the optical path length of the cuvette ($L = 1$ cm), and A_{film} is the area of the photoelectrode films ($A_{film} = 0.4$ cm²).

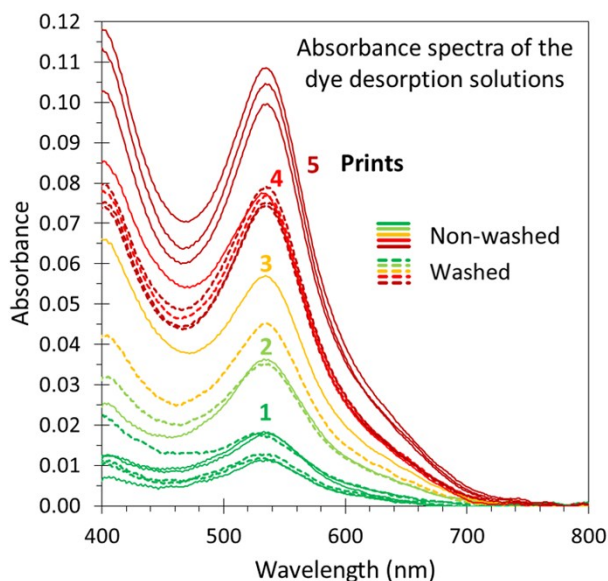


Figure S5. UV-VIS absorbance spectra of the dye desorption solutions (C101 dye), from which the dye loading shown in Figure 4c of the paper were calculated with equation SE6. The figure shows the spectra obtained after subtracting the background according to equation (SE5). The dyed TiO₂ films were 7 μm thick and had 0.4 cm² area. The dye was desorbed from them to a solution volume of 4 ml, and measured with in a cuvette with 1 cm optical path.

Statistical analysis of the IV results: initial performance

Nomenclature and details of the statistical testing are given in the end of the document.

Initial performance of all prepared cells

All cells initial		<i>N</i>				
Printed	7	J_{sc} (mA/cm ²)	V_{oc} (V)	<i>FF</i>	η (%)	R_{cell} (Ω)
P1		14.1	0.659	0.721	6.68	33.8
P2		14.2	0.637	0.723	6.52	30.4
P3		14.0	0.658	0.719	6.64	37.1
P4		14.0	0.652	0.689	6.29	45.7
P5		14.1	0.642	0.722	6.55	33.1
P6		13.7	0.653	0.677	6.05	50.3
P7		13.8	0.639	0.655	5.79	55.3
ave		14.0	0.649	0.701	6.36	40.8
std		0.2	0.009	0.027	0.33	9.6
std/ave		1.2 %	1.4 %	3.9 %	5.2 %	23.5 %
sem		0.1	0.003	0.010	0.13	3.6
95% CI		0.2	0.008	0.025	0.31	8.9
Reference	5	J_{sc} (mA/cm ²)	V_{oc} (V)	<i>FF</i>	η (%)	R_{cell} (Ω)
R1		14.1	0.650	0.724	6.62	31.8
R2		13.6	0.639	0.648	5.63	55.8
R3		13.9	0.665	0.693	6.39	43.9
R4		13.4	0.664	0.718	6.40	38.2
R5		14.0	0.652	0.645	5.87	59.3
ave		13.8	0.654	0.686	6.18	45.8
std		0.3	0.011	0.037	0.41	11.6
std/ave		2.0 %	1.7 %	5.5 %	6.7 %	25.4 %
sem		0.1	0.005	0.017	0.18	5.2
95% CI		0.3	0.013	0.046	0.51	14.5

Table 1. Comparison of two different cell types - initial performance

	<i>N</i>	J_{sc} (mA/cm ²)	V_{oc} (mV)	<i>FF</i> (%)	η (%)	R_{cell} (Ω)
Initial performance						
Printed	7	14 ± 0.2	649 ± 9	70 ± 3	6.4 ± 0.3	41 ± 10
Reference	5	13.8 ± 0.3	654 ± 11	69 ± 4	6.2 ± 0.4	46 ± 12
Difference		1.4 %	-0.8 %	2.2 %	2.8 %	-10.8 %
<i>p</i> -value		0.21	0.41	0.47	0.46	0.46

Differences in the initial performance (Table 1)

The results show no statistically significant differences ($p < 0.05$) between the two types of cells, for any of the IV parameters. The differences in the average values are also practically insignificant (< 5 %), except for the R_{cell} which shows relatively high variance between the samples.

Statistical analysis of the IV results: aging test at 1 Sun and 35 C

All but the following four samples (two in each series) were put to a 1000 h aging test.

Samples excluded from the aging test

Printed	2	J_{sc} (mA/cm ²)	V_{oc} (V)	FF	η (%)	R_{cell} (Ω)
P6		13.7	0.653	0.677	6.05	50.3
dif from ave		-2.1 %	0.7 %	-3.4 %	-4.8 %	23.3 %
P7		13.8	0.639	0.655	5.79	55.3
dif from ave		-1.1 %	-1.4 %	-6.5 %	-8.9 %	35.4 %
Reference	2	J_{sc} (mA/cm ²)	V_{oc} (V)	FF	η (%)	R_{cell} (Ω)
R2		13.6	0.639	0.648	5.63	55.8
dif from ave		-2.8 %	-1.5 %	-7.5 %	-11.4 %	36.8 %
R5		14.0	0.652	0.645	5.87	59.3
dif from ave		-0.1 %	0.5 %	-8.0 %	-7.7 %	45.3 %

Notes

Seven cells with printed dye (P1...P7) and five reference cells (R1...R5) were prepared and characterized, of which five and three highest efficiency cells were selected for the aging study, respectively. The excluded lower efficiency cells (P6, P7, R2, R5) had high R_{cell} , most likely due to bad electrical contacts, and therefore lower FF. P6 and P7 had additionally slightly lower J_{sc} than the top five cells in the same group. The excluded P6 and R5 were aged in parallel, at the same conditions, while monitoring their performance with an in-situ measurement set-up, and exhibited similar aging behaviour as the rest of the cells (data not shown). P7 and R5 were stored and not used for further measurements.

Aging test

0 Hours

Printed	5	J_{sc} (mA/cm ²)	V_{oc} (V)	FF	η (%)	R_{cell} (Ω)
P1		14.1	0.659	0.721	6.68	33.8
P2		14.2	0.637	0.723	6.52	30.4
P3		14.0	0.658	0.719	6.64	37.1
P4		14.0	0.652	0.689	6.29	45.7
P5		14.1	0.642	0.722	6.55	33.1
ave		14.1	0.650	0.715	6.53	36.0
std		0.1	0.010	0.014	0.15	5.9
std/ave		0.5 %	1.5 %	2.0 %	2.3 %	16.4 %
sem		0.0	0.004	0.006	0.07	2.6
95% CI		0.1	0.012	0.018	0.19	7.3
Reference	3	J_{sc} (mA/cm ²)	V_{oc} (V)	FF	η (%)	R_{cell} (Ω)
R1		14.1	0.650	0.724	6.62	31.8
R3		13.9	0.665	0.693	6.39	43.9
R4		13.4	0.664	0.718	6.40	38.2
ave		13.8	0.660	0.712	6.47	37.9
std		0.3	0.008	0.016	0.13	6.0
std/ave		2.5 %	1.3 %	2.3 %	2.0 %	15.9 %
sem		0.2	0.005	0.010	0.08	3.5
95% CI		0.8	0.021	0.041	0.32	15.0

250 Hours

N

Printed	5	J_{sc} (mA/cm ²)	V_{oc} (V)	<i>FF</i>	η (%)	R_{cell} (Ω)
P1		13.4	0.674	0.723	6.53	35.3
P2		14.6	0.636	0.715	6.63	28.8
P3		13.7	0.665	0.717	6.53	36.0
P4		14.8	0.648	0.685	6.56	36.7
P5		14.2	0.657	0.716	6.67	30.2
ave		14.1	0.656	0.711	6.58	33.4
std		0.6	0.015	0.015	0.06	3.6
std/ave		4.1 %	2.3 %	2.1 %	0.9 %	10.9 %
sem		0.3	0.007	0.007	0.03	1.6
95% CI		0.7	0.018	0.018	0.08	4.5
Reference	3	J_{sc} (mA/cm ²)	V_{oc} (V)	<i>FF</i>	η (%)	R_{cell} (Ω)
R1		14.4	0.662	0.719	6.86	31.8
R3		14.2	0.665	0.703	6.66	36.5
R4		14.1	0.664	0.710	6.67	34.8
ave		14.3	0.664	0.711	6.73	34.3
std		0.1	0.001	0.008	0.11	2.4
std/ave		1.0 %	0.2 %	1.1 %	1.7 %	6.9 %
sem		0.1	0.001	0.005	0.07	1.4
95% CI		0.3	0.003	0.020	0.28	5.9

500 Hours

N

Printed	5	J_{sc} (mA/cm ²)	V_{oc} (V)	<i>FF</i>	η (%)	R_{cell} (Ω)
P1		13.9	0.673	0.720	6.73	34.5
P2		14.9	0.633	0.711	6.72	30.0
P3		14.0	0.656	0.716	6.57	33.2
P4		14.9	0.638	0.687	6.51	35.6
P5		14.1	0.653	0.716	6.60	31.2
ave		14.3	0.651	0.710	6.63	32.9
std		0.5	0.016	0.013	0.10	2.3
std/ave		3.5 %	2.4 %	1.9 %	1.5 %	7.0 %
sem		0.2	0.007	0.006	0.04	1.0
95% CI		0.6	0.020	0.016	0.12	2.8
Reference	3	J_{sc} (mA/cm ²)	V_{oc} (V)	<i>FF</i>	η (%)	R_{cell} (Ω)
R1		14.4	0.666	0.723	6.94	29.6
R3		13.7	0.669	0.711	6.53	33.8
R4		14.3	0.668	0.712	6.80	32.4
ave		14.2	0.667	0.715	6.76	32.0
std		0.4	0.002	0.007	0.21	2.1
std/ave		2.6 %	0.2 %	0.9 %	3.1 %	6.6 %
sem		0.2	0.001	0.004	0.12	1.2
95% CI		0.9	0.004	0.017	0.52	5.3

750 Hours

N

Printed	5	J_{sc} (mA/cm ²)	V_{oc} (V)	<i>FF</i>	η (%)	R_{cell} (Ω)
P1		13.6	0.661	0.729	6.53	32.6
P2		15.2	0.634	0.700	6.74	30.6
P3		13.7	0.655	0.713	6.39	34.7
P4		14.8	0.623	0.691	6.37	34.5
P5		14.2	0.646	0.716	6.56	29.2
ave		14.3	0.644	0.710	6.52	32.3
std		0.7	0.015	0.015	0.15	2.4
std/ave		4.9 %	2.4 %	2.1 %	2.3 %	7.4 %
sem		0.3	0.007	0.007	0.07	1.1
95% CI		0.9	0.019	0.018	0.19	3.0
Reference	3	J_{sc} (mA/cm ²)	V_{oc} (V)	<i>FF</i>	η (%)	R_{cell} (Ω)
R1		14.2	0.661	0.725	6.80	31.0
R3		13.0	0.674	0.724	6.36	34.8
R4		13.1	0.674	0.725	6.39	35.4
ave		13.4	0.670	0.725	6.52	33.8
std		0.7	0.008	0.001	0.25	2.4
std/ave		5.0 %	1.2 %	0.1 %	3.8 %	7.0 %
sem		0.4	0.005	0.000	0.14	1.4
95% CI		1.7	0.020	0.001	0.62	5.9

1000 Hours

N

Printed	5	J_{sc} (mA/cm ²)	V_{oc} (V)	<i>FF</i>	η (%)	R_{cell} (Ω)
P1		13.8	0.662	0.724	6.62	32.7
P2		14.4	0.632	0.703	6.39	31.8
P3		13.5	0.635	0.718	6.14	34.0
P4		15.1	0.616	0.690	6.43	32.1
P5		14.4	0.637	0.720	6.63	28.1
ave		14.2	0.636	0.711	6.44	31.8
std		0.6	0.017	0.014	0.20	2.2
std/ave		4.5 %	2.6 %	2.0 %	3.1 %	7.1 %
sem		0.3	0.007	0.006	0.09	1.0
95% CI		0.8	0.021	0.018	0.25	2.8
Reference	3	J_{sc} (mA/cm ²)	V_{oc} (V)	<i>FF</i>	η (%)	R_{cell} (Ω)
R1		13.8	0.664	0.718	6.58	32.4
R3		12.2	0.691	0.715	6.04	38.4
R4		13.3	0.662	0.728	6.41	33.0
ave		13.1	0.672	0.720	6.34	34.6
std		0.8	0.016	0.007	0.28	3.3
std/ave		6.1 %	2.4 %	1.0 %	4.4 %	9.6 %
sem		0.5	0.009	0.004	0.16	1.9
95% CI		2.0	0.040	0.018	0.69	8.3

Table 2. Comparison of the two type of cells during the aging test

	<i>N</i>	<i>J</i> _{sc} (mA/cm ²)	<i>V</i> _{oc} (mV)	<i>FF</i> (%)	<i>η</i> (%)	<i>R</i> _{cell} (Ω)
0 h						
Printed	5	14.1 ± 0.1	650 ± 10	71.5 ± 1.4	6.53 ± 0.15	36 ± 6
Reference	3	13.8 ± 0.3	660 ± 8	71.2 ± 1.6	6.47 ± 0.13	38 ± 6
Difference		2.1 %	-1.5 %	0.4 %	1.0 %	<u>-5%</u>
<i>p</i> -value		0.29	0.19	0.80	0.57	0.69
250 h						
Printed	5	14.1 ± 0.6	656 ± 15	71.1 ± 1.5	6.58 ± 0.06	33 ± 4
Reference	3	14.3 ± 0.1	664 ± 1	71.1 ± 0.8	6.73 ± 0.11	34 ± 2
Difference		-1.0 %	-1.2 %	0.1 %	-2.2 %	-3%
<i>p</i> -value		0.62	0.31	0.94	0.14	0.67
500 h						
Printed	5	14.3 ± 0.5	651 ± 16	71 ± 1.3	6.63 ± 0.1	33 ± 2
Reference	3	14.2 ± 0.4	667 ± 2	71.5 ± 0.7	6.76 ± 0.21	32 ± 2
Difference		1.3 %	-2.5 %	-0.7 %	-2.0 %	3.0 %
<i>p</i> -value		0.57	0.08	0.49	0.39	0.58
750 h						
Printed	5	14.3 ± 0.7	644 ± 15	71 ± 1.5	6.52 ± 0.15	32 ± 2
Reference	3	13.4 ± 0.7	670 ± 8	72.5 ± 0.1	6.52 ± 0.25	34 ± 2
Difference		<u>6.3 %</u>	-3.9 %	-2.1 %	-0.02%	-4.3 %
<i>p</i> -value		0.16	<u>0.02</u>	0.09	0.99	0.45
1000 h						
Printed	5	14.2 ± 0.6	636 ± 17	71.1 ± 1.4	6.44 ± 0.2	32 ± 2
Reference	3	13.1 ± 0.8	672 ± 16	72 ± 0.7	6.34 ± 0.28	35 ± 3
Difference		<u>8.6 %</u>	<u>-5.3 %</u>	-1.3 %	1.5 %	<u>-8.3 %</u>
<i>p</i> -value		0.11	<u>0.04</u>	0.27	0.63	0.27

Table 3. Comparison final vs. initial performance for each type of cells

	<i>N</i>	<i>J</i> _{sc} (mA/cm ²)	<i>V</i> _{oc} (mV)	<i>FF</i> (%)	<i>η</i> (%)	<i>R</i> _{cell} (Ω)
Printed						
0 hours	5	14.1 ± 0.1	650 ± 10	71.5 ± 1.4	6.53 ± 0.15	36 ± 6
Rel. stdev		0.5 %	1.5 %	2.0 %	2.3 %	<u>16.4 %</u>
1000 hours	5	14.2 ± 0.6	636 ± 17	71.1 ± 1.4	6.44 ± 0.2	32 ± 2
Rel. stdev		4.5 %	2.6 %	2.0 %	3.1 %	<u>7.1 %</u>
Difference		1.2 %	-2.0 %	-0.5 %	-1.4 %	<u>-11.9 %</u>
<i>p</i> -value		0.58	0.14	0.46	0.47	0.17
Reference						
0 hours	3	13.8 ± 0.3	660 ± 8	71.2 ± 1.6	6.47 ± 0.13	38 ± 6
Rel. stdev		2.5 %	1.3 %	2.3 %	2.0 %	<u>15.9 %</u>
1000 hours	3	13.1 ± 0.8	672 ± 16	72 ± 0.7	6.34 ± 0.28	35 ± 3
Rel. stdev		<u>6.1 %</u>	2.4 %	1.0 %	4.4 %	<u>9.6 %</u>
Difference		-4.9 %	1.9 %	1.3 %	-1.9 %	<u>-8.7 %</u>
<i>p</i> -value		0.30	0.27	0.37	0.39	0.24

Nomenclature

<i>N</i>	Number of samples
<i>ave</i>	Average
<i>std</i>	Standard deviation
<i>std/ave, Rel. stdev</i>	Relative standard deviation compared to average
<i>sem</i>	Standard error of the mean
<i>95% CI</i>	Half of the full 95 % confidence interval based on Student's t-distribution
Difference	Relative difference of average values: Printed vs reference, or Batch 2 vs Batch 1.
<i>p-value</i>	Calculated with two-tailed two-sample t-test with unequal variances. A paired t-test was used for comparing the initial and final data of the same batch of cells.
<i>J_{sc}</i>	Short circuit current density
<i>V_{oc}</i>	Open circuit voltage
<i>FF</i>	Fill factor
<i>η</i>	Efficiency
<i>R_{cell}</i>	Cell resistance (inverse slope of the IV curve at <i>V_{oc}</i>)

Statistical analysis of the EIS results

The tables 4 – 6 below show results from the electrochemical impedance spectroscopy of the printed dye and reference DSSCs. See ref [MO] for the description and definitions of the equivalent circuit impedance model and its parameters shown in the tables. The results are commented with conclusions below the tables in the panel “Notes”.

Table 4. Difference in the initial EIS characteristics

Initial data		N	PHOTOELECTRODE							COUNTER ELECTRODE					DIFFUSION			TOTAL R
Printed	5	R_s (Ω)	R_{PE} (Ω)	$Q_{CPE,PE}$	$\beta_{CPE,PE}$	C_{PE} (F) *	τ_{PE} (s) *	f_{PE}^* (Hz) *	R_{CE} (Ω)	$Q_{CPE,CE}$	$\beta_{CPE,CE}$	C_{CE} (F) *	τ_{CE} (s) *	f_{CE}^* (Hz) *	R_D (Ω)	τ_D (s)	f_D^* (Hz) *	R_{TOT} (Ω)
P1		11.360	12.250	3.824E-04	0.986	3.535E-04	4.330E-03	36.75	3.321	1.679E-04	0.646	2.765E-06	9.182E-06	17333	6.456	1.765	9.017E-02	33.39
P2		9.308	10.450	4.037E-04	0.993	3.877E-04	4.051E-03	39.29	2.355	5.398E-05	0.784	4.591E-06	1.081E-05	14720	6.744	1.788	8.901E-02	28.86
P3		12.940	12.720	4.019E-04	0.971	3.437E-04	4.372E-03	36.40	3.226	5.702E-05	0.711	1.724E-06	5.561E-06	28619	6.155	1.466	1.086E-01	35.04
P4		13.850	13.260	3.993E-04	0.997	3.926E-04	5.206E-03	30.57	4.895	1.645E-04	0.559	5.894E-07	2.885E-06	55164	7.238	1.713	9.291E-02	39.24
P5		8.604	13.030	4.418E-04	0.965	3.666E-04	4.776E-03	33.32	2.025	3.564E-05	0.824	4.659E-06	9.434E-06	16870	6.614	1.628	9.776E-02	30.27
ave		11.2	12.3	4.058E-04	0.982	3.688E-04	4.547E-03	35.3	3.16	9.581E-05	0.705	2.866E-06	7.575E-06	26541	6.64	1.67	9.568E-02	33.4
std		2.3	1.1	2.182E-05	0.014	2.115E-05	4.501E-04	3.4	1.12	6.480E-05	0.107	1.781E-06	3.262E-06	16894	0.40	0.13	7.950E-03	4.1
std/ave		20.1 %	9.1 %	5.4 %	1.4 %	5.7 %	9.9 %	9.6 %	35.2 %	67.6 %	15.1 %	62.2 %	43.1 %	63.7 %	6.0 %	7.8 %	8.3 %	12.3 %
sem		1.0	0.5	9.756E-06	0.006	9.460E-06	2.013E-04	1.5	0.50	2.898E-05	0.048	7.965E-07	1.459E-06	7555	0.18	0.06	3.555E-03	1.8
95% CI		2.8	1.4	2.709E-05	0.017	2.627E-05	5.589E-04	4.2	1.38	8.045E-05	0.132	2.211E-06	4.051E-06	20977	0.50	0.16	9.871E-03	5.1
Reference	3	R_s (Ω)	R_{PE} (Ω)	$Q_{CPE,PE}$	$\beta_{CPE,PE}$	C_{PE} (F) *	τ_{PE} (s) *	f_{PE}^* (Hz) *	R_{CE} (Ω)	$Q_{CPE,CE}$	$\beta_{CPE,CE}$	C_{CE} (F) *	τ_{CE} (s) *	f_{CE}^* (Hz) *	R_D (Ω)	τ_D (s)	f_D^* (Hz) *	R_{TOT} (Ω)
R1		7.640	13.140	4.108E-04	0.977	3.633E-04	4.774E-03	33.34	3.257	7.607E-05	0.750	4.758E-06	1.550E-05	10269	6.360	1.614	9.861E-02	30.40
R3		13.330	12.290	3.739E-04	1.008	3.902E-04	4.796E-03	33.19	4.364	1.758E-04	0.619	2.107E-06	9.196E-06	17307	6.422	1.492	1.067E-01	36.41
R4		11.750	12.140	3.694E-04	0.985	3.407E-04	4.136E-03	38.48	4.205	1.426E-04	0.640	2.215E-06	9.313E-06	17089	6.025	1.517	1.049E-01	34.12
ave		10.9	12.5	3.847E-04	0.990	3.647E-04	4.568E-03	35.0	3.9	1.315E-04	0.670	3.027E-06	1.134E-05	14888	6.27	1.54	1.034E-01	33.6
std		2.9	0.5	2.271E-05	0.016	2.482E-05	3.750E-04	3.0	0.6	5.079E-05	0.070	1.501E-06	3.605E-06	4002	0.21	0.06	4.240E-03	3.0
std/ave		26.9 %	4.3 %	5.9 %	1.6 %	6.8 %	8.2 %	8.6 %	15.2 %	38.6 %	10.5 %	49.6 %	31.8 %	26.9 %	3.4 %	4.2 %	4.1 %	9.0 %
sem		1.7	0.3	1.311E-05	0.009	1.433E-05	2.165E-04	1.7	0.3	2.933E-05	0.041	8.664E-07	2.081E-06	2310	0.12	0.04	2.448E-03	1.8
95% CI		7.3	1.3	5.641E-05	0.040	6.165E-05	9.315E-04	7.5	1.5	1.262E-04	0.175	3.728E-06	8.956E-06	9941	0.53	0.16	1.053E-02	7.5

* Quantities marked with "*" are calculated from the unmarked values in the previous columns. The unmarked values were obtained by fitting an equivalent circuit model to the measured EIS data.

Comparison of two groups

Initial data		N	PHOTOELECTRODE							COUNTER ELECTRODE					DIFFUSION			TOTAL R
Printed	5	R_s (Ω)	R_{PE} (Ω)	$Q_{CPE,PE}$ ($\cdot 10^{-3}$)	$\beta_{CPE,PE}$	C_{PE} (mF) *	τ_{PE} (ms) *	f_{PE}^* (Hz) *	R_{CE} (Ω)	$Q_{CPE,CE}$ ($\cdot 10^{-3}$)	$\beta_{CPE,CE}$	C_{CE} (μ F) *	τ_{CE} (μ s) *	f_{CE}^* (kHz) *	R_D (Ω)	τ_D (s)	f_D^* (mHz) *	R_{TOT} (Ω)
ave		11.2 \pm 2.3	12.3 \pm 1.1	0.41 \pm 0.02	0.98 \pm 0.01	0.37 \pm 0.02	4.5 \pm 0.5	35 \pm 3	3.16 \pm 1.12	0.1 \pm 0.06	0.7 \pm 0.11	2.9 \pm 1.8	7.6 \pm 3.3	27 \pm 17	6.6 \pm 0.4	1.67 \pm 0.13	96 \pm 8	33 \pm 4
std/ave		20%	9%	5%	1%	6%	10%	10%	35%	68%	15%	62%	43%	64%	6%	8%	8%	12%
Reference	3	10.9 \pm 2.9	12.5 \pm 0.5	0.38 \pm 0.02	0.99 \pm 0.02	0.36 \pm 0.02	4.6 \pm 0.4	35 \pm 3	3.94 \pm 0.6	0.13 \pm 0.05	0.67 \pm 0.07	3 \pm 1.5	11.3 \pm 3.6	15 \pm 4	6.3 \pm 0.2	1.54 \pm 0.06	103 \pm 4	34 \pm 3
std/ave		27%	4%	6%	2%	7%	8%	9%	15%	39%	10%	50%	32%	27%	3%	4%	4%	9%
Difference		2.8 %	-1.4 %	5.5 %	-0.8 %	1.1 %	-0.5 %	0.8 %	-19.7 %	-27.1 %	5.3 %	-5.3 %	-33.2 %	78.3 %	5.9 %	8.5 %	-7.5 %	-0.8 %
p-value		0.886	0.769	0.263	0.522	0.824	0.946	0.914	0.247	0.424	0.595	0.896	0.214	0.204	0.137	0.108	0.124	0.916

* Quantities marked with "*" are calculated from the unmarked values in the previous columns. The unmarked values were obtained by fitting an equivalent circuit model to the measured EIS data.

Notes

R_s and all CE parameters have high relative standard deviations in both type of cells. This means that the experimental accuracy of these parameters is somewhat limited, limiting also the comparison between the two types of cells with respect to these parameters. For example std/ave is 35% and 15% for R_{ce} in printed and reference cells respectively. However, in this study the PE performance is a more relevant subject for comparison. Moreover, the R_{ce} is so low that the large variation in its value is practically insignificant from the point of view of device performance as a whole. **None of the EIS parameters show statistically significant differences between the two types of cells.** For example for the PE parameters this means that any differences that might exist are smaller than the relative standard deviations, which were less than 10 % in all cases.

Table 5. Difference in the final (1000 h aged) EIS characteristics

1000h		N	PHOTOELECTRODE							COUNTER ELECTRODE							DIFFUSION			TOTAL R
Printed	5	R_s (Ω)	R_{PE} (Ω)	$Q_{CPE,PE}$	$\beta_{CPE,PE}$	C_{PE} (F) *	τ_{PE} (s) *	f_{PE}^* (Hz) *	R_{CE} (Ω)	$Q_{CPE,CE}$	$\beta_{CPE,CE}$	C_{CE} (F) *	τ_{CE} (s) *	f_{CE}^* (Hz) *	R_D (Ω)	τ_D (s)	f_D^* (Hz) *	R_{TOT} (Ω)		
P1		9.553	11.860	4.228E-04	0.992	4.056E-04	4.811E-03	33.08	2.895	6.305E-05	0.730	2.632E-06	7.619E-06	20889	6.668	1.967	8.091E-02	30.98		
P2		7.130	11.720	5.096E-04	0.977	4.529E-04	5.308E-03	29.99	1.821	5.474E-05	0.793	4.923E-06	8.965E-06	17753	5.718	1.568	1.015E-01	26.39		
P3		9.636	13.010	4.472E-04	0.980	4.035E-04	5.250E-03	30.32	2.397	5.000E-05	0.736	1.954E-06	4.707E-06	33812	6.355	1.650	9.646E-02	31.40		
P4		9.748	11.410	4.671E-04	0.998	4.618E-04	5.269E-03	30.21	2.474	2.188E-04	0.624	2.360E-06	5.838E-06	27263	6.705	1.738	9.157E-02	30.34		
P5		7.220	11.090	4.562E-04	0.988	4.287E-04	4.754E-03	33.48	2.125	1.257E-04	0.678	2.505E-06	5.322E-06	29902	6.420	1.664	9.565E-02	26.86		
ave		8.7	11.8	4.606E-04	0.987	4.305E-04	5.078E-03	31.4	2.34	1.024E-04	0.712	2.877E-06	6.490E-06	25924	6.37	1.72	9.322E-02	29.2		
std		1.4	0.7	3.191E-05	0.008	2.660E-05	2.715E-04	1.7	0.40	7.185E-05	0.064	1.171E-06	1.758E-06	6557	0.40	0.15	7.732E-03	2.4		
std/ave		15.7 %	6.2 %	6.9 %	0.8 %	6.2 %	5.3 %	5.5 %	17.1 %	70.1 %	9.0 %	40.7 %	27.1 %	25.3 %	6.2 %	8.9 %	8.3 %	8.2 %		
sem		0.6	0.3	1.427E-05	0.004	1.190E-05	1.214E-04	0.8	0.18	3.213E-05	0.029	5.238E-07	7.864E-07	2932	0.18	0.07	3.458E-03	1.1		
95% CI		1.7	0.9	3.962E-05	0.010	3.303E-05	3.371E-04	2.1	0.50	8.922E-05	0.079	1.454E-06	2.183E-06	8141	0.49	0.19	9.601E-03	3.0		
Reference	3	R_s (Ω)	R_{PE} (Ω)	$Q_{CPE,PE}$	$\beta_{CPE,PE}$	C_{PE} (F) *	τ_{PE} (s) *	f_{PE}^* (Hz) *	R_{CE} (Ω)	$Q_{CPE,CE}$	$\beta_{CPE,CE}$	C_{CE} (F) *	τ_{CE} (s) *	f_{CE}^* (Hz) *	R_D (Ω)	τ_D (s)	f_D^* (Hz) *	R_{TOT} (Ω)		
R1		7.886	13.750	4.777E-04	0.971	4.109E-04	5.650E-03	28.17	2.477	1.805E-05	0.901	6.021E-06	1.491E-05	10671	6.577	2.013	7.906E-02	30.69		
R3		9.094	14.410	3.815E-04	0.986	3.534E-04	5.093E-03	31.25	3.563	6.520E-05	0.748	3.899E-06	1.389E-05	11457	6.529	1.540	1.033E-01	33.60		
R4		9.327	12.830	4.081E-04	0.983	3.726E-04	4.780E-03	33.30	3.418	6.384E-05	0.732	2.899E-06	9.910E-06	16059	6.006	1.670	9.530E-02	31.58		
ave		8.8	13.7	4.224E-04	0.980	3.790E-04	5.174E-03	30.9	3.2	4.903E-05	0.794	4.273E-06	1.291E-05	12729	6.37	1.74	9.257E-02	32.0		
std		0.8	0.8	4.970E-05	0.008	2.926E-05	4.406E-04	2.6	0.6	2.684E-05	0.093	1.594E-06	2.644E-06	2911	0.32	0.24	1.237E-02	1.5		
std/ave		8.8 %	5.8 %	11.8 %	0.8 %	7.7 %	8.5 %	8.3 %	18.7 %	54.7 %	11.8 %	37.3 %	20.5 %	22.9 %	5.0 %	14.0 %	13.4 %	4.7 %		
sem		0.4	0.5	2.869E-05	0.005	1.689E-05	2.544E-04	1.5	0.3	1.549E-05	0.054	9.204E-07	1.526E-06	1680	0.18	0.14	7.142E-03	0.9		
95% CI		1.9	2.0	1.235E-04	0.019	7.268E-05	1.094E-03	6.4	1.5	6.667E-05	0.232	3.960E-06	6.567E-06	7230	0.79	0.61	3.073E-02	3.7		

* Quantities marked with "*" are calculated from the values unmarked values in the previous columns. The unmarked values were obtained by fitting an equivalent circuit model to the measured EIS data.

Comparison of two groups

1000h		N	PHOTOELECTRODE							COUNTER ELECTRODE							DIFFUSION			TOTAL R
Printed	5	R_s (Ω)	R_{PE} (Ω)	$Q_{CPE,PE}$ ($\cdot 10^{-3}$)	$\beta_{CPE,PE}$	C_{PE} (mF) *	τ_{PE} (ms) *	f_{PE}^* (Hz) *	R_{CE} (Ω)	$Q_{CPE,CE}$ ($\cdot 10^{-3}$)	$\beta_{CPE,CE}$	C_{CE} (μ F) *	τ_{CE} (μ s) *	f_{CE}^* (kHz) *	R_D (Ω)	τ_D (s)	f_D^* (mHz) *	R_{TOT} (Ω)		
Printed	5	8.7 \pm 1.4	11.8 \pm 0.7	0.46 \pm 0.03	0.99 \pm 0.01	0.43 \pm 0.03	5.1 \pm 0.3	31 \pm 2	2.34 \pm 0.4	0.1 \pm 0.07	0.71 \pm 0.06	2.9 \pm 1.2	6.5 \pm 1.8	26 \pm 7	6.4 \pm 0.4	1.72 \pm 0.15	93 \pm 8	29 \pm 2		
std/ave		16%	6%	7%	1%	6%	5%	5%	17%	70%	9%	41%	27%	25%	6%	9%	8%	8%		
Reference	3	8.8 \pm 0.8	13.7 \pm 0.8	0.42 \pm 0.05	0.98 \pm 0.01	0.38 \pm 0.03	5.2 \pm 0.4	31 \pm 3	3.15 \pm 0.59	0.05 \pm 0.03	0.79 \pm 0.09	4.3 \pm 1.6	12.9 \pm 2.6	13 \pm 3	6.4 \pm 0.3	1.74 \pm 0.24	93 \pm 12	32 \pm 1		
std/ave		9%	6%	12%	1%	8%	9%	8%	19%	55%	12%	37%	20%	23%	5%	14%	13%	5%		
Difference		-1.3 %	-13.5 %	9.0 %	0.8 %	13.6 %	-1.9 %	1.6 %	-25.7 %	108.9 %	-10.3 %	-32.7 %	-49.7 %	103.7 %	0.0 %	-1.4 %	0.7 %	-8.7 %		
p-value		0.887	0.030	0.319	0.263	0.067	0.756	0.781	0.122	0.189	0.270	0.271	0.032	0.008	0.992	0.890	0.940	0.091		

* Quantities marked with "*" are calculated from the values unmarked values in the previous columns. The unmarked values were obtained by fitting an equivalent circuit model to the measured EIS data.

Notes

Statistically significant difference is found only for the printed cells vs. reference cells: Rpe (-13.5%) and CE time constant (-50%). The difference in Rpe is modest though. Since also Voc showed statistically significant difference in this case (-5.3%) definite analysis for the difference in Rpe is beyond the scope of this data. Considering the high relative standard deviations in the CE parameters, the 50 % lower CE time constant in printed cells, could well be a false positive. We can thus conclude that the printed cells do not markedly differ from the reference cells after the aging test, in terms of their EIS characteristics measured at open circuit condition under one Sun equivalent illumination.

Table 6. EIS aging behavior of each cell type

Comparison of each group before and after aging																								
		SERIES R							PHOTOELECTRODE							COUNTER ELECTRODE					DIFFUSION			TOTAL R
	N	$R_s (\Omega)$	$R_{PE} (\Omega)$	$Q_{CPE,PE} (-10^{-3})$	$\beta_{CPE,PE}$	$C_{PE} (mF)^*$	$\tau_{PE} (ms)^*$	$f_{PE}^* (Hz)^*$	$R_{CE} (\Omega)$	$Q_{CPE,CE} (-10^{-3})$	$\beta_{CPE,CE}$	$C_{CE} (\mu F)^*$	$\tau_{CE} (\mu s)^*$	$f_{CE}^* (kHz)^*$	$R_D (\Omega)$	$\tau_D (s)$	$f_D^* (mHz)^*$	$R_{TOT} (\Omega)$						
Printed																								
Initial	5	11.2 ± 2.3	12.3 ± 1.1	0.41 ± 0.02	0.98 ± 0.01	0.37 ± 0.02	4.5 ± 0.5	35 ± 3	3.2 ± 1.1	0.1 ± 0.06	0.7 ± 0.11	2.9 ± 1.8	7.6 ± 3.3	27 ± 17	6.6 ± 0.4	1.67 ± 0.13	96 ± 8	33 ± 4						
std/ave		20 %	9 %	5 %	1 %	6 %	10 %	10 %	35 %	68 %	15 %	62 %	43 %	64 %	6 %	8 %	8 %	12 %						
1000h	5	8.7 ± 1.4	11.8 ± 0.7	0.46 ± 0.03	0.99 ± 0.01	0.43 ± 0.03	5.1 ± 0.3	31 ± 2	2.3 ± 0.4	0.1 ± 0.07	0.71 ± 0.06	2.9 ± 1.2	6.5 ± 1.8	26 ± 7	6.4 ± 0.4	1.72 ± 0.15	93 ± 8	29 ± 2						
std/ave		16 %	6 %	7 %	1 %	6 %	5 %	5 %	17 %	70 %	9 %	41 %	27 %	25 %	6 %	9 %	8 %	8 %						
Difference		-22.8 %	-4.2 %	13.5 %	0.5 %	16.7 %	11.7 %	-10.9 %	-26.0 %	6.9 %	1.1 %	0.4 %	-14.3 %	-2.3 %	-4.0 %	2.7 %	-2.6 %	-12.5 %						
p-value		0.007	0.445	0.023	0.467	0.000	0.093	0.096	0.127	0.851	0.865	0.987	0.398	0.934	0.317	0.581	0.594	0.026						
Reference																								
Initial	3	10.9 ± 2.9	12.5 ± 0.5	0.38 ± 0.02	0.99 ± 0.02	0.36 ± 0.02	4.6 ± 0.4	35 ± 3	3.9 ± 0.6	0.13 ± 0.05	0.67 ± 0.07	3 ± 1.5	11.3 ± 3.6	15 ± 4	6.3 ± 0.2	1.54 ± 0.06	103 ± 4	34 ± 3						
std/ave		27 %	4 %	6 %	2 %	7 %	8 %	9 %	15 %	39 %	10 %	50 %	32 %	27 %	3 %	4 %	4 %	9 %						
1000h	3	8.8 ± 0.8	13.7 ± 0.8	0.42 ± 0.05	0.98 ± 0.01	0.38 ± 0.03	5.2 ± 0.4	31 ± 3	3.2 ± 0.6	0.05 ± 0.03	0.79 ± 0.09	4.3 ± 1.6	12.9 ± 2.6	13 ± 3	6.4 ± 0.3	1.74 ± 0.24	93 ± 12	32 ± 1						
std/ave		9 %	6 %	12 %	1 %	8 %	9 %	8 %	19 %	55 %	12 %	37 %	20 %	23 %	5 %	14 %	13 %	5 %						
Difference		-19.6 %	9.1 %	9.8 %	-1.0 %	3.9 %	13.3 %	-11.7 %	-20.0 %	-62.7 %	18.5 %	41.2 %	13.8 %	-14.5 %	1.6 %	13.0 %	-10.5 %	-5.0 %						
p-value		0.242	0.146	0.159	0.238	0.638	0.069	0.063	0.000	0.033	0.020	0.060	0.430	0.372	0.274	0.194	0.149	0.232						

* Quantities marked with "" are calculated from the values unmarked values in the previous columns. The unmarked values were obtained by fitting an equivalent circuit model to the measured EIS data.

Notes

High relative standard deviations are observed for Rs and the CE parameters. Statistically significant difference of the EIS parameters after aging compared to their initial values is found only for Cpe (+17%) and Rtot (-12.5%) of the printed cells and Rce (-20%) of the reference cells. Note that no change in the Rpe was observed, which means that any changes that might have occurred to the PE parameters are smaller than the relative standard deviations, which were less than 10 % for all PE parameters. This stability of the EIS characteristics is well in line with the stability of the IV characteristics, showing that neither the printed nor the reference cells showed any significant degradation of their electrochemical characteristics. Quite the contrary, the only (abovementioned) statistically significant changes in the EIS parameters were all performance improvements.

About statistical analysis

Criteria for practically significant difference and acceptable sample-to-sample variation (relative standard deviation, std/ave)

Criteria **	$R_s (\Omega)$	$R_{PE} (\Omega)$	$Q_{CPE,PE}$	$\beta_{CPE,PE}$	$C_{PE} (F)^*$	$\tau_{PE} (s)^*$	$f_{PE}^* (Hz)^*$	$R_{CE} (\Omega)$	$Q_{CPE,CE}$	$\beta_{CPE,CE}$	$C_{CE} (F)^*$	$\tau_{CE} (s)^*$	$f_{CE}^* (Hz)^*$	$R_D (\Omega)$	$\tau_D (s)$	$f_D^* (Hz)^*$	$R_{TOT} (\Omega)$
Acceptable std/ave.	10 %	10 %	10 %	10 %	10 %	10 %	10 %	10 %	10 %	10 %	10 %	10 %	10 %	10 %	10 %	10 %	10 %
Practically signif. difference	20 %	20 %	20 %	20 %	20 %	20 %	20 %	20 %	20 %	20 %	20 %	20 %	20 %	20 %	20 %	20 %	20 %

* Quantities marked with "" are calculated from the values unmarked values in the previous columns. The unmarked values were obtained by fitting an equivalent circuit model to the measured EIS data.

** These criteria are subjectively chosen by the researcher to set a criteria for satisfactory repeatability of one type of sample and practically relevant difference between different type of samples

Statistical testing

Statistical confidence level	95 %
α	0.05

The p-value is calculated with two-tailed paired t-test

Underlined in the comparison table are:

- Relative standard deviations (std/ave) larger than or equal to the acceptable value (also highlighted with pink in the data table)
- Differences larger than or equal to the practical significance level
- p-values lower than or equal to α (e.g. 0.05 for 5 % significance)

Nomenclature

- N** number of samples
- ave** average
- std** standard deviation
- std/ave** relative standard deviation compared to average
- sem** standard error of the mean
- 95%CI** Half of the full 95 % confidence interval based on Student's t-distribution
- Difference** relative difference of average values: Printed vs reference, or Batch 2 vs Batch 1.

Statistical analysis of the IV results: aging test at half Sun and 60 C

<i>N</i>					
Initial	5	J_{sc} (mA/cm ²)	V_{oc} (V)	<i>FF</i>	η (%)
P1		10.7	0.711	0.775	6.15
P2		11.8	0.674	0.759	6.38
P3		11.6	0.689	0.751	6.32
P4		11.9	0.684	0.747	6.38
P5		11.6	0.691	0.761	6.39
ave		11.5	0.690	0.759	6.32
std		0.5	0.013	0.011	0.10
std/ave		4.3 %	1.9 %	1.4 %	1.6 %
sem		0.2	0.006	0.005	0.05
95% CI		0.6	0.017	0.013	0.13
170 hours	5	J_{sc} (mA/cm ²)	V_{oc} (V)	<i>FF</i>	η (%)
P1		11.0	0.697	0.785	6.25
P2		12.9	0.633	0.725	6.14
P3		11.9	0.679	0.743	6.14
P4		12.5	0.661	0.734	6.21
P5		11.7	0.684	0.758	6.26
ave		12.0	0.671	0.749	6.20
std		0.7	0.025	0.024	0.06
std/ave		5.9 %	3.7 %	3.1 %	0.9 %
sem		0.3	0.011	0.011	0.03
95% CI		0.9	0.031	0.029	0.07
386 hours	5	J_{sc} (mA/cm ²)	V_{oc} (V)	<i>FF</i>	η (%)
P1		11.9	0.673	0.782	6.45
P2		12.8	0.625	0.738	6.10
P3		12.2	0.655	0.751	6.21
P4		12.5	0.642	0.742	6.17
P5		12.3	0.664	0.755	6.40
ave		12.4	0.652	0.754	6.27
std		0.3	0.019	0.017	0.15
std/ave		2.7 %	2.9 %	2.3 %	2.4 %
sem		0.1	0.008	0.008	0.07
95% CI		0.4	0.023	0.021	0.19
530 hours	5	J_{sc} (mA/cm ²)	V_{oc} (V)	<i>FF</i>	η (%)
P1		12.6	0.664	0.774	6.60
P2		14.0	0.621	0.718	6.40
P3		12.8	0.645	0.736	6.20
P4		13.2	0.635	0.733	6.28
P5		13.0	0.655	0.738	6.49
ave		13.1	0.644	0.740	6.39
std		0.5	0.017	0.021	0.16
std/ave		4.2 %	2.6 %	2.8 %	2.5 %
sem		0.2	0.008	0.009	0.07
95% CI		0.7	0.021	0.026	0.20

986 hours		5	J_{SC} (mA/cm ²)	V_{OC} (V)	FF	η (%)
P1			12.7	0.637	0.768	6.52
P2			13.2	0.604	0.726	6.11
P3			13.2	0.625	0.721	6.29
P4			13.0	0.614	0.724	6.05
P5			12.4	0.636	0.733	6.06
ave			12.9	0.623	0.734	6.21
std			0.3	0.014	0.019	0.20
std/ave			2.6 %	2.3 %	2.6 %	3.2 %
sem			0.2	0.006	0.009	0.09
95% CI			0.4	0.018	0.024	0.25
1154 hours		5	J_{SC} (mA/cm ²)	V_{OC} (V)	FF	η (%)
P1			13.7	0.631	0.710	6.42
P2			13.6	0.599	0.715	6.17
P3			12.7	0.620	0.729	6.01
P4			13.1	0.606	0.717	6.02
P5			12.9	0.630	0.736	6.25
ave			13.2	0.617	0.721	6.17
std			0.4	0.014	0.011	0.17
std/ave			3.1 %	2.3 %	1.5 %	2.8 %
sem			0.2	0.006	0.005	0.08
95% CI			0.5	0.017	0.013	0.21

Table 7. All aging data and t-test for initial and last data set

	N	J_{SC} (mA/cm ²)	V_{OC} (mV)	FF (%)	η (%)
Initial	5	11.5 ± 0.5	690 ± 13	76 ± 1	6.3 ± 0.1
170 hours	5	12 ± 0.7	671 ± 25	75 ± 2	6.2 ± 0.1
386 hours	5	12.4 ± 0.3	652 ± 19	75 ± 2	6.3 ± 0.2
530 hours	5	13.1 ± 0.5	644 ± 17	74 ± 2	6.4 ± 0.2
986 hours	5	12.9 ± 0.3	623 ± 14	73 ± 2	6.2 ± 0.2
1154 hours	5	13.2 ± 0.4	617 ± 14	72 ± 1	6.2 ± 0.2
Difference		-0.13	0.12	0.05	0.02
p-value		0.01	0.00	0.01	0.25

Aging behavior of the printed dye cells in the additional 1154 hours at half Sun at 60 °C type (Table 7)

Table 7 shows that the efficiency of the five DSSCs did not degrade at all in the additional aging test carried out at half Sun at 60 °C for 1154 hours: the drop from 6.3 % to 6.2 % is within the standard deviation of the five cells, which was relatively low. Statistically significant decrease of V_{OC} and FF was nevertheless observed, however, their effect on the cell efficiency was compensated by a significant increase of J_{SC} during the aging. It therefore seems the photoelectrochemical properties of the photoelectrode changed, however, without affecting the photovoltaic efficiency.

APPENDIX 5



Inkjet-printed platinum counter electrodes for dye-sensitized solar cells



Merve Özkan ^{a,*}, Syed Ghufuran Hashmi ^b, Janne Halme ^b, Alp Karakoç ^{a,c}, Teemu Sarikka ^d, Jouni Paltakari ^a, Peter D. Lund ^b

^a Department of Forest Products Technology, Aalto University, Finland

^b Department of Applied Physics, Aalto University, Finland

^c Department of Civil and Environmental Engineering, University of California Los Angeles, USA

^d Department of Mechanical Engineering, Aalto University, Finland

ARTICLE INFO

Article history:

Received 17 December 2016

Received in revised form

4 February 2017

Accepted 11 February 2017

Available online 16 February 2017

Keywords:

Dye-sensitized solar cells

Inkjet printing

Platinum

Catalyst

Stability

ABSTRACT

In this study, inkjet printing method was successfully demonstrated to produce catalytic platinum layers for dye-sensitized solar cells. Our work includes meticulous optical, morphological, and electrocatalytic analyses of precisely inkjet-patterned counter electrodes as well as traditionally drop-cast samples. Similar catalytic performance was obtained with both methods ($R'_{CT} = 1.2 \Omega \text{ cm}^2$ for drop-cast and $R'_{CT} = 1.6 \Omega \text{ cm}^2$ for inkjet-printed) at same Pt loading (ca. $2.5 \mu\text{g}/\text{cm}^2$), and correspondingly almost same cell efficiencies ($\eta_{\text{drop-cast}} = 6.5\%$ and $\eta_{\text{printed}} = 6.7\%$). All the cells exhibited high stability by keeping their efficiencies after being subjected to a 1000 h aging test under 1 Sun and 35 °C at the open circuit condition. These results highlight the potential of inkjet printing to realize precisely patterned and no-material-wasting counter electrodes by controlled dispensing of the functional solution.

© 2017 Elsevier B.V. All rights reserved.

1. Introduction

Dye-sensitized solar cells (DSSCs) have been widely investigated due to the potential of their possible utilization in low-power electronics [1]. The traditional device structure of a DSSC employs a dye-impregnated photo electrode (PE) and a counter electrode (CE) that consists of a platinum (Pt) catalyst layer loaded over a fluorine tin oxide (FTO) coated glass substrate [2]. PE and CE remain separated through a thermoplastic layer (typically a Surlyn or Bynel foil) and exchange the holes and electrons through a redox mediator (traditionally I_3^-/I^- based redox couple). Though many alternatives for catalysts have been tested [3], the conventional Pt catalyst layer in DSSC is still the most widely used material due to its high catalytic activity, good adhesion, superior transparency, and high stability [4]. On the other hand, its high cost motivates to develop cost efficient deposition methods without compromising the optimum performance of the cell operation [5,6]. For small area

DSSC, the Pt layer is typically produced over clean FTO-glass by drop casting, namely, placing a drop (4–5 μl) of a 5–10 mM chloroplatinic acid hydrate ($\text{H}_2\text{PtCl}_4 \cdot 6\text{H}_2\text{O}$) solution (in 2-propanol) to the center of the planned active area at room temperature, and the platinization is completed upon the thermal decomposition of the drop-cast layer at 385–410 °C [7]. With this technique, the best catalytic activity obtained in terms of charge transfer resistance (R'_{CT}) is $0.4 \Omega \text{ cm}^2$ with $10 \mu\text{g}/\text{cm}^2$ platinum loading [8].

The characteristics of the catalyst layer in a DSSC affect the maximum potential power conversation efficiency related to the losses in R'_{CT} , which also depends on the electrolyte composition [9,10]. Depending on the platinization technique, the CEs fabricated with high Pt loading amounts generally provide favorable low R'_{CT} values, however, with a compromise in the short-circuit current density as a result of less sunlight harvested in case of bifacial illumination [11]. Table 1 summarizes some examples of CEs employing differently prepared Pt layers on FTO-glass along with the Pt layer transmittance and thickness outcomes as well as R'_{CT} of the electrolyte/catalyst surface. In addition to these techniques, other methods for Pt catalyst deposition include electrochemical deposition [12,13], vacuum thermal decomposition [14], electrospinning [15], spin coating [16], dip coating [17], doctor-blading

* Corresponding author.

E-mail addresses: merve.ozkan@aalto.fi, merve.ozkan85@gmail.com (M. Özkan).

Table 1

Physical and electrical properties of CEs with various platinization methods in the presence of different electrolytes. T_{550} (%) = Pt layer transmittance at 550 nm wavelength, d (nm) = Pt layer average thickness, L ($\mu\text{g}/\text{cm}^2$) = Pt loading, MPN = 3-methoxypropionitrile, ACN = Acetonitrile, VLN = Valeronitrile.

Method	T_{550}	d	L	R_{CT}	Electrolyte
Drop casting [8,20] ^a	96	4.6 ^b	10	0.4	Γ^-/I_3^- in MPN
Drop casting ^{a,c}	93	1.2 ^b	2.5	1.2	Γ^-/I_3^- in MPN
Drop casting ^{a,c}	90	2.4 ^b	5.1	–	Γ^-/I_3^- in MPN
Sputtering [21]	92 ^d	2	4.3 ^b	1.2	Γ^-/I_3^- in MPN
Spray coating [22] ^a	88	9 ^b	19	1.6	Γ^-/I_3^- in ACN-VLN
Electrodeposition [23]	99	0.64	1.4 ^b	8	Γ^-/I_3^- in ACN-VLN
Electrodeposition [23]	66	6.4	14	2	Γ^-/I_3^- in ACN-VLN
Inkjet printing ^{a,c}	90	4.6 ^b	9.8	0.7	Γ^-/I_3^- in MPN
Inkjet printing ^{a,c}	95	1.1 ^b	2.4	1.6	Γ^-/I_3^- in MPN

^a Followed by thermal decomposition.

^b Calculated from thickness of the Pt layer = Pt loading/Pt density (21.45 g/cm³).

^c Current study.

^d Data extracted from related figure or measurement results.

[18], and atomic layer deposition [19].

Here we report a versatile method of Pt precursor solution deposition, i.e., the inkjet printing of the traditional Pt precursor that is used to fabricate small area DSSC devices through the drop casting technique. Integrating the inkjet printing technique in the DSSC manufacturing proposes numerous advantages such as controlled dispensing of the solution with no waste of expensive Pt, drop-on-demand patterning as well as non-contact and direct-write materials deposition with no additional printing mask along with high purity. Moreover, realizing the inkjet printing of Pt was the last step to achieve 100% inkjet printed DSSC after inkjet printed mesoporous photoanode [24] and our inkjet printed sensitizer and electrolyte reports [25,26].

The inkjet printing for this study was performed with 5 mM chloroplatinic acid hydrate ($\text{H}_2\text{PtCl}_4 \cdot 6\text{H}_2\text{O}$) solution (in 2-Propanol) using a disposable silicon based piezoelectric inkjet cartridge storage and jetting unit. The jetting module has 16 identical nozzles embedded on a single line and each nozzle consists of a piezoelectric driven pumping chamber and an orifice to the ambient with 21.5 μm diameter. The distance between the substrate and the nozzle orifice is mostly adjusted to be minimum by the user in order to reduce the ambient interaction, which may increase the inaccuracy of the desired drop position on the substrate [27]. A user defined driving signal is applied to the chamber to form droplets and after the drops are ejected from the nozzles, they travel until the substrate and the amount of dispensed ink is altered by a user-defined parameter “drop spacing” (DS), which is the distance between the centers of two neighboring drops on the substrate. Aforementioned Pt precursor solution exhibits complete wetting over the FTO due to the low surface tension of the precursor along with the Lewis type acid-base interaction [28].

The drop formation and reliable jetting of inkjet printing inks are related to their physicochemical characteristics of the ink such as viscosity, surface tension, density, boiling point, and particle size [29]. For example, a rapid evaporation rate and big particles in the liquid can lead to a deviation in the travel path of the drop between the nozzle orifice and the substrate, eventually clogging the jetting nozzles [30,31] or an ink with sub-optimal properties may result in drops with axis-asymmetric tails or secondary unwanted droplet formation called “satellite drop” which jeopardizes printing quality as well [32]. For an ideal print output satellite-free drops following a vertical and linear trajectory with a proper speed are aimed [29,33,34].

In this study, platinization ink was characterized prior to the inkjet printing process and the jetting trajectory of the ejected

drops was evaluated by implementing a special algorithm on the extracted images from stroboscopic camera built-in the inkjet printer [30]. Altered drop spacing controllably changed the amount of platinum deposited on the FTO-glass substrates, and the charge transfer resistance and transparency of the films were systematically varied. Additionally, due to the good jetting obtained we were able to pattern FTO-glass precisely without a mask (Fig. 1 a) which is vital for printed electronics [35].

2. Experimental Section

2.1. Materials

Chloroplatinic acid hydrate ($\text{H}_2\text{PtCl}_4 \cdot 6\text{H}_2\text{O}$) and all the solvents were purchased from Sigma Aldrich. All chemicals were used without further purification. 3-methoxypropionitrile based high stability electrolyte (EL-HSE), TiO_2 nanocrystalline (18-NRT) and scattering (WER2-0) pastes were obtained from Dyesol. Dye N719 was purchased from Solaronix.

2.2. Measurements

The transmittance spectra of bare and platinum coated FTO-glass substrates were captured with a UV–Vis spectrophotometer (Perkin Elmer lambda 950) using air as the background. The goniometric behaviors of the sessile drop on the FTO-glass substrate and pendant drop on air were investigated with a CAM 200 optical tensiometer (KSV instruments). The recorded images from both experiments were analyzed by using a built-in image analysis software in order to calculate the contact angle of the drop on the substrate and the surface tension of the solution in accordance with Young and Laplace equation. A scanning electron microscope (SEM) (Zeiss Ultra 55 FEG-SEM) and a MultiMode 8 atomic force microscope (AFM) equipped with a NanoScope V controller (Bruker Corporation, Billerica, MA) were used to examine the platinized surfaces. Obtained images from AFM were handled by using NanoScope 8.15 software (Bruker) without any image correction (except flattening). Keithley 2400 source meter was used to measure the current-voltage (I-V) characteristics of the solar cells (0.17 cm² masking area) which were illuminated in a solar simulator (Pecell Technologies, Japan, Model PEC-L01) with a Xe lamp and light intensity of 1 Sun (1000 W/m²). The calibration of the simulator was carried out with a silicon reference solar cell (PV Measurements Inc.). Electrochemical impedance spectroscopy (EIS) data was recorded at open circuit voltage conditions using Zahner-Elektrik IM6 potentiostat under the same illumination as the photovoltaic performance measurements and the data was fitted by Zview2 software (Scribner Associates Inc.). In this study all data fitting was carried out in accordance with the typical equivalent circuit model [36].

2.3. Fabrication of counter electrodes (CE) and CE-CE symmetrical cells

Identical system components and assembly technique were employed to produce inkjet-printed and drop-cast platinum based CE-CE symmetrical cells. The reference CEs were platinized by drop casting of 5 mM $\text{H}_2\text{PtCl}_4 \cdot 6\text{H}_2\text{O}$ solution (in 2-propanol) on cleaned and UV treated FTO-coated glasses with 15 Ω/sq sheet resistance. The digitally printed samples were prepared by heating the substrate during the printing process (50 °C) and altering the amount of ejected solution systematically. After the deposition of the platinum precursor with different methods (inkjet printing and drop casting) the layers were sintered at 385 °C for 15 min. Two identical CEs were sandwiched by a Surlyn frame foil spacer

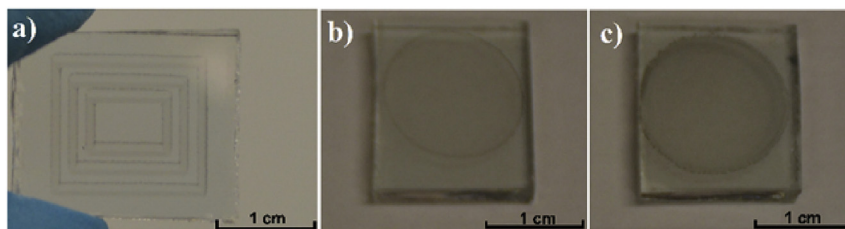


Fig. 1. Pt patterned FTO-glasses (TEC 15) by: **a)** inkjet printing of 20 mM solution without any mask, **b** and **c)** casting of a 4 μL drop from 5 mM and 10 mM solution, respectively.

(25 μm) on a hot plate at 155 $^{\circ}\text{C}$ and the electrolyte was injected between the CEs through two holes followed by the sealing the holes with a Surlyn cover foil (25 μm) and thick glass cover by hot press. In both cases the electrochemically active areas were 1.2 cm^2 , as defined by the dimensions of the opening in the sealant frame (15 mm \times 8 mm). In the case of the drop-cast samples, the active areas were positioned in the center of the larger (1.6 cm^2), circular Pt spread pattern (Fig. 1 b), thus excluding its edge regions.

2.4. Fabrication of photo electrode (PE)

The PEs were produced similar to our previous studies [37]. Briefly, the pre-cleaned FTO glass substrates (A9X-NSG, $R_{\text{SH}} = 10 \Omega/\text{Sq}$) were treated with a 40 mM aqueous TiCl_4 solution followed by rinsing with water and ethanol and drying with compressed air. Sequential screen printing of TiO_2 layers (0.8 mm \times 0.5 mm, 0.4 cm^2) was performed by depositing first nanocrystalline paste of 20 nm TiO_2 nano particles (18-NRT, Dyesol) and then scattering titania particles based paste (WER2-0, Dyesol) on TiCl_4 treated FTO-glass substrates. Then the substrates were sintered at 450 $^{\circ}\text{C}$ for 30 min and were cooled down to room temperature. After that the second TiCl_4 treatment step was performed for 30 min and the substrates were once again undergone to sintering at 450 $^{\circ}\text{C}$ and were cooled down to room temperature. These photoelectrodes consisting of 12 μm nanocrystalline and 4 μm scattering layers were then sensitized at room temperature with a 0.33 mM concentrated solution of dye N-719 in ethanol for 16 h before the final cell assembly.

2.5. DSSC assembly

The PEs and CEs were parted through a Surlyn frame foil (inner dimensions: 15 mm \times 8 mm, 1.2 cm^2 area) and were fused together on the hot plate at 155 $^{\circ}\text{C}$. The cell channel between two electrodes was filled with the electrolyte through the pre-drilled holes at CE side. After the filling process the cell was sealed with a Surlyn cover foil and thin glass cover with a hot press. The contacts were produced by applying copper tape and quick drying silver paint at the non-active area and the contacts were protected with a slow drying epoxy.

2.6. Inkjet printing of platinum

Prior to an inkjet printing process, the jetting solution is characterized to have a rough estimation of the starting point for the jetting procedure [25]. An optimal parameter set of the physicochemical characteristics of the ink has been recommended by the printer manufacturer for the ideal jetting performance (density > 1000 kg/m^3 , boiling point > 100 $^{\circ}\text{C}$, surface tension = 28–42 mN/m , viscosity = 10–12 cps, particle size < 200 nm) [38] and the fluids having a viscosity value of between 2 and 30 cps are defined as jettable [39]. Inkjet printing for this study was performed with a

laboratory bench top materials printer (Dimatix 2831, Fuji Film) by loading 5 mM chloroplatinic acid hydrate ($\text{H}_2\text{PtCl}_4 \cdot 6\text{H}_2\text{O}$) solution (in 2-Propanol) inside a reusable and disposable silicon based piezoelectric inkjet cartridge with a nominal drop volume of $10 \text{ pL} \pm 2 \text{ pL}$.

2.7. Droplet trajectory determination

The flight path of the drops and the jetting angle of the drops are two crucial requirements for the stability of the inkjet printers [40,41]. In order to determine these two for the Pt based ink, at first, the videos of the drop paths were recorded with the built-in camera of the printer and related frames were extracted. Thereafter, extracted frames were binarized in order to obtain foreground and background pixel data as shown in Fig. 2. For binarization threshold, Otsu method was used, which minimizes the combined spread of foreground and background pixels [42]. As a result of binarization, ink droplet region was represented with white color referring to foreground pixels. Following the binarization, morphological analysis was performed on the foreground pixels to define droplet centroid coordinates for the i th frame as

$$(X_i, Y_i) = \left(\frac{\sum_{j=1}^n X_j}{n}, \frac{\sum_{j=1}^n Y_j}{n} \right) \quad (1)$$

in which are the coordinates of j th foreground pixel and n is the total number of foreground pixels inside the investigated droplet. This step was followed by determination of the droplet trajectory by means of the centroid data for each consecutive frame obtained from Equation (1). For this purpose, the data was fitted to first order polynomial to investigate whether the droplet follows a linear trajectory. Here, Y coordinate data was simply taken to be dependent on X coordinate data.

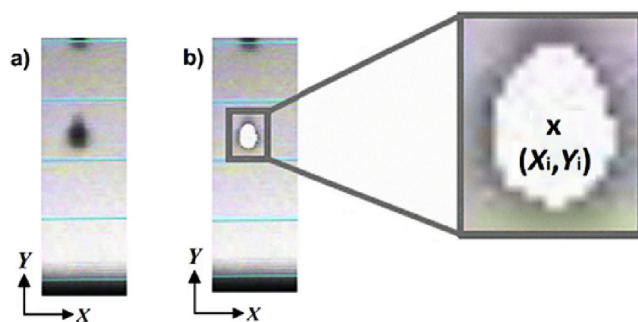


Fig. 2. Demonstration of the image processing of the drop ejected from the nozzle: **a)** original image, **b)** binary image with white colored foreground pixels and schematic representation of centroid.

3. Results and discussion

3.1. Inkjet printing

The solvent density and boiling point for 5 mM $\text{H}_2\text{PtCl}_4 \cdot 6\text{H}_2\text{O}$ solution (~ 0.25 wt %) are 790 kg/m^3 and 82.6°C , respectively. The surface tension was measured as $20.92 \pm 0.4 \text{ mN/m}$ and the viscosity of the jetting ink was determined in a plate/plate geometry between 500 and 0.1 s^{-1} shear rates (almost constant 1.2 cps over the whole shear window larger than 10 s^{-1}). These characteristics of the liquid is close to the jettable ink properties defined by the printer manufacturer and applied in our previous studies [17,30,38,39].

Further investigation was made in order to determine the drop formation, impact, and jettability by calculating a set of non-dimensional parameters, inverse Ohnesorge number (Z), Reynolds number (Re), and Weber number (We), that are used to benchmark inkjet liquids [43–45] (Table 2). Even though different optimal ranges for these parameters have been reported in the literature, the most popular ranges were taken as reference values for this study. A slightly higher Z value compared to the optimal range determined by the previous experimental studies [41,46] indicates that due to the low viscosity, the drops formed from platinum precursor are prone to travel with satellites, which makes the nozzle driving waveform signal adjustment crucial for this application [40]. After the jetting took place, the speed was determined in order to identify Re and We . As an indicator of the ratio of the inertial forces to viscous dissipation, Re of the platinum ink indicates stable break-up of the drops and the ratio of ink's inertial forces at the nozzle orifice to surface tension forces, We , is higher than 4, therefore, the platinum ink system reserves enough energy for the droplet formation without splashing on the substrate [29].

A custom-made waveform signal with 5 kHz jetting frequency and different voltages were applied to the nozzles in order to fine-tune the jetting performance. The amplitude of this signal affects not only the drop speed drastically (recommended by the manufacturer the ideal range is 7–9 m/s for this printer geometry) but also the trajectory of the drops along with the satellite formation. Starting from 16 V the driving amplitude was stepwise increased until 28 V. As the amplitude was increased, the drop speed escalated and upon applying higher amplitudes than 21 V the trajectory of the drops was spoiled and satellite formation was observed. At this point the optimal amplitude resulted in a speed of 5.3 m/s (Fig. 3 a) and a detailed analysis of the stroboscopic images through one cycle of the inkjet printing with the developed technique (explained in the Experimental Section) made it possible to precisely define the drop path for the optimized applied voltage (Fig. 3 b). As a result the droplet trajectory by means of the centroid data for each consecutive frame lead to a fitted polynomial, i.e. $Y = 76.03X - 1690.49$ with angular difference of only 0.8° from Y -axis.

Due to the complete wetting observed in the sessile drop experiments on FTO-glass the substrates were heat treated on the

embedded platen of the printer to different temperatures during the inkjet printing process and the distance between the print head and the substrate was 2.5 mm. The best printing outcome was achieved by adjusting the temperature of the printing platform at 50°C for each drop spacing value. From $10 \text{ pL} \pm 2 \text{ pL}$ nominal drop volume, 10, 11, 12, 13, 14, 15, 20, 40 and $60 \text{ }\mu\text{m}$ DS settings were calculated to result 9.8, 8.1, 6.8, 5.8, 5, 4.4, 2.4, 0.6, $0.3 (\pm 20\%) \text{ }\mu\text{g/cm}^2$ platinum loading by a single pulse firing signal and 4.6 nm, 3.8 nm, 3.2 nm, 2.7 nm, 2.3 nm, 2 nm, 1.1 nm, 0.3 nm and 0.1 nm average Pt layer thicknesses, respectively. The Pt loading of 5 mM and 10 mM drop-cast samples from $4 \text{ }\mu\text{L}$ solution were calculated as around $2.5 \text{ }\mu\text{g/cm}^2$ and $5.1 \text{ }\mu\text{g/cm}^2$ equivalent to 1.2 nm and 2.4 nm average film thicknesses, respectively. In this experiment, the Pt amount for the drop-cast samples was estimated from the radius ($0.71 \pm 0.072 \text{ cm}$) of the approximately circle shaped spread layer of the Pt precursor which also includes the wasted material situated outside the active area of the solar cells and the CE-CE samples (Fig. 1b and c). Because this includes also the Pt accumulated at higher concentration to the edge of the spread layer (coffee ring effect), the calculated value represents an upper limit for Pt loading in the more uniform center region. Because the ring stain constitutes less than 9% of the area of the whole Pt covered area, the estimated error is less than 9%. However, in the inkjet-printed CEs the dispensed solution was used to precisely decorate the solar active area with Pt, therefore, the loading was calculated from the printer geometry, and it is, consequently, more precise. A more comparable method of evaluating the Pt loading is provided by the optical transmittance measurements through the active area of the samples, which is discussed next.

3.2. Transparency of the films

Neglecting multiple reflections and interference effects, the transmittance measured through the counter electrode (T_{CE}) can be approximated as the product of the transmittance of each component of the electrode system, namely the FTO-glass substrate ($T_{\text{FTO-glass}}$), and the platinum layer deposited on it (T_{Pt}) Equation (2).

$$T_{\text{CE}} = T_{\text{FTO-glass}} T_{\text{Pt}} \quad (2)$$

Assuming that light passes only once through the Pt layer, the optical transmittance through the Pt layer can be related to its thickness by:

$$T_{\text{Pt}} = (1 - R_{\text{Pt}})e^{-\alpha d} \sim \frac{T_{\text{CE}}}{T_{\text{FTO-glass}}} \quad (3)$$

where R_{Pt} is the reflectance of the platinum layer, α is the absorption coefficient and d is the film thickness. The semilogarithmic relation between the transmittance of the Pt layers at 550 nm wavelength and the Pt loading amount is presented in Fig. 4 b in accordance with:

$$\log_{10}(T_{\text{Pt}}) = \log_{10}(1 - R_{\text{Pt}}) - \log_{10}(e)\alpha L/\rho \quad (4)$$

which was obtained from Equation (3), by relating the film thickness d to the Pt loading L through the density of bulk Pt metal ρ (21.45 g/cm^3) as $d = L/\rho$. A linear fit of Equation (4) to the transmittance vs. loading data allows estimating the (Napierian) absorption coefficient of the Pt film, α , from the slope ($= \log_{10}(e)\alpha/L$) and the reflectance of the Pt layer from the y-intercept ($= \log_{10}(1 - R_{\text{Pt}})$), yielding $\alpha \approx 0.00289 \text{ m}^{-1}$ and $R_{\text{Pt}} = 0.04\%$ for the inkjet-printed Pt samples. The values obtained for the drop-casted Pt were $\alpha \approx 0.00324 \text{ m}^{-1}$ and $R_{\text{Pt}} = 0.05\%$, but is considered less reliable due to fewer data points. The low Pt reflectance values are

Table 2

Reported optimal range of Z , Re and We of Pt ink compared with the calculated values of platinum precursor according to the printer's geometry.

Parameter	Optimal range	Platinum precursor
Ohnesorge number (Z)	$1 < Z < 10$ [46] $1 < Z < 14$ [41]	16
Reynolds number (Re)	$1 < Re < 100$ [47]	75
Weber number (We)	$1 < We < 100$ [47]	23

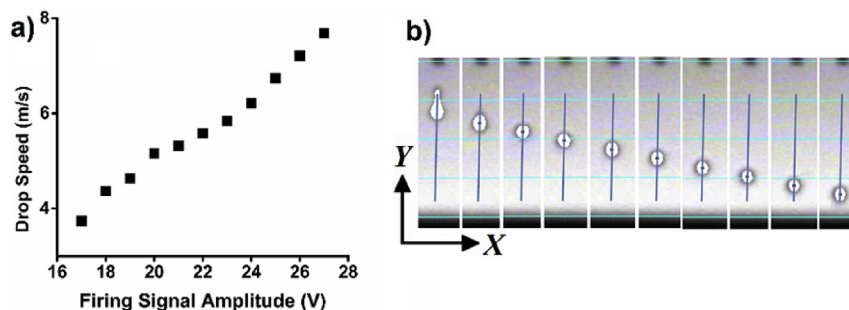


Fig. 3. a) Potential difference applied to the nozzles and resulting drop speed relation, b) Trajectory of the drop processed from the captures of the embedded stroboscopic drop-camera at 21 V and 24.0 ± 0.1 °C jetting temperature.

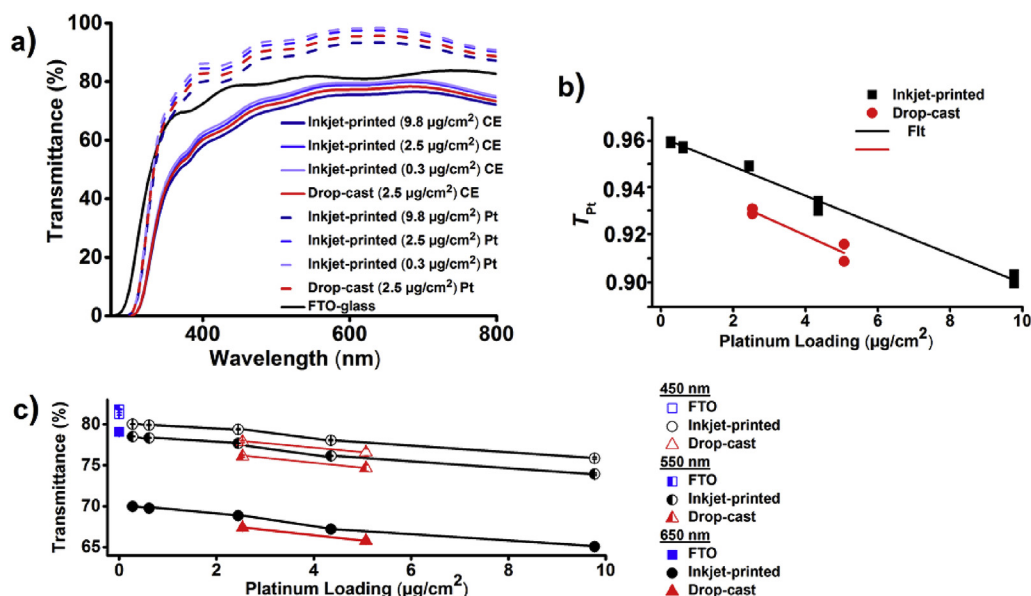


Fig. 4. Transmittance of Pt inkjet-printed and drop-cast FTO-glass samples. a) Measured transmittance spectra of bare and platinized substrates by drop casting (5 mM) and inkjet printing (60, 20 and 10 DS) along with the calculated Pt layer transmittance of the platinized substrates (dashed lines), b) Semilogarithmic relation of the calculated transmittance of the Pt layers at 550 nm and deposited Pt loading amount, c) Measured transmittance of CEs at 450, 550 and 650 nm wavelength as a function of Pt loading. In b) and c), three samples from inkjet-printed and two samples from drop-cast CEs were used in calculating the mean.

in line with the dark (instead of metallic shiny) appearance of these Pt coatings. We also note that the calculated transmittance spectra of the Pt layers, and the absorption coefficient obtained based on them, are only rough estimates, because Equation (3) neglected interference effects, which are nevertheless clearly observed in the measured transmittance spectra (Fig. 4). Nevertheless, the linear relation observed (Fig. 4b) confirms that the light absorption in the Pt layers depends on the Pt loading as expected.

In order to evaluate the reduction of the light irradiance from the CE side stemming from the catalyst deposition, the transmittance values of bare FTO-glass and platinized FTO-glasses at 450 nm, 550 nm and 650 nm with respect to the platinum loading amounts are presented in Fig. 4 c. At 550 nm, the transmittance of printed Pt layers gradually decreases from 95.9% to 90.5% as the DS falls from $60 \mu\text{m}$ to $10 \mu\text{m}$ whereas the drop-cast samples exhibit 93% and 91.2% transmittance for 5 and 10 mM concentrations, respectively. Interestingly, for the same Pt loading, the inkjet-printed Pt gives somewhat higher transmittance than the drop-cast Pt (Fig. 4b and c), which would lead to an efficiency

increase in case of a device architecture employing a transparent mesoporous photoanode [9]. A possible reason to this difference may be related to the morphology of the Pt layers, which is discussed next.

3.3. Morphology of the Pt electrodes

After the impact of a drop from the Pt precursor on the FTO-glass substrate, the drop spreads depending on the surface-solution-ambient conditions and the sintered drops (in order to extract platinum particles) create platinized layers of different quality [28]. After the thermal decomposition of traditionally cast Pt solution drop of microliter-size, the amount, agglomeration and size of Pt particles on the FTO layer are mostly reported as uncontrollable and randomly distributed [22]. During the inkjet printing process the picoliter-size drops ejected on the FTO do not spread as much as in the drop-cast samples due to the mildly heated substrate in this study, nevertheless, sufficiently close drop spacing provides a continuous coverage of the FTO surface.

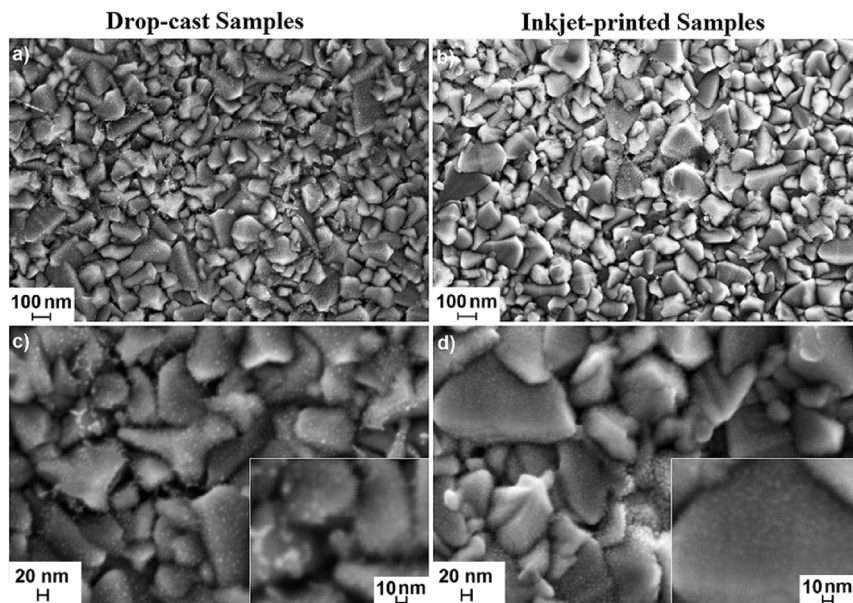


Fig. 5. SEM images of platinum catalysts on FTO-glass surface: **a-b)** lower magnification **and c-d)** higher magnification of drop-cast and inkjet-printed samples.

The morphology of the platinum layers deposited by drop casting and inkjet printing (15 μm DS) of 5 mM platinum solution were investigated with SEM imaging and obtained micrographs of the fully platinized FTO surfaces are presented in Fig. 5. The drop-cast sample was prepared by dispensing 4 μl drop leading to around 2.5 $\mu\text{g}/\text{cm}^2$ platinum loading (spread over the ca. 1.6 cm^2 circular area) while in the inkjet printing process slightly less than 1.8 μl precursor was consumed leading to 4.4 $\mu\text{g}/\text{cm}^2$ platinum loading over the printer-defined 0.4 cm^2 rectangular area. In Fig. 5a, one can count more discernible areas with more Pt than its surroundings compared to Fig. 5b meaning that the Pt particles settled more isolated on the inkjet-printed surface. In the higher magnification (Fig. 5c and d) the disparity is more pronounced as the drop-cast electrode surface had bigger grain size (around 2–3 times) with agglomerations and less uniform coating than the inkjet-printed sample. This is possibly due to more separation of H_2PtCl_6 particles by faster evaporation of evenly spaced ink-jetted pico-size drops on the heated substrate. On the other hand, a bulk amount of solution placed on the glass at room temperature gives more chances for the H_2PtCl_6 particles to merge and localize together on FTO surface. The information extracted from SEM coincides well with a previous report studying spray deposition of Pt particles on heated FTO surface [22].

The altered settlement of the Pt on FTO-glass stemming from different deposition methods was further analyzed by topographical images (Fig. 6). The surface profile of the drop-cast CE consisted of Pt nano-clusters in diverse sizes reaching around 20–25 nm determined through the phase imaging. On the other hand, the Pt grains obtained from the inkjet printing were distinctly smaller (~ 10 nm) and uniform (Inset Fig. 6c). (The white dots seen in Fig. 6a inset are the defects stemming from the cantilever tip).

3.4. Electrochemical characterization of Pt layers

3.4.1. Electrochemical impedance spectroscopy (EIS) of CE-CE symmetrical cells

At first, CE-CE symmetrical cells were devised and the catalytic activity of the platinum layers deposited with different methods was determined with EIS measurements between 100 mHz and 100 kHz frequency range. The Nyquist diagram and imaginary impedance of the CE-CE cells produced by drop casting and inkjet printing with different DS settings are presented in Fig. 7 and the series resistance (R_s), diffusion resistance (R_D), charge transfer resistance (R'_{CT}) for two electrodes and (calculated from 1.2 cm^2 sealant area) the charge transfer resistance for one electrode (R'_{CT}) are listed in Table S1 given as Supplementary Data. The R'_{CT} and

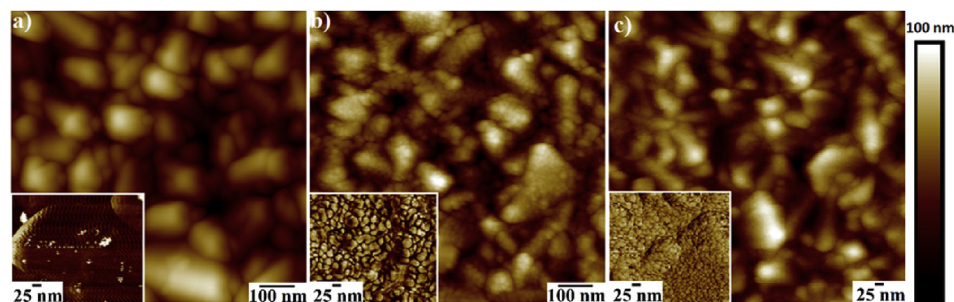


Fig. 6. 1 $\mu\text{m} \times 1 \mu\text{m}$ AFM height images of: **a)** bare FTO-glass surface, **b)** drop-cast platinized FTO-glass surface, **c)** inkjet-print platinized FTO-glass surface. The insets are phase imaging with 25 nm scale bar.

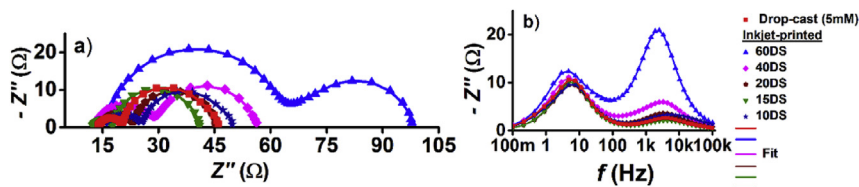


Fig. 7. EIS measurements of the best symmetrical CE-CE cells (drop-cast and inkjet-printed type of CEs): a) Nyquist plot, b) Imaginary impedance.

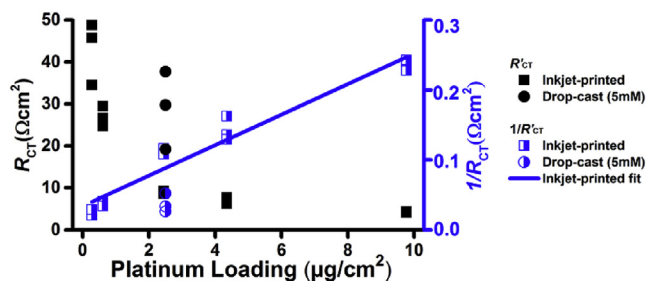


Fig. 8. The R_{CT} and inverse R_{CT} with the platinum loading varied by the deposition type and the drop spacing in inkjet-printed samples.

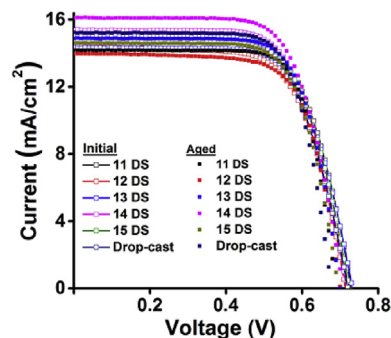


Fig. 10. Initial and final (after 1000 h ageing) IV curves of the best devices produced with different CEs (inkjet-printed and drop-cast).

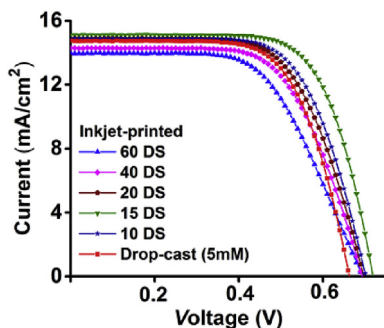


Fig. 9. Examples of IV curves of DSSCs with inkjet-printed and drop-cast CEs.

inverse R_{CT} of the inkjet printed electrodes in the symmetric cells reveal an inverse proportion with the Pt amount (Fig. 8) in low Pt loadings, revealing that the surface area where the charge transfer reaction takes place, is increasing proportionally to the Pt loading, meaning that at the low loadings the particles do not overlap with each other significantly. The inkjet-printed samples with 10 DS gave superior electrocatalytic activity results ($R_{CT} = 4.2 \pm 0.1 \Omega\text{cm}^2$) compared with the drop-cast samples ($6.2 \pm 2.2 \Omega\text{cm}^2$), however, when compared at similar Pt loading (Fig. 8), the drop-cast Pt shows some higher $1/R_{CT}$ values, i.e. lower R_{CT} , suggesting higher catalytic activity than in the inkjet-printed Pt ($9.0 \pm 0.4 \Omega\text{cm}^2$ R_{CT} value for $2.4 \mu\text{g}/\text{cm}^2$ platinum loaded inkjet-printed and 6.2 ± 2.2

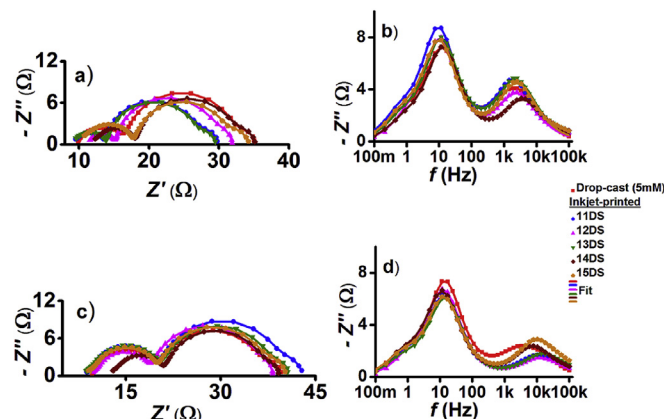


Fig. 11. EIS measurements of the best devices. Fresh devices: a) Nyquist plot, b) Imaginary impedance, aged devices: c) Nyquist plot, d) Imaginary impedance.

Ωcm^2 for $2.5 \mu\text{g}/\text{cm}^2$ platinum loaded drop-cast samples). However, statistical analysis showed no significance difference between the groups ($p = 0.15$, see the Supplementary Data for the complete data set and details of its statistical testing).

In order to gain more insight regarding to the interfacial charge transfer characteristics of the catalyst and electrolyte a batch of

Table 3

The IV parameters and R_{CT} values of DSSCs devices with different CEs. The R_{CT} values are from EIS measurements of DSSCs at open circuit at the same conditions as the IV.

Cell type	Pt Loading ($\mu\text{g}/\text{cm}^2$)	J_{SC} (mA/cm^2)	V_{OC} (mV)	FF (%)	η (%)	R_{CELL} (Ω)	R_{CT} (Ωcm^2)
60 DS	0.3	14.0	695	59.1	5.7	98	8.0
40 DS	0.6	14.3	693	63.4	6.3	61	2.6
20 DS	2.4	15.0	697	65	6.7	55	1.6
15 DS	4.4	15.1	719	70	7.6	38	1.0
10 DS	9.8	14.9	702	66.5	6.9	49	1.2
Drop-cast	2.5	14.8	663	67.0	6.5	44	1.2

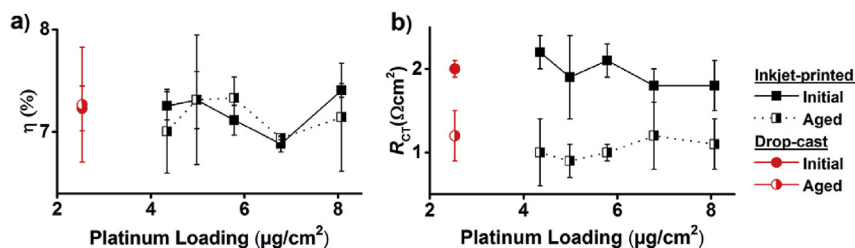


Fig. 12. Aging trend of the inkjet-printed and drop-cast CE based DSSCs: a) Device efficiency and b) Charge transfer resistance.

DSSCs employing the previously mentioned CEs were assembled using the same type of manufacturing technique and their IV curves along with the photovoltaic parameters are presented in Fig. 9 and Table 3, respectively. All the cells produced with inkjet printed CEs exhibited superior efficiencies to the drop-cast CE cells except the 40 and 60 μm DS samples. Interestingly, by consuming only 0.11 μL of $\text{H}_2\text{PtCl}_4 \cdot 6\text{H}_2\text{O}$ solution it was possible to produce a device with 5.7% efficiency (60 DS) and by increasing the precursor amount up to 1.8 μL it was possible to reach a cell efficiency of 7.6% (15 DS). Again, compared at similar Pt loading (20 DS vs. drop-cast in Table 3) the inkjet-printed and drop-cast Pt performed equally well yielding 6.7% and 6.5% cell efficiencies, respectively.

The IV characteristics exhibit expected general qualitative correlations with the Pt loading, namely, the conversion efficiency increases as more Pt is printed on the CE, because it increases decreases R_{CT} , which improves FF. No correlation is evident between the Pt loading and V_{OC} , which is understandable because according theory, V_{OC} is not affected by the electrochemical properties of the CE [36]. Interestingly, however, J_{SC} increased systematically by 14% with increasing Pt loading (Table 3). Although the reason for this increase is at present unclear, at least optical enhancement due Pt layer reflectance can be ruled out because, being equipped with a scattering layer, the photoelectrodes in this work were hardly transparent the reflectance of these thin Pt coating was low (see Section 3.2).

3.4.2. Stability of devices

Encouraged by the results from the CE-CE devices and their corresponding DSSCs, the stability of the Pt coated electrodes was examined in DSSCs with drop-cast (2.5 $\mu\text{g}/\text{cm}^2$ platinum loading) and inkjet printed (11–15 μm DS corresponding to 8.1, 6.8, 5.8, 5, 4.4 $\mu\text{g}/\text{cm}^2$ platinum loading) CEs. The DS values of inkjet-printed samples were specifically chosen starting from 15 DS due to the similar charge transfer resistance values obtained in the previous batch (1 Ωcm^2 for the 15 DS inkjet-printed sample and 1.16 Ωcm^2 for the drop-cast sample.) Fig. 10 and Fig. 11 show the IV and EIS behavior of the best performing devices before and after the 1000 h aging test, respectively. The pre- and post-measurements demonstrated the step-wise change in terms of R_{CT} with respect to the Pt loading in the inkjet-printed samples proving the controlled dispensing of the liquid (Fig. 12). The statistical analysis of the IV and EIS data revealed excellent stability for both type of cells over the time period (Table S and S3, respectively). The charge transfer resistance of the cells as well as the total device resistance dropped in the 1000 h test both in the case of inkjet-printed and drop-cast samples, and most of the devices were able to keep their efficiencies or even increased in efficiency.

The inkjet printing provided the fine-tuning of the catalyst layer transparency and its electrolyte interface charge transfer resistance by systematically altered Pt loading amount in stable DSSCs. In this study, the transmittance of the Pt layer decreased from 95.9% to 90.5% (Fig. 4b) and R_{CT} reduced from 8 Ωcm^2 to 0.7 Ωcm^2 (Table 3)

as the Pt loading increases from 0.3 $\mu\text{g}/\text{cm}^2$ to 9.8 $\mu\text{g}/\text{cm}^2$ by using 0.1 μL –4 μL of precursor solution, respectively. In the literature, Pt catalyst was deposited by different techniques, which also offers such a tuning opportunity, such as sputtering and electrodeposition [21,23]. In both type of the coating methods acceptable R_{CT} values around 2 Ωcm^2 was achieved by more opaque CEs (94% and 66%, respectively) compared to the CEs produced in this study.

4. Conclusions

In conclusion, the platinum catalyst solution was inkjet-printed on the FTO-glass to fabricate counter electrodes (CEs) for dye-sensitized solar cells (DSSCs). The CEs patterned by inkjet printing technique demonstrated higher transparency than the conventional drop-cast samples, which have the same platinum loading, but waste some of the precursor solution to non-active regions of the substrate. The initial electrical characterization tests revealed less catalytic activity in the inkjet-printed samples compared to the drop-cast samples, which have almost the same calculated platinum amount; however, the cells exhibited almost the same efficiencies. All the cells were proven stable after the accelerated 1000 h aging test under 1 Sun illumination at 35 °C. The improvement in the optical property of the CE along with its controlled tuning and the reduction in the material cost during the electrode manufacturing makes the inkjet printing a promising candidate for less expensive CEs and bifacial DSSCs.

Acknowledgements

Merve Özkan thanks Environomical Pathways for Sustainable Energy Services (SELECT+) doctoral programme for her PhD scholarship. Ghufuran Hashmi thanks Academy of Finland for Post-Doctoral Research Fellowship (Grant Number: 287641). Alp Karakoc is grateful to acknowledge the financial support of Tekniikan edistämissäätiö TES through Foundations' Post Doc Pool, Finland. Bio economy infrastructure is acknowledged for the use of the equipment.

Appendix A. Supplementary data

Supplementary data related to this article can be found at <http://dx.doi.org/10.1016/j.orgel.2017.02.015>.

References

- [1] G. Hashmi, K. Miettunen, T. Peltola, J. Halme, I. Asghar, K. Aitola, M. Toivola, P. Lund, Review of materials and manufacturing options for large area flexible dye solar cells, *Renew. Sustain. En. Rev.* 15 (2011) 8, <http://dx.doi.org/10.1016/j.rser.2011.06.004>.
- [2] B. O'Regan, M. Grätzel, A low-cost, high-efficiency solar cell based on dye-sensitized colloidal TiO_2 films, *Nature* 353 (6346) (1991) 737–740, <http://dx.doi.org/10.1038/353737a0>.
- [3] M. Wu, X. Lin, Y. Wang, L. Wang, W. Guo, D. Qi, X. Peng, A. Hagfeldt, M. Grätzel, T. Ma, Economical Pt-free catalysts for counter electrodes of dye-sensitized solar cells, *J. Am. Chem. Soc.* 134 (2012) 7, <http://dx.doi.org/10.1021/>

- ja209657v.
- [4] G. Hashmi, K. Miettunen, J. Halme, I. Asghar, H. Vahlman, T. Saukkonen, Z. Huajin, P. Lund, Comparison of plastic based counter electrodes for dye sensitized solar cells, *J. Electrochem. Soc.* 159 (2012) 7, <http://dx.doi.org/10.1149/2.059207jes>.
 - [5] C.H. Yoon, R. Vittal, J. Lee, W.-S. Chae, K.-J. Kim, Enhanced performance of a dye-sensitized solar cell with an electrodeposited-platinum counter electrode, *Electrochim. Acta* 53 (2008) 6, <http://dx.doi.org/10.1016/j.electacta.2007.10.074>.
 - [6] G. Calogero, P. Calandra, A. Irrera, A. Sinopoli, I. Citro, G. Di Marco, A new type of transparent and low cost counter-electrode based on platinum nanoparticles for dye-sensitized solar cells, *Energy Environ. Sci.* 4 (2011) 5, <http://dx.doi.org/10.1039/C0EE00463D>.
 - [7] N. Papageorgiou, W.F. Maier, M. Grätzel, An iodine/triiodide reduction electrocatalyst for aqueous and organic media, *J. Electrochem. Soc.* 144 (1997) 876, <http://dx.doi.org/10.1149/1.1837502>.
 - [8] L. Kavan, J.H. Yum, M. Grätzel, Optically transparent cathode for dye-sensitized solar cells based on graphene nanoplatelets, *ACS Nano* 5 (2011) 165, <http://dx.doi.org/10.1021/nn102353h>.
 - [9] J. Wu, Y. Li, Q. Tang, G. Yue, J. Lin, M. Huang, L. Meng, Bifacial dye-sensitized solar cells: a strategy to enhance overall efficiency based on transparent polyaniline electrode, *Sci. Rep.* 4 (2014) 4028, <http://dx.doi.org/10.1038/srep04028>.
 - [10] J.-L. Lan, T.-C. Wei, S.-P. Feng, C.-C. Wan, G. Cao, Effects of iodine content in the electrolyte on the charge transfer and power conversion efficiency of dye-sensitized solar cells under low light intensities, *J. Phys. Chem. C* 116 (2012) 25727, <http://dx.doi.org/10.1021/jp309872n>.
 - [11] Y.L. Lee, C.L. Chen, L.W. Chong, C.H. Chen, Y.F. Liu, C.F. Chi, A platinum counter electrode with high electrochemical activity and high transparency for dye-sensitized solar cells, *Electrochem. Commun.* 12 (11) (2010) 1662–1665, <http://dx.doi.org/10.1016/j.elecom.2010.09.022>.
 - [12] Y. Xiao, J. Wu, G. Yue, J. Lin, M. Huang, L. Fan, Z. Lan, Fabrication of high performance Pt/Ti counter electrodes on Ti mesh for flexible large-area dye-sensitized solar cells, *Electrochim. Acta* 58 (2011) 621–627, <http://dx.doi.org/10.1016/j.electacta.2011.10.008>.
 - [13] J. Wu, Y. Xiao, Q. Tang, G. Yue, J. Lin, M. Huang, Y. Huang, Y. Huang, L. Fan, Z. Lan, S. Yin, T. Sato, A large-area light-weight dye-sensitized solar cell based on all titanium substrates with an efficiency of 6.69% outdoors, *Adv. Mater.* 24 (14) (2012) 1884–1888, <http://dx.doi.org/10.1002/adma.201200003>.
 - [14] Y. Xiao, J. Wu, G. Yue, J. Lin, M. Huang, L. Fan, Z. Lan, The surface treatment of Ti meshes for use in large-area flexible dye-sensitized solar cells, *J. Power Sources* 208 (2012) 197–202, <http://dx.doi.org/10.1016/j.jpowsour.2012.02.019>.
 - [15] Y. Xiao, G. Han, High performance platinum nanofibers with interconnecting structure using in dye-sensitized solar cells, *Org. Electron.* 37 (2016) 239–244, <http://dx.doi.org/10.1016/j.orgel.2016.06.041>.
 - [16] L.N. Lewis, J.L. Spivack, S. Gasaway, E.D. Williams, J.Y. Gui, V. Manivannan, O.P. Sclouvan, A novel UV-mediated low-temperature sintering of TiO₂ for dye-sensitized solar cells, *Sol. Energy Mater. Sol. Cells* 90 (2006) 7–8, <http://dx.doi.org/10.1016/j.solmat.2005.05.019>, 1041–1051.
 - [17] J.L. Lan, Y.Y. Wang, C.C. Wan, T.C. Wei, H.P. Feng, C. Peng, H.P. Cheng, Y.H. Chang, W.C. Hsu, The simple and easy way to manufacture counter electrode for dye-sensitized solar cells, *Curr. Appl. Phys.* 10 (2) (2010) 168–171, <http://dx.doi.org/10.1016/j.cap.2009.11.064>.
 - [18] J.H. Lim, Y.H. Ko, J.W. Leem, J.S. Yu, Improvement in light harvesting of dye-sensitized solar cells with antireflective and hydrophobic textile PDMS coating by facile soft imprint lithography, *Opt. Express* 23 (3) (2015) 169–179, <http://dx.doi.org/10.1364/OE.23.00A169>.
 - [19] D. Garcia-Alonso, V. Zardetto, A.J.M. Mackus, F. De Rossi, M.A. Verheijen, T.M. Brown, W.M.M. Kessels, M. Creatore, Atomic layer deposition of highly transparent platinum counter electrodes for metal/polymer flexible dye-sensitized solar cells, *Adv. Energy Mater.* 4 (2014) 4, <http://dx.doi.org/10.1002/aenm.201300831>.
 - [20] L. Kavan, J.-H. Yum, M. Graetzel, Graphene-based cathodes for liquid-junction dye sensitized solar cells: electrocatalytic and mass transport effects, *Electrochim. Acta* 128 (2014) 349, <http://dx.doi.org/10.1016/j.electacta.2013.08.112>.
 - [21] X. Fang, T. Ma, G. Guan, M. Akiyama, T. Kida, E. Abe, Effect of the thickness of the Pt film coated on a counter electrode on the performance of a dye-sensitized solar cell, *J. Electroanal. Chem.* 570 (2) (2004) 257–263, <http://dx.doi.org/10.1016/j.jelechem.2004.04.004>.
 - [22] A. Iefanova, J. Nepal, P. Poudel, D. Davoux, U. Gautam, V. Mallam, Q. Qiao, B. Logue, M.F. Baroughi, Transparent platinum counter electrode for efficient semi-transparent dye-sensitized solar cells, *Thin Solid Films* 562 (2014) 578–584, <http://dx.doi.org/10.1016/j.tsf.2014.03.075>.
 - [23] D. Fu, P. Huang, U. Bach, Platinum coated counter electrodes for dye-sensitized solar cells fabricated by pulsed electrodeposition—Correlation of nanostructure, catalytic activity and optical properties, *Electrochim. Acta* 77 (2012) 121–127, <http://dx.doi.org/10.1016/j.electacta.2012.05.158>.
 - [24] Y. Oh, H.G. Yoon, S. Lee, H. Kim, J. Kim, Inkjet-printing of TiO₂ co-solvent ink: from uniform ink-droplet to TiO₂ photoelectrode for dye-sensitized solar cells, *J. Electrochem. Soc.* 159 (2011) 1, <http://dx.doi.org/10.1149/2.024201jes>.
 - [25] S.G. Hashmi, M. Özkan, J. Halme, Shaik Mohammed Zakeeruddin, S.M. Zakeeruddin, J. Paltakari, M. Grätzel, P.D. Lund, Dye-sensitized solar cells with inkjet-printed dyes, *Energy Environ. Sci.* 9 (2016) 2453–2462, <http://dx.doi.org/10.1039/C6EE00826G>.
 - [26] S.G. Hashmi, M. Özkan, J. Halme, K.D. Mistic, S.M. Zakeeruddin, J. Paltakari, M. Grätzel, P.D. Lund, High performance dye-sensitized solar cells with inkjet printed ionic liquid electrolyte, *Nano Energy* 17 (2015) 206–215, <http://dx.doi.org/10.1016/j.nanoen.2015.08.019>.
 - [27] G. Cummins, M. Desmulliez, Inkjet printing of conductive materials: a review, *Circuit World* 38 (4) (2012) 193–213, <http://dx.doi.org/10.1108/03056121211280413>.
 - [28] V.-D. Dao, H.-S. Choi, An optimum morphology of platinum nanoparticles with excellent electrocatalytic activity for a highly efficient dye-sensitized solar cell, *Electrochim. Acta* 93 (2013) 287, <http://dx.doi.org/10.1016/j.electacta.2013.01.085>.
 - [29] B. Derby, Inkjet printing of functional and structural materials: fluid property requirements, feature stability, and resolution, *Annu. Rev. Mater. Res.* 40 (2010) 395–414, <http://dx.doi.org/10.1146/annurev-matsci-070909-104502>.
 - [30] M. Özkan, K. Dimic-misic, A. Karakoc, S.G. Hashmi, P. Lund, T. Maloney, J. Paltakari, Rheological characterization of liquid electrolytes for drop-on demand inkjet printing, *Org. Electron.* 38 (2016) 307–315, <http://dx.doi.org/10.1016/j.orgel.2016.09.001>.
 - [31] B.J. de Gans, P.C. Duineveld, U.S. Schubert, Inkjet printing of polymers: state of the art and future developments, *Adv. Mater.* 16 (3) (2004) 203–213, <http://dx.doi.org/10.1002/adma.200300385>.
 - [32] N. Reis, C. Ainsley, B. Derby, Ink-jet delivery of particle suspensions by piezoelectric droplet ejectors, *J. Appl. Phys.* 97 (2005) 094903, <http://dx.doi.org/10.1063/1.1888026>.
 - [33] G. Cummins, R. Kay, J. Terry, M.P.Y. Desmulliez, A.J. Walton, Optimization and characterization of drop-on-demand inkjet printing process for platinum organometallic inks, in: IEEE 13th Electronics Packaging Technology Conference (EPTC), 2011, pp. 256–261, <http://dx.doi.org/10.1109/EPTC.2011.6184427>.
 - [34] S.D. Hoath, S. Jung, W.-K. Hsiao, I.M. Hutchings, How PEDOT: PSS solutions produce satellite-free inkjets, *Org. Electron.* 13 (12) (2012) 3259–3262, <http://dx.doi.org/10.1016/j.orgel.2012.10.004>.
 - [35] E. Özkol, A.M. Wätjen, R. Bermejo, M. Deluca, J. Ebert, R. Danzer, R. Telle, Mechanical characterisation of miniaturised direct inkjet printed 3Y-TZP specimens for microelectronic applications, *J. Eur. Ceram. Soc.* 30 (2010) 15, <http://dx.doi.org/10.1016/j.jeurceramsoc.2010.07.016>.
 - [36] J. Halme, P. Vahermaa, K. Miettunen, P. Lund, Device physics of dye solar cells, *Adv. Mater.* 22 (2010) 35, <http://dx.doi.org/10.1002/adma.201000726>.
 - [37] S.G. Hashmi, M. Özkan, J. Halme, J. Paltakari, P.D. Lund, Highly conductive, non-permeable, fiber based substrate for counter electrode application in dye-sensitized solar cells, *Nano Energy* 9 (2014) 212, <http://dx.doi.org/10.1016/j.nanoen.2014.07.013>.
 - [38] Fujifilm, Dimatix Materials Printer DMP-2800 Series User Manual, 2008.
 - [39] Fujifilm, Materials Printer & Cartridge DMP-2800 Series Printer & DMC-11600 Series Cartridge FAQs, 2008 available at: http://www.fujifilmusa.com/shared/bin/FAQs_DMP-2800_Series_Printer_DMC-11600+Series+Cartridge.pdf (Accessed: 05 December 2016).
 - [40] H. Wijshoff, The dynamics of the piezo inkjet printhead operation, *Phys. Rep.* 4–5 (2010) 491, <http://dx.doi.org/10.1016/j.physrep.2010.03.003>.
 - [41] D. Jang, D. Kim, J. Moon, Influence of fluid physical properties on ink-jet printability, *Langmuir* 25 (5) (2009) 2629, <http://dx.doi.org/10.1021/la900059m>.
 - [42] A. Karakoc, J. Freund, A direct simulation method for the effective in-plane stiffness of cellular materials, *Int. J. Appl. Mech.* 5 (3) (2013) 1350034, <http://dx.doi.org/10.1142/S1758825113500348>.
 - [43] E. Tekin, P.J. Smith, U.S. Schubert, Inkjet printing as a deposition and patterning tool for polymers and inorganic particles, *Soft Matter* 4 (2008) 4, <http://dx.doi.org/10.1039/B711984D>.
 - [44] J.F. Dijkstra, A. Pierik, Biomicrofluidics Fluid dynamical analysis of the distribution of ink jet printed biomolecules in microarray substrates for genotyping applications, *Biomicrofluidics* 2 (2008) 044101, <http://dx.doi.org/10.1063/1.2994715>.
 - [45] G.D. Martin, S.D. Hoath, I.M. Hutchings, Inkjet printing - the physics of manipulating liquid jets and drops, *J. J. Phys. Conf. Ser.* 105 (2008) 1, <http://dx.doi.org/10.1088/1742-6596/105/1/012001>.
 - [46] B. Derby, Inkjet printing ceramics: from drops to solid, *J. Eur. Ceram. Soc.* 31 (4) (2011) 2543–2550, <http://dx.doi.org/10.1016/j.jeurceramsoc.2011.01.016>.
 - [47] A. Kosmala, Q. Zhang, R. Wright, P. Kirby, Development of high concentrated aqueous silver nanofluid and inkjet printing on ceramic substrates, *Mater. Chem. Phys.* 132 (2012) 2–3, <http://dx.doi.org/10.1016/j.matchemphys.2011.12.013>.

Supplementary Data

Inkjet-printed Platinum Counter Electrodes for Dye-Sensitized Solar Cells

Merve Özkan,^{*a} Syed Ghufuran Hashmi,^b Janne Halme,^b Alp Karakoç,^{ac} Teemu Sarikka,^d Jouni

Paltakari^a and Peter D. Lund^b

^a Department of Forest Products Technology, Aalto University, Finland

^b Department of Applied Physics, Aalto University, Finland

^c Department of Civil and Environmental Engineering, University of California Los Angeles, USA

^c Department of Mechanical Engineering, Aalto University, Finland

Corresponding Author: merve.ozkan@aalto.fi, merve.ozkan85@gmail.com

Table S1: Statistical analysis of the EIS results: CE-CE cells

The corresponding nomenclature and specifications of the statistical testing can be found after each type of table.

Table S1 a: EIS data of CE-CE symmetrical cells						
<i>N</i>						
Inkjet-printed (10 DS)	3	R_S (Ω)	R_D (Ω)	R_{CT} (Ω)	R'_{CT} (Ωcm^2)	
	P1	10.0	0.52	7.0	4.2	
	P2	9.3	0.67	6.9	4.1	
	P3	10.5	0.60	7.3	4.4	
ave		9.9	0.60	7.1	4.2	
std		0.6	0.08	0.2	0.1	
std/ave		0.06	0.13	0.03	0.03	
sem		0.3	0.04	0.1	0.1	
95% CI		1.4	0.19	0.6	0.3	
Inkjet-printed (15 DS)	3	R_S (Ω)	R_D (Ω)	R_{CT} (Ω)	R'_{CT} (Ωcm^2)	
	P1	10.3	0.57	12.3	7.4	
	P2	10.8	0.51	12.9	7.7	
	P3	10.3	0.56	10.3	6.2	
ave		10.4	0.55	11.8	7.1	
std		0.3	0.03	1.4	0.8	
std/ave		0.03	0.06	0.12	0.12	
sem		0.2	0.02	0.8	0.5	
95% CI		0.7	0.08	3.4	2.0	
Inkjet-printed (20 DS)	3	R_S (Ω)	R_D (Ω)	R_{CT} (Ω)	R'_{CT} (Ωcm^2)	
	P1	10.9	0.53	14.3	8.6	
	P2	10.7	0.59	15.5	9.3	
	P3	10.7	0.57	15.4	9.3	
ave		10.7	0.56	15.1	9.0	
std		0.1	0.03	0.6	0.4	
std/ave		0.01	0.06	0.04	0.04	
sem		0.1	0.02	0.4	0.2	
95% CI		0.3	0.08	1.6	1.0	

Inkjet-printed (40 DS)		3	$R_S (\Omega)$	$R_D (\Omega)$	$R_{CT} (\Omega)$	$R'_{CT} (\Omega\text{cm}^2)$
	P1		13.9	0.73	41.2	24.7
	P2		11.9	0.69	44.4	26.7
	P3		12.1	0.81	49.0	29.4
ave			12.7	0.74	44.9	26.9
std			1.1	0.06	4.0	2.4
std/ave			0.09	0.08	0.09	0.09
sem			0.6	0.04	2.3	1.4
95% CI			2.8	0.15	9.8	5.9
Inkjet-printed (60 DS)		3	$R_S (\Omega)$	$R_D (\Omega)$	$R_{CT} (\Omega)$	$R'_{CT} (\Omega\text{cm}^2)$
	P1		11.9	-	76.2	45.7
	P2		12.3	-	81.3	48.8
	P3		10.7	-	57.5	34.5
ave			11.6	-	71.7	43.0
std			0.9	-	12.5	7.5
std/ave			0.07	-	0.17	0.17
sem			0.5	-	7.2	4.3
95% CI			2.1	-	31.1	18.6
Drop-cast		3	$R_S (\Omega)$	$R_D (\Omega)$	$R_{CT} (\Omega)$	$R'_{CT} (\Omega\text{cm}^2)$
	D1		10.5	0.57	9.3	5.6
	D2		10.9	0.59	7.4	4.4
	D3		10.9	0.49	14.5	8.7
ave			10.7	0.55	10.4	6.2
std			0.3	0.05	3.7	2.2
std/ave			0.02	0.10	0.35	0.35
sem			0.1	0.03	2.1	1.3
95% CI			0.6	0.13	9.1	5.5

Table S1 b: Average data and comparison of the drop-cast and 20 DS CE

	N	$R_S (\Omega)$	$R_D (\Omega)$	$R_{CT} (\Omega)$	$R'_{CT} (\Omega\text{cm}^2)$
10 DS	3	9.9 ± 0.6	0.6 ± 0.1	7.1 ± 0.2	4.2 ± 0.1
15 DS	3	10.4 ± 0.3	0.5 ± 0	11.8 ± 1.4	7.1 ± 0.8
20 DS	3	10.7 ± 0.1	0.6 ± 0	15.1 ± 0.6	9 ± 0.4
40 DS	3	12.7 ± 1.1	0.7 ± 0.1	44.9 ± 4	26.9 ± 2.4
60 DS	3	11.6 ± 0.9	-	71.7 ± 12.5	43 ± 7.5
Drop-cast	3	10.7 ± 0.3	0.5 ± 0.1	10.4 ± 3.7	6.2 ± 2.2
Drop-cast and inkjet-printed samples (20 DS)					
Difference		0.00 %	2.21 %	<u>45.06 %</u>	<u>45.06 %</u>
p -value		1.00	0.75	0.15	0.15

Nomenclature

N	number of samples
ave	average
std	standard deviation
std/ave	relative standard deviation compared to average
sem	standard error of the mean
95% CI	half of the full 95 % confidence interval based on Student's t-distribution
Difference	relative difference of average values: Printed vs drop-cast
p -value	calculated with two-tailed two-sample t-test with unequal variances

$R_S (\Omega)$	sheet resistance
$R_D (\Omega)$	diffusion resistance
$R_{CT} (\Omega)$	charge transfer resistance
$R'_{CT} (\Omega\text{cm}^2)$	charge transfer resistance for one electrode

About statistical analysis in Table S1

Statistical testing

Statistical confidence level	95 %	α : 0.05
t-test of two independent groups (Batch 1 vs Batch 2):		two-tailed, two-sample, unequal variances
t-test of the same group before and after aging:		two-tailed, paired t-test

Criteria for practically significant difference and acceptable sample-to-sample variation (std/ave)

Criteria	$R_S (\Omega)$	$R_D (\Omega)$	$R_{CT} (\Omega)$	$R'_{CT} (\Omega\text{cm}^2)$
Practically signif. difference	5 %	5 %	5 %	5 %
Acceptable level of std/ave	5 %	5 %	5 %	10 %

Underlined in the comparison tables are

- p -values lower than or equal to α (e.g. 0.05 for 5 % significance)
- Differences larger than the practical significance level
- Relative standard deviations larger than the acceptable value

CE-CE cells analysis

The systematical reduction in the drop spacing value during the inkjet printing procedure increased the deposited Pt amount resulting a step-wise decrease in the R'_{CT} values from the EIS measurements of CE-CE cells. Almost equally Pt loaded samples from each type (inkjet-printed CEs with 20 DS setting and reference drop-cast samples) showed no statistically significant difference in their average R'_{CT} values ($p = 0.15$).

Table S2: Statistical analysis of the IV measurements: aging test at 1 Sun and 35 °C for 1000

h

Table S2 a: Aging Test						
0 hours						
N						
Inkjet-printed (11 DS)	3	J_{SC} (mA/cm ²)	V_{OC} (V)	FF	η (%)	R_{cell} (Ω)
P1_11		14.0	0.738	0.716	7.42	40.8
P2_11		14.0	0.731	0.717	7.33	39.0
P3_11		14.7	0.729	0.695	7.46	41.9
ave		14.2	0.733	0.710	7.41	40.5
std		0.4	0.005	0.012	0.07	1.5
std/ave		0.03	0.006	0.018	0.01	0.04
sem		0.2	0.003	0.007	0.04	0.8
95% CI		1.0	0.012	0.031	0.17	3.6
Inkjet-printed (12 DS)	3	J_{SC} (mA/cm ²)	V_{OC} (V)	FF	η (%)	R_{cell} (Ω)
P1_12		13.2	0.734	0.705	6.85	45.2
P2_12		14.4	0.714	0.679	6.98	43.2
P3_12		13.0	0.741	0.710	6.82	47.0
ave		13.5	0.730	0.698	6.88	45.1
std		0.8	0.014	0.017	0.08	1.9
std/ave		0.06	0.019	0.024	0.01	0.04
sem		0.4	0.008	0.010	0.05	1.1
95% CI		1.9	0.035	0.042	0.20	4.7
Inkjet-printed (13 DS)	3	J_{SC} (mA/cm ²)	V_{OC} (V)	FF	η (%)	R_{cell} (Ω)
P1_13		13.3	0.744	0.702	6.96	49.9
P2_13		14.3	0.733	0.689	7.24	46.9
P3_13		14.2	0.734	0.685	7.15	48.1
ave		14.0	0.737	0.692	7.11	48.3
std		0.6	0.006	0.009	0.14	1.5
std/ave		0.04	0.009	0.013	0.02	0.03
sem		0.3	0.004	0.005	0.08	0.9
95% CI		1.4	0.016	0.023	0.36	3.7
Inkjet-printed (14 DS)	3	J_{SC} (mA/cm ²)	V_{OC} (V)	FF	η (%)	R_{cell} (Ω)
P1_14		15.1	0.729	0.662	7.30	48.0
P2_14		14.4	0.737	0.663	7.04	52.2
P3_14		15.4	0.717	0.689	7.60	42.3
ave		15.0	0.728	0.671	7.31	47.5
std		0.5	0.010	0.015	0.28	5.0
std/ave		0.033	0.013	0.023	0.038	0.105
sem		0.3	0.006	0.009	0.16	2.9
95% CI		1.2	0.024	0.038	0.70	12.4
Inkjet-printed (15 DS)	3	J_{SC} (mA/cm ²)	V_{OC} (V)	FF	η (%)	R_{cell} (Ω)
P1_15		14.2	0.739	0.691	7.27	48.3
P2_15		14.8	0.723	0.690	7.38	43.1
P3_15		13.9	0.741	0.691	7.11	47.5
ave		14.3	0.734	0.691	7.25	46.3
std		0.4	0.009	0.004	0.14	2.8
std/ave		0.031	0.013	0.001	0.019	0.061
sem		0.3	0.005	0.000	0.08	1.6
95% CI		1.1	0.024	0.001	0.34	7.0
Drop-cast	3	J_{SC} (mA/cm ²)	V_{OC} (V)	FF	η (%)	R_{cell} (Ω)
D1		13.6	0.727	0.705	6.98	48.2
D2		13.8	0.746	0.714	7.38	43.0
D3		15.1	0.720	0.673	7.33	46.4
ave		14.2	0.731	0.698	7.23	45.8
std		0.8	0.013	0.022	0.22	2.6
std/ave		0.057	0.018	0.031	0.030	0.057
sem		0.5	0.008	0.012	0.13	1.5
95% CI		2.0	0.033	0.054	0.54	6.5

1000 hours						
N						
Inkjet-printed (11 DS)	3	J_{SC} (mA/cm²)	V_{OC} (V)	FF	η (%)	R_{cell} (Ω)
P1_11		14.2	0.690	0.749	7.33	30.1
P2_11		12.1	0.721	0.753	6.55	36.5
P3_11		14.5	0.694	0.749	7.55	30.3
ave		13.6	0.702	0.751	7.14	32.3
std		1.3	0.017	0.002	0.53	3.6
std/ave		0.099	0.024	0.003	0.074	0.113
sem		0.8	0.010	0.001	0.30	2.1
95% CI		3.3	0.042	0.006	1.31	9.0
Inkjet-printed (12 DS)	3	J_{SC} (mA/cm²)	V_{OC} (V)	FF	η (%)	R_{cell} (Ω)
P1_12		13.2	0.722	0.728	6.93	37.7
P2_12		14.0	0.701	0.710	6.96	34.4
P3_12		13.5	0.701	0.732	6.93	35.0
ave		13.6	0.708	0.723	6.94	35.7
std		0.4	0.012	0.012	0.02	1.8
std/ave		0.030	0.018	0.016	0.002	0.049
sem		0.2	0.007	0.007	0.01	1.0
95% CI		1.0	0.031	0.029	0.04	4.4
Inkjet-printed (13 DS)	3	J_{SC} (mA/cm²)	V_{OC} (V)	FF	η (%)	R_{cell} (Ω)
P1_13		14.9	0.694	0.729	7.51	32.6
P2_13		15.4	0.681	0.704	7.37	38.3
P3_13		14.9	0.672	0.711	7.11	35.4
ave		15.0	0.682	0.715	7.33	35.4
std		0.3	0.011	0.013	0.21	2.9
std/ave		0.019	0.016	0.018	0.028	0.081
sem		0.2	0.006	0.007	0.12	1.7
95% CI		0.7	0.026	0.031	0.51	7.1
Inkjet-printed (14 DS)	3	J_{SC} (mA/cm²)	V_{OC} (V)	FF	η (%)	R_{cell} (Ω)
P1_14		16.1	0.699	0.707	7.94	36.3
P2_14		14.9	0.699	0.705	7.34	37.6
P3_14		13.4	0.720	0.692	6.67	46.6
ave		14.8	0.706	0.701	7.31	40.2
std		1.3	0.012	0.008	0.63	5.6
std/ave		0.091	0.018	0.012	0.086	0.140
sem		0.8	0.007	0.005	0.36	3.3
95% CI		3.3	0.031	0.020	1.57	14.0
Inkjet-printed (15 DS)	3	J_{SC} (mA/cm²)	V_{OC} (V)	FF	η (%)	R_{cell} (Ω)
P1_15		14.6	0.696	0.716	7.28	36.3
P2_15		14.4	0.703	0.711	7.20	40.2
P3_15		12.8	0.721	0.708	6.54	47.2
ave		13.9	0.707	0.711	7.01	41.2
std		1.0	0.013	0.004	0.41	5.5
std/ave		0.071	0.018	0.006	0.058	0.134
sem		0.6	0.008	0.002	0.24	3.2
95% CI		2.5	0.032	0.010	1.01	13.7
Drop-cast	3	J_{SC} (mA/cm²)	V_{OC} (V)	FF	η (%)	R_{cell} (Ω)
D1		15.1	0.675	0.734	7.50	32.5
D2		15.2	0.689	0.734	7.67	32.4
D3		11.9	0.735	0.755	6.63	38.3
ave		14.1	0.699	0.741	7.27	34.4
std		1.9	0.031	0.012	0.56	3.4
std/ave		0.132	0.045	0.016	0.077	0.099
sem		1.1	0.018	0.007	0.32	2.0
95% CI		4.6	0.078	0.030	1.39	8.4

Table S2 b: Comparison of inkjet printed and drop-cast cells during the aging test

0 hours

	<i>N</i>	<i>J_{SC}</i> (mA/cm ²)	<i>V_{OC}</i> (V)	<i>FF</i>	<i>η</i> (%)	<i>R_{cell}</i> (Ω)
Inkjet-printed (11 DS)	3	14.2 ± 0.4	733 ± 5	71 ± 1.2	7.41 ± 0.07	41 ± 1
Drop-cast	3	14.2 ± 0.8	731 ± 13	70 ± 2.2	7.23 ± 0.22	46 ± 3
Difference		0.39 %	0.24 %	1.71 %	2.44 %	<u>-11.57 %</u>
<i>p</i> -value		0.922	0.843	0.465	0.296	0.051
Inkjet-printed (12 DS)	3	13.5 ± 0.8	730 ± 14	69.8 ± 1.7	6.88 ± 0.08	45 ± 2
Drop-cast	3	14.2 ± 0.8	731 ± 13	70 ± 2.2	7.23 ± 0.22	46 ± 3
Difference		-4.64 %	-0.19 %	0.06 %	-4.77 %	-1.57 %
<i>p</i> -value		0.361	0.908	0.979	0.099	0.721
Inkjet-printed (13 DS)	3	14 ± 0.6	737 ± 6	69.2 ± 0.9	7.11 ± 0.14	48 ± 1
Drop-cast	3	14.2 ± 0.8	731 ± 13	70 ± 2.2	7.23 ± 0.22	46 ± 3
Difference		-1.59 %	0.77 %	-0.83 %	-1.58 %	<u>5.37 %</u>
<i>p</i> -value		0.714	0.556	0.702	0.498	0.245
Inkjet-printed (14 DS)	3	15 ± 0.5	728 ± 10	67.1 ± 1.5	7.31 ± 0.28	47 ± 5
Drop-cast	3	14.2 ± 0.8	731 ± 13	70 ± 2.2	7.23 ± 0.22	46 ± 3
Difference		<u>5.51 %</u>	-0.44 %	-3.83 %	1.13 %	3.60 %
<i>p</i> -value		0.239	0.752	0.163	0.713	0.646
Inkjet-printed (15 DS)	3	14.3 ± 0.4	734 ± 9	69.1 ± 0	7.25 ± 0.14	46 ± 3
Drop-cast	3	14.2 ± 0.8	731 ± 13	70 ± 2.2	7.23 ± 0.22	46 ± 3
Difference		0.82 %	0.44 %	-1.00 %	0.35 %	1.01 %
<i>p</i> -value		0.841	0.750	0.634	0.876	0.846

1000 hours

	<i>N</i>	<i>J_{SC}</i> (mA/cm ²)	<i>V_{OC}</i> (V)	<i>FF</i>	<i>η</i> (%)	<i>R_{cell}</i> (Ω)
Inkjet-printed (11 DS)	3	13.6 ± 1.3	702 ± 17	75.1 ± 0.2	7.14 ± 0.53	32 ± 4
Drop-cast	3	14.1 ± 1.9	699 ± 31	74.1 ± 1.2	7.27 ± 0.56	34 ± 3
Difference		-3.53 %	0.32 %	1.26 %	-1.70 %	<u>-6.24 %</u>
<i>p</i> -value		0.728	0.921	0.315	0.795	0.497
Inkjet-printed (12 DS)	3	13.6 ± 0.4	708 ± 12	72.3 ± 1.2	6.94 ± 0.02	36 ± 2
Drop-cast	3	14.1 ± 1.9	699 ± 31	74.1 ± 1.2	7.27 ± 0.56	34 ± 3
Difference		-3.76 %	1.25 %	-2.44 %	-4.52 %	3.72 %
<i>p</i> -value		0.673	0.689	0.140	0.417	0.603
Inkjet-printed (13 DS)	3	15 ± 0.3	682 ± 11	71.5 ± 1.3	7.33 ± 0.21	35 ± 3
Drop-cast	3	14.1 ± 1.9	699 ± 31	74.1 ± 1.2	7.27 ± 0.56	34 ± 3
Difference		<u>6.71 %</u>	-2.44 %	-3.58 %	0.87 %	2.96 %
<i>p</i> -value		0.471	0.452	0.059	0.868	0.712
Inkjet-printed (14 DS)	3	14.8 ± 1.3	706 ± 12	70.1 ± 0.8	7.31 ± 0.63	40 ± 6
Drop-cast	3	14.1 ± 1.9	699 ± 31	74.1 ± 1.2	7.27 ± 0.56	34 ± 3
Difference		4.93 %	0.96 %	<u>-5.40 %</u>	0.67 %	<u>16.68 %</u>
<i>p</i> -value		0.629	0.755	<u>0.013</u>	0.926	0.220
Inkjet-printed (15 DS)	3	13.9 ± 1	707 ± 13	71.1 ± 0.4	7.01 ± 0.41	41 ± 6
Drop-cast	3	14.1 ± 1.9	699 ± 31	74.1 ± 1.2	7.27 ± 0.56	34 ± 3
Difference		-1.00 %	1.08 %	-4.05 %	-3.58 %	<u>19.78 %</u>
<i>p</i> -value		0.915	0.729	<u>0.040</u>	0.554	0.158

Table S2 c: Comparison of the final and initial performance for each type of cells						
	<i>N</i>	<i>J_{sc}</i> (mA/cm ²)	<i>V_{oc}</i> (V)	<i>FF</i>	<i>η</i> (%)	<i>R_{cell}</i> (Ω)
Inkjet-printed (11 DS)						
0 hours	3	14.2 ± 0.4	733 ± 5	71 ± 1.2	7.41 ± 0.07	41 ± 1
std/ave		2.9 %	0.65 %	1.76 %	0.9 %	3.6 %
1000 hours	3	13.6 ± 1.3	702 ± 17	75.1 ± 0.2	7.14 ± 0.53	32 ± 4
std/ave		<u>9.9 %</u>	2.42 %	0.33 %	<u>7.4 %</u>	<u>11.3 %</u>
Difference		-4.6 %	-4.3 %	<u>5.8 %</u>	-3.5 %	<u>-20.4 %</u>
<i>p</i> -value		0.492	0.076	<u>0.026</u>	0.481	<u>0.044</u>
Inkjet-printed (12 DS)						
0 hours	3	13.5 ± 0.8	730 ± 14	69.8 ± 1.7	6.88 ± 0.08	45 ± 2
std/ave		<u>5.6 %</u>	1.93 %	2.43 %	1.2 %	4.2 %
1000 hours	3	13.6 ± 0.4	708 ± 12	72.3 ± 1.2	6.94 ± 0.02	36 ± 2
std/ave		3.0 %	1.76 %	1.64 %	0.2 %	4.9 %
Difference		0.2 %	-3.0 %	3.6 %	0.8 %	<u>-20.9 %</u>
<i>p</i> -value		0.961	0.117	0.112	0.362	<u>0.003</u>
Inkjet-printed (13 DS)						
0 hours	3	14 ± 0.6	737 ± 6	69.2 ± 0.9	7.11 ± 0.14	48 ± 1
std/ave		4.0 %	0.86 %	1.32 %	2.0 %	3.0 %
1000 hours	3	15 ± 0.3	682 ± 11	71.5 ± 1.3	7.33 ± 0.21	35 ± 3
std/ave		1.9 %	1.56 %	1.77 %	2.8 %	<u>8.1 %</u>
Difference		<u>7.7 %</u>	<u>-7.4 %</u>	3.3 %	3.0 %	<u>-26.6 %</u>
<i>p</i> -value		0.062	<u>0.003</u>	0.071	0.220	<u>0.006</u>
Inkjet-printed (14 DS)						
0 hours	3	15 ± 0.5	728 ± 10	67.1 ± 1.5	7.31 ± 0.28	47 ± 5
std/ave		3.3 %	1.34 %	2.28 %	3.8 %	<u>10.5 %</u>
1000 hours	3	14.8 ± 1.3	706 ± 12	70.1 ± 0.8	7.31 ± 0.63	40 ± 6
std/ave		<u>9.1 %</u>	1.76 %	1.17 %	<u>8.6 %</u>	<u>14.0 %</u>
Difference		-1.3 %	-3.0 %	4.5 %	0.1 %	<u>-15.4 %</u>
<i>p</i> -value		0.836	0.078	0.055	0.991	0.168
Inkjet-printed (15 DS)						
0 hours	3	14.3 ± 0.4	734 ± 9	69.1 ± 0	7.25 ± 0.14	46 ± 3
std/ave		3.1 %	1.29 %	0.06 %	1.9 %	<u>6.1 %</u>
1000 hours	3	13.9 ± 1	707 ± 13	71.1 ± 0.4	7.01 ± 0.41	41 ± 6
std/ave		<u>7.1 %</u>	1.84 %	0.57 %	<u>5.8 %</u>	<u>13.4 %</u>
Difference		-2.5 %	-3.7 %	3.0 %	-3.4 %	<u>-10.9 %</u>
<i>p</i> -value		0.611	<u>0.047</u>	<u>0.012</u>	0.407	0.253
Drop-cast						
0 hours	3	14.2 ± 0.8	731 ± 13	70 ± 2.2	7.23 ± 0.22	46 ± 3
std/ave		<u>5.7 %</u>	1.81 %	3.10 %	3.0 %	<u>5.7 %</u>
1000 hours	3	14.1 ± 1.9	699 ± 31	74.1 ± 1.2	7.27 ± 0.56	34 ± 3
std/ave		<u>13.2 %</u>	4.5 %	1.6 %	<u>7.7 %</u>	<u>9.9 %</u>
Difference		-0.7 %	-4.4 %	<u>6.2 %</u>	0.5 %	<u>-24.9 %</u>
<i>p</i> -value		0.936	0.214	0.052	0.921	<u>0.011</u>

Nomenclature

N	number of samples
ave	average
std	standard deviation
std/ave	relative standard deviation compared to average
sem	standard error of the mean
95% CI	half of the full 95 % confidence interval based on Student's t-distribution
Difference	relative difference of average values: Printed vs drop-cast, or initial vs final.
p -value	calculated with two-tailed two-sample t-test with unequal variances
J_{sc}	short circuit current density
V_{oc}	open circuit voltage
FF	fill factor
η	efficiency
R_{cell}	cell resistance (inverse slope of the IV curve at V_{oc})

About statistical analysis in Table S2

Statistical testing

Statistical confidence level	95 %	α : 0.05
t-test of two independent groups (Batch 1 vs Batch 2):		two-tailed, two-sample, unequal variances
t-test of the same group before and after aging:		two-tailed, paired t-test

Criteria for practically significant difference and acceptable sample-to-sample variation (std/ave)

Criteria	J_{sc} (mA/cm ²)	V_{oc} (mV)	FF (%)	η (%)	R_{cell} (Ω)
Practically signif. difference	5 %	5 %	5 %	5 %	5 %
Acceptable level of std/ave	5 %	5 %	5 %	10 %	15 %

Underlined in the comparison tables are

- p -values lower than or equal to α (e.g. 0.05 for 5 % significance)
- Differences larger than the practical significance level
- Relative standard deviations larger than the acceptable value

IV measurement analysis of aging test

All the inkjet-printed devices employ more than twice the Pt loading amount as compared to the drop-cast samples, yet show no significant rise in the device efficiency. Therefore, the catalyst might have reached a saturation point beyond which the over potential at the CE is insignificant and does not noticeably affect the IV curve. All the devices remained stable during the aging tests.

Table S3: Statistical analysis of the EIS results: aging test at 1 Sun and 35 °C for 1000 h

Initial data	N	PHOTOELECTRODE										COUNTER ELECTRODE					DIFFUSION			TOTAL R
Printed (11-15 DS)	3	R_s (Ω)	R_{PE} (Ω)	$Q_{CPE,PE}$	$\beta_{CPE,PE}$	C_{PE} (F) *	τ_{PE} (s) *	f_{PE}^* (Hz) *	R_{CE} (Ω)	$Q_{CPE,CE}$	$\beta_{CPE,CE}$	C_{CE} (F) *	τ_{CE} (s) *	f_{CE}^* (Hz) *	R_D (Ω)	τ_D (s)	f_D^* (Hz) *	R_{TOT} (Ω)		
P1_11		7.770	16.780	1.050E-03	0.950	8.494E-04	1.425E-02	11.17	11.640	3.365E-05	0.829	6.706E-06	7.806E-05	2039	3.546	0.668	2.382E-01	39.74		
P2_11		8.166	15.920	1.108E-03	0.950	8.954E-04	1.426E-02	11.16	8.459	4.465E-05	0.808	6.832E-06	5.779E-05	2754	3.002	0.529	3.009E-01	35.55		
P3_11		8.988	18.580	1.072E-03	0.944	8.499E-04	1.579E-02	10.08	11.720	3.141E-05	0.839	6.921E-06	8.112E-05	1962	3.610	0.665	2.393E-01	42.90		
ave		8.3	17.1	1.077E-03	0.948	8.649E-04	1.477E-02	10.8	10.61	3.657E-05	0.826	6.820E-06	7.232E-05	2252	3.39	0.62	2.595E-01	39.4		
std		0.6	1.4	2.948E-05	0.004	2.644E-05	8.871E-04	0.6	1.86	7.085E-06	0.016	1.083E-07	1.268E-05	437	0.33	0.08	3.592E-02	3.7		
std/ave		7.5 %	7.9 %	2.7 %	0.4 %	3.1 %	6.0 %	5.8 %	17.5 %	19.4 %	2.0 %	1.6 %	17.5 %	19.4 %	9.9 %	12.8 %	13.8 %	9.4 %		
sem		0.4	0.8	1.702E-05	0.002	1.526E-05	5.122E-04	0.4	1.07	4.091E-06	0.009	6.254E-08	7.320E-06	252	0.19	0.05	2.074E-02	2.1		
95% CI		1.5	3.4	7.323E-05	0.009	6.567E-05	2.204E-03	1.6	4.62	1.760E-05	0.040	2.691E-07	3.150E-05	1085	0.83	0.20	8.924E-02	9.2		
P1_12		10.020	18.730	9.303E-04	0.950	7.508E-04	1.406E-02	11.32	9.813	3.060E-05	0.835	5.173E-06	6.057E-05	2627	2.948	0.419	3.794E-01	41.51		
P1_12		9.941	16.740	1.052E-03	0.950	8.508E-04	1.424E-02	11.17	9.307	3.194E-05	0.841	6.850E-06	3.676E-05	2496	2.315	0.347	4.590E-01	38.30		
P1_12		9.172	18.950	9.747E-04	0.946	7.765E-04	1.471E-02	10.82	11.860	3.528E-05	0.817	6.177E-06	7.326E-05	2173	3.150	0.592	2.689E-01	43.13		
ave		9.7	18.1	9.856E-04	0.949	7.927E-04	1.434E-02	11.1	10.33	3.261E-05	0.831	6.400E-06	6.586E-05	2432	2.80	0.45	3.691E-01	41.0		
std		0.5	1.2	6.152E-05	0.002	5.195E-05	3.363E-04	0.3	1.35	2.407E-06	0.012	3.900E-07	6.599E-06	234	0.44	0.13	9.542E-02	2.5		
std/ave		4.8 %	6.7 %	6.2 %	0.2 %	6.6 %	2.3 %	2.3 %	13.1 %	7.4 %	1.5 %	6.1 %	10.0 %	9.6 %	15.5 %	27.8 %	25.9 %	6.0 %		
sem		0.3	0.7	3.552E-05	0.001	2.999E-05	1.942E-04	0.1	0.78	1.390E-06	0.007	2.252E-07	3.810E-06	135	0.25	0.07	5.509E-02	1.4		
95% CI		1.2	3.0	1.528E-04	0.005	1.291E-04	8.355E-04	0.6	3.36	5.980E-06	0.031	9.688E-07	1.639E-05	582	1.08	0.31	2.370E-01	6.1		
P1_13		8.859	16.870	1.008E-03	0.941	7.798E-04	1.315E-02	12.10	12.090	2.746E-05	0.834	5.585E-06	6.752E-05	2357	3.014	0.571	2.787E-01	40.83		
P2_13		10.930	17.950	9.640E-04	0.934	7.228E-04	1.297E-02	12.27	13.170	3.283E-05	0.804	4.993E-06	6.576E-05	2420	3.046	0.614	2.591E-01	45.10		
P3_13		10.350	17.430	1.119E-03	0.941	8.728E-04	1.521E-02	10.46	11.370	2.382E-05	0.844	5.237E-06	5.954E-05	2673	3.521	0.593	2.683E-01	42.67		
ave		10.0	17.4	1.030E-03	0.938	7.918E-04	1.378E-02	11.6	12.21	2.804E-05	0.828	5.271E-06	6.427E-05	2484	3.19	0.59	2.687E-01	42.9		
std		1.1	0.5	8.019E-05	0.004	7.576E-05	1.244E-03	1.0	0.91	4.534E-06	0.021	2.974E-07	4.191E-06	167	0.28	0.02	9.826E-03	2.1		
std/ave		10.6 %	3.1 %	7.8 %	0.4 %	9.6 %	9.0 %	8.6 %	7.4 %	16.2 %	2.5 %	5.6 %	6.5 %	6.7 %	8.9 %	3.7 %	3.7 %	5.0 %		
sem		0.6	0.3	4.630E-05	0.002	4.374E-05	7.184E-04	0.6	0.52	2.618E-06	0.012	1.717E-07	2.420E-06	96	0.16	0.01	5.673E-03	1.2		
95% CI		2.6	1.3	1.992E-04	0.010	1.882E-04	3.091E-03	2.5	2.25	1.126E-05	0.051	7.388E-07	1.041E-05	415	0.71	0.05	2.441E-02	5.3		
P1_14		11.400	18.230	1.106E-03	0.937	8.514E-04	1.552E-02	10.25	11.840	2.660E-05	0.835	5.405E-06	6.400E-05	2487	3.227	0.556	2.861E-01	44.70		
P2_14		10.820	18.150	1.011E-03	0.944	7.974E-04	1.447E-02	11.00	13.830	2.195E-05	0.856	5.610E-06	7.759E-05	2051	3.163	0.576	2.762E-01	45.96		
P3_14		12.850	15.320	9.678E-04	0.948	7.679E-04	1.176E-02	13.53	8.536	3.302E-05	0.808	4.737E-06	4.044E-05	3936	2.531	0.493	3.227E-01	39.24		
ave		11.7	17.2	1.028E-03	0.943	8.056E-04	1.392E-02	11.6	11.40	2.719E-05	0.833	5.251E-06	6.068E-05	2825	2.97	0.54	2.950E-01	43.3		
std		1.0	1.7	7.095E-05	0.005	4.234E-05	1.938E-03	1.7	2.67	5.559E-06	0.024	4.567E-07	1.880E-05	987	0.38	0.04	2.446E-02	3.6		
std/ave		8.9 %	9.6 %	6.9 %	0.6 %	5.3 %	13.9 %	14.8 %	23.5 %	20.4 %	2.9 %	8.7 %	31.0 %	34.9 %	12.9 %	8.0 %	8.3 %	8.3 %		
sem		0.6	1.0	4.096E-05	0.003	2.444E-05	1.119E-03	1.0	1.54	3.210E-06	0.014	2.637E-07	1.085E-05	570	0.22	0.02	1.412E-02	2.1		
95% CI		2.6	4.1	1.763E-04	0.014	1.052E-04	4.815E-03	4.3	6.64	1.381E-05	0.060	1.134E-06	4.670E-05	2451	0.96	0.11	6.077E-02	8.9		
P1_15		10.510	16.820	1.109E-03	0.944	8.774E-04	1.476E-02	10.78	13.230	3.384E-05	0.803	5.083E-06	6.725E-05	2367	2.882	0.575	2.766E-01	43.44		
P2_15		9.310	17.440	1.085E-03	0.919	7.667E-04	1.337E-02	11.90	13.650	2.289E-05	0.838	4.817E-06	6.576E-05	2420	2.974	0.625	2.546E-01	43.37		
P3_15		9.298	16.490	1.147E-03	0.946	9.134E-04	1.506E-02	10.57	11.120	2.371E-05	0.851	5.580E-06	6.205E-05	2565	3.393	0.599	2.656E-01	40.30		
ave		9.7	16.9	1.114E-03	0.937	8.525E-04	1.440E-02	11.1	12.67	2.682E-05	0.830	5.160E-06	6.502E-05	2451	3.08	0.60	2.656E-01	42.4		
std		0.7	0.5	3.137E-05	0.015	7.649E-05	9.018E-04	0.7	1.36	6.099E-06	0.025	3.873E-07	2.677E-06	103	0.27	0.02	1.103E-02	1.8		
std/ave		7.2 %	2.9 %	2.8 %	1.6 %	9.0 %	6.3 %	6.5 %	10.7 %	22.7 %	3.0 %	7.5 %	4.1 %	4.2 %	8.8 %	4.2 %	4.2 %	4.2 %		
sem		0.4	0.3	1.811E-05	0.009	4.416E-05	5.207E-04	0.4	0.78	3.522E-06	0.014	2.236E-07	1.546E-06	59	0.16	0.01	6.368E-03	1.0		
95% CI		1.7	1.2	7.792E-05	0.037	1.900E-04	2.240E-03	1.8	3.37	1.515E-05	0.062	9.621E-07	6.650E-06	255	0.68	0.06	2.740E-02	4.5		
Drop-cast	3	R_s (Ω)	R_{PE} (Ω)	$Q_{CPE,PE}$	$\beta_{CPE,PE}$	C_{PE} (F) *	τ_{PE} (s) *	f_{PE}^* (Hz) *	R_{CE} (Ω)	$Q_{CPE,CE}$	$\beta_{CPE,CE}$	C_{CE} (F) *	τ_{CE} (s) *	f_{CE}^* (Hz) *	R_D (Ω)	τ_D (s)	f_D^* (Hz) *	R_{TOT} (Ω)		
D1		11.230	15.630	9.955E-04	0.923	7.023E-04	1.098E-02	14.50	11.760	4.124E-05	0.786	5.182E-06	6.094E-05	2612	2.354	0.507	3.136E-01	40.97		
D2		10.480	17.480	1.190E-03	0.939	9.247E-04	1.616E-02	9.85	12.210	4.951E-05	0.806	8.314E-06	1.015E-04	1568	3.143	0.617	2.579E-01	43.31		
D3		9.559	15.320	1.096E-03	0.936	8.277E-04	1.268E-02	12.55	11.300	5.133E-05	0.785	6.662E-06	7.528E-05	2114	3.439	0.643	2.475E-01	39.62		
ave		10.4	16.1	1.094E-03	0.932	8.182E-04	1.327E-02	12.3	11.8	4.736E-05	0.792	6.719E-06	7.924E-05	2098	2.98	0.59	2.730E-01	41.3		
std		0.8	1.2	9.709E-05	0.009	1.115E-04	2.643E-03	2.3	0.5	5.375E-06	0.012	1.567E-06	2.058E-05	522	0.56	0.07	3.558E-02	1.9		
std/ave		8.0 %	7.2 %	8.9 %	0.9 %	13.6 %	19.9 %	19.0 %	3.9 %	11.3 %	1.5 %	23.3 %	26.0 %	24.9 %	18.8 %	12.2 %	13.0 %	4.5 %		
sem		0.5	0.7	5.606E-05	0.005	6.436E-05	1.526E-03	1.3	0.3	3.103E-06	0.007	9.046E-07	1.188E-05	301	0.32	0.04	2.054E-02	1.1		
95% CI		2.1	2.9	2.412E-04	0.021	2.769E-04	6.567E-03	5.8	1.1	1.335E-05	0.029	3.892E-06	5.111E-05	1297	1.39	0.18	8.838E-02	4.6		

* Quantities marked with "*" are calculated from the values unmarked values in the previous columns. The unmarked values were obtained by fitting an equivalent circuit model to the measured EIS data.

Comparison of two groups

		SERIES R							PHOTOELECTRODE							COUNTER ELECTRODE							DIFFUSION			TOTAL R
Initial data	N	R_s (Ω)	R_{PE} (Ω)	$Q_{CPE,PE}$ ($\cdot 10^{-3}$)	$\beta_{CPE,PE}$	C_{PE} (mF) *	τ_{PE} (ms) *	f_{PE}^+ (Hz) *	R_{CE} (Ω)	$Q_{CPE,CE}$ ($\cdot 10^{-3}$)	$\beta_{CPE,CE}$	C_{CE} (μ F) *	τ_{CE} (μ s) *	f_{CE}^+ (kHz) *	R_D (Ω)	τ_D (s)	f_D^+ (mHz) *	R_{TOT} (Ω)								
Printed (11-15 DS)																										
11 DS	3	8.3 ± 0.6	17.1 ± 1.4	1.08 ± 0.03	0.95 ± 0	0.86 ± 0.03	14.8 ± 0.9	11 ± 1	10.61 ± 1.86	0.04 ± 0.01	0.83 ± 0.02	6.8 ± 0.1	72.3 ± 12.7	2 ± 0	3.4 ± 0.3	0.62 ± 0.08	259 ± 36	39 ± 4								
	std/ave	7 %	8 %	3 %	0 %	3 %	6 %	6 %	<u>18 %</u>	<u>19 %</u>	2 %	2 %	<u>18 %</u>	<u>19 %</u>	10 %	<u>13 %</u>	<u>14 %</u>	9 %								
12 DS	3	9.7 ± 0.5	18.1 ± 1.2	0.99 ± 0.06	0.95 ± 0	0.79 ± 0.05	14.3 ± 0.3	11 ± 0	10.33 ± 1.35	0.03 ± 0	0.83 ± 0.01	6.4 ± 0.4	65.9 ± 6.6	2 ± 0	2.8 ± 0.4	0.45 ± 0.13	369 ± 95	41 ± 2								
	std/ave	5 %	7 %	6 %	0 %	7 %	2 %	2 %	<u>13 %</u>	7 %	1 %	6 %	<u>10 %</u>	10 %	<u>16 %</u>	<u>28 %</u>	<u>26 %</u>	6 %								
13 DS	3	10 ± 1.1	17.4 ± 0.5	1.03 ± 0.08	0.94 ± 0	0.79 ± 0.08	13.8 ± 1.2	12 ± 1	12.21 ± 0.91	0.03 ± 0	0.83 ± 0.02	5.3 ± 0.3	64.3 ± 4.2	2 ± 0	3.2 ± 0.3	0.59 ± 0.02	269 ± 10	43 ± 2								
	std/ave	<u>11 %</u>	3 %	8 %	0 %	10 %	9 %	9 %	7 %	<u>16 %</u>	3 %	6 %	7 %	7 %	9 %	4 %	4 %	5 %								
14 DS	3	11.7 ± 1	17.2 ± 1.7	1.03 ± 0.07	0.94 ± 0.01	0.81 ± 0.04	13.9 ± 1.9	12 ± 2	11.4 ± 2.67	0.03 ± 0.01	0.83 ± 0.02	5.3 ± 0.5	60.7 ± 18.8	3 ± 1	3 ± 0.4	0.54 ± 0.04	295 ± 24	43 ± 4								
	std/ave	9 %	10 %	7 %	1 %	5 %	<u>14 %</u>	<u>15 %</u>	<u>23 %</u>	<u>20 %</u>	3 %	9 %	<u>31 %</u>	<u>35 %</u>	<u>13 %</u>	8 %	8 %	8 %								
15 DS	3	9.7 ± 0.7	16.9 ± 0.5	1.11 ± 0.03	0.94 ± 0.01	0.85 ± 0.08	14.4 ± 0.9	11 ± 1	12.67 ± 1.36	0.03 ± 0.01	0.83 ± 0.02	5.2 ± 0.4	65 ± 2.7	2 ± 0	3.1 ± 0.3	0.6 ± 0.02	266 ± 11	42 ± 2								
	std/ave	7 %	3 %	3 %	2 %	9 %	6 %	6 %	<u>11 %</u>	<u>23 %</u>	3 %	8 %	4 %	4 %	9 %	4 %	4 %	4 %								
Drop-cast	3	10.4 ± 0.8	16.1 ± 1.2	1.09 ± 0.1	0.93 ± 0.01	0.82 ± 0.11	13.3 ± 2.6	12 ± 2	11.76 ± 0.46	0.05 ± 0.01	0.79 ± 0.01	6.7 ± 1.6	79.2 ± 20.6	2 ± 1	3 ± 0.6	0.59 ± 0.07	273 ± 36	41 ± 2								
	std/ave	8 %	7 %	9 %	1 %	<u>14 %</u>	<u>20 %</u>	<u>19 %</u>	4 %	<u>11 %</u>	1 %	<u>23 %</u>	<u>26 %</u>	<u>25 %</u>	<u>19 %</u>	<u>12 %</u>	<u>13 %</u>	5 %								
15 DS and drop-cast difference		-6.9 %	4.8 %	1.9 %	0.4 %	4.2 %	8.5 %	-9.9 %	7.7 %	<u>-43.4 %</u>	4.8 %	<u>-23.2 %</u>	-17.9 %	16.8 %	3.5 %	1.8 %	-2.7 %	2.6 %								
p-value		0.320	0.376	0.759	0.707	0.686	0.546	0.468	0.367	0.012	0.101	0.223	0.354	0.363	0.791	0.827	0.759	0.514								

* Quantities marked with "*" are calculated from the values unmarked values in the previous columns. The unmarked values were obtained by fitting an equivalent circuit model to the measured EIS data.

EIS measurement analysis of the initial data before the aging test

R_{CE} ($=R'_{CT}$) of most of the inkjet printed cells exhibited low or close to 'acceptable' standard deviations and the total cell resistances of all devices exhibited minute variations. 15 DS inkjet-printed sample group, which has the lowest Pt loading amongst the inkjet printed samples (double Pt loading as the drop-cast sample), was significantly different from the drop-cast samples in terms of Pt/electrolyte interfacial capacitance, Q_{CPE} , however, the charge transfer resistance R_{CE} showed no statistically significant difference..

1000h	N	SERIES R	PHOTOELECTRODE						COUNTER ELECTRODE						DIFFUSION			TOTAL R
Printed (11-15 DS)	3	$R_s (\Omega)$	$R_{PE} (\Omega)$	$Q_{CPE,PE}$	$\beta_{CPE,PE}$	$C_{PE} (F)^*$	$\tau_{PE} (s)^*$	$f_{PE}^* (Hz)$	$R_{CE} (\Omega)$	$Q_{CPE,CE}$	$\beta_{CPE,CE}$	$C_{CE} (F)^*$	$\tau_{CE} (s)^*$	$f_{CE}^* (Hz)$	$R_D (\Omega)$	$\tau_D (s)$	$f_D^* (Hz)$	$R_{TOT} (\Omega)$
P1_11		9.192	13.140	1.085E-03	0.953	8.612E-04	1.159E-02	13.75	4.636	3.151E-05	0.786	2.857E-06	1.324E-05	12017	2.899	0.574	2.772E-01	29.86
P2_11		9.542	14.160	9.958E-04	0.952	8.027E-04	1.137E-02	14.00	4.460	3.616E-05	0.758	2.237E-06	9.975E-06	15955	2.416	0.529	3.007E-01	30.58
P3_11		9.127	16.850	8.897E-04	0.940	6.791E-04	1.144E-02	13.91	8.957	4.131E-05	0.731	2.248E-06	2.015E-05	7900	2.872	0.657	2.422E-01	37.81
ave		9.3	14.7	9.901E-04	0.948	7.877E-04	1.146E-02	13.9	6.02	3.633E-05	0.758	2.448E-06	1.445E-05	11957	2.73	0.59	2.734E-01	32.7
std		0.2	1.9	9.767E-05	0.008	1.019E-04	1.074E-04	0.1	2.55	4.903E-06	0.028	3.546E-07	5.192E-06	4028	0.27	0.06	2.943E-02	4.4
std/ave		2.4 %	13.0 %	9.9 %	0.8 %	12.9 %	0.9 %	0.9 %	42.3 %	13.5 %	3.7 %	14.5 %	35.9 %	33.7 %	9.8 %	11.1 %	10.8 %	13.4 %
sem		0.1	1.1	5.639E-05	0.004	5.881E-05	6.200E-05	0.1	1.47	2.831E-06	0.016	2.047E-07	2.998E-06	2325	0.15	0.04	1.699E-02	2.5
95% CI		0.6	4.8	2.426E-04	0.019	2.530E-04	2.668E-04	0.3	6.33	1.218E-05	0.069	8.809E-07	1.290E-05	10005	0.67	0.16	7.310E-02	10.9
P1_12		11.170	17.280	8.918E-04	0.953	7.271E-04	1.256E-02	12.67	5.617	2.895E-05	0.800	3.259E-06	1.830E-05	8695	2.464	0.392	4.059E-01	36.53
P2_12		11.270	14.320	1.059E-03	0.946	8.341E-04	1.194E-02	13.33	4.002	3.091E-05	0.794	3.000E-06	1.201E-05	13257	2.300	0.365	4.366E-01	31.89
P3_12		10.430	16.200	9.672E-04	0.950	7.756E-04	1.256E-02	12.67	5.738	3.366E-05	0.774	2.700E-06	1.585E-05	10051	2.504	0.554	2.872E-01	34.87
ave		11.0	15.9	9.728E-04	0.950	7.789E-04	1.236E-02	12.9	5.12	3.117E-05	0.789	3.006E-06	1.538E-05	10668	2.42	0.44	3.766E-01	34.4
std		0.5	1.5	8.395E-05	0.004	5.356E-05	5.582E-04	0.4	0.97	2.366E-06	0.014	2.496E-07	3.174E-06	2343	0.11	0.10	7.891E-02	2.4
std/ave		4.2 %	9.4 %	8.6 %	0.4 %	6.9 %	2.9 %	2.9 %	18.9 %	7.6 %	1.7 %	8.3 %	20.6 %	22.0 %	4.5 %	23.5 %	21.0 %	6.8 %
sem		0.3	0.9	4.847E-05	0.002	3.092E-05	2.068E-04	0.2	0.56	1.366E-06	0.008	1.441E-07	1.832E-06	1353	0.06	0.06	4.556E-02	1.4
95% CI		1.1	3.7	2.085E-04	0.009	1.331E-04	8.899E-04	0.9	2.41	5.877E-06	0.034	6.201E-07	7.884E-06	5820	0.27	0.25	1.960E-01	5.8
P1_13		9.044	12.960	1.034E-03	0.952	8.329E-04	1.071E-02	14.86	5.015	2.419E-05	0.782	1.997E-06	9.812E-06	16220	2.620	0.598	2.661E-01	29.54
P2_13		14.570	13.010	1.063E-03	0.951	8.514E-04	1.108E-02	14.37	6.088	3.197E-05	0.749	1.815E-06	1.105E-05	14404	2.659	0.581	2.740E-01	36.33
P3_13		10.700	13.070	1.186E-03	0.946	9.364E-04	1.224E-02	13.00	6.213	1.857E-05	0.791	1.688E-06	1.049E-05	15177	2.749	0.617	2.578E-01	32.73
ave		11.4	13.0	1.094E-03	0.950	8.736E-04	1.134E-02	14.1	5.77	2.491E-05	0.774	1.820E-06	1.045E-05	15267	2.68	0.60	2.660E-01	32.9
std		2.8	0.1	8.053E-05	0.003	5.518E-05	7.975E-04	1.0	0.66	6.727E-06	0.022	1.345E-07	6.194E-07	911	0.07	0.02	8.068E-03	3.4
std/ave		24.8 %	0.8 %	7.4 %	0.3 %	6.3 %	7.0 %	6.8 %	11.4 %	27.0 %	2.9 %	7.4 %	5.9 %	6.0 %	2.5 %	3.0 %	3.0 %	10.3 %
sem		1.6	0.1	4.649E-05	0.002	3.186E-05	4.604E-04	0.6	0.38	3.884E-06	0.013	7.763E-08	3.576E-07	526	0.04	0.01	4.658E-03	2.0
95% CI		7.0	0.3	2.000E-04	0.008	1.371E-04	1.981E-03	2.4	1.64	1.671E-05	0.055	3.340E-07	1.539E-06	2264	0.16	0.05	2.004E-02	8.4
P1_14		12.090	13.960	1.159E-03	0.948	9.231E-04	1.289E-02	12.35	6.155	2.252E-05	0.820	3.200E-06	1.970E-05	8080	2.921	0.570	2.791E-01	35.13
P2_14		15.720	12.040	1.119E-03	0.960	9.355E-04	1.126E-02	14.13	4.954	4.590E-05	0.710	1.503E-06	7.445E-06	21377	2.533	0.464	3.428E-01	35.25
P3_14		12.780	16.300	9.708E-04	0.945	7.612E-04	1.241E-02	12.83	9.284	2.207E-05	0.813	3.193E-06	2.964E-05	5370	2.666	0.538	2.960E-01	41.03
ave		13.5	14.1	1.083E-03	0.951	8.733E-04	1.219E-02	13.1	6.80	3.026E-05	0.781	2.632E-06	1.893E-05	11609	2.71	0.52	3.060E-01	37.1
std		1.9	2.1	9.887E-05	0.008	9.728E-05	8.337E-04	0.9	2.24	1.354E-05	0.061	9.778E-07	1.112E-05	8567	0.20	0.05	3.301E-02	3.4
std/ave		14.2 %	15.1 %	9.1 %	0.9 %	11.1 %	6.8 %	7.0 %	32.9 %	44.8 %	7.9 %	37.2 %	58.7 %	73.8 %	7.3 %	10.4 %	10.8 %	9.1 %
sem		1.1	1.2	5.708E-05	0.005	5.616E-05	4.813E-04	0.5	1.29	7.819E-06	0.035	5.646E-07	6.419E-06	4946	0.11	0.03	1.906E-02	1.9
95% CI		4.8	5.3	2.456E-04	0.020	2.417E-04	2.071E-03	2.3	5.55	3.364E-05	0.152	2.429E-06	2.762E-05	21282	0.49	0.13	8.201E-02	8.4
P1_15		9.358	15.290	1.130E-03	0.945	8.941E-04	1.367E-02	11.64	6.188	2.256E-05	0.815	3.021E-06	1.869E-05	8514	2.690	0.541	2.942E-01	33.53
P2_15		12.640	14.790	1.005E-03	0.951	8.086E-04	1.196E-02	13.31	4.833	3.798E-05	0.746	2.033E-06	9.825E-06	16199	2.328	0.370	4.297E-01	34.59
P3_15		12.170	13.440	1.069E-03	0.952	8.618E-04	1.158E-02	13.74	8.165	3.462E-05	0.714	1.320E-06	1.078E-05	14767	2.683	0.585	2.721E-01	36.46
ave		11.4	14.5	1.068E-03	0.949	8.548E-04	1.240E-02	12.9	6.40	3.172E-05	0.759	2.125E-06	1.310E-05	13160	2.57	0.50	3.320E-01	34.9
std		1.8	1.0	6.240E-05	0.003	4.319E-05	1.113E-03	1.1	1.68	8.109E-06	0.052	8.542E-07	4.869E-06	4087	0.21	0.11	8.535E-02	1.5
std/ave		15.6 %	6.6 %	5.8 %	0.4 %	5.1 %	9.0 %	8.6 %	26.2 %	25.6 %	6.8 %	40.2 %	37.2 %	31.1 %	8.1 %	22.7 %	25.7 %	4.3 %
sem		1.0	0.6	3.603E-05	0.002	2.494E-05	6.426E-04	0.6	0.97	4.681E-06	0.030	4.932E-07	2.811E-06	2360	0.12	0.07	4.928E-02	0.9
95% CI		4.4	2.4	1.550E-04	0.008	1.073E-04	2.765E-03	2.8	4.16	2.014E-05	0.128	2.122E-06	1.209E-05	10152	0.51	0.28	2.120E-01	3.7
Drop-cast	3	$R_s (\Omega)$	$R_{PE} (\Omega)$	$Q_{CPE,PE}$	$\beta_{CPE,PE}$	$C_{PE} (F)^*$	$\tau_{PE} (s)^*$	$f_{PE}^* (Hz)$	$R_{CE} (\Omega)$	$Q_{CPE,CE}$	$\beta_{CPE,CE}$	$C_{CE} (F)^*$	$\tau_{CE} (s)^*$	$f_{CE}^* (Hz)$	$R_D (\Omega)$	$\tau_D (s)$	$f_D^* (Hz)$	$R_{TOT} (\Omega)$
D1		9.147	16.280	9.055E-04	0.943	7.008E-04	1.141E-02	13.95	8.856	3.828E-05	0.740	2.301E-06	2.038E-05	7810	2.604	0.590	2.698E-01	36.89
D2		9.586	15.300	8.465E-04	0.961	7.086E-04	1.084E-02	14.68	7.299	7.855E-05	0.731	5.056E-06	3.691E-05	4312	2.954	0.630	2.525E-01	35.14
D3		12.330	12.830	9.705E-04	0.950	7.711E-04	9.893E-03	16.09	5.154	5.282E-06	0.747	3.280E-06	1.691E-05	9414	2.275	0.533	2.984E-01	32.59
ave		10.4	14.8	9.075E-04	0.951	7.268E-04	1.071E-02	14.9	7.1	5.655E-05	0.739	3.546E-06	2.473E-05	7179	2.61	0.58	2.736E-01	34.9
std		1.7	1.8	6.203E-05	0.009	3.855E-05	7.655E-04	1.1	1.9	2.039E-05	0.008	1.397E-06	1.069E-05	2609	0.34	0.05	2.318E-02	2.2
std/ave		16.7 %	12.0 %	6.8 %	0.9 %	5.3 %	7.1 %	7.3 %	26.2 %	36.1 %	1.1 %	39.4 %	43.2 %	36.3 %	13.0 %	8.3 %	8.5 %	6.2 %
sem		1.0	1.0	3.582E-05	0.005	2.226E-05	4.420E-04	0.6	1.1	1.177E-05	0.005	8.064E-07	6.170E-06	1506	0.20	0.03	1.338E-02	1.2
95% CI		4.3	4.4	1.541E-04	0.022	9.577E-05	1.902E-03	2.7	4.6	5.066E-05	0.020	3.469E-06	2.655E-05	6481	0.84	0.12	5.758E-02	5.4

* Quantities marked with "*" are calculated from the values unmarked values in the previous columns. The unmarked values were obtained by fitting an equivalent circuit model to the measured EIS data.

Comparison of two groups

SERIES R		PHOTOELECTRODE							COUNTER ELECTRODE						DIFFUSION			TOTAL R
N	R_s (Ω)	R_{PE} (Ω)	$Q_{CPE,PE}$ ($\cdot 10^{-3}$)	$\beta_{CPE,PE}$	C_{PE} (mF) *	τ_{PE} (ms) *	f_{PE}^+ (Hz) *	R_{CE} (Ω)	$Q_{CPE,CE}$ ($\cdot 10^{-3}$)	$\beta_{CPE,CE}$	C_{CE} (μ F) *	τ_{CE} (μ s) *	f_{CE}^+ (kHz) *	R_D (Ω)	τ_D (s)	f_D^+ (mHz) *	R_{TOT} (Ω)	
1000h																		
11 DS	3	9.3 ± 0.2	14.7 ± 1.9	0.99 ± 0.1	0.95 ± 0.01	0.79 ± 0.1	11.5 ± 0.1	14 ± 0	6.02 ± 2.55	0.04 ± 0	0.76 ± 0.03	2.4 ± 0.4	14.5 ± 5.2	12 ± 4	2.7 ± 0.3	0.59 ± 0.06	273 ± 29	33 ± 4
	std/ave	2 %	13 %	10 %	1 %	13 %	1 %	1 %	42 %	13 %	4 %	14 %	36 %	34 %	10 %	11 %	11 %	13 %
12 DS	3	11 ± 0.5	15.9 ± 1.5	0.97 ± 0.08	0.95 ± 0	0.78 ± 0.05	12.4 ± 0.4	13 ± 0	5.12 ± 0.97	0.03 ± 0	0.79 ± 0.01	3 ± 0.2	15.4 ± 3.2	11 ± 2	2.4 ± 0.1	0.44 ± 0.1	377 ± 79	34 ± 2
	std/ave	4 %	9 %	9 %	0 %	7 %	3 %	3 %	19 %	8 %	2 %	8 %	21 %	22 %	4 %	23 %	21 %	7 %
13 DS	3	11.4 ± 2.8	13 ± 0.1	1.09 ± 0.08	0.95 ± 0	0.87 ± 0.06	11.3 ± 0.8	14 ± 1	5.77 ± 0.66	0.02 ± 0.01	0.77 ± 0.02	1.8 ± 0.1	10.4 ± 0.6	15 ± 1	2.7 ± 0.1	0.6 ± 0.02	266 ± 8	33 ± 3
	std/ave	25 %	1 %	7 %	0 %	6 %	7 %	7 %	11 %	27 %	3 %	7 %	6 %	6 %	2 %	3 %	3 %	10 %
14 DS	3	13.5 ± 1.9	14.1 ± 2.1	1.08 ± 0.1	0.95 ± 0.01	0.87 ± 0.1	12.2 ± 0.8	13 ± 1	6.8 ± 2.24	0.03 ± 0.01	0.78 ± 0.06	2.6 ± 1	18.9 ± 11.1	12 ± 9	2.7 ± 0.2	0.52 ± 0.05	306 ± 33	37 ± 3
	std/ave	14 %	15 %	9 %	1 %	11 %	7 %	7 %	33 %	45 %	8 %	37 %	59 %	74 %	7 %	10 %	11 %	9 %
15 DS	3	11.4 ± 1.8	14.5 ± 1	1.07 ± 0.06	0.95 ± 0	0.85 ± 0.04	12.4 ± 1.1	13 ± 1	6.4 ± 1.68	0.03 ± 0.01	0.76 ± 0.05	2.1 ± 0.9	13.1 ± 4.9	13 ± 4	2.6 ± 0.2	0.5 ± 0.11	332 ± 85	35 ± 1
	std/ave	16 %	7 %	6 %	0 %	5 %	9 %	9 %	26 %	26 %	7 %	40 %	37 %	31 %	8 %	23 %	26 %	4 %
Drop-cast	3	10.4 ± 1.7	14.8 ± 1.8	0.91 ± 0.06	0.95 ± 0.01	0.73 ± 0.04	10.7 ± 0.8	15 ± 1	7.1 ± 1.86	0.06 ± 0.02	0.74 ± 0.01	3.5 ± 1.4	24.7 ± 10.7	7 ± 3	2.6 ± 0.3	0.58 ± 0.05	274 ± 23	35 ± 2
	std/ave	17 %	12 %	7 %	1 %	5 %	7 %	7 %	26 %	36 %	1 %	39 %	43 %	36 %	13 %	8 %	8 %	6 %
15 DS and drop-cast difference		10.0 %	-2.0 %	17.7 %	-0.2 %	17.6 %	15.8 %	-13.5 %	-10.0 %	-43.9 %	2.6 %	-40.1 %	-47.0 %	83.3 %	-1.7 %	-14.7 %	21.3 %	0.0 %
p-value		0.509	0.815	0.034	0.765	0.019	0.105	0.088	0.650	0.158	0.586	0.221	0.191	0.112	0.859	0.323	0.358	0.993

* Quantities marked with *** are calculated from the values unmarked values in the previous columns. The unmarked values were obtained by fitting an equivalent circuit model to the measured EIS data.

EIS measurement analysis of the cells after the aging test

The photoelectrode parameter set of all samples are dominated by results with low standard deviations meaning that the sufficient experimental accuracy was obtained. 15 DS inkjet-printed sample group, which has the lowest Pt loading amongst the inkjet printed samples (double Pt loading as the drop-cast samples), resulted almost the same charge transfer resistance value as the drop-cast sample.

Almost all type of cells exhibited high standard deviations in R_{CE} ($=R'_{CT}$).

Comparison of each group before and after aging

SERIES R		PHOTOELECTRODE							COUNTER ELECTRODE						DIFFUSION			TOTAL R
N	R_s (Ω)	R_{PE} (Ω)	$Q_{CPE,PE}$ ($\cdot 10^{-3}$)	$\beta_{CPE,PE}$	C_{PE} (mF) *	τ_{PE} (ms) *	f_{PE}^+ (Hz) *	R_{CE} (Ω)	$Q_{CPE,CE}$ ($\cdot 10^{-3}$)	$\beta_{CPE,CE}$	C_{CE} (μ F) *	τ_{CE} (μ s) *	f_{CE}^+ (kHz) *	R_D (Ω)	τ_D (s)	f_D^+ (mHz) *	R_{TOT} (Ω)	
11 DS																		
Initial	3	8.3 ± 0.6	17.1 ± 1.4	1.08 ± 0.03	0.95 ± 0	0.86 ± 0.03	14.8 ± 0.9	11 ± 1	10.6 ± 1.9	0.04 ± 0.01	0.83 ± 0.02	6.8 ± 0.1	72.3 ± 12.7	2 ± 0	3.4 ± 0.3	0.62 ± 0.08	259 ± 36	39 ± 4
std/ave		7%	8%	3%	0%	3%	6%	6%	18%	19%	2%	2%	18%	19%	10%	13%	14%	9%
1000h	3	9.3 ± 0.2	14.7 ± 1.9	0.99 ± 0.1	0.95 ± 0.01	0.79 ± 0.1	11.5 ± 0.1	14 ± 0	6 ± 2.5	0.04 ± 0	0.76 ± 0.03	2.4 ± 0.4	14.5 ± 5.2	12 ± 4	2.7 ± 0.3	0.59 ± 0.06	273 ± 29	33 ± 4
std/ave		2%	13%	10%	1%	13%	1%	1%	42%	13%	4%	14%	36%	34%	10%	11%	11%	13%
Difference		11.8%	-13.9%	-8.0%	0.0%	-8.9%	-22.4%	28.5%	-43.3%	-0.7%	-8.1%	-64.1%	-80.0%	431.0%	-19.5%	-5.5%	5.4%	-16.9%
p-value		0.145	0.064	0.310	0.925	0.320	0.024	0.015	0.068	0.969	0.085	0.004	0.008	0.044	0.004	0.379	0.385	0.054
12 DS																		
Initial	3	9.7 ± 0.5	18.1 ± 1.2	0.99 ± 0.06	0.95 ± 0	0.79 ± 0.05	14.3 ± 0.3	11 ± 0	10.3 ± 1.4	0.03 ± 0	0.83 ± 0.01	6.4 ± 0.4	65.9 ± 6.6	2 ± 0	2.8 ± 0.4	0.45 ± 0.13	369 ± 95	41 ± 2
std/ave		5%	7%	6%	0%	7%	2%	2%	13%	7%	1%	6%	10%	10%	16%	28%	26%	6%
1000h	3	11 ± 0.5	15.9 ± 1.5	0.97 ± 0.08	0.95 ± 0	0.78 ± 0.05	12.4 ± 0.4	13 ± 0	5.1 ± 1	0.03 ± 0	0.79 ± 0.01	3 ± 0.2	15.4 ± 3.2	11 ± 2	2.4 ± 0.1	0.44 ± 0.1	377 ± 79	34 ± 2
std/ave		4%	9%	9%	0%	7%	3%	3%	19%	8%	2%	8%	21%	22%	4%	23%	21%	7%
Difference		12.8%	-12.2%	-1.3%	0.1%	-1.7%	-13.8%	16.1%	-50.4%	-4.4%	-5.0%	-53.0%	-76.6%	338.6%	-13.6%	-3.5%	2.0%	-16.0%
p-value		0.002	0.030	0.443	0.735	0.178	0.015	0.017	0.011	0.019	0.006	0.006	0.008	0.026	0.181	0.452	0.669	0.020
13 DS																		
Initial	3	10 ± 1.1	17.4 ± 0.5	1.03 ± 0.08	0.94 ± 0	0.79 ± 0.08	13.8 ± 1.2	12 ± 1	12.2 ± 0.9	0.03 ± 0	0.83 ± 0.02	5.3 ± 0.3	64.3 ± 4.2	2 ± 0	3.2 ± 0.3	0.59 ± 0.02	269 ± 10	43 ± 2
std/ave		11%	3%	8%	0%	10%	9%	9%	7%	16%	3%	6%	7%	7%	9%	4%	4%	5%
1000h	3	11.4 ± 2.8	13 ± 0.1	1.09 ± 0.08	0.95 ± 0	0.87 ± 0.06	11.3 ± 0.8	14 ± 1	5.8 ± 0.7	0.02 ± 0.01	0.77 ± 0.02	1.8 ± 0.1	10.4 ± 0.6	15 ± 1	2.7 ± 0.1	0.6 ± 0.02	266 ± 8	33 ± 3
std/ave		25%	1%	7%	0%	6%	7%	7%	11%	27%	3%	7%	6%	6%	2%	3%	3%	10%
Difference		13.9%	-25.5%	6.2%	1.2%	10.3%	-17.7%	21.3%	-52.7%	-11.2%	-6.5%	-65.5%	-83.7%	514.7%	-16.2%	1.0%	-1.0%	-23.3%
p-value		0.342	0.004	0.088	0.074	0.074	0.016	0.006	0.010	0.132	0.000	0.002	0.002	0.002	0.055	0.795	0.790	0.005
14 DS																		
Initial	3	11.7 ± 1	17.2 ± 1.7	1.03 ± 0.07	0.94 ± 0.01	0.81 ± 0.04	13.9 ± 1.9	12 ± 2	11.4 ± 2.7	0.03 ± 0.01	0.83 ± 0.02	5.3 ± 0.5	60.7 ± 18.8	3 ± 1	3 ± 0.4	0.54 ± 0.04	295 ± 24	43 ± 4
std/ave		9%	10%	7%	1%	5%	14%	15%	23%	20%	3%	9%	31%	35%	13%	8%	8%	8%
1000h	3	13.5 ± 1.9	14.1 ± 2.1	1.08 ± 0.1	0.95 ± 0.01	0.87 ± 0.1	12.2 ± 0.8	13 ± 1	6.8 ± 2.2	0.03 ± 0.01	0.78 ± 0.06	2.6 ± 1	18.9 ± 11.1	12 ± 9	2.7 ± 0.2	0.52 ± 0.05	306 ± 33	37 ± 3
std/ave		14%	15%	9%	1%	11%	7%	7%	33%	45%	8%	37%	59%	74%	7%	10%	11%	9%
Difference		15.7%	-18.2%	5.3%	0.8%	8.4%	-12.5%	13.0%	-40.4%	11.3%	-6.2%	-49.9%	-68.8%	311.0%	-9.0%	-3.3%	3.7%	-14.2%
p-value		0.356	0.278	0.215	0.310	0.247	0.285	0.318	0.245	0.799	0.387	0.076	0.136	0.246	0.352	0.745	0.736	0.263
15 DS																		
Initial	3	9.7 ± 0.7	16.9 ± 0.5	1.11 ± 0.03	0.94 ± 0.01	0.85 ± 0.08	14.4 ± 0.9	11 ± 1	12.7 ± 1.4	0.03 ± 0.01	0.83 ± 0.02	5.2 ± 0.4	65 ± 2.7	2 ± 0	3.1 ± 0.3	0.6 ± 0.02	266 ± 11	42 ± 2
std/ave		7%	3%	3%	2%	9%	6%	6%	11%	23%	3%	8%	4%	4%	9%	4%	4%	4%
1000h	3	11.4 ± 1.8	14.5 ± 1	1.07 ± 0.06	0.95 ± 0	0.85 ± 0.04	12.4 ± 1.1	13 ± 1	6.4 ± 1.7	0.03 ± 0.01	0.76 ± 0.05	2.1 ± 0.9	13.1 ± 4.9	13 ± 4	2.6 ± 0.2	0.5 ± 0.11	332 ± 85	35 ± 1
std/ave		16%	7%	6%	0%	5%	9%	9%	26%	26%	7%	40%	37%	31%	8%	23%	26%	4%
Difference		17.3%	-14.2%	-4.1%	1.4%	0.3%	-13.8%	16.4%	-49.5%	18.3%	-8.7%	-58.8%	-79.9%	437.0%	-16.7%	-16.9%	25.0%	-17.7%
p-value		0.359	0.034	0.304	0.305	0.941	0.117	0.122	0.069	0.610	0.245	0.043	0.002	0.044	0.087	0.320	0.347	0.056
Drop-cast																		
Initial	3	10.4 ± 0.8	16.1 ± 1.2	1.09 ± 0.1	0.93 ± 0.01	0.82 ± 0.11	13.3 ± 2.6	12 ± 2	11.8 ± 0.5	0.05 ± 0.01	0.79 ± 0.01	6.7 ± 1.6	79.2 ± 20.6	2 ± 1	3 ± 0.6	0.59 ± 0.07	273 ± 36	41 ± 2
std/ave		8%	7%	9%	1%	14%	20%	19%	4%	11%	1%	23%	26%	25%	19%	12%	13%	5%
1000h	3	10.4 ± 1.7	14.8 ± 1.8	0.91 ± 0.06	0.95 ± 0.01	0.73 ± 0.04	10.7 ± 0.8	15 ± 1	7.1 ± 1.9	0.06 ± 0.02	0.74 ± 0.01	3.5 ± 1.4	24.7 ± 10.7	7 ± 3	2.6 ± 0.3	0.58 ± 0.05	274 ± 23	35 ± 2
std/ave		17%	12%	7%	1%	5%	7%	7%	26%	36%	1%	39%	43%	36%	13%	8%	8%	6%
Difference		-0.7%	-8.3%	-17.0%	2.0%	-11.2%	-19.3%	21.2%	-39.6%	19.4%	-6.7%	-47.2%	-68.8%	242.2%	-12.3%	-0.8%	0.2%	-15.6%
p-value		0.967	0.312	0.143	0.014	0.291	0.264	0.249	0.039	0.456	0.041	0.002	0.017	0.061	0.472	0.940	0.985	0.034

* Quantities marked with "*" are calculated from the values unmarked values in the previous columns. The unmarked values were obtained by fitting an equivalent circuit model to the measured EIS data.

About statistical analysis

Criteria for practically significant difference and acceptable sample-to-sample variation (relative standard deviation, std/ave)

Criteria **	R_s (Ω)	R_{PE} (Ω)	$Q_{CPE,PE}$	$\beta_{CPE,PE}$	C_{PE} (F) *	τ_{PE} (s) *	f_{PE}^* (Hz) *	R_{CE} (Ω)	$Q_{CPE,CE}$	$\beta_{CPE,CE}$	C_{CE} (F) *	τ_{CE} (s) *	f_{CE}^* (Hz) *	R_D (Ω)	τ_D (s)	f_D^* (Hz) *	R_{TOT} (Ω)
Acceptable relative stdev.	10 %	10 %	10 %	10 %	10 %	10 %	10 %	10 %	10 %	10 %	10 %	10 %	10 %	10 %	10 %	10 %	10 %
Practically signif. difference	20 %	20 %	20 %	20 %	20 %	20 %	20 %	20 %	20 %	20 %	20 %	20 %	20 %	20 %	20 %	20 %	20 %

* Quantities marked with *** are calculated from the values unmarked values in the previous columns. The unmarked values were obtained by fitting an equivalent circuit model to the measured EIS data.

** These criteria are subjectively chosen by the researcher to set a criteria for satisfactory repeatability of one type of sample and practically relevant difference between different type of samples

Statistical testing

Statistical confidence level	95 %
α	0.05

The p-value is calculated with two-tailed two-sample t-test with unequal variances

Underlined in the comparison table are:

- Relative standard deviations (std/ave) larger than or equal to the acceptable value (also highlighted with pink in the data table)
- Differences larger than or equal to the practical significance level
- p-values lower than or equal to α (e.g. 0.05 for 5 % significance)

Nomenclature

N	number of samples
ave	average
std	standard deviation
std/ave	relative standard deviation compared to average
sem	standard error of the mean
95%CI	Half of the full 95 % confidence interval based on Student's t-distribution
Difference	relative difference of average values: Printed vs reference, or Batch 2 vs Batch 1.

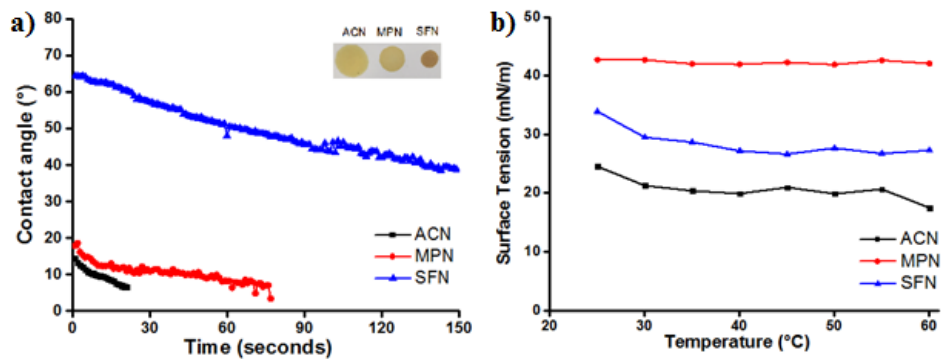
EIS measurement analysis of aging test

Even though R_s values (sheet resistance) remained the same in almost all the cells, a drop in R_{CE} ($=R'_{CT}$) was observed after the aging test. This means that all the counter electrodes cells remained stable, or actually improved. Also it can be concluded that all the Pt layers remained attached to the FTO surface and no detachment of the catalyst has been taken place over the 1000 h aging test period.

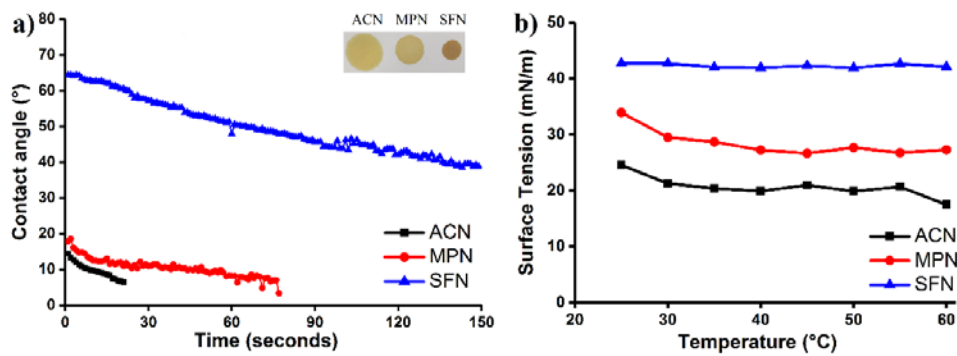
APPENDIX 6

- Figure 4b, in Publication II, had a mistake on the symbols representing the data. The surface tension values of ACN and SFN were inverted.

Presented figure:



Correct figure:



- In Publication II, the caption of Figure 2 mentions the shear rate of 50 s^{-1} . The correct value should be 500 s^{-1} as mentioned in the text.